UNIVERSITÀ
DEGLI STUDI
DI PADOVA

Sede Amministrativa: Università degli Studi di Padova

Dipartimento di Ingegneria Industriale

SCUOLA DI DOTTORATO DI RICERCA IN INGEGNERIA INDUSTRIALE
INDIRIZZO: INGEGNERIA CHIMICA
CICLO XXV

DEVELOPMENT OF MICROFLUIDIC CELL CULTURE TECHNOLOGY FOR THE STUDY OF TYPE 2 DIABETES

Direttore della Scuola: Ch.mo Prof. Paolo Colombo
Coordinatore d'indirizzo: Ch.mo Prof. Alberto Bertucco
Supervisore: Ch.mo Prof. Nicola Elvassore

Dottorando: Alessandro Zambon

Foreword

The work of this PhD program was performed at “Dipartimento di Ingegneria Industriale sede M via marzolo” of “Università degli Studi di Padova” and at “Venetian Institute of Molecular Medicine” of “Fondazione per la ricerca biomedica avanzata onlus”. Part of the design and fabrication of multilayer microfluidic platform for study type 2 diabetes was carried out at the Bioengineering Department of Stanford University, Stanford (CA), under the supervision of Prof. S. R. Quake.

I would like to thank Alice Zoso for her support in these years, and Prof. S. R. Quake for the great opportunity of working with his group in the “Quake lab” at Stanford.

All the material reported in this dissertation is original unless explicit references to studies carried out by other people are indicated.

During this PhD program the following publications have been produced:

1. Cimetta E, Franzoso M, Trevisan M, Serena E, Zambon A, Giulitti S, Barzon L, Elvassore N. 2012. “Microfluidic-driven viral infection on cell cultures: theoretical and experimental study”. *Biomicrofluidics* 6, 024127

2. Lamberti F, Luni C., Zambon A., Serra P.A., Giomo M., Elvassore N. 2012. “Flow biosensing and sampling in indirect electrochemical detection”. Biomicrofluidic 6(2): 024114–024114-13

3. Martewicz S, Michielin F, Serena E, Zambon A, Mongillo M, Elvassore N. 2012. “Reversible alteration of calcium dynamics in cardiomyocytes during acute hypoxia transient in a microfluidic platform”. Integrative Biology 4(2):153-164

4. Zambon A., Zoso A., Luni C., Frommer W., Elvassore N. High resolution measurement of glucose uptake within microfluidic device in myoblast. To be submitted to Integrative Biology

5. Zambon A., Zoso A., Magrofuco M., Flaibani M., Quake S.R., Fadini G.P., Elvassore N. "Diabetes on a chip". In writing.

Part of this work have been presented at the following national and international conference:

1. Microfluidic chip for high-resolution glucose uptake measurements on patient-derived adipose tissue culture. BMES 2012, Atlanta, Georgia (USA), October 24th– 27th 2012.

2. Patient-specific insulin resistance investigation through in vitro microfluidic glucose uptake assay. 11th Annual VIMM meeting. Marostica (VI), Italy October 19th – 20th 2012.

3. Sviluppo di una piattaforma microfluidica automatizzata per la misura ad alta risoluzione del consumo di glucosio in tessuto adiposo e muscolare. GRICU 2012, Pescara, Italy, September 16th – 19th 2012.

4. Automazione e integrazione di piattaforme microfluidiche. GRICU 2012, Pescara, Italy, September 16th – 19th 2012.

5. Foto-pattern in situ per l'adesione e la coltura selettiva di cellule in microfluidica. GRICU 2012, Pescara, Italy, September 16th – 19th 2012.

6. On-chip flow biosensing and sampling. GEI-ERA 2012, Santa Marina Salina (ME), Italy, June 17th – 21st 2012.

7. Probing the Effects of Cyanobacteria Cell Density on Growth Rate Using a Parallel Microfluidic Platform. ASM 2012 112th General Meeting. San Francisco, California. June 16th-19th.

8. Reversible alteration of calcium dyanamic in cardyomyocytes during acute hypoxia transient in microfluidic platform. Lab-on-a-chip World Congress 2011, South San Francisco (CA), September 29th-30th.

9. Engineering an *in vitro* model of human muscle dystrophy for highthroughput screenings and development of therapeutic strategies. Riva del Garda (TN), Italy. March 7th – 9th 2011.

10. Alteration of calcium dynamics in murine cardiomyocytes during acute hypoxia. Keystone Symposia on Molecular and Cellular Biology. Mechanisms of Cardiac Growth, Death and Regeneration, Keystone, Colorado, USA. February 22nd – 27th, 2011.

11. Microfluidic technologies for biotechnology applications. SAB visit. Venetian Institute of Molecular Medicine, Padova, Italy. 20th-21st February 2011.

12. Three-dimensional human adipose organ culture in microfluidic system for multi-parametric patient-specific screening. Annual VIMM meeting. Marostica (VI), Italy November 12th – 13th 2010.

13. Microfluidic technology for multi-parametric studies on patient-derived three-dimensional human adipose tissue model. 46th EASD Annual Meeting. Stockholm, Sweden September 20th – 24th 2010.

14. Microfluidic technologies for cell culture experiments during space flights. International Info Days on the 4th Space call and 3rd Galileo call in FP7 at the University of Padova. Padova, Italy, September 15th – 16th 2010.

15. An in vitro model for cardiac cell therapy: coupling a microfluidic platform with arrayed human embryonic stem cells-derived cardiomyocytes for screening pathological conditions. Frontiers in Cardiovascular Biology, Berlin, Germany. July 15th-19th 2010.

16. Highthroughput screening on human Embryonic Stem Cells-derived cardiomyocytes. International Society for Heart Research, XXth World Congress, Kyoto, Japan, May 13-16th 2010.

17. Microfluidic-driven processes enhance control and optimization of adenoviral infection efficiency on cell cultures. 4th European Congress of Virology, Cernobbio, Italy April, 7th-11th 2010.

Summary

Type 2 Diabetes Mellitus (T2DM) is a multi-factorial disease due to metabolic disorder with injuries in glucose homeostasis and body's glucose uptake. The complexity of this disease led to the use of different classes of drugs acting with different mechanisms and targets and with effects that often change between patients.
The number of people in the world with diagnosed T2DM is constantly increasing and consequently the cost for healthcare. Nowadays, a defined cure for T2DM patients has been not clearly identified.

In the study of diabetes, animal models are one of the most popular systems used to underline its pathogenesis and to screen new drugs before clinical trials on humans. Even though their undeniable utility, they showed many limitations. Moreover, studies *in vivo* in humans are possible but tremendously expensive and require a huge effort in terms of ethical approval and safety issues. Therefore *in vivo* studies often do not permit an evaluation at specific tissue level: their interplay complexity allow a very difficult outcome interpretation. For all these reasons there is a great interest in developing alternative in vitro models that facilitate pharmaceutical and pathology studies.

Thus, the aim of this thesis is the development of an *in vitro* model that closely resemble the human physiology and mimic the pathophysiological conditions of type 2 diabetes. In particular, this work concerns the design and development of microfluidic technology for the study of insulin resistance and glucose uptake in cell and tissue culture from Type 2 Diabetes patients. High temporal resolution glucose uptake measurements were achieved by coupling microfluidic technologies and glucose detection measurements

with a non invasive manner. The technology was applied to skeletal muscle and *ex vivo* adipose tissue, with the obtainment of high sensitive and reproducible experiments.

During this PhD, a microfluidic platform was developed and fabricated with multilayer soft lithography techniques. The platform was able to integrate 2D (cells) and 3D (*ex vivo* tissue) culture allowing long term viability and metabolic activity. High experiment feasibility was achieved by the long term culture capability.

Micro components were included into the device allowing automation and liquid handling control. Integrated microvalves and micropumps allowed the development of injection systems for high spatio temporal control of biochemical stimulus delivery, such as insulin and other anti-diabetic drugs.
Glucose uptake was investigated measuring high temporal resolution glucose concentration in the downstream culture chamber medium by high sensitive analytical measurements on nanoliter sampling, providing glucose dynamic with temporal resolution of minutes.
The measurement of intracellular glucose concentration was evaluated by encoded FRET nanosensor. The coupling between intracellular and extracellular glucose detection allowed the determination of novel glucose uptake and glycolytic rate evaluation technique within the cell.

These results show a good potential in future pharmaceutical and clinical experimentation, in which the use of a microfluidic *ex vivo* human patient assays could be useful in drug screening studies and patient specific therapies.

Sommario

Il Diabete Mellito di Tipo 2 (T2DM) è una patologia molto complessa provocata da una disfunzione a livello omeostatico che ha come conseguenza l'alterazione del normale consumo di glucosio da parte delle cellule e, conseguentemente, una elevata concentrazione di glucosio nel sangue. La complessità della malattia comporta l'utilizzo di molti farmaci che agiscono con diversi meccanismi e modi, e con effetti che spesso sono differenti tra pazienti.

Il numero di persone nel mondo con T2DM diagnosticato è sempre più elevato e con esso l'impatto sul costo dell'assistenza sanitaria. Al giorno d'oggi una cura definita per questa patologia non esiste.

I modelli animali sono tra i sistemi più usati nello studio della patologia e per valutare l'effetto di nuovi farmaci in fase preclinica. Anche se validi, ed essendo tuttora i più usati, questi modelli mostrano numerose limitazioni. Gli studi *in vivo* su uomo sono possibili ma molto costosi; richiedono inoltre un enorme contributo in termini di provvedimenti etici e di sicurezza. Molto spesso non si riesce ad ottenere una valutazione a livello di singolo tessuto con la conseguente difficoltà di una corretta interpretazione dei risultati. Per tutte queste ragioni è elevato l'interesse nello sviluppare modelli *in vitro* alternativi che facilitino da un lato lo studio della patologia e dall'altro la ricerca farmacologica.

Obiettivo di questa tesi è di sviluppare un modello *in vitro* rappresentativo della fisiologia di tessuti umani in grado di simulare la fisiopatologia del Diabete Mellito di Tipo 2. In particolare, questa tesi riporta la progettazione e lo sviluppo di una tecnologia microfluidica applicata allo studio dell'insulino-resistenza e del consumo di glucosio in

colture cellulari e tessuti umani *in vitro*. Attraverso l'impiego di tecnologie microfluidiche, applicate a tecniche di misurazione del glucosio, è stato possibile misurare con elevata risoluzione temporale il consumo di glucosio in modo completamente non invasivo. La tecnologia è stata applicata al muscolo scheletrico e al tessuto adiposo, ottenendo elevato grado di riproducibilità degli esperimenti e sensibilità nelle misure.

Durante questa tesi alcuni prototipi di piattaforma microfluidica sono stati sviluppati e prodotti attraverso tecniche di *soft* litografia multistrato. Il dispositivo è in grado di integrare al suo interno sia colture cellulari 2D che di tessuto 3D *ex vivo*, mantenendole metabolicamente attive e vitali per diversi giorni. La capacità di coltura a lungo termine ottenuta ha permesso elevata flessibilità degli esperimenti.

Il dispositivo è stato dotato di microcomponenti integrati per il controllo e la movimentazione di liquidi. Microvalvole e micropompe integrate permettono un elevato grado di automazione della piattaforma, con possibilità di controllo *off chip* tramite software. Tali sistemi di controllo hanno permesso lo sviluppo di sistemi di iniezione per un elevato controllo spazio temporale di sostanze biochimiche, come ad esempio insulina o altri farmaci antidiabetici.

Il consumo di glucosio è stato valutato attraverso misure ad alta risoluzione del *medium* di coltura post camera attraverso tecniche analitiche di misura su nanolitri di campioni, generando profili temporali di concentrazione di glucosio con risoluzione di decine di minuti. È stata misurata la concentrazione di glucosio intracellulare attraverso nano sensori FRET. L'accoppiamento di queste due tecniche ha permesso una valutazione innovativa del consumo di glucosio e attività cellulare.

I risultati ottenuti rivelano buone potenzialità per future sperimentazioni farmaceutiche e cliniche. Lo sviluppo di tecnologie microfluidiche integrate a colture *ex vivo* derivate da pazienti può dare buoni risultati nello sviluppo di terapie paziente specifiche.

Contents

Chapter 1

Introduction and motivation

Type 2 Diabetes is a chronic disease, in which the defects in action or secretion of insulin lead to a reduction in the body's glucose uptake. Data from ATLAS report that in 2012 more than 371 million people in the world have diabetes and the number is increasing in every country. 4.8 million people died of diabetes and more than 471 billion USD were spent on healthcare for diabetes. Actually, a defined therapeutically strategy has not been univocally identified. In this perspective there is an enormous public and economic interest in figuring out an alternative methodology that facilitates the therapy development process and the study of this disease.

1.1 Introduction: Type 2 Diabetes

Type 2 Diabetes Mellitus (T2DM or DM) is a metabolic disorder that results from defects in insulin secretion, insulin action or both. It is characterized by chronic hyperglycemia. The effects of DM include failure of various organs (e.g. heart, kidney) [1].

The earliest detectable abnormality is impairment in body's ability to respond to insulin. Impaired tissue sensitivity to insulin (insulin resistance) involves both hepatic and peripheral tissues (muscle and adipose tissues) [2].

Changes in human lifestyle over the last century have resulted in a dramatic increase in the incidence of diabetes worldwide. Nowadays Diabetes Mellitus has reached epidemic proportions [3] and affects more than 360 million individuals worldwide [39]. About 80% live in low- and middle-income countries (Figure 1.1). "If these trends continue, by 2030, some 552 million people, or one adult in 10, will have diabetes" [39]. The socio-

economical affliction of the disease relay on its associated complications (mostly cardiovascular and microvascular) [4], which impose huge efforts on health-care systems.

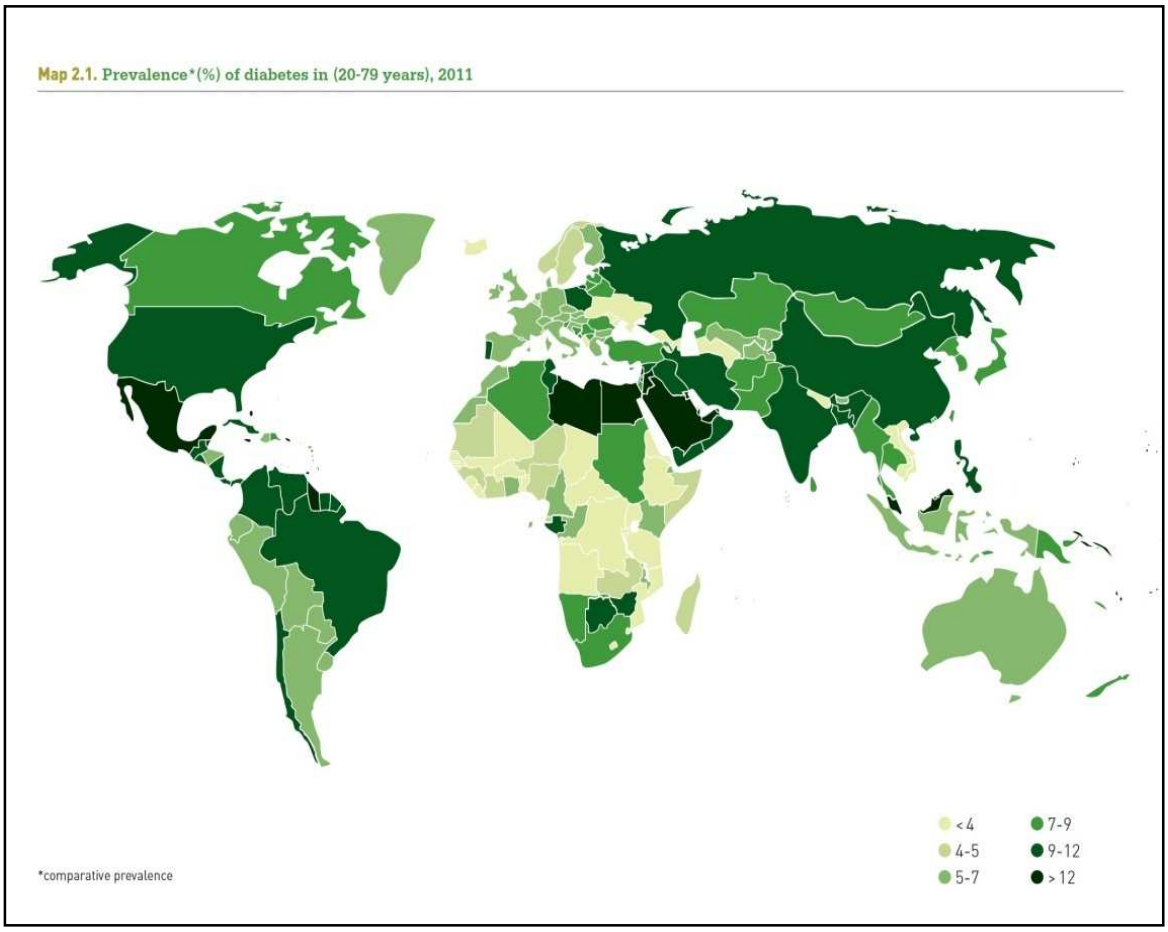

Figure 1.1: *Distribution of diabetes in the world. Data and map from: IDF – International Diabetes Federation- Atlas 2011*

After glucose ingestion, basal hematic glucose level is disrupted. The maintenance of physiological glucose homeostasis depends on three processes tightly regulated and coordinated: first of all, glucose stimulates insulin secretion by pancreatic beta-cells; insulin consequently stimulates massive glucose uptake by muscle and adipose tissue and suppresses hepatic glucose release [5].

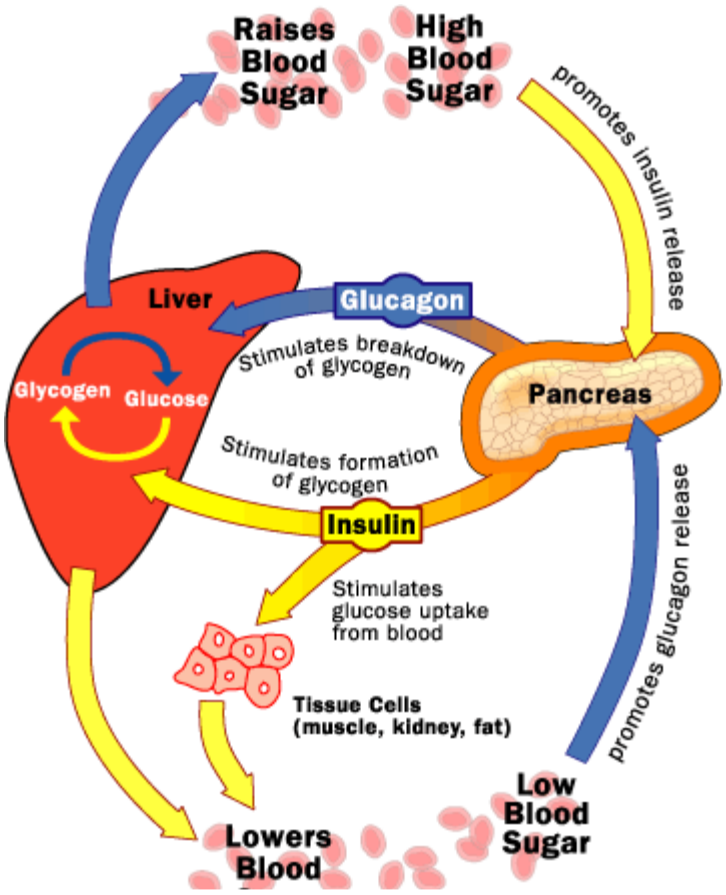

Figure 1.2: *Homeostatic balance of insulin and glucagon and their interplay in the organ's network. (Source: health.howstuffworks.com/ diabetes1.htm)*

In most T2DM patients, insulin resistance represents the primary defect for the onset of the disease. The reduced insulin-mediated glucose disposal leads to a hyperglycemia that acts with negative effects on beta-cells action and on insulin-stimulated glucose uptake itself [6]. The simultaneous presence of these two major deficiencies causes over T2DM with the correlated long-term damages, dysfunction and failure of different organs [3].

1.2 Motivation for technology development

In the study of diabetes, animal models are one of the most popular systems used to underline its pathogenesis and to screen new drugs before clinical trials on humans. To this purpose, biologists have generated mouse and rat models by transgenic overexpression or deletion of a candidate gene/protein [7].

The most popular mouse model for diabetes pathology is the mouse *ob/ob* [8] which lacks the expression of the protein leptin, a key hormone in the regulation of energy metabolism [9].

These models are widely used and showed to be of paramount usefulness in gaining understanding of biochemical mechanisms involved in the pathogenesis of diabetes [7]. However, results obtained in animal models cannot always be directly associated with humans [10].

Diabetes mechanisms can be investigated also in human patients, but these studies require ethical approval, safety issues and they are remarkably expensive.

Moreover, studies *in vivo* in humans are limited by the high variability among control subjects and T2DM patients and among patients themselves (e.g. variability on metabolic parameters such as glucose or free fatty acid plasma concentrations). This variability leads to results difficult to understand [11].

For all these reason, an alternative approach is the utilization of *in vitro* models of human derived muscle and adipose tissue.

1.3 State of the art about *in vitro* models

1.3.1 Biological *in vitro* models

In the study of molecular and biochemical mechanisms involved in diabetes, *in vitro* models of muscle and adipose tissue can result very advantageous, since skeletal muscle represents the principal tissue involved in insulin-stimulated glucose metabolism,

whereas adipose tissue is easily available and highly insulin sensitive and responsive [12].

In vitro cultures of human differentiated skeletal muscle cells are a widely diffuse model. It exhibits biochemical and molecular features of insulin-stimulated glucose metabolism comparable with the *in vivo* situation and it permits to study cells from different subjects under standardized and well-controlled experimental conditions. More importantly, skeletal muscle cells established from T2DM patients maintain the diabetic phenotype, including the decrease of insulin-dependent glucose uptake [13, 14].

Adipose tissue models are mainly based on culture of adipocytes isolated from biopsy or on organ-culture of whole adipose tissue explants. The major strength of this second method is the good maintenance of gene expression and adipocytes function within the adipose tissue for up to 2 weeks. Moreover, adipose tissue obtained from T2DM patients maintains the insulin resistance characteristics [15-17]. Furthermore, few papers have been recently published on the *in vitro* tests of anti-diabetic drugs [10, 18] for comparing their effects and studying their mechanism of action on murine and human cell lines.

1.3.2 Lab on a chip for biological studies

Although standard *in vitro* cultures are required to fully understand the molecular basis of physio-pathological responses in complex diseases, these models do not always simulate the complex cell-cell and cell-matrix interactions and the signaling dynamics exhibited *in vivo*. These lacks, together with control restrictions limiting the use of animal models, have generated interest in developing human-based assays for disease modeling and drug testing [19,20].

Microfluidic approaches can provide *in vitro* new tools useful to manipulate and transport particles and cells, to generate dynamic biochemical gradients, to provide a controlled supply of nutrients and removal of metabolites and to allow multiple and parallel analyses of specific cell culture readouts. Integration of *in vitro* cell cultures with microfluidic technologies may overcome current limitation in therapy design, by

reproducing *in vitro* models of the disease for a targeted drug investigation or toxicity evaluation, even in a patient-specific way [21].

To date, organs-on-a-chip have already been generating. An example is the generation of a "human breathing lung-on-a-chip", a microsystem capable to reproduce the complex organ response to bacteria and inflammatory cytokines introduced into the alveolar space [22]. Another example of cell integration into a microfluidic device is the generation of a liver-on-a-chip, useful for drug research and screening, with a precise control of cell microenvironment [23]. The future could be the generation of biomimetic microsystems with different organs that are integrated into a single microdevice. The complex model will be able to study physiologically relevant manners [40].

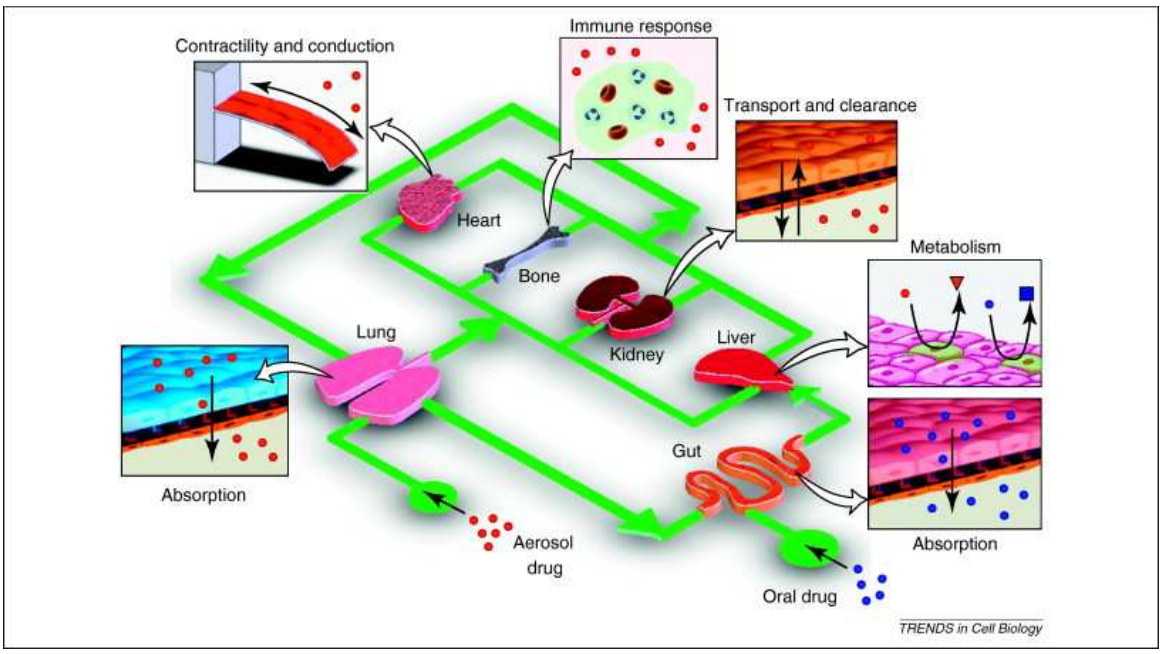

Figure 1.3: *The human-on-a-chip concept.* ***(****Source Huh et al, "From 3D to organs on chipstrend in cell biology 2011")*

Other organs-on-a-chip have been described so far (e.g. skeletal muscle [24], blood vessels [25], kidney [26], and also tumor tissue models [27]), but none of them has been reported to be specifically addressed to the study and drug testing of diabetes.

To this purpose few papers reported the behaviour of pancreatic cells on microfluidic devices. More precisely they report the maintenance of pancreatic islets in microfluidic

conditions [28], the on-line monitoring of their glucagon release [29] and the investigation of the effect of adipokines on beta-cells apoptosis [30].

The possibility to maintain cells on a chip and test their behavior referring to insulin resistance on peripheral tissues has not been so far investigated.

1.4 Rationale of microfluidic cell culture technology for the study of Type 2 Diabetes

Dramatic changes in the ability to treat diseases have resulted by innovations in the health sciences with a consequent improvement of the quality of life [31]. New drugs development can proceed along various pathways for different compounds but a general model has been developed, articulated and explained in detail elsewhere [32,33]. Drug screening demands robust, cheap and fast methods to test drug candidates [34]. Due to the increasing accessibility of such powerful tools, life scientists and bioengineers have started to use Lab on a chip technologies as platforms for cell culture, in order to better answer some fundamental biological questions [35]. The distinctive ability to integrate biosensor technology with microscopy-based readouts is peculiar of microfluidic technologies. In combination with automated imaging systems possessing high-throughput capabilities, new data processing and storage strategies, microfluidics provides new tools for highly parallel, multiplexed assays with a higher information quality [36, 37]. Microfluidics devices promise better diagnosis for sickle cell disease and others, as drug discovery platform [38]. With this perspective microfluidic technology seems to be a very good system for studying and treating of complex and multifactorial diseases such as Type 2 Diabetes.

Type 2 Diabetes led to the use of different classes of drugs acting with different mechanism and targets and with effects that often change between patients. Specific studies on human patients are possible but are tremendously expensive and require a huge effort in terms of ethical approval and safety issues. Therefore *in vivo* studies often

don't permit an evaluation at specific tissue level: their interplay complexity allow a very difficult outcome interpretation. For all these reasons, the interest in developing new models, able to contain times and costs, is continuously increasing and leads to the development of new ways to identify decision making criterias for therapies. Figure 1.4 shows the scheme of the rationale of patient specific microfluidic cell culture technology for the study of Type 2 Diabetes acting for multi-parametric screening of anti-diabetic drugs on patient-derived human skeletal muscle and adipose tissue.

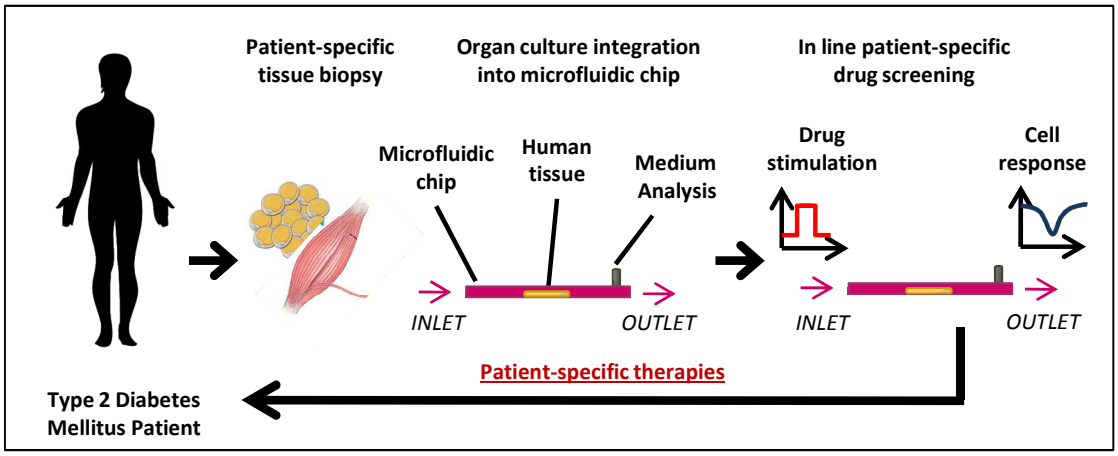

Figure 1.4: *Schematic representation of microfluidic in vitro model strategy for the study of type 2 diabetes.*

The utilization of *in vitro* models of muscle and adipose tissue may be a good alternative since the conservation of diabetic phenotype and insulin resistance characteristics have been maintained [12,13,15,16,17]. The conservation of diabetic phenotype is a crucial point and it is an essential prerequisite for a reliable screening of anti-diabetic drugs with a perspective of translational medicine and testing of *ad hoc* therapies for each patient.

In particular, through *ad hoc* microfluidic technology, it may be possible to associate the response of patient derived tissue to specific dose-time drug stimulation acting as insulin resistance antagonist, with the obtainment of useful information to create a patient specific therapy. By using microfluidic technology platforms, the time evolution of the culture conditions can be achieved by an accurate control of metabolites concentration

(such as glucose), mimicking as close as possible the physiopathological conditions. It will be possible to reproduce the pharmacokinetics and pharmacodynamics of patient specific pharmacological treatments. The microfluidic technology will highly increase the aspect-ratio between volume of the living tissue and the net medium volume in culture chamber. These intrinsic properties of microscale technology lead to high sensitivity of measuring glucose uptake. In fact, due to the very low medium volume, small glucose uptake causes high glucose concentration perturbation in the medium that can be monitored by small volume sampling or in line biosensor measurements. With this system we will be able to track the glucose concentration evolution for several days and to define the glucose profile from minutes to hours following drug stimulation. In this way the use of radiotracer fluorescent glucose analogs will be avoided, having culture condition as close as possible to physiological and physiopathological *in vivo* conditions.

1.5 Aim of this thesis

This thesis aims at the developing of microfluidic cell culture technology for the study of Type 2 Diabetes. Since insulin resistance plays a key role in Type 2 Diabetes Mellitus (T2DM) by affecting skeletal muscle glucose uptake, we aimed at developing an *in vitro* patient-specific assay for high resolution measurement of glucose uptake and glycolytic rates on patient-derived human *ex vivo* adipose tissue and skeletal muscle. Within this scenario the development of Microfluidic Large Scale integration has been specifically designed with the integration of microcomponents, such as micro-valves, micro-pumps, injectors and mixers allowing to perform *in vitro* highthroughput patient-specific tests. With this system we will be able to track the glucose concentration evolution for several days and to define the glucose profile from minutes to hours following biochemical stimulations. Microfluidic platform has been built using recent multilayer soft lithography technique and its automation has been reached by chip interface with modern software controller. The accurate time evolution control of the culture condition has been achieved by intrinsic properties of microfluidic technology applied to glucose measurement techniques. The development of microfluidic glucose-uptake and

glycolytic rates measurements has been possible by coupling different measurement strategies and levels: i) off-line glucose measurement, ii) in line glucose measurement; iii) intra cellular glucose measurement. Whereas the first method is relatively simple and requires a sampling at outlet of medium, the other two require integration of biosensors within microfluidic platform. The former one requires in line micro-biosensors placed downstream the culture chambers, the latter genetically encoded FRET glucose nanosensor.

In this thesis the evolution to get glucose uptake and glycolytic rate measurement on muscle and human *ex vivo* adipose tissue has been divided in specific chapters.
In Chapter 2 the cell culture integration within microfluidic chip is illustrated. Limitation and perspective will be discussed and alternative cell culture and *ex vivo* tissue integration will be shown.
In Chapter 3 microfluidic chip integration is reported with a Large Scale integration approach. The chip was specifically designed for Type 2 Diabetes studies.
In Chapter 4 the development of glucose uptake measurement is described. Both extracellular and intracellular glucose uptake measurement have been developed by integration of advanced glucose detection techniques with a deeply investigation at cellular level.
Chapter 5 is focused on muscle cells and adipose tissue; it reports results about high temporal resolution uptake measurement obtained during this thesis and some perspectives.
Appendix will give more details about specific contents in the chapters.

1.6 Conclusions

In the perspective of managing practices that reduce the development times and facilitate development decision-making in pharmacological drug screening process, the implementation of alternative *in vitro* models, advanced technologies and readout methodologies are crucial aspects. Moreover, the intrinsic correlation between these

three aspects can be represented the core power for new alternative method where their integration led to synergic results. In this perception it has been proposed the application of microfluidic technology for the study of type 2 diabetes by integration of *ex vivo* human tissues with the capability to measure glucose uptake without using radiotracer or fluorescent glucose analogs. The high temporal resolution of the measure will be able to investigate on the pathology with a new prospective which is not possible with traditional strategies. The possibility to study a new pharmacological treatment might offer new therapy development process, that should ultimately bring therapies to the patients with an enormous benefit for the entire society.

1.7 References

[1] Alberti KG, Zimmet PZ. 1998. Diabet Med. Jul;15(7):539-53.

[2] DeFronzo RA, Bonadonna RC, Ferrannini E. 1992. Diabetes Care. Mar;15(3):318-68.

[3] Stumvoll M, Goldstein BJ, van Haeften TW. 2005. Lancet. Apr 9-15;365(9467):1333-46.

[4] Wei M, Gaskill SP, Haffner SM, Stern MP. 1998. Jul;21(7):1167-72.

[5] Shepherd PR, Kahn BB. 1999. N Engl J Med. 1999 Jul 22;341(4):248-57.

[6] Beck-Nielsen H, Vaag A, Damsbo P, Handberg A, Nielsen OH, Henriksen JE, Thye-Rønn P. 1992. Diabetes Care. 1992 Mar;15(3):418-29.

[7] Islam MS, Wilson RD. 2012. Methods Mol Biol. 2012;933:161-74.

[8] Zhang Y, Proenca R, Maffei M, Barone M, Leopold L, Friedman JM. 1994. Nature. Dec 1;372(6505):425-32.

[9] Fève B, Bastard JP. 2012. Biochimie. 2012 Oct;94(10):2065-8.

[10] van de Venter M, Roux S, Bungu LC, Louw J, Crouch NR, Grace OM, Maharaj V, Pillay P, Sewnarian P, Bhagwandin N, Folb P. 2008. J Ethnopharmacol. 2008 Sep 2;119(1):81-6.

[11] Basu A, Dalla Man C, Basu R, Toffolo G, Cobelli C, Rizza RA. 2009. Diabetes Care. 2009 May;32(5):866-72.

[12] Ciaraldi TP, Abrams L, Nikoulina S, Mudaliar S, Henry RR. 1995. J Clin Invest. 1995 Dec;96(6):2820-7.

[13] Henry RR, Abrams L, Nikoulina S, Ciaraldi TP. 1995. Diabetes. 1995 Aug;44(8):936-46.

[14] Thompson DB, Pratley R, Ossowski V. 1996. J Clin Invest. 1996 Nov 15;98(10):2346-50.

[15] Fried S and Moustaid-Moussa N. Methods in Molecular Biology, 2001 Vol 155, 197-212

[16] Phillips SA, Ciaraldi TP, Oh DK, Savu MK, Henry RR. 2008. Am J Physiol Endocrinol Metab 295:E842–E850.

[17] Trujillo ME, Lee M-J, Sullivan S, Feng J, Schneider SH, Greenberg AS, Fried SK. 2006. J Clin Endocrinol Metab 91:1484–1490.

[18] Alonso-Castro AJ, Salazar-Olivo LA. 2008. J Ethnopharmacology 118:252–256.

[19] van der Meer AD, van den Berg A. 2012. Integr Biol (Camb). 2012 May;4(5):461-70.

[20] Ghaemmaghami AM, Hancock MJ, Harrington H, Kaji H, Khademhosseini A. 2012. Drug Discov Today. 2012 Feb;17(3-4):173-81.

[21] Neuži P, Giselbrecht S, Länge K, Huang TJ, Manz A. 2012. Nat Rev Drug Discov. 2012 Aug;11(8):620-32.

[22] Huh D, Matthews BD, Mammoto A, Montoya-Zavala M, Hsin HY, Ingber DE. 2010. Science. 2010 Jun 25;328(5986):1662-8.

[23] van Midwoud PM, Verpoorte E, Groothuis GM. 2011. Integr Biol (Camb). 2011 May;3(5):509-21.

[24] Tourovskaia A, Figueroa-Masot X, Folch A. 2005. Lab Chip. 2005 Jan;5(1):14-9.

[25] van der Meer AD, Poot AA, Duits MH, Feijen J, Vermes I. 2009. J Biomed Biotechnol. 2009;2009:823148.

[26] Jang KJ, Suh KY. 2010. Lab Chip. 2010 Jan 7;10(1):36-42.

[27] Zhao L, Wang Z, Fan S, Meng Q, Li B, Shao S, Wang Q. 2010. Biomed Microdevices. 2010 Apr;12(2):325-32.

[28] Sankar KS, Green BJ, Crocker AR, Verity JE, Altamentova SM, Rocheleau JV. 2011. PLoS One. 2011;6(9):e24904.

[29] Shackman JG, Reid KR, Dugan CE, Kennedy RT. 2012. Anal Bioanal Chem. 2012 Mar;402(9):2797-803.

[30] Lin P, Chen L, Li D, Liu J, Yang N, Sun Y, Xu Y, Fu Y, Hou X. 2009. Tohoku J Exp Med. 2009 Jan;217(1):59-65.

[31] DiMasi et al, *Journal of Health Economics* 22, no. 2 (Marzo 2003): 151-185.

[32] DiMasi et al., *Journal of Health Economics* 10, no. 2 (Luglio 1991): 107-142.

[33] Center for Drug Evaluation and Research, "Information for Consumers (Drugs)," WebContent, http://www.fda.gov/Drugs/ResourcesForYou/Consumers/default.htm.

[34] Dittrich and Manz *Nat Rev Drug Discov* 5,no. 3 (Marzo 2006): 210-218.

[35] Figeys and Pinto, *Anal. Chem.*, 2000, 72 (9), pp 330 A–335 A

[36] Neužil et al, Nature Reviews Drug Discovery 11, 620-632 (August 2012)

[37] Hong et al, Drug Discovery Today, 2009, Volume 14, Issues 3–4, Pages 134–146

[38] Hersher, Nature Medicine;2012, Vol. 18 Issue 4, p475

[39] IDF – International Diabetes Federation- Atlas 2011

[40] Huh et al, trends in cell biology, Volume 21, Issue 12, December 2011, Pages 745–754

Chapter 2

Cell culture integration into microfluidic technology

This chapter relates to microfluidic cell culture integration and its importance as base in cell culture applications. The chapter is divided into two main parts; it starts with an introduction about motivation and state of art about microfluidic cell culture integration, followed by practical examples. In the second part some of the results achieved during this thesis work will be used as applications examples.

2.1 Motivation

In biological and pharmaceutical research an adequate cell-based assay scheme that faithful mimics the *in vivo* behaviour is crucial [1]. Successful cell-based assay significantly relies on the fundamental understanding of the cellular response to the given culture conditions. To deeply investigate the effect of environmental conditions on cells behaviours, a homogeneous and stable culture system is decisive [2]. Therefore to study cells under simulated physiological microenvironments, it is necessary to develop tools, that enable quantitative real time control of cells microenvironment. This approach requires the ability to both actuate and sense the spatio-temporal distribution of nutrient, growth factors, adhesive signals and cell secreted products in the cellular microenvironments [3]. Microscale technologies are emerging as powerful tools for

tissue engineering and biological studies [4]. By reducing the operational dimensions of a conventional macrofluidics-based system down to the micron scale, you cannot only reduce the sample volume, but you also need to access a range of unique characteristics, which are not achievable in conventional macro-scale systems [5,6]. Latter goals in microfluidics technology lead to several advantages in application of microfluidic-based cell culture, making it a promising alternative to the conventional cell culture methods [1]. Microfluidics provides the opportunity to study cells effectively on both a single- and multi-cellular level with high-resolution and localized application of experimental environment with biomimetic physiological conditions [7].

2.2 State of art of microfluidic cell and *ex vivo* cultures technologies

Microscale cell cultures are promising supports for high-throughput experimentation in many fields, such as drug screening tests and complex biological studies [8]. Culturing cells at microscale further allows more precise control of the extracellular microenvironment [9]. Microfluidics has the potential to revolutionize the way to approach cell biology research and one of the key benefits of microfluidic for basic biology is the ability to control parameters of the cell microenvironment at relevant length and time scales [10,11].

Microfluidic cell culture platforms combine the advantages of miniaturization and real-time microscopic observation with the ability to pattern cell culture substrates [12] to vary the composition of culture medium over space using gradient generators [13], and to create cell culture conditions that are more physiological than those found in other *in vitro* systems, in terms of nutrients exchange rates and to unable mechanical stimulation [14]. Microfluidic cell systems are applied to many different situations, from 2D and 3D cell culture systems [15]. These systems differ on how cells are seeded: as monolayer on a substrate surface (2D systems), or on 3D scaffolds (3D systems). 3D cell-culture models have recently garnered great attention because they often promote levels of cell

differentiation and tissue organization not possible in conventional 2D culture [16]. A number of 3D microfluidic perfusion culture systems have been developed recently for application in complex biological processes such as in vitro organ development [17]. For tissue types that are highly perfused *in vivo*, such as the liver and kidney, microfluidic perfusion culture may more accurately mimic the *in vivo* microenvironment, where cells are in close proximity with the microvascular network [18, 19]. Considerable progress has been made in the design and use of novel microfluidic devices for culturing cells and for subsequent treatment and analysis [10,20]. Automated cell culture screening systems based on a microfluidic chip are recently built including valves, mixers and pumps, capable of controlling fluid [39]. Microfluidic technology holds great promise for the creation of advanced cell culture models characterization [21].

As regards *ex vivo* tissue, in the past the common method to incubate ex vivo biopsies was to place them in medium filled in well plates [35]. However, in this in vitro system the medium was usually refreshed every 24 hours resulting in decreasing concentration of nutrient and accumulation of metabolites and waste products. To prevent this behaviour, some systems used a different approach, consisting of a perfused bioreactor in which the biopsy is closely maintained in a perfused chamber [36]. Recently, the use of microfluidic chip for liver slices led to a highly controlled microenvironment with the maintenance of viability and metabolic function up to one day [37,38].

2.2.1 Actual limitations and perspectives

Microfluidic technology emerges as a convenient route to apply automated and reliable assays in a high-throughput manner with low cost [22]. In order to combine microsystems with culture methods, it's important to define the proper assumptions to scale down the system to microchannels [21, 25]. Although this characterization is just at the beginning, several research groups have already contributed to a better understanding of the multiple aspects of microfluidic environments [23, 24]. An important challenge for the microfluidics community is to produce simple and biology user-friendly microfluidic devices [26]. Although the utility of microfluidic devices is

becoming increasingly evident, such devices will not be adopted by medical and life science researchers unless they can be used without the aid of engineers [27]. The integration of cell culture and microfluidic operations are required to better design microfluidic routing systems for applications in biomedical fields. The feedback between biologists using the devices and engineers designing them is the essential key for moving microfluidics-based cell culture forward [28]. When microfluidic systems will be able to establish a sufficiently complete microenvironment for human cells in culture, and material cell-interface issues will be solved [29,30], these may lead to *in vitro* models that would outperform both conventional cell culture and animal ones in predicting tissue-specific responses in humans [21]. Highly integrated microdevices will find application in basic biomedical and pharmaceutical research, whereas robust and portable point-of-care devices will be used in clinical settings [9].

2.3 Cell culture microfluidic technology approach

The aim of this paragraph is to describe the guiding principles and the main phases for robust cell culture integration into microfluidic technology. Correspondently results that I have achieved during this thesis work will be used and explained.

In this paragraph, we would like to start with common considerations about prerequisites and general issues that we had to consider during design. We want to underline this aspect because the different background between biology and engineering may otherwise lead to difficulties in correct design of systems.. it is uneasy to reach cell integration and therefore beyond classical technological design requirement, there is an entire world about cell culture that cannot be underestimated.

The design of a microfluidic cell culture system involves many decisions, including the choice of based-materials, fabrication process and sterilization techniques [28]. While prerequisites such as biocompatibility and sterility are non-negotiable, other design

constraints are set by the specific applications. Microfluidic culture system's biomaterial can be divided into two main groups: the former is the material for microfluidic device fabrication; the latter is the material onto cells are direct in contact and attach. All materials must be at least non cytotoxic. The elastomeric polymer most commonly used in microfluidic cell culture is Polydimethylsiloxane (PDMS) because of its advantageous qualities as cell culture material [31,32,33]. Despite the advantages to using PDMS, this elastomer also presents some challenge issues that have to be considered during experiments. The most important factor during cell culture in temperature incubated environment are steam and organic solvents permeation. These inconvenients can potentially cause undesired evaporation and changes in osmolality, with injuries for the cell culture [34]. Others, emerged recently [29], are the biological implications of PDMS-based microfluidic cell culture.

Practically cell culture in microfluidic needs to answer two relevant questions:

- how to integrate cells in microdevices;
- how to provide feeding turnover and biochemical factors.

Cell culture integration concerns the cells inserct into microfluidic systems. The integration can be subdivided as reversible or irreversible as shown in Figure 2.1. In the reversible integration cell cultures are integrated through microfluidic devices after a pre-conventional culture on glass patterned/coated substrates. The integration between cell culture system and microfluidic devices allows systems interface and collaboration, taking advantages from both the best characteristics. These systems are useful when reuse microfluidic devices is important, especially when fabrication processes are pretty long and complicated. Reversible integration is also useful in fast and repeated experiments, in order to reduce costs due to microfluidic devices fabrications. The irreversible integration is the most commonly used in microfluidic cell culture world, due to the utilization of closed and more robust devices. Irreversible integration uses all the potentiality of microfluidic systems during all the cell phases: from seeding and attachment to proliferation and differentiation.

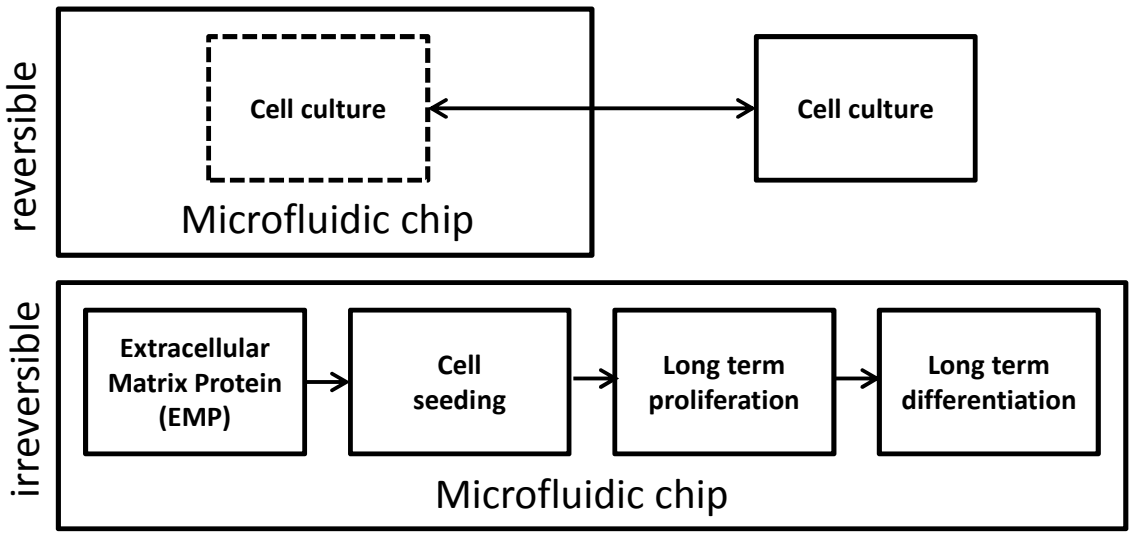

Figure 2.1*: schematic representation of reversible and irreversible cell culture strategies.*

As regards feeding turn over and biochemical factor, many strategies are possible with the common goal of precise culture medium delivery.

2.3.1 Reversible integration

When standard and common tissue-culture substrates can be incorporated into the microfluidic perfusion culture system, this is a preferred route because it avoids any question of biological effect due to cell substrate [28].

With reference to the publication reported in Appendix A, in this section a reversible integration of multilayer microfluidic platform is presented.

I have designed the platform to accurate tune the virus delivery from a diffusive-limited regime to a convective-dominated regime. This platform can be easily and reversibly coupled to cell cultures, allowing the performance of multi-parametric experiments and exerting a precise control over the soluble extracellular microenvironment and thus increasing the efficiency of infection. Moreover the microfluidic device was used for the optimization of the process of cell infection through an approach that combines mathematical modeling with the experimental validation. Figure 2.2 shows an extract of

the multilayer microfluidic devices and picture of the platform prototype operated owing a color tracer (fluorescein) in two of the 8 channels.

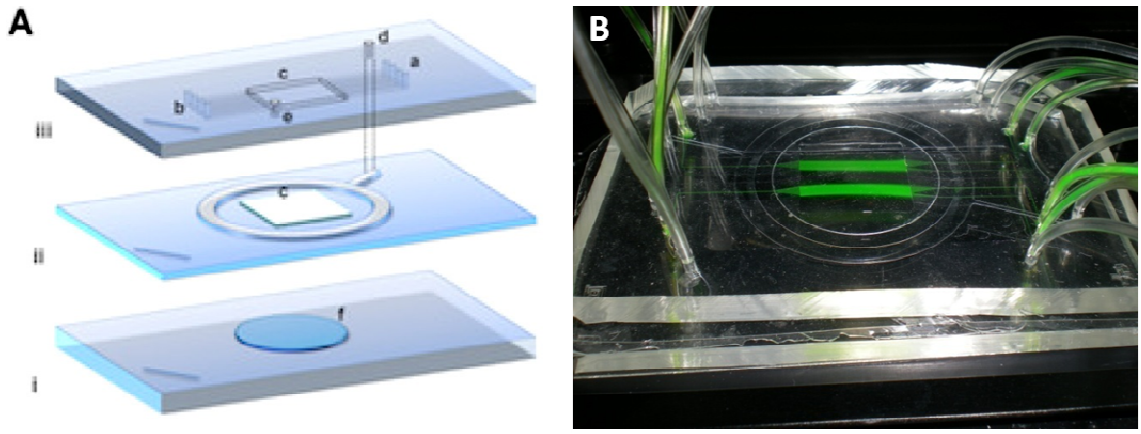

Figure 2.2*: (A): The platform comprised (i) a supporting glass slide with a PDMS slab carved to accommodate the cell culture coverslip (f), (ii) a membrane-based vacuum system for the reversible sealing of (i), and (iii) the microfluidic channels, 0.2x0.1mm (wxh), delivering fluids to the cultured cells (inlets in (a) and outlets in (b)). The assembled platform formed a 16X16X0.5mm culture chamber (c) where cells were exposed to the fluid streams. The top layer embedded connections to the vacuum system (d) and to a pressure-monitoring auxiliary service (e). (B) Reports an image of the assembled platform, which was entirely optically transparent, operated flowing a color tracer (fluorescein) in 2 of the 8 channels*

The multilayered microfluidic platform (overall dimensions: 75x50 mm) was designed for an easy interface with the cell system, and fabricated using lithographic techniques and molded in Polydimethylsiloxane (PDMS). The platform comprised:

i) a supporting glass slide with a PDMS slab carved to accommodate the cell culture coverslip,

ii) a membrane-based vacuum system for its reversible sealing,

iii) the microfluidic channels (width x height, 0.2x0.1 mm) delivering fluids to the cultured cells.

The circular channel creates the suction sealing between the two layer faces of PDMS slab in i) and is thermally (and irreversibly) bonded to the upper microfluidic layer iii). The assembled platform formed a 16x16 mm culture chamber, area in which the cultured cells were exposed to the fluid streams from the microfluidic channels. The height of the chamber could be varied as needed; for all the experiments presented here a 0.5 mm high membrane has been used. The platform was entirely optically

transparent, allowing in-line observations of the cultures by easy interface with standard microscopes.

With reference to the publication reported in Appendix B in Fig 2.3 a schematic view of another reversible cell culture integration devices is reported.

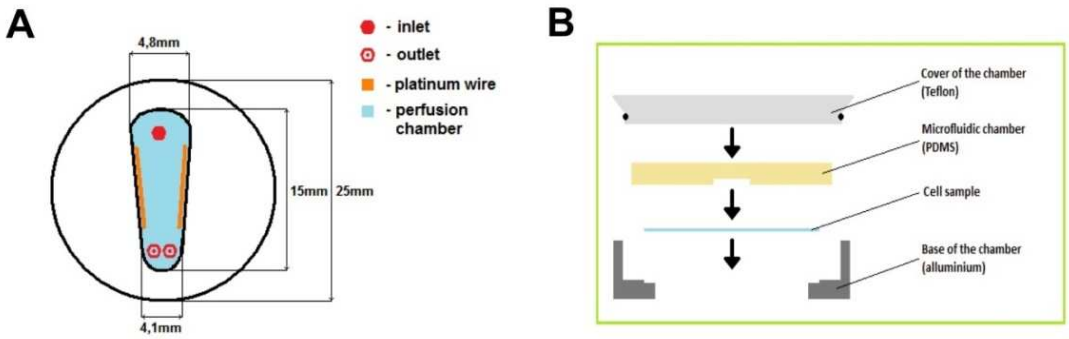

Figure 2.3: *(A) Schematic top view of PDMS microfluidic chamber. (B) Assembly of the microfluidic chamber within microscope holder to perform on line detection.*

I have developed this culture system to fast and easily couple neonatal rat cardiomyocytes cultured on a glass coverslip and analyzed calcium dynamic on a confocal microscope. In order to ensure an electrical stimulation to the cell culture, a platinum wire was also inserted in the PDMS chamber and connected to an electrical stimulator. The glass slide hosting the cell culture was located in a standard microscopy aluminum holder covered by the PDMS mold and pressure sealed by a Teflon cover.

2.3.2 Irreversible integration

The irreversible integration allows the direct insertion of cells inside microfluidic chamber, followed by long term culture and differentiation. Irreversible integration allows more robust and controlled devices with the capability to better interface with modern automated systems. The most precise culture chamber dimensions and medium leaking absence characteristics allow these systems to be more suitable for micro environmental conditions control. On the other hand a robust culture protocol is needed in order to obtain healthy proliferative or differentiated cells, essential conditions to

have successful experiments and confident data. The direct integration follows the temporal evolution of a sequence of phases directly in the microfluidic chip:

- Extracellular matrix chamber coating;
- Cells seeding;
- Cell proliferation;
- Cell differentiation.

2.3.2.1 Extracellular matrix coating and cell seeding

The choice of substrate material is critical to achieve cell adhesion in 2D microfluidic systems. In the PDMS microfluidic device, glass is often used as cell culture substrate because it can be permanently bonded to the PDMS microfluidic chip. While glass is an attractive cell substrate material for PDMS microfluidic devices and microscope imaging, it can present many issues to cell attachment. The cell substrate material allows cell attachment via adhesive proteins or peptides adsorbed from the cell culture media, or pre-immobilized cell attachment protein such as gelatin and collagen. Cell attachment is a critical step in microfluidic cell culture systems, because it can preclude the future of experiments and the healthy state of the culture. Usually the best Extracellular Matrix Protein (EMP) has to be chosen for the specific cell type and substrates. For example in Figure 2.4 different EMP have been tested on the same thin glass type in murine myoblasts cell line (C2C12), resulting in singular cellular behavior at 1 day from seeding. The EMP needs to be placed in contact with the whole culture chambers and incubated for some time. Cell seeding is made after EMP coating and consists of cell loading and attachment into coated chambers. The seeding density and adhesion times are two important variables that influence cell proliferation. We saw that the faster the cell adhesion was, the better the culture differentiation.

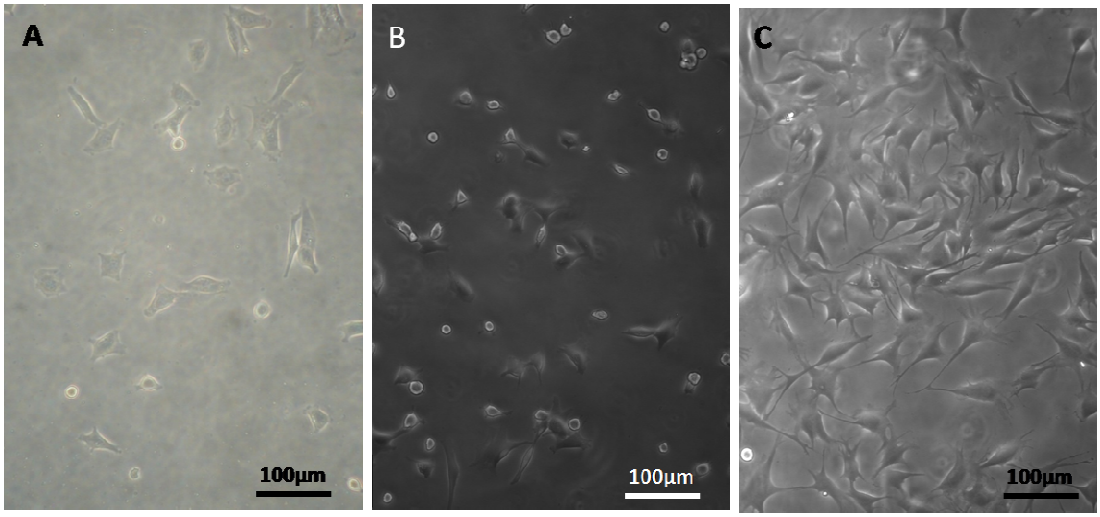

Figure 2.4: *Picture at 20X of C2C12 after 1 day from seeding on glass without coating (A) or after 1 hour incubation coating with gelatin (B), and Matrigel (C).*

As regards the seeded cell number ,there was an optimum around 250 cells/mm^2. Figure 2.5 shows a time evolution in a microfluidic cell culture chamber from cell loading, represented by round cells, up to cell attachment. We obtained that cell attached after 1 hour using 2.5 % Matrigel in DMEM. After cell adhesion, remaining cells, that did not adhere, needed to be washed out to avoid further cell culture illness due to the presence of dead cells.

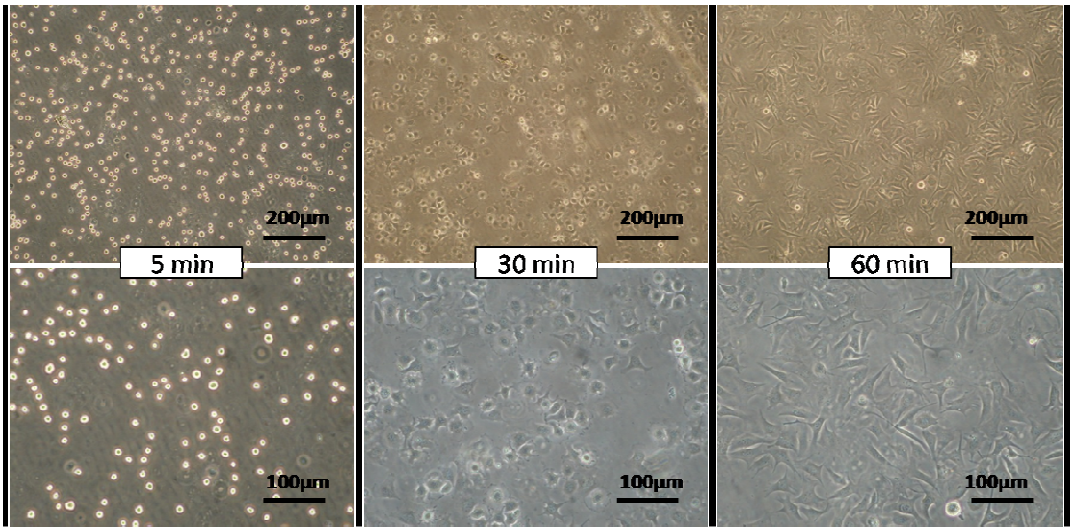

Figure 2.5: *Picture at 10X (up) and 20X (bottom) of C2C12 during time, of the cell adhesion evolution from cell loading.*

2.3.2.2 Long term proliferation and differentiation

After cell seeding and adhesion, the cell culture integration lead to cell proliferation and, if possible or necessary, cell differentiation. The quality of proliferation and differentiation is due to system capability of cell integration and moreover to feeding turnover. By referring C2C12 cell culture protocol in microfluidic, reported in Appendix F, data from long term proliferation and differentiation into microfluidic devices are reported in Figure 2.6.

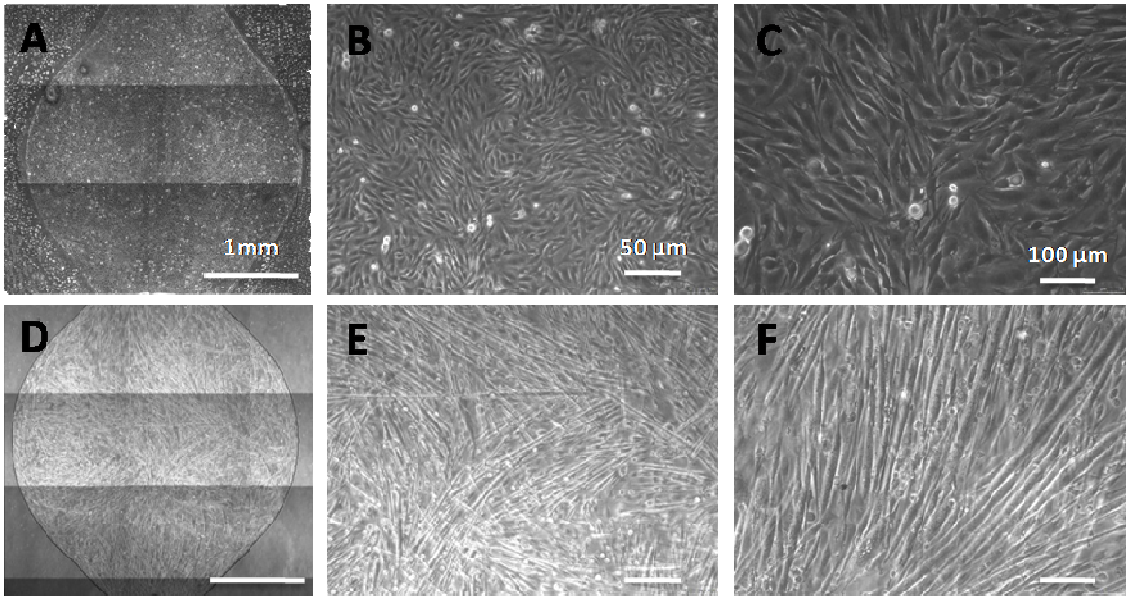

Figure 2.6*: (A) picture of a whole microfluidic chambers with confluent C2C12 (3 days after seeding)and particular at 10X (B) and 20X (C). (D) Picture of a whole microfluidic chambers with differentiated C2C12 (10 days after seeding) and particular of myotubes at 10X (E) and 20X (F).*

Figure 2.6 shows a picture of C2C12 cell lines inside microfluidic culture chamber at confluence and at differentiated states respectively at 3 and 10 days from cell seeding. Images demonstrate the microfluidic chip reliability in performing long-term culture and differentiation. Healthy cell culturing conditions are also confirmed by data of Figure 2.7 that show immunuofluorescence analysis for myosin in differentiated myotubes inside microfluidic culture chambers. A high differentiation in myotubes was obtained in the whole chamber after 6 days from confluence with the evidence of streaks and

contracting myotubes. These data validate the possibility to obtain strong and robust long term cell culture in our microfluidic systems.

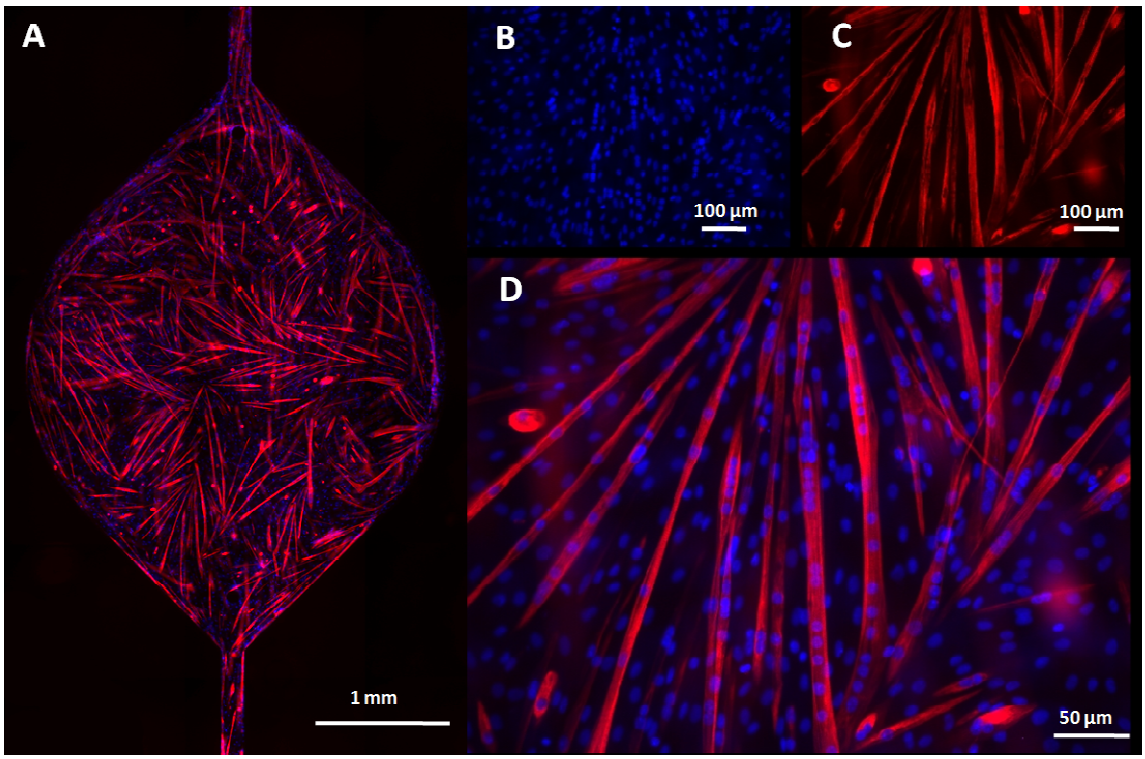

Figure 2.7*: (A) picture of immunoflurescence analysis of the whole microfluidic chambers for myosin (red) and nuclei (blue). (B) Picture at 20x of nuclei and (B) myosin. (D) Merged of enlargement of B and D.*

2.3.3 Liquid handling systems

Microfluidic cell culture devices need the support of liquid handling system, in order to obtain precise and uniform delivery of medium and factors into the culture chamber. In Chapter 3 automated on chip micro-perfusion apparatus will be presented. Aim of this paragraph is to make a list of practical issues and some notes adopted for cell culture. Independently from the device that has been utilized (reversible or irreversible), a robust cell culture protocol has to be optimized. The optimization can be achieved by continuous or discontinuous processes. There is evidence in literature for both continuous [40] and discontinuous [41] culture technique to enhance cell proliferation and differentiation but the best method has to be chosen case after case. Obviously

programmable systems are preferred especially to manage all the cell culture integration phases: coating, seeding included. During this thesis work both syringe pump and pressurized system have been used, connected with control systems for their automation. Many technical notes are reported in the material and methods in Appendixes: the lab made apparatus for pressure driving liquid is reported in Appendix E. Other information regarding protocols and feeding turnover are reported in Appendix F.

2.4 *Ex vivo* organ tissue culture and microfluidic integration

More details of this study are reported in Chapter 5 about adipose tissue integration into microfluidic chip and glucose uptake detection.

The integration of *ex vivo* organ tissue into microfluidic chip requires specific characteristics. The maintenance of cell tissue viability and the maintenance of cell tissue behavior are very important for further applications and specific experiments. The integrations of *ex vivo* adipose tissue has to guarantee the creation of an *in vitro* microenvironmental that is able to mimic as close as possible *in vivo* physiological conditions. If this characteristic is not achieved all the following experiments will not have reasonable biological feedback.

The integration of *ex vivo* tissue in microfluidic can be considered as intermediate between reversible and irreversible integration. From the concept to open-closed system necessary to tissue insertion it can be considered as reversible, but with the possibility of long term culture, the concept can be extended to an irreversible integration. Long term culture is very tissue-technology dependent [36,38].

In the application of *ex vivo* adipose tissue biopsy, a microfluidic culture chamber was specifically designed to allocate the *ex vivo* organ tissues and create a physiological environment that is able to guarantee tissue viability and metabolic activity for days.

Figure 2.8 shows the microfluidic devices fabricated for organ culture integration. Biopsies are usually cut in slices or small pieces and placed in contact with a specific medium dispenser by insertion through chamber holes. Medium dispenser was created covering the bottom of the culture chambers with circular microposts array. The microposts ensure constantly fresh medium perfusion in contact with an high biopsy surface by reducing the formation of dead volume due to biopsy leaking to the PDMS bottom chamber. Microposts also contrast the blocking of the inlet-outlet channels that are possible by biopsy insertion. The sealing was ensured by biocompatible PMMA-PDMS cup.

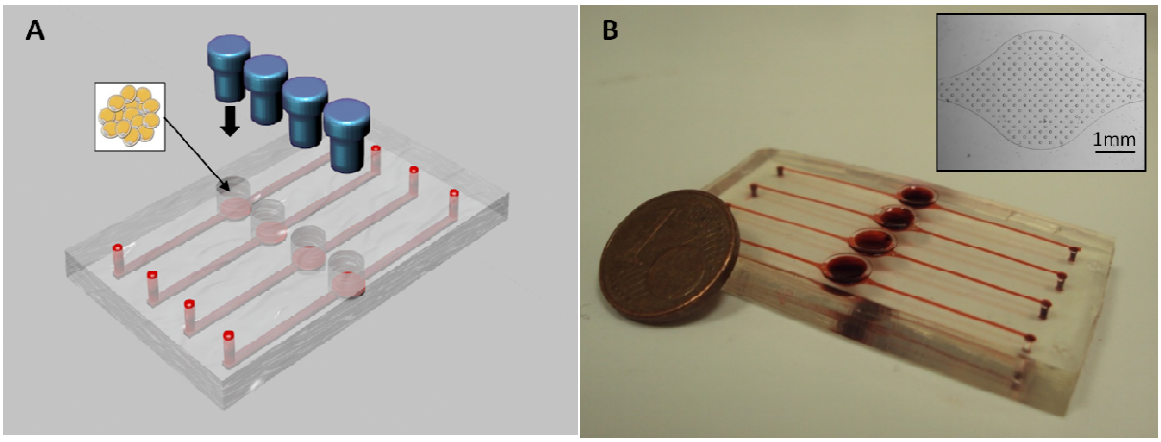

Figure 2.8: (A) schematic 3D platform with biocompatible cup. (B)*Picture of microfluidic devices for adipose tissue with red dye; inset show micropost array chamber.*

2.5 Conclusions

Microfluidic emerged as a potential tool able to influence subject areas in many fields. In biological research many advantages are possible with the introduction of microfluidic technology. The accurate control of microenvironment is one of the crucial aspects that can be achieved with miniaturization. Microfluidic cell culture integration needs the coupling of cell culture and microfluidic knowledge. In this chapter the guiding principles of microfluidic technique for cell and *ex vivo* tissue culture integration have been reported. Using some of the microfluidic devices that have been developed during this PhD thesis, practical issues have been described. Microfluidic cell culture integration

represents an indispensable prerequisite for the strong development of in vitro cell culture assay.

2.6 References

[1] Wu et al, *Lab Chip*, 2010, 10, 939-956

[2] Shuguang Zhang, *Nat Biotech* 22, 2004, 2: 151-152.

[3] Mehta et al, Biomed Microdevices, 2007, 9:123-134

[4] Khademhosseini et al., PNAS, 2006, 8: 2480- 2487.

[5]. Seeberger and Blume, *New Avenues to Efficient Chemical Synthesis*, 2006

[6] Zhang X, Haswell SJ. Ernst Schering Found Symp Proc. 2006 ;(3):21-37.

[7] Breslauer et al, Mol Biosyst. 2006 Feb; 2(2):97-112

[8] Zang et al, *Intern. Journal of Biotech. for Wellness Industries,* 2012, 1*,* 31-51

[9] El-Ali et al, *Nature* 442, 403-411 (27 July 2006)

[10] Young and Beebe, Chem. Soc Rev. 2010 Mar; 39(3):1036-48

[11] Tomaiuolo et al, Lab Chip. 2011 Feb 7;11(3):449-54.

[12] Rhee et al, Lab Chip. 2005 Jan; 5(1):102-7.

[13] Kim et al, Integr Biol (Camb). 2010 Nov; 2(11-12):584-603.

[14] Zhou and Niklason, Integr Biol (Camb). 2012 Nov 19; 4(12):1487-97

[15] Kuo et al, *NPG Asia Materials* (2012) 4, e27; doi:10.1038/am.2012.50

[16] Pampaloni et al, Nat. Rev. Mol. Cell Biol. 2007:8, 839-845

[17] Huh et al, Trends in Cell Biology, Volume 21, Issue 12, 745-754, 26 October 2011

[18]Domansky et al, Lab Chip. 2010 Jan 7;10(1):51-8. doi: 10.1039/b913221j.

[19] Midwound et al, Intgr Biol, 2011,3,509-521

[20] Pasirayi et al, Micro and Nanosystems, 2011,3,137-160

[21] Meyvantsson and Beebe, Annual Review of Analytical Chemistry, Vol. 1: 423-449

[22] Wen and Yang, Expert Opinion on Drug Discovery, October 2008, Vol. 3, No. 10: Pages 1237-1253

[23] Walker eta al, *Lab Chip 2004,* 4:91–972004.

[24] Atencia and Beebe *Nature, 2005,* 437:648–55

[25] Quake ans Squires, Rev. Mod. Phys., 2005, Vol. 77: 977-1026

[26] Csete, *Journal of Biology* 2010, 9:1

[27] Whitesides, *Nature* 442, 368-373 (27 July 2006) | doi:10.1038/nature05058

[28] Kim et al, *Lab Chip 2007,* 7:681–94

[29] Regehr et al, Lab Chip. 2009 Aug 7; 9(15):2132-9.

[30] Mukhopadhyay, *Analytical Chemistry* (2007),79, 3248-3253

[31] Leclerc et al, Biomedical Microdevices June 2003, Volume 5, Issue 2, pp 109-114

[32] Lee et al, Langmuir, 2004,20,11684-11691

[33] Unger et al, science, 2000, vol 288, 113-116

[34]Heo et al, Anal Chem. 2007 Feb 1;79(3):1126-34.

[35] Fried and Moustaid-Moussa, Methods in molecultar Biology, vol155: adipose tissue protocols.

[36] Sjöström et al., The journal of biological chemistry: 1977, 252,8833-8839

[37] van Midwoud et al., Lab Chip. 2010 Oct 21;10(20):2778-86

[38] van Midwoud et al., Biotechnol Bioeng. 2010 Jan 1;105(1):184-94.

[39] Sjöberg et al., Analytical Chemistry 79, no. 22 (2007): 8557-8563.

[40] Tourovskaia et al., Lab on a Chip, 2005, 5, 14–19

[41] Korin et al., Biomed Microdevices, 2009, 11:87-94

Chapter 3

Microfluidic integration for Diabetes studies on a chip: Large Scale Integration advance

3.1 Motivation

In the obtainment of efficient human *in vitro* model for study diseases, the ability to study cells under simulated *ex vivo* physiological microenvironments is of crucial importance [1]. To achieve that, the capability to enable quantitative real time control of the cell culture microenvironment is require. The miniaturization of the systems can offer many advantages [2], but in order to manage tiny volume with high spatial-temporal distribution, microfluidic systems are useless without accurate liquid handling, distribution and control. In the past, researchers have developed micropumps [3], microvalves [4], and micromixers [5] in order to avoid the use of labscale syringes or peristaltic pumps that do not always permit uniform flow control. Microvalves and micropumps allow very precise doses of medium or reagents into each specific area designed for the experiments. Volumes, frequency, reagents and concentrations can be modulated easily increasing the flexibility on design test. Therefore, microvalves have been successfully applied to the field of lab on a chip [6]. Applications with integrated microcomponenents changed the ability to manipulate liquid at micron scale and started a new era of effective automation in microdevices [7]. Large number of experiments can be carried out independently without assistance for extended period of time.

3.2 State of art of microfluidic Large Scale Integration

Micromechanical valves increase the flexibility for applications with microfluidic devices, creating many highly complex integrated systems [8]. Adding micromechanical valves many devices have been developed for applications in many fields [9,10]. Currently, microvalves can be generally classified into two main groups: active microvalves, that use mechanical and non-mechanical moving parts, and passive microvalves. Similarly a diverse series of micropumps have been reported for the development of highly integrated chip [3,4,11]. Most of microfluidic devices have self-contained active micropump, whose packaging size is comparable to the fluid volume that have to be pumped [12,13].

With the coming of a series of microfluidic systems developed by multilayer soft lithography, pioneered by Quake's group, the introduction of monolithic PDMS valves changed the approach to microfluidic design fabrication and experiments. These valves are made by two PDMS layers bonded together in a crossed-channel architecture [14,15,16]. The bonded structure is sealed onto the top of a rigid substrate. When pressure is applied to the pneumatic control channels, the thin elastomeric membrane that separates the two channels' layer, deflects causing closure to the other channel. The on-chip microvalves needed an external pneumatic controller to be actuated. Automation is achieved by interface to a controller's programmable software.

The idea of a Large-scale integration (LSI) in microfluidic systems has been fashioned as analogous to that in electronic integrated circuits. mLSI was realized by adding hundred and thousand of in line microvalve, that can be actuated by multiplex control [17]. For a mLSI technology two basic requirements are needed: monolithic microvalves and multiplex control. The rising of mLSI technology has combined the automation in biological instrumentation improving throughput, sensitivity and dynamic range with a low expenditure [18]. Recently Araci and Quake proposed the last evolution of LSI,

building a device with 1 million valves per cm^2, describing this technology as microfluidic very large scale integration mVLSI, analogous to its electronic counterpart [19].

3.2.1 Conclusion and actual limitations

mLSI changed radically the microfluidic research world in the past 10 years increasing features and possible applications. Despite the exponential growth of microfluidic, only a few numbers of devises are actually used in routine process [20]. Must part of the current mLSI devices still need the addressing of challenges to enter in the commercial world. In particular, microfluidic devices must be simple and highly versatile to permit their use in both industrial and academic laboratories [21]. The high number of control lines and the complexity of operation, that are usually necessary to manage mLSI devices, don't make them user friendly.

3.3 Rationale of microfluidic platform design for the study of Type 2 Diabetes

In the present research study for type 2 diabetes we aimed to investigate glucose uptake with high temporal resolution in adipose tissue and skeletal muscle. First of all, biological issues have to be considered in order to define the main constrain for platform design.

Concerning cell culture integration, cell culture in microfluidic chip has already been presented in Chapter 2 for both *ex vivo* tissue and cell culture. A previous PhD work, E. Magrofuoco 2011 [22], defined some important variable values for the design (chamber height, biopsy thickness, flow rate) by the help of multiscale mathematical model.

Here the rational design of a microfluidic platform for type 2 diabetes will be reported. More technical notes and details about multilayer platform design are reported in Appendix E.

Design has to consider biological and technical requirements. Moreover a precise equilibrium between biological and technical design is necessary for the best results. We focus our design in a simplified mLSI in order to obtain an automated microfluidic chip as simple as possible, maintaining the following capability:

- integrate cell culture;
- permit drug stimulation;
- sampling medium downstream culture chamber;

Using a low number of control lines, the troubleshoots during fabrication and experimental set up decrease a lot. Even the operative protocols are easier and the automation program simple to adjust.

Fig 3.1 shows a schematic representation of a single microfluidic chamber. In order to continue measure glucose concentration in the downstream medium, and avoid sample contamination, single inlet and single outlet have been chosen. Culture medium is moved by peristaltic micropump placed just after the medium inlet.

Micropump was designed to perfuse medium precisely with a low flow rate. This system can also be coupled with standard syringe pump, thank to the independency between each unit. Push up microvalves operate the injection system and isolate the culture chambers during conventional operation, such as chamber coating and cell seeding. The injection system was designed as 16 cm long serpentine channel, 100 µm wide and 50 µm high, that is able to contain up to one and half of the total chamber volume.

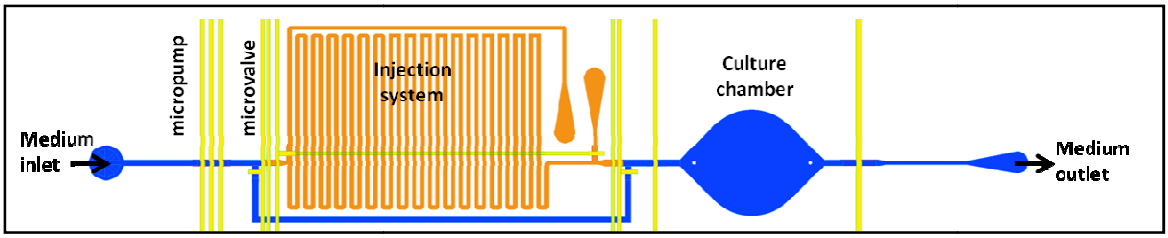

Figure 3.1: *Single unit schematic representation from integrated microfluidic chip; medium distribution channels and culture channel (blue), injection system (orange) and pneumatic control (yellow).*

The serpentine has independent inlet and outlet that permit to insert easily the solution. Injection system works alternatively with by-pass channels by acting microvalves. By-

pass channel is used in alternative with the injection system to insert medium in the chamber. Injection time is flow rate dependent due to the volume of the reservoir. For long term stimulation the fast reloading permits to repeat quickly the injection procedure. The “loop system” operates as biochemical reservoirs for drug stimulation and can be fast and easily refilled with pressurized system or by manual pipetting. The length of the stimulus can be changed as required, repeating the stimulation process (see validation 3.5). The loop-inlet/outlet of different units are separated each other in order to be coupled with robotic harm for automated liquid handling. The use of reservoirs allows to load fresh biochemicals; fresh drugs can be inserted few minutes before injection, avoiding thermo sensitive degradation.

3.4 Fabrication of microfluidic platform for the study of Type 2 Diabetes

This paragraph reports the technique used for mold and chip production. We refers to Appendix E “multilayer soft lithography” for protocols and more information. Using the words forged by S. Quake and group, the layer that contains channels for flowing liquid is called flow layer (FL), and the other one is called control layer (CL). The latter has channels able to deflect the membrane valve into the flow channel, stopping the liquid in the flow when they are pressurized with a pneumatic fluid.

In order to fabricate a multilayer microfluidic platform, 2 molds are required. For both CL and FL mold, multilayer photoresist-based mold have been fabricated. The CL mold is made by three layers of negative resist which conduct rectangular cross section; the FL mold is made using one layer of positive resist and also other layers of negative resist. In the CL the blanket layer provides a surface with uniform wetting properties for PDMS casting. The third negative layer is made to create a microfluidic chamber via intersection in the thin PDMS layer. During chip production a hole in correspondence of the culture chambers is created by this via. The FL mold is produced by a first layer with

positive resist, obtaining round channel in the correspondence of valve area, followed by a square layer in order to create all the channels and chambers. Another further layer is necessary for adipose tissue applications in order to create microposts in the chambers.

During chip production, multilayer PDMS chip are fabricated and thermal bonding technique has been used. In multilayer soft lithography the bond of multiple PDMS layers is a necessary condition that has to be achieved during fabrication. Moreover the two layers have to be allocated in a precise position in which the control channels create the valve areas in the right point over the flow channels. Thermal bonding has been preferred for mLSI because it is more yielding during alignment: it is not a one shot process (as plasma bonding) and the operator has more time to ensure the best alignment condition.

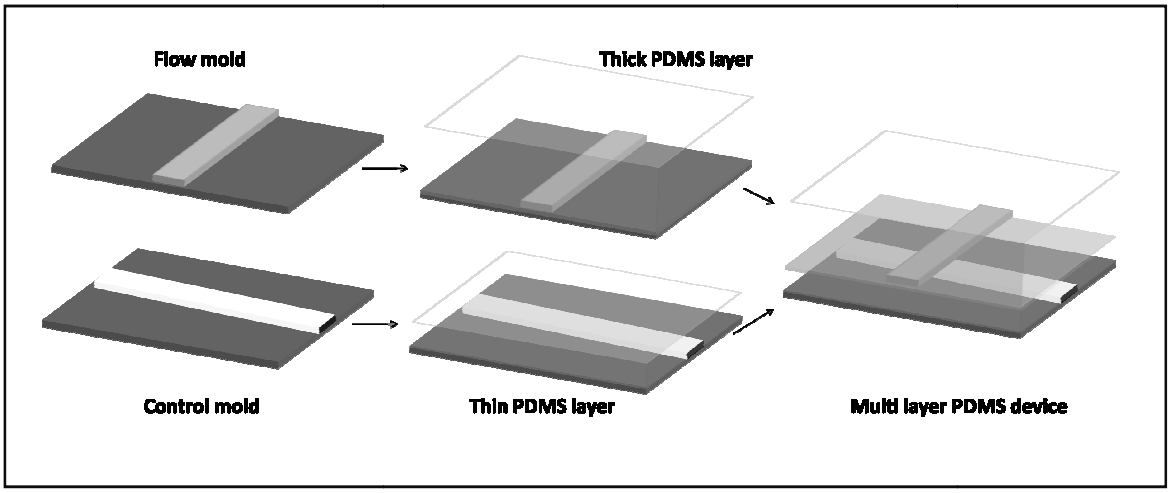

Figure 3.2*: Multi layer PDMS chip is made by more than 1 PDMS layer in which the bond is ensure usually by plasma or by off ratio PDMS curing. In Thermal bonding, partially cured PDMS layer are aligned and placed in contact before put them together in oven to complete the curing and ensure the bond. Therefore with plasma bonding the surfaces are treated with plasma and made in contact. Strong covalent bonds are guaranteed.*

PDMS consists of two components: the base and the cure agent. The thermal bonding technique were achieved by the ratio modification of the two PDMS layers from the manufacture recommendation 10:1. One PDMS layer is made at high ratio (5:1) and the other one at low ratio (20:1); the two layers are partially cured before put in contact and

aligned. A following bake creates an irreversible bonding at the interface due to rapid diffusion of the catalyst from the rich layer to the poor layer (about 10-40 µm).

The final chip for adipose tissue integration will consist of three layers of PDMS, first with the channels where liquid flow occurs (flow layer), second with dead-ended channels that control the valves (control layer) and the last with holes to insert the biopsy. For cell culture applications the 2 layers chip is bounded to a glass substrate. Figure 3.3 shows a multilayer PDMS chip with 8 independent culture chambers (blue). In yellow control channels are empathized.

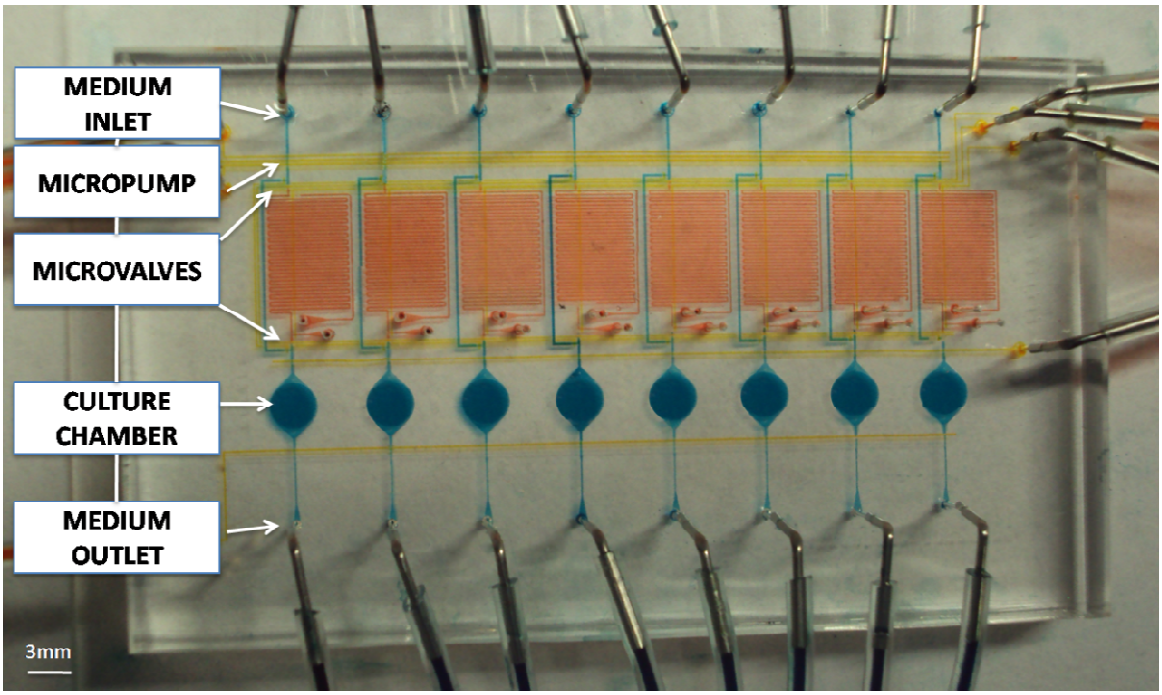

Figure 3.3*: Image of multilayer PDMS chip with dye; medium channels and chamber (blue), reservoir (orange), and control channels (yellow).*

3.5 Validation of microfluidic platform for the study of Type 2 Diabetes

Microfluidic chip has been technically and biologically validated. All the valves in the chip have to close automatically together when the relative control line is pressurized;

delaminating has to be absent. Figure 3.2 shows a valve in open and closed configuration. When the control channel is pressurized the thin membrane, that separates the two channels, deflects and a complete sealing is created. Valve is actuated with a minimum pressure of 0.6 bar.

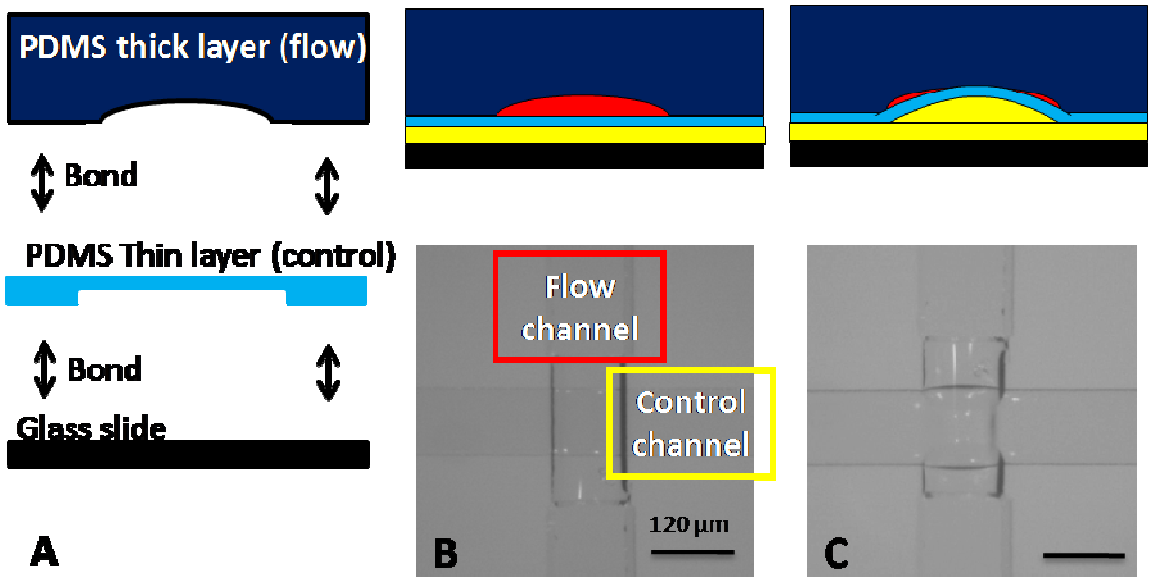

Figure 3.4*: (A) schematic representation on monolithic valves; it is fabricated by the overlapping of two channels separated by thin membrane. These layers are bonded together first, and then on a rigid substrate such as a glass slide. (B) Schematic section and image of a microvalve when the control channel is not pressurized (valve open). (C) Schematic section and image of a microvalve when the control channel is pressurized (0.6 bar) causing a membrane deflection with channel sealing.*

Microfluidic pump was created by 3 microvalves in series; they are actuated in the pattern 101, 100, 110, 010, 011, 001 (1 refer valve close, 0 valve open) respectively. In this way a peristaltic sequence has been generated, allowing fluid flowing. Micropumps need to be calibrated in order to determine the effective flow rate at the relative frequency of solenoid electron valves. Pumping rates were determined by measuring the distance traveled by a column of water in thin (ID 0.51 mm, OD 1.52 mm) tubing as proposed by Urgen et al [14]. Figure 3.3 shows the calibration curves of peristaltic pump. Flow rate increases linearly with the frequency up to a maximum that corresponds to 200 µl/min. Maximum is due by the equilibrium of the maximum frequency of the offchip solenoid control valves and the valve deflection frequency response.

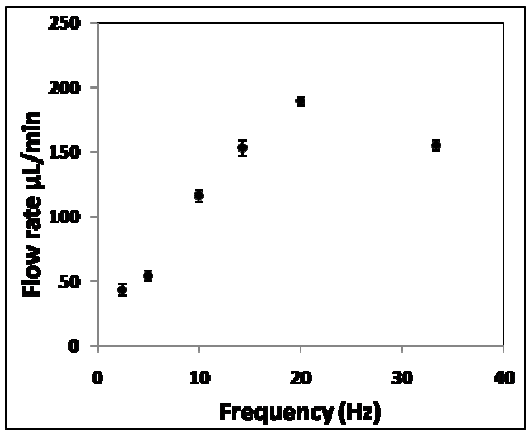

Figure 3.5*: peristaltic pump calibration curve for a 130X170 area peristaltic micropump.*

Injection system has been validated with food dyes and fluorescent tracers in order to stimulate a drug pulse delivery. Figure 3.5 shows an example of drug delivery using injection system temporally controlled.

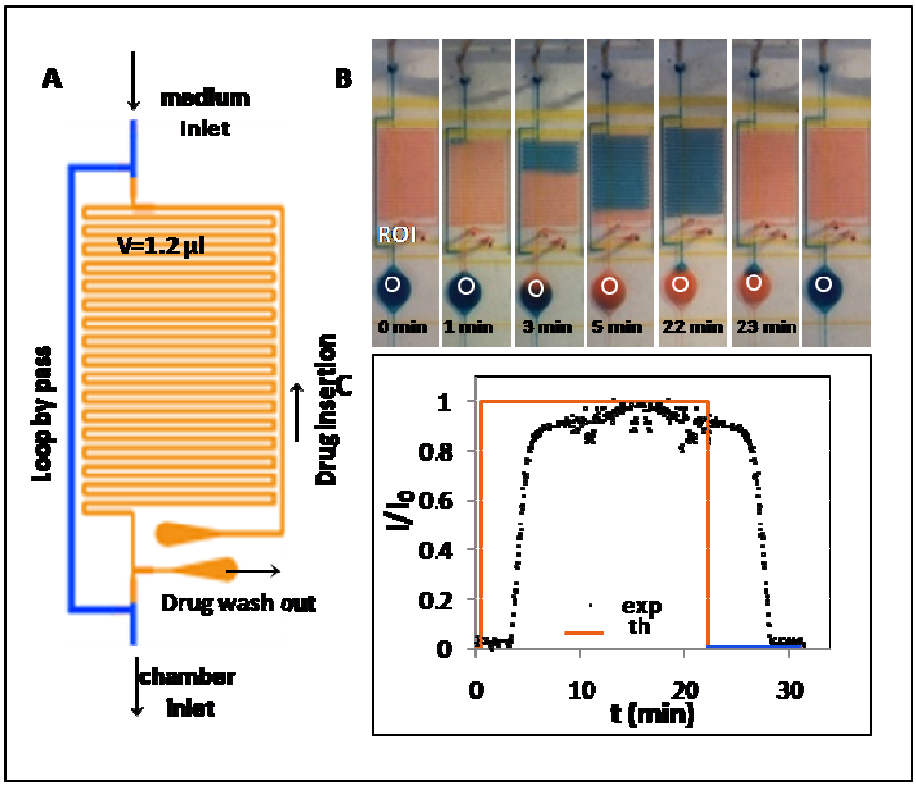

Figure 3.6*: (A) schematic top view of injection system; culture medium (blue) and drug (orange). (B) Temporal simulation of insulin (orange) injection through the culture chamber. (C) Dispersion curve at the center of the culture chamber during 30 minutes stimulus, theoretical and experimental.*

The device allows the reduction of the dead volume and an accurate fluid control; moreover, the opening and closing of injector system microvalves permit to create pulses of insulin or other drugs and factors. By the use of injection system directly in the chambers, the dispersion phenomena are really deducted as shown by the dye dispersion curves during time. The system had demonstrated the fully capacity to perform multiple stimulation into the chamber with high spatio-temporal resolution.

Cell culture integration has been demonstrated by preliminary experiments with HEK (human embryonic kidney cell line; data not shown) and C2C12. These first experiments demonstrate the prototype reliability in performing long-term culture and differentiation. By these experiments, a robust culture protocol in microfluidics has been defined. Some results have been already shown in Chapter 2 (Fig 2.3 and 2.4). Afterwards, on the grounds of C2C12 protocol, the microfluidic culture chamber has been adapted to human myoblasts obtaining good preliminary results (Method is reported in Appendix F). Figure 3.7 shows primary human skeletal muscle cells (HMSC) after few hours from seeding and at 3 and 10 days. Immunuofluorescence analyses for miogenic markers myosin, actin and desmin demonstrated a good differentiation in myotubes. These first results led a strong proof of concept about the good reliability in this project.

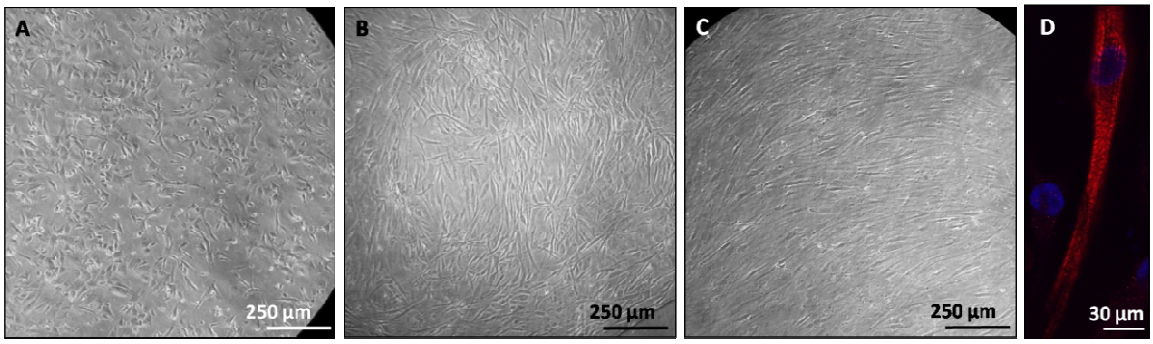

Figure 3.7*: Particular of HMSC in microfluidic chamber (10X) at 3 hours (A), 3 days (B) and 10 day (C). (D)* Immunofluorescence (40x) for myosin (red) and DAPI (blue).

3.6 Conclusions

Microfluidic large scale integration technology has introduced the automation in biological instrumentation improving throughput, sensitivity and dynamic range with a low expenditure. In line microvalves and micropump allowed to increase the ability to study cells under simulated physiological microenvironments *ex vivo*. We developed and fabricated a multilayer microfluidic platform for type 2 diabetes study. The platform is able to precisly control the culture microenvironment by accurate delivery of culture medium. Insulin and other drugs can be easily inserted into the chamber with minimum dispersion. Temporal drug pulse evolution can be modulated specifically for each experiment, acting on the automation control software. Microfluidic platform validation with dye, fluorescent tracer and moreover with different cell line and primary human muscle cell, has demonstrated the capability of the system to be a robust and flexible tool for *in vitro* cell based technology for diabetes study. In Chapter 4 and moreover in Chapter 5 we demonstrate its ability and role in glucose uptake detection.

3.7 References

[1] El-Ali et al, Nature 442, 403-411 (27 July 2006)

[2] Quake and Squires, Rev. Mod. Phys., 2005, Vol. 77: 977-1026

[3] Laser and Santiago, J. Micromech. Microeng. 14 (2004) R35–R64

[4] Oh and Ahn, J. Micromech. Microeng.2006, 16 R13

[5] Nguyen and Wu, J. Micromech. Microeng. 15 (2005) R1–R16

[6] Au et al, Micromachines 2011, *2*(2), 179-220

[7] Zeng et al, Design Automation Methods and Tools for Microfluidics-Based Biochips, Springer ISBN 978-1-4020-5123-4

[8] Hong and Quake *Nat* Biotechnol. 2003 Oct; 21(10):1179-83. Review

[9] Ottesen et al, *S*cience. 1 December 2006, 314:1464-67

[10] Wu et al, Lab on a Chip 9, 1365-1370, 2009

[11] Zhang Xing and Li, Biotechnology Advances 25 (2007) 483 – 514

[12] Chun-Wei Huang *et al* 2006 *J.* Micromech. Microeng. 16 2265

[13] Lien et al, Biosens Bioelectron 2007;22:1739–48.

[14] Unger et al, Science 7 April 2000: Vol. 288 no. 5463 pp. 113-116

[15] Quake SR and Scherer A, "From Micro to Nano Fabrication with Soft Materials", *Science* 290: 1536-40 (2000

[16] Melin and Quake, Annu. Rev. Biophys. Biomol. Struct. 2007. 36:213–31

[17] Thorsen T, Maerkl SJ, Quake SR, "Microfluidic Large Scale Integration", Science 298: 580-584

[18] Gomez et al, Anal. Chem. 2007, 79, 8557-8563

[19] Araci and Quake, Lab Chip, 2012,12, 2803-2806

[20] Ouellette, American Institute of Physics, 2003, 14-17

[21] Kang et al, Drug Discov Today. 2008 January; 13(1-2): 1–13

[22] Magrofuoco E. 2011. PhD dissertation, University of Padova

Chapter 4

Development of glucose uptake measurements

4.1 Introduction

Glucose is the main energy source for cells in an organism and its blood concentration is tightly regulated in healthy individuals (3.9-6.1 mmol/L) [1,2].

However, impaired blood glucose control has been found in diseases such as metabolic syndrome and diabetes, with serious consequences for patients [3,4]. Diabetes affects the body's capacity to use glucose, reducing tissue glucose uptake with consequently increasing of hyperglycemia.

In vivo, the study of glucose regulation is complicated by the limited accessibility to measurements (usually peripheral blood samples are taken) and by the interconnected action of multiple organs (e.g.: pancreas, liver, skeletal muscle, adipose tissue), despite mathematical models help dissecting the different contributions [5]. On the other hand, *in vitro* studies can take advantage of biological measurements with even single-cell resolution.

Detecting the components involved in the different steps of intracellular glucose processing is very relevant to identify which mechanisms are disrupted under disease conditions. However, measuring the rate of each single step is not an easy task also *in vitro*. Glucose uptake represents the quantity of glucose that enters cells from the extracellular space. Once within the cell, glucose is phosphorylated by the enzyme hexokinase. Phosphorylated glucose then proceeds through glycolysis. In patients showing insulin resistance, a pre-diabetic state, cells in adipose tissue and skeletal muscle show impaired glucose uptake dynamics [6]. However, the defect could be related both to the mechanism of glucose uptake itself or to other downstream reactions that limit the overall rate of the process.

The ability to monitor glucose concentration it's crucially important in order to obtain a strong read out for *in vitro* experiments' interpretation in diabetic studies. In this sigh, great achievements derive from the use and application of advanced and novel culture technologies, trying to mimic the *in vivo* cellular microenvironments.

Microfluidic technology offers the capability to highly increase the ratio between volume of the cell-tissue culture and the net volume of culture chamber, offering capabilities not achievable in other systems.

In this chapter I have reported the methodology developed and validated during this thesis that regard the coupling of microfluidic technology with glucose concentration measurements in order to detect glucose uptake with a high temporal resolution and non invasive manner. Three methodologies are reported: two of them regards the measurement of extracellular glucose concentration by off line or on line measurements on the downstream culture chamber medium, the other one the measurement of intracellular glucose concentration by FRET encoded nanosensors.

4.2 Available methods and limitations

Conventionally, glucose uptake is measured in *in vitro* cell cultures through the utilization of non-metabolizable glucose analogs. The most used are radioactive hexoses, such as 2-[^{14}C]-deoxyglucose (2DG). They were designed similar to glucose, to cross cell membrane (in both directions) by facilitated diffusion through membrane proteins, called glucose transporters (GLUTs). However, unlike glucose, they are not processed through glycolysis. Thus, it is possible to estimate the uptake rate of these glucose analogs by measuring their intracellular concentration, which is proportional to cell radioactivity [7]. Since radiolabeled analogs require specialized training and equipment, fluorescent glucose analogs [8] or F-2-deoxy-2-fluoro-glucose (FDG) [9] were developed: these compounds are detectable by using fluorescence or positron emission tomography (PET) respectively. Moreover, enzymatic assays that take advantage of non-radiolabeled 2DG are now established. These assays indirectly measure 2DG uptake quantifying by fluorescence microscopy specific intracellular metabolites involved in its oxidation. However, this last approach requires a considerable number of cells and may have background interference due to other biochemical molecules [10]

All the methods described above show many criticalities and limitations:

- glucose analogs are not handled by enzymes in the same way as glucose, and they can be toxic, even at low doses [11];
- glucose analogs can have slightly different kinetics compared to glucose because of a different interaction with the membrane GLUTs;
- isotopic techniques offer low spatio-temporal resolution which precludes detecting rapid dynamics.

Furthermore the inconvenience and cost associated with radioactive waste disposal and cleanup lead to practical routine issues.

Recently, a new method has been developed for real-time glucose detection at single-cell resolution [12]. It is based on the interaction of intracellular glucose with a

nanosensor that, upon glucose binding, undergoes a conformational change detectable thanks to the phenomenon of Förster resonance energy transfer (FRET). Thus, monitoring of FRET can be correlated to intracellular glucose concentration in real-time. This high temporal resolution opens the prospect of measuring not only intracellular glucose concentration but also glucose flux through cell membrane and through phosphorylation, by monitoring cell response to dynamic extracellular perturbations, such as a step or sequential pulses of glucose concentration. To fully exploit the potential of glucose FRET nanosensors, the extracellular environment should be accurately controlled at the micrometer scale, with high space and time resolution. Microfluidic technology is well suited for this task [13].

4.3 Development of non invasive glucose uptake measurements

This paragraph reports the methodology for measuring glucose uptake in culture with single-cell resolution and fast dynamics. More details can be found in Appendix D.

Glucose concentration was detected in extracellular and intracellular environment by two non invasive manner: the former is based on continuous downstream culture chamber medium sampling and analysis, the latter is based on FRET detection.
We developed an experimental system composed of a microfluidic chip for cell culture, a liquid handling apparatus, a detection system, and an external system for control and data acquisition (Figure 4.1A). The microfluidic culture system is composed of 3 o more culture chambers where experiments are performed independently in parallel (Figure 4.1B and C). Same results can be achieved using the multilayer chip (Chapter 3). Medium perfusion was performed by two different means: by external pumping and by pressure driven perfusion (Figure 4.1A). The second method was chosen for experiments where fast dynamic changes of glucose inlet concentration were required.

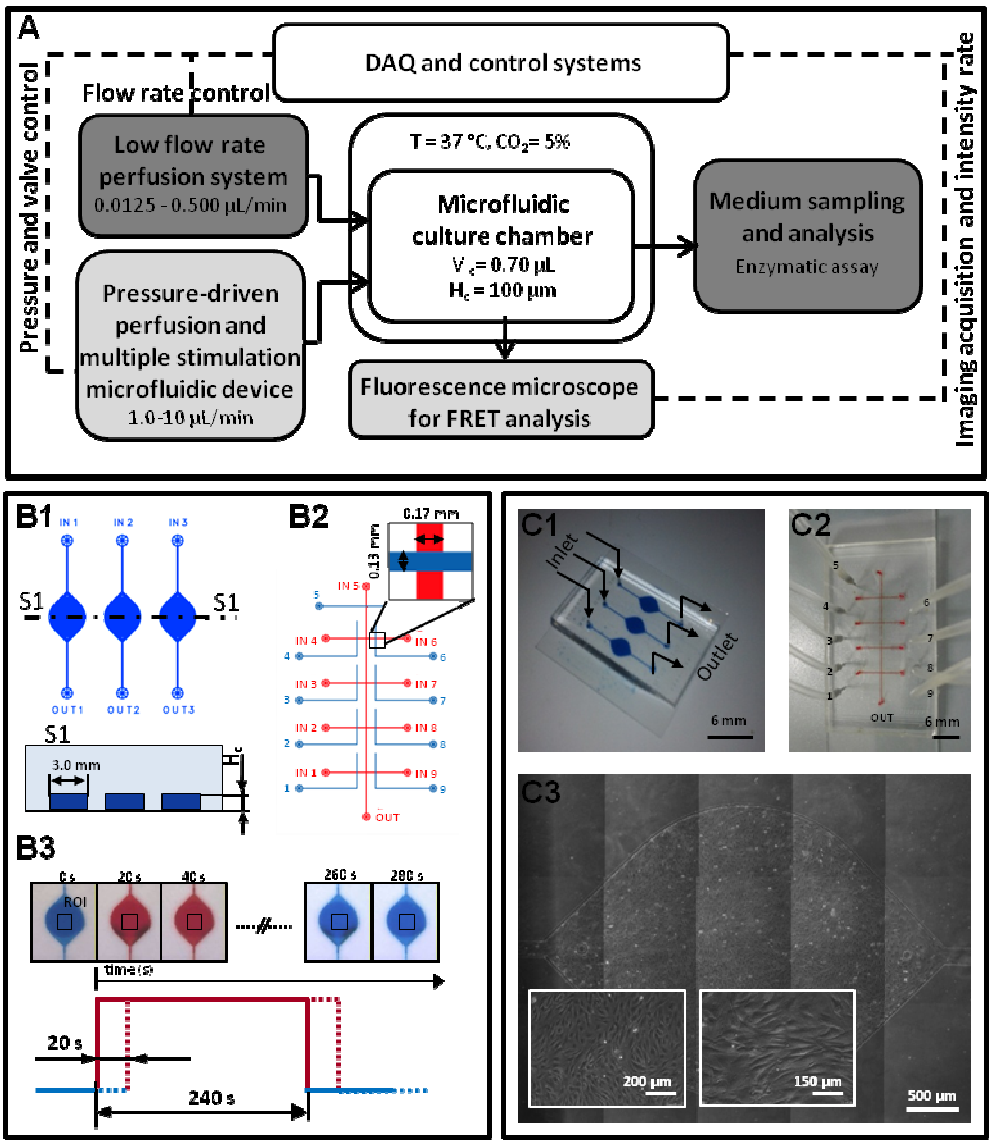

Figure 4.1. *Experimental setup. (A) Schematic view of experimental setup. Dark gray boxes describe off-line medium glucose measurements, light gray boxes experiments with FRET nanosensor. (B1) Schematic representation of the 3 culture chambers in the microfluidic chip (top view and section). (B2) Schematic representation of the microfluidic device used to change inlet medium glucose concentration. Round flow channels in red and square control channels in blue. (B3) Sequence of chamber images during the fast stimulation simulated by red and blue dyes. (C1) Image of PDMS culture chamber chip. (C2) Image of multiple stimulation microfluidic platform; flow channels were filled with a red dye; tubes are connected to pressure-driven control channels. (C3) Microscopic image of the whole culture chamber with confluent C2C12, 2 days after seeding. Insets represent different magnifications.*

Two sets of experiments can be performed with this set up. First, the measurement of glucose concentration at the outlet at multiple time points by sampling and off-line sensing via enzymatic assay. These experiments were used to detect glucose uptake of the whole cell population. In the second set of experiments FRET experiments under

fluorescent microscope can be performed, in order to detect single cell intracellular glucose concentration. Other information about material and method related to systems fabrication, detection and analysis can be found in the related Appendix D.

4.3.1 Extracellular detection

For the off line measure two phases are needed: sampling and sensing. For medium sampling we used a dropping trap for medium collection; it is placed downstream of the microfluidic culture chamber and it collects a small quantity of medium (<1 uL). We used small dispensing needle closed with PMMA male luer cup to avoid medium evaporation. For sensing, glucose concentration was determined offline using enzymatic kit assays. Easy and fast enzymatic assay have been identified in FreeStyle Lite® glucometer and strips (Abbott Diabetes Care): 0.3 uL is required for each single measurements.

Glucose uptake was calculated as result of the macroscopic balance considering the whole chamber as the system of interest. The average glucose uptake per cell, $N_m^{\exp}$, was calculated by the following expression:

$$N_m^{\exp} = \frac{G_{IN} - G_{OUT}}{N_{cell}} \cdot \dot{V} \qquad (4.1)$$

Where G_{IN} is the fixed glucose concentration at the inlet, $\dot{V}$ is medium flow rate, N_{cell} the number of cells in the culture chamber and G_{OUT} the glucose concentration at the outlet, that was measured experimentally after sampling.

G_{OUT} measurements were taken using a glucometer after sampling a medium volume of 0.6 µL, a bit larger than the minimum required by the instrument. The time needed to obtain the sampling volume is inversely dependent on medium perfusion rate (Figure 4.2A, inset), and this poses an upper bound to the temporal resolution achievable.

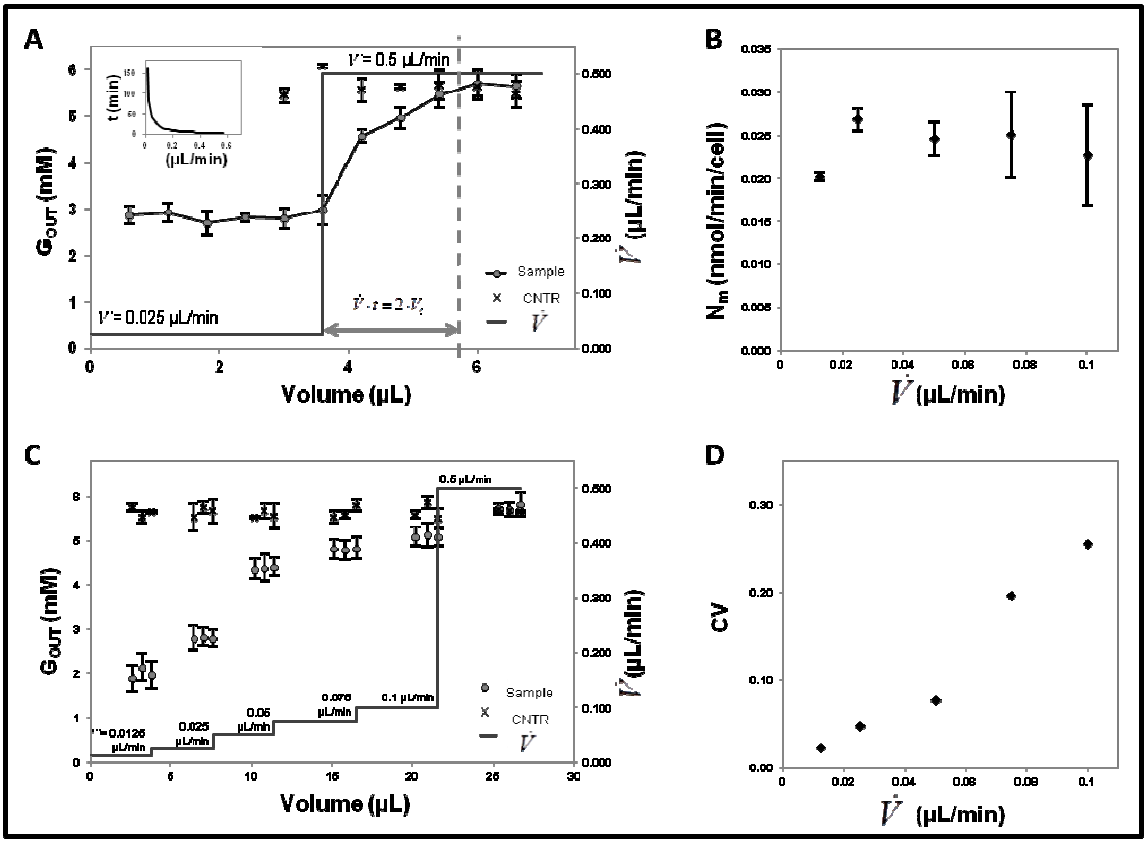

Figure 4.2. Effect of flow rate on glucose uptake measurements. (A) Transient of G_{OUT} concentration after a change in flow rate. G_{OUT} is shown as a function of the eluted volume. Sampling was performed continuously (each 0.6 µL-volume collected was analyzed). Results from 6 repeated experiments. Inset shows duration of sampling as a function of volumetric flow rate for a sampling volume of 0.6 µL. (B) Steady-state glucose uptake calculated by (4.1) from G_{OUT} measurements in (C) at different flow rates. (C) Steady-state G_{OUT} measurements at different flow rates. For each condition, 3 samples were taken at steady-state from each of the 3 culture chambers and analyzed. (D) Coefficient of variation of N_m as a function of flow rate. (A-D) G_{IN} was fixed and equal to 5.5 mM. Error bars represent standard deviations.

The validation has been achieved studying the effect of different operative variables on measurement sensitivity (Figure 4.2). In particular, for a fixed inlet glucose concentration (5.5 mM), we analyzed the measurement sensitivity at different flow rates and the duration of the transient before a new steady-state is established after changing flow rate. These experiments were performed at maximum time resolution, i.e. medium was continuously collected and analyzed every 0.6 µL eluted. Thus, at low flow rate (0.025

µL/min) measurements were taken every 24 min, while at high flow rate (0.5 µL/min) every 1.2 min (Figure 3A).

On the other hand, the higher temporal resolution at high flow rate comes at the expenses of reduced measurement sensitivity. Specifically, the steady-state outlet concentration at 0.5 µL/min is not significantly different to the concentration of the control experiment (perfusion through a chamber without cells), despite the small variance of the data between samples, and the signal-to-noise ratio is too small for accurate detection.

The residence time, t_r, of medium in the culture chamber is calculated by the following equation:

$$t_r = \frac{V_c}{\dot{V}} \tag{4.2}$$

where V_c represents the cell chamber volume. As during this time cells uptake glucose, the longer is t_r, the lower is G_{OUT}. In our experimental system, the culture chamber had a volume of 0.7 µL/min. Thus, residence time was reduced from 24 min to 1.2 min increasing the flow rate as in Figure 4.2A.

We also calculated the duration of transient after a change in flow rate. A new steady-state is established after infusing into the culture chamber an amount of medium that is approximately the double of its volume (Figure 4.2A).

To define the optimal trade-off between high temporal resolution and sensitivity of measurement, we performed an experiment where step changes of flow rate were applied to 3 culture chambers in parallel (Figure 4.2C). The experimental values obtained for G_{OUT} were then used to calculate steady-state glucose uptake, $N_m^{\exp}$, from (4.1). As expected, glucose uptake does not depend on the flow rate, when this is high enough to avoid extracellular mass transfer limitations, as in the case of 0.0125 µL/min (Figure 4.2B). However, variability is higher at large flow rates due to measurement inaccuracy

(Figure 4.2D). Taken together, these considerations supported the choice of using a flow rate of 0.05 µL/min, allowing a 10 minute temporal resolution.

4.3.2 Intracellular detection

FRET glucose nanosensors are able to measure dynamic changes in glucose concentration with cellular and subcellular resolution. They exploit resonance energy transfer between a coupled pair of cyan and yellow fluorescent proteins (eYFP, eCFP) to detect conformational changes induced by sugar-binding .They consist of a recognition element for glucose (a member of the bacterial periplasmic-binding protein family MglB [14]) fused to eCYP and eYFP, whose peculiarity is the overlapping emission spectra [15-17]. Glucose binding to the recognition element induces conformational changes that lead to a change in transferred excitation energy between the attached eCFP and eYFP [18,19]. This change in FRET efficiency can be visualized as a change in intensity ratio I_a/I_d (where I_d and I_a are the fluorescence intensities in the donor and acceptor emission channels upon excitation of the donor) and it can be directly correlated to intracellular glucose concentration [12]. FRET glucose nanosensors need to be encoded within the cells by DNA transfection [20].

We tested FRET nanosensor performance in our system (Figure 4) with C2C12. (Sensor was also tested preliminary with HEK, data not shown). At least two cells transfected with the sensor were analyzed for experiment under a fluorescence microscope at 40X, collecting the signal at the wavelength of cyan (CFP) and yellow (YFP) fluorescent proteins at high temporal resolution. When glucose concentration in a cell increases, CFP fluorescence intensity decreases and YFP fluorescence increases, because of the conformational change of the nanosensor (Figure 4.3A). Images were analyzed as reported in previous work by Huei et al. [12], with spectral bleed-through (SBT) and baseline correction using polynomial fit. The analysis produced the normalized baseline-corrected FRET index, F^c/D, an indirect measure of intracellular glucose. After analyzing a sequence of images like those in Figure 4.3A, we obtained F^c/D as a function of time

during a cyclic pulse stimulation of cells with 1.5 mM glucose concentration. The normalized FRET index decreases when a high glucose concentration enters the system and returns to its baseline value when glucose is removed (Figure 4.3B). The results are consistent and reproducible for the cells measured.

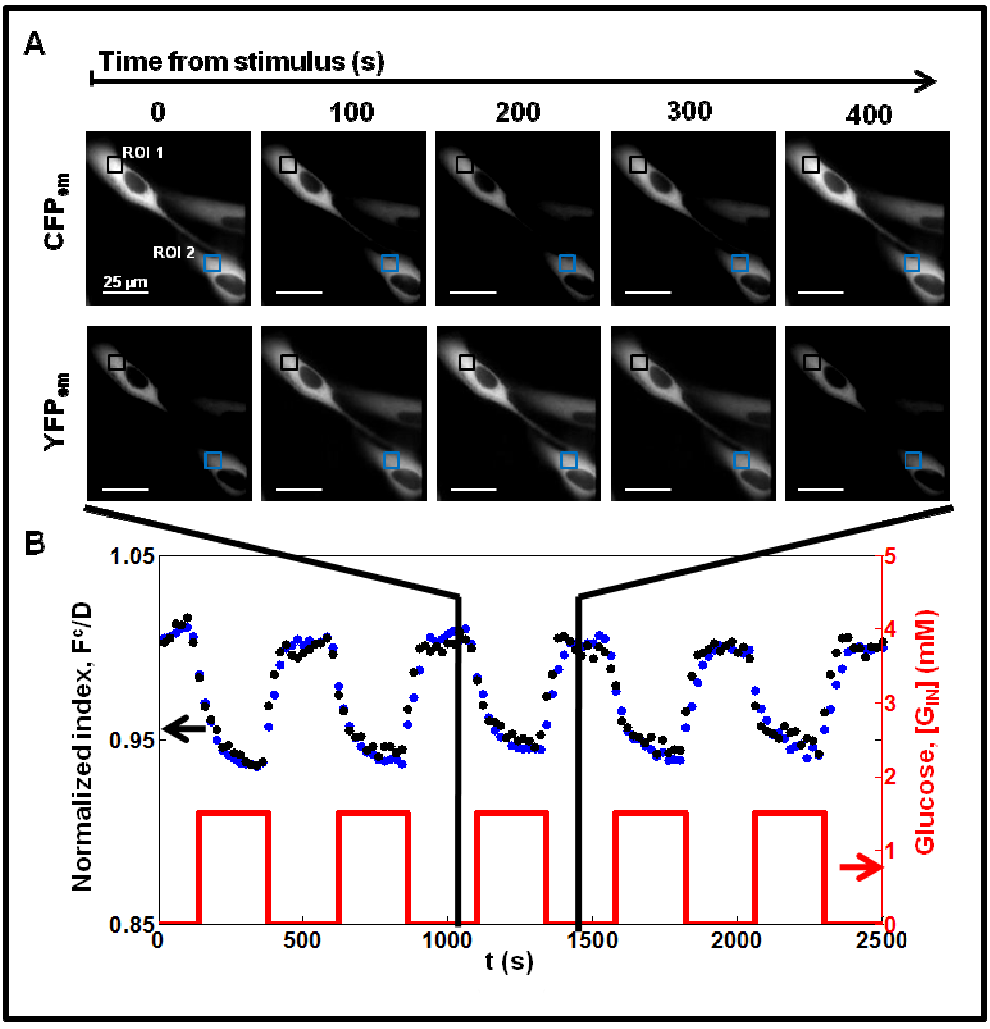

Figure 4.3. *Dynamic measurements of intracellular glucose concentration via FRET nanosensor. (A) Sequence of images, obtained by fluorescence microscopy, of cyan (CFP) and yellow (YFP) fluorescent proteins during pulse perfusion at 1.5 mM glucose concentration. (B) Normalized FRET index, F^c/D, during an experiment of cyclic pulses of 1.5-mM glucose concentration. Blue and black dots refer to the two regions of interest (ROIs) shown in (A).*

4.3.3 Electrochemical on line extracellular glucose detection

This part of the chapter is focused on the design of integration between microfluidics and biosensor in order to obtain on line glucose measurement. Furthermore data about amperometric measurements, methods and mathematical model can be found in Appendix C “Flow sampling and sensing in indirect electrochemical detection”. In this work, we investigated how the electrochemical measurement of an analyte involving the detection of a mediator is affected by flow conditions in a miniaturized biosensor.

The on line measurement provide continues glucose detection by the use of sensor placed directly inside microfluidic channels. Two prerequisites are needed: a sensitive sensor able to detect glucose in microfluidic conditions, and a microfluidic chip interface able to contain the sensor.

In this technology development, a microelectrode biosensor have been coupled into microfluidic channel. Figure 4.4a shows a schematic representation of biosensor into microfluidic device: the working microelectrode, a counter electrode and a reference electrode have been housed within the microfluidic unit. Microelectrode biosensors have been provided by Prof. P.A. Serra (Univ.of Sassari) [21,22].

The distance between reference and working electrodes is sufficiently little not to interfere the electrochemical measurement, as we tested interchanging electrode positions. The enlargement of the channel section at the electrodes assures complete wetting of the sensing tip in case of bubble formation at the walls. Glucose was amperometically detected after its enzymatic conversion to H_2O_2 by glucose oxidase (GOx). The oxidases are a subclass of oxidoreductases that produces H_2O_2 when substrate is oxidized. The application of an electrochemical positive potential to a platinum (Pt) electrode generates an anodic current proportional to the rate of the H_2O_2.

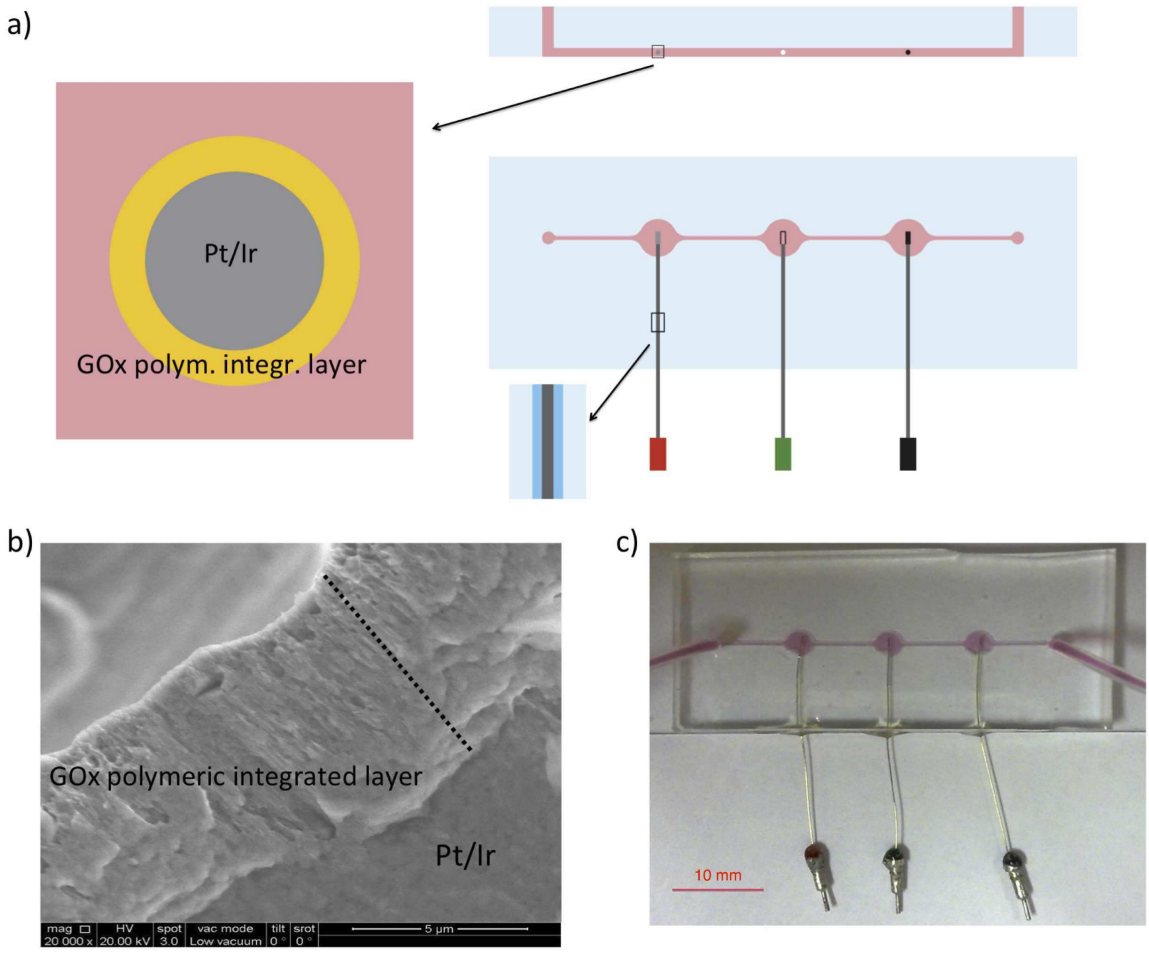

Figure 4.4: *Microfluidic biosensor. (a) Lateral and top views of the main channel. Working (red), reference (green), and counter (black) electrodes. Enlargements of the transversal and longitudinal sections of the working electrode tip and of the insulated part, not on scale. (b) Scanning electron micrograph of the transversal section of the electrode tip: a GOx polyurethane integrated layer, whose thickness is indicated by the dotted line, coats a Pt/Ir wire. (c) Picture of the microfluidic system schematically described in (a) with pink medium flowing.*

The influence of flow rate on the current was investigated changing the manipulated variable in a range between a few µL/h up to $6 \cdot 10^4$ µL/h. Data (in Appendix C) showed the raising of the detected current value by increasing flow rate (more concentrated is the solution, more remarkable is the effect), up to a plateau when the current value does not undergo more changes against further increases in flow rate.

The previous analysis demonstrated the importance to control the volumetric flow rate during biosensor. For this reason, we have developed a new design for performing biosensing measurements that decouples the flow rate used for the measurement from the sampling flow rate. The new system includes a loop filled offline with the sample at

an independent flow rate respect to that in the main channel (Fig. 4.5). The loop is connected to the main inlet through a microfluidic valve system and can be connected/disconnected (on/off) when requested. The advantage of this design is to decoupling sampling and sensing allowing their independent control.

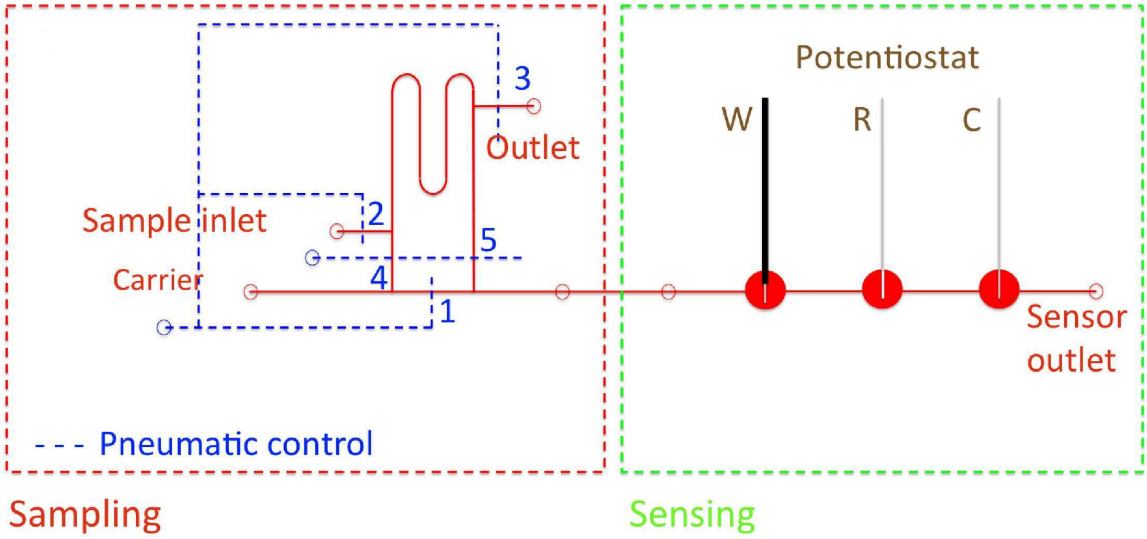

Figure 4.5 : *Sampling and sensing units integration. Schematic view of the entire system. Loop loading: open 1, 2, 3; close 4, 5. Sample analysis: open 1, 2, 3; close 4, 5.*

The data from this work confirm the feasibility of integrating microbiosensors within microfluidic platform for fast on line measurement of glucose. The biosensor can be directly integrated within the microfluidic platform downstream the cell culture chamber. This microfluidic-integrated biosensor can acquire data every minute regardless of the medium flow rates. This methodology is more complicated than the off line medium drop detection, but highly enhance the resolution measurements of glucose uptake.

4.4 Conclusions

This chapter focused on the development of glucose uptake measurement within microfluidic technology. Using intrinsic microfluidic properties I developed a robust non invasive methodology for glucose uptake measuring by extracellular glucose detection in medium sampling. Data showed high reproducibility and sensitivity. With this system I

was able to track glucose concentration with high temporal resolution, up to few minutes. Moreover with FRET nanosensor I was able to measure intracellular glucose concentration dynamic with high accuracy with single cell resolution. I demonstrated the capability to use on line electrochemical biosensor to detect glucose directly and automatically. The decoupling between sampling and sensing has increased the capability and efficiency of the system.

The high resolution approach of glucose uptake measurement obtained with this method can be translated for the study of the effect of insulin diabetic studies. It permits to highlight the different phases of the insulin-activated glucose uptake, such as, time lag of insulin action, uptake rate increasing, steady state threshold and glucose uptake decreasing to the basal level. These data will provide completely new insight in the insulin-dependent glucose uptake, insulin pathway and insulin resistance.

4.5 References

[1] Frier, B. M. Diabetologia 52, 31–34 (2009).

[2] Laakso, M. Diabetes 48, 937–942 (1999).

[3] Cryer, P. E., Davis, S. N. & Shamoon, H. Diabetes Care 26, 1902–1912 (2003).

[4] Rolo, A. P. & Palmeira, C. M. Toxicology and Applied Pharmacology 212, 167–178 (2006).

[5] Ferrannini, E. & Cobelli, C. Diabetes Metab Rev 3, 335–363 (1987).

[6] Odegaard, J. I. & Chawla, A. Science 339, 172–177 (2013).

[7] Sokoloff et al., J. Neurochem. 28, 897–916. (1977)

[8] Yamada et al., J. Biol. Chem., 275, 22278–22283 (2000)

[9] Maschauer et al., J. Nucl. Med. 45, 455–460. (2004)

[10] Yamamoto et al., Anal. Biochem. 404, 238–240, (2010)

[11] Kurtoglu et al., Antioxidants & Redox Signaling; 9(9):1383-1390 (2009)

[12] Hou et al., Nat Protoc.; 6(11):1818-33 (2011)

[13] Tsung-Hsi Hsieh, Microfluidics and Nanofluidics (2009), Volume 6, Issue 3, pp 391-401,

[14] Vyas, Vyas, and Quiocho, Science (New York, N.Y.) 242, no. 4883 (1988): 1290-1295.

[15] Deuschle et al., Protein Science: A Publication of the Protein Society 14, no. 9 (2005): 2304-2314.

[16] Fehr et al., Journal of Fluorescence 14, no. 5 (Settembre 2004): 603-609.

[17] Fehr et al., Proceedings of the National Academy of Sciences of the United States of America 99, no. 15 (Luglio 23, 2002): 9846-9851.

[18] Deuschle et al. Protein Sci. 2005 September; 14(9): 2304–2314.

[19] Takanaga et al., Biochimica Et Biophysica Acta 1778, no. 4 (Aprile 2008): 1091-1099.

[20] Pampinella et al., Molecular Therapy (2002) 5, 161

[21] Serra et al., Sens. Actuators B 122, 118–126 (2007).

[22] Serra et al., (InTech, 2010).

Chapter 5

High resolution glucose uptake measurement in skeletal muscle and adipose tissue

5.1 Introduction

This chapter reports the results obtained in muscle cells and adipose tissue integrations within microfluidic chip. The chapter can be subdivided in two main parts: the first related to muscle cells and the other to adipose tissue. For muscle cells, the detection of intracellular glucose concentration at single-cell level via FRET nanosensors has been coupled with glucose uptake derived from direct enzymatic measure of downstream culture medium (methodology have been already reported in Chapter 4 for the single method). We then analyzed these experimental data through a simplified mathematical model to obtain the kinetic constants of each step of the process. More information can be found in Appendix D “Method for dynamically measuring intracellular glucose kinetics with single-cell resolution”.

For the adipose, the measurement of tissue glucose uptake through the intracellular glucose detection is not straightforward; FRET analysis requires plasmid transfection within adipo-cells that is not possible to achieved with high efficiency in adipose tissues slices. Moreover three-dimensional tissues show intrinsic limitations for the application of optical fluorescence analysis. For all these reasons the evaluation of glucose concentration in adipose tissue was limited to off line measurements. At the end of the

related paragraph the proof of concept for insulin resistance evaluation on glucose uptake is reported.

5.2 Skeletal muscle cell culture

In the previous Chapter 4, high-resolution intracellular and extracellular glucose measuremens have been shown and described. In this paragraph we want to report a further evolution offered by their coupling in skeletal muscle cell C2C12. To achieve that, we coupled the detection of intracellular glucose concentration at single-cell level via a FRET nanosensor, with glucose uptake derived from direct off line measure on outlet culture medium.

5.2.1 Dynamic measurements of intracellular glucose concentration via FRET nanosensor

The experiment described in paragraph 4.3.2, related to intracellular glucose concentration evaluation, has been repeated applying glucose pulses of increasing concentration (Figure 5.1). Figure 5.1A shows the signal collected from 3 cells after analysis: consistent results were obtained, FRET index (F^c/D) had larger amplitude of oscillation for pulses of higher glucose concentration. Measurement noise was relevant at low glucose concentration, but the sensor response showed good signal-to-noise ratio for concentrations higher than 1 mM (Figure 5.1A). We calculated the integral of F^c/D during each pulse of stimulation as a measurement of the total glucose up taken during that time span. Results show that the sensor has a linear response up to about 4 mM (Figure 5.1B). Curves from Figure 5.1A were overlapped in Figure 5.1C. Qualitatively, the data show a faster response during cellular uptake at higher glucose concentrations (Figure 5.1C). A further analysis has required a simplified analytical model. It has been developed to obtain the kinetic parameters of glucose uptake and phosphorylation from measurements of glucose uptake and of cytosolic glucose concentration via FRET nanosensor.

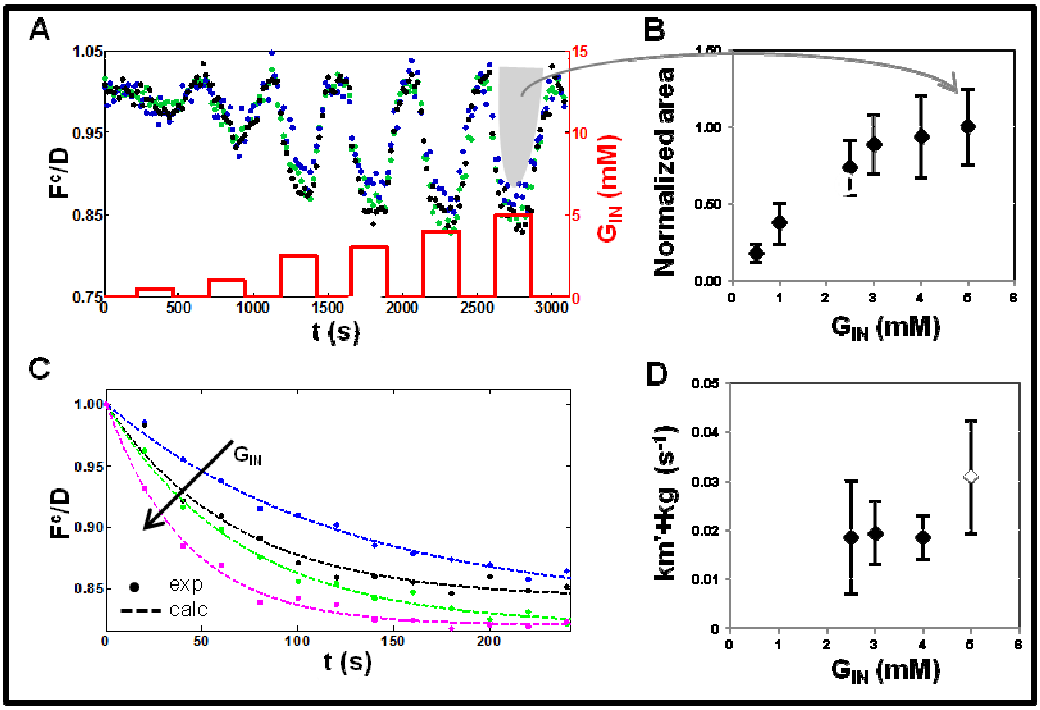

Figure 5.1. *Effect of glucose concentration on FRET nanosensor response. (A) Normalized FRET index, F^c/D, as a function of time during repeated pulses of increasing glucose concentration (0.5, 1, 2.5, 3, 4, and 5 mM). Black, blue and green dotes refer to the signal from 3 different cells. Flow rate was 4 µL/min. (B) Integral of Fc/D during each glucose pulse, normalized by its value at 5 mM glucose concentration. (C) Transients of FRET sensor response at different glucose concentrations (2.5, 3, 4, and 5 mM) were overlapped and fitted by Eq.(5.6). (D) Results of the fitting performed in (C), $k'_m + k_g$ are represented as a function of glucose concentration.*

In order to analyze FRET data, a single-cell mass balance was performed. The equation is given by:

$$\frac{dG_{cyt}}{dt} = \frac{N_m}{V_{cell}} - R_{gly} \tag{5.1}$$

where the left-hand side term accounts for the accumulation of glucose inside the cell with time, t, and the two terms on the right represent glucose inflow through the cell membrane, N_m, per unit cell volume, V_{cell}, and glucose consumption rate through glycolysis, R_{gly}, respectively.

Glucose inflow through plasma membrane was expressed as:

$$N_m = k_m A_{cell} \left(G_{bulk} - G_{cyt} \right) \tag{5.2}$$

where k_m is the overall mass transfer coefficient, $A_{cell}$is cell surface, $G_{bulk}$and G_{cyt} represent glucose concentration in medium bulk and in the cytosol, respectively. G_{bulk} is assumed equal to glucose inlet concentration, G_{IN}. The difference of glucose concentrations represents the overall driving force of two sequential processes: glucose transport from medium bulk to cell membrane and glucose passage through the membrane. An average intracellular glucose concentration, G_{cyt}, was used, neglecting the spatial inhomogeneity within the cell.

Intracellular glucose consumption due to glycolysis was assumed to occur irreversibly and according to a linear kinetic expression:

$$R_{gly} = k_g G_{cyt} \tag{5.3}$$

where $k_g$is a kinetic parameter.

We integrated Eq. (5.1) after substituting the terms in Eq. (5.2) and (5.3) with, as initial condition, a null intracellular glucose concentration. We obtained the following analytical solution:

$$G_{cyt} = G_{bulk} \frac{k_m^{'}}{k_m^{'} + k_g} \left[1 - \exp\left(-\left(k_m^{'} + k_g \right) t \right) \right] \tag{5.4}$$

where $k_m^{'} = k_m A_{cell} / V_{cell}$.

The normalized FRET index, F^c/D, is correlated to glucose intracellular concentration, G_{cyt}, according to the following expression:

$$G_{cyt} = \alpha \left(1 - F^c/D \right) \tag{5.5}$$

where α is a parameter used to convert concentration to fluorescence units. Substituting (5.4) in (5.5), we obtained the equation:

$$\frac{F^c}{D} = 1 - \frac{G_{bulk}}{\alpha} \frac{k_m^{'}}{k_m^{'} + k_g} \left[1 - \exp\left(-\left(k_m^{'} + k_g \right) t \right) \right] \tag{5.6}$$

that was used to obtain the value $(k'_m + k_g)$by fitting FRET experimental data at different glucose concentrations. Eq. (5.2) was used to fit the experimental data derived in eq. (4.1) and to obtain the value of each parameter, k'_m and k_g.

At this point the transient of the normalized FRET index during the pulses at different glucose concentrations (Figure 5.1C) have been analyzed by performing a fitting of these data by Eq. (5.6) to quantify the increasing trend at higher glucose level. We obtained the value of $(k'_m + k_g)$ different glucose concentrations (Figure 5.1D). This sum represents the inverse of the time constant of the overall process (uptake and phosphorylation). The data showed that the simplified model we developed is able to capture the main dynamics involved, as it shows a constant value for $(k'_m + k_g)$ at different glucose concentrations. A little discrepancy is visible for 5 mM glucose concentration, which is attributable to the loss of sensor linearity at this concentration (Figure 5.1B).

5.2.2 Estimation of kinetic parameters

We coupled the kinetic information obtained during FRET experiments with measurements of glucose uptake at different glucose concentration. We measured glucose uptake at a flow rate of 0.05 µL/min at 3, 5, and 10 mM glucose concentrations. Glucose uptake by the whole cell population was linear within this range (Figure 5.2A). We fitted these results by Eq. (5.2) to discriminate between the values of k'_m and k_g, as we obtained only their sum from FRET experiments. The values of these two parameters were almost constant regardless throughout all glucose concentrations (Figure 5.2B).

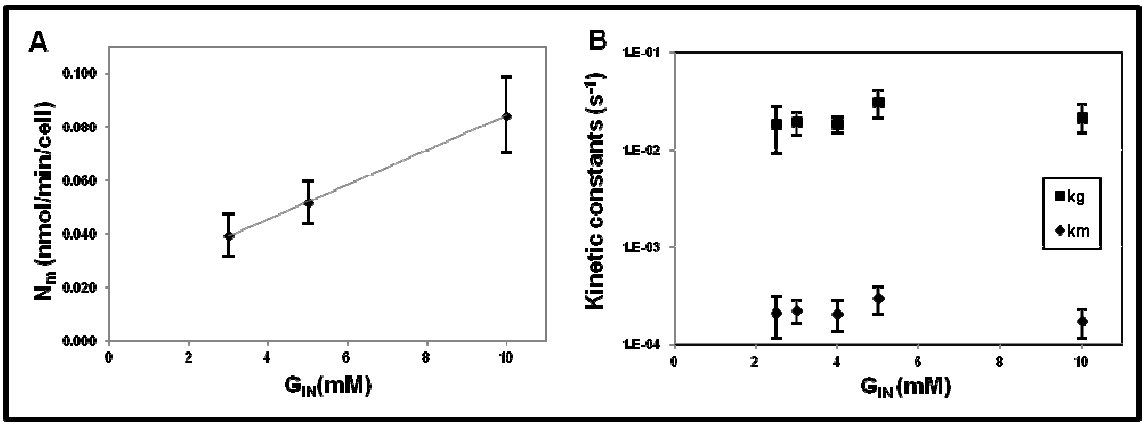

Figure 5.2. *Glucose uptake and parameter evaluation. (A) Glucose uptake calculated from off-line measurements of* G_{OUT} *at different glucose inlet concentrations. Flow rate was 0.05 µL/min. (B) Results of parameter estimation at different glucose concentrations.*

In coupling the information from the two measurement methodologies, we neglected the differences in the external mass transfer, due the different flow rate used in the two sets of experiments. However, both the fitting results (Figure 5.1D and 5.2A) and a theoretical estimation of the overall mass transfer coefficients in the two systems by non-dimensional analysis (data not shown) support this assumption. Thus, for perfusion as low as 0.05 µL/min in our culture system, glucose concentration at cell membrane can be approximated with bulk (or inlet) glucose concentration

5.3 *Ex vivo* adipose tissue culture

This chapter relates to the validation of *ex vivo* human adipose tissue culture within microfluidic chip, and the continuous measurement of extracellular glucose concentration in the downstream culture medium. Microfluidic culture chamber system was already introduced in chapter 2, while the automated chip with microvalves, pumps and injection system was introduced in chapter 3. Biological protocol are also reported in Appendix F.

Adipose tissue was integrated into microfluidic platform one day after surgery. The system was a reversible open-closed device that allows adipose slices insertion (Figure

5.3B). In order to limit biopsy floating, it was placed upside-down (Figure 5.3A). The chamber has been specifically design in order to integrate AT into microfluidic chamber and measure downstream glucose concentration through the medium perfused in the chamber. The organ culture was inserted through a hole chamber placed over the microfluidic medium distribution system (Figure 5.3A). The array of circular microposts ensures a constant medium volume at the biopsy surface, reducing the formation of dead volumes due to biopsy leaking from the PDMS bottom chamber. Microposts also avoid the blocking of the inlet-outlet channels consequent to biopsy insertion.

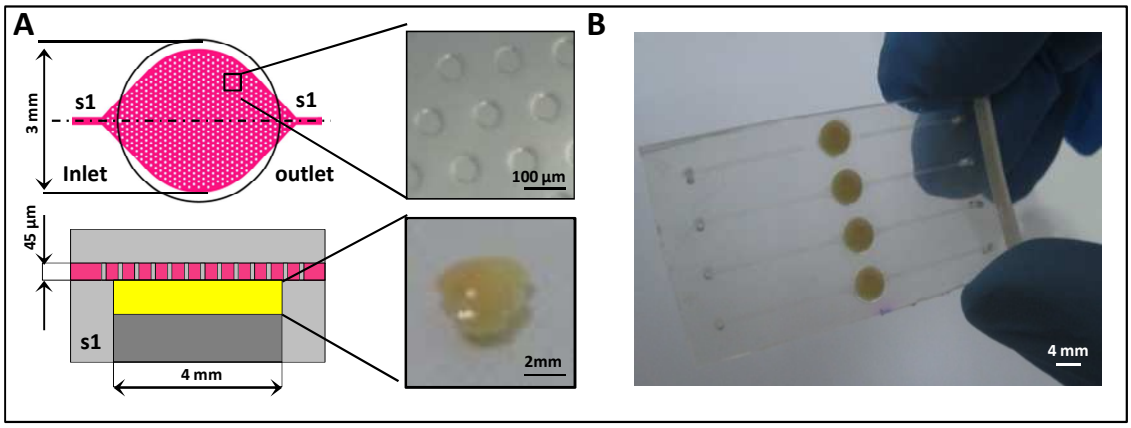

Figure 5.3: Microfluidic culture chamber: design, modeling and validation. *(A) Schematic culture chamber representation (top view and section) and microposts and biopsy slice images. (B) Image of four culture chambers 3D prototype with adipose tissue samples*

In order to determine adipose tissue viability, MTT assay has been performed after 1 week of dynamic microfluidic culture and values were compared with static cultures (conventional organ culture in wells, medium replaced every day). There were no substantial differences between static and microfluidic cultures (Figure 5.4A), confirming thus the possibility of long term viability as seen in static conditions. Moreover, tissue morphology from H&E stain (Figure 5.4C) doesn't show significant differences between static or microfluidic conditions after 8 days of culture, even compared with tissue morphology immediately after surgery. The maintenance of metabolic activity during culture has been achieved also by glucose detection during different days (Figure 5.4B) at 0.025 µl/min flow rate perfusion. Glucose concentration is maintained pretty constant

for the entire 5 days of investigation, confirming high metabolic tissue activity for several days. Higher glucose values in the first day of culture seems to be correlated to biopsy adaptation to the new *ex vivo* condition, as we saw also in static conditions (data not shown). Data reported are referred to 4 biopsies from the same patient.

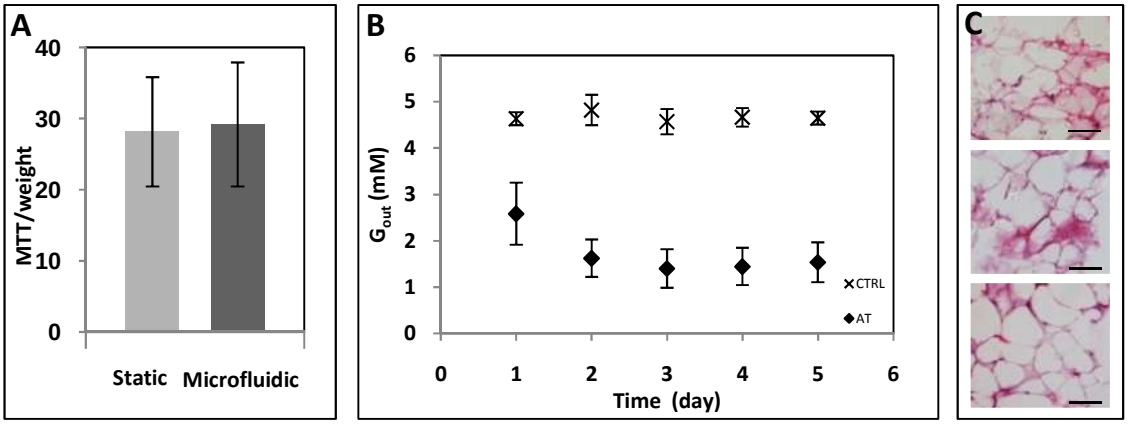

Figure 5.4. Adipose tissue viability. *(A) Adipose tissue viability after 7 days of culture; static and microfluidic (B) Adipose tissue glucose consumption during days (flow rate 0.025 µl/min, n= 6) and relative control. (C) Hematoxylin and eosin stain: static (top) and microfluidic (center) after 7 days of culture; control (bottom).*

After confirming adipose tissue viability and accurate response and consumption, we investigated the effect of flow rate on glucose concentration from low to high values. These experiments were performed at maximum time resolution possible, i.e. medium was continuously collected and analyzed every 0.6 µL eluded. Thus increasing flow rate has the effect in higher temporal resolution up to 1 minutes for the highest flow rate investigated (0.6 µL/min).

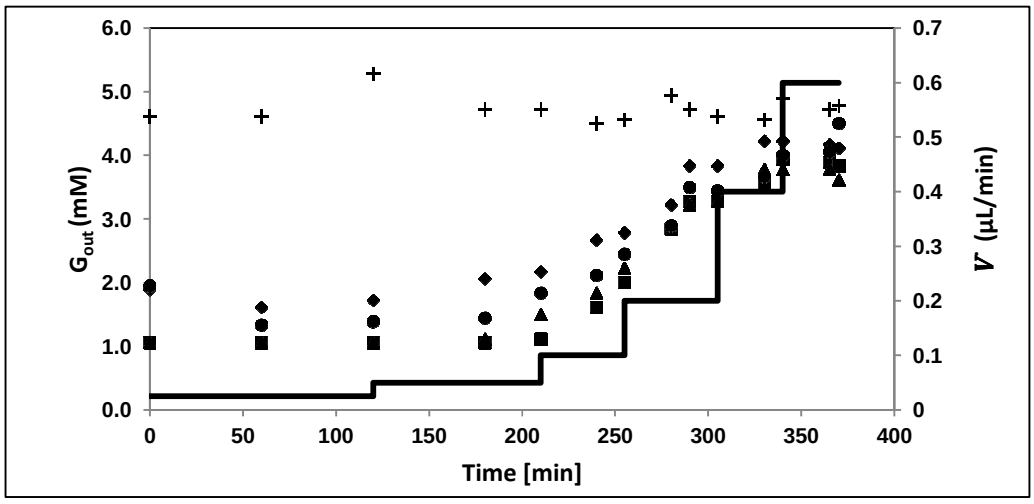

Figure 5.5. *Continuous glucose concentration measurement at increasing flow rate. (0.025-0.6 µl/min). Data related to four samples from same patient and control (+); continue line refers to flow rate steps.*

Figure 5.5 shows a continuous glucose profile during time at increasing flow rates for 4 samples coming from the same patient. Surprisingly, glucose concentration profile was maintained for different samples with low variability. We obtained consistent data from analyses at different flow rates after the establishment of the new steady states (average from multiple samples, n=4), as reported in Figure 5.6A. Moreover, the robustness of the measurements was evaluated by the comparison of glucose profile obtained from similar experiments repeated for several days. We obtained high measurement reproducibility for 3 following days for the same biopsy sample (Figure 5.6B). This important data has a positive feedback in robustness and in experimental feasibility, key parameters for a robust *in vitro* drug screening test. In regard of glucose uptake calculation and measurement, the complexity due to adipose tissue has a negative effect on the obtainment of consistent data as now. Further modeling and other experiments need to be performed and are still pursued.

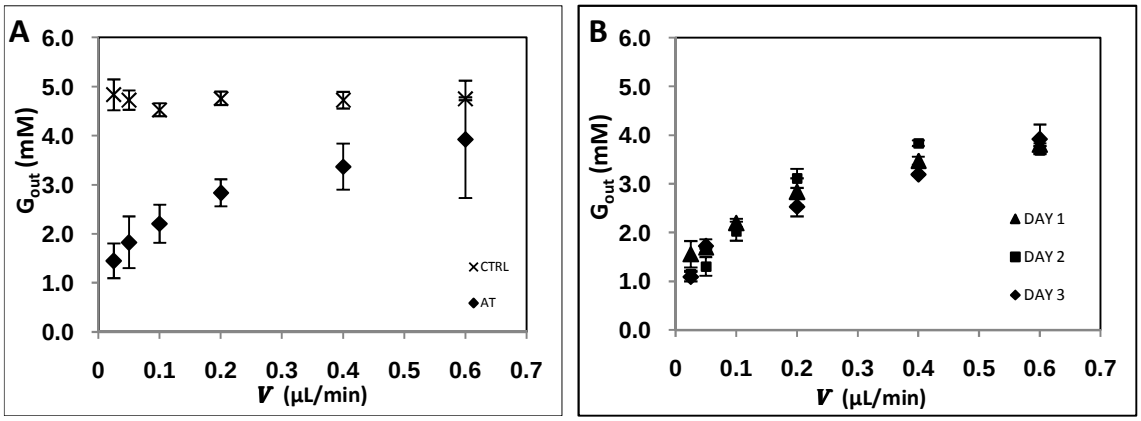

Figure 5.6. *Glucose concentration measurement: flow rate effect and long term response. (A) Steady-state* G_{OUT} *measurements at different flow rates. Average of 4 samples from patients. (B) Steady-state* G_{OUT} *measurements at different flow rates. Average from same sample during 3 following days.*

5.3.1 Proof of concept of insulin resistance evaluation

At the end of this chapter we want to produce the proof of concept of the designed microfluidic device for the obtainment of specific information on insulin effects. The microfluidic chamber has been endowed with automated injection system for insulin or other anti-diabetic drugs, as reported in Chapter 3. Specific experiments have been performed using the injection system with integrated *ex vivo* tissue. In order to validate the uniformity and distribution of stimulus, a fluorescent tracer (fluorescein sodium) has been added to insulin in the reservoir loop channels (Figure 5.7A). We observed uniform distribution of fluorescent tracer inside the chamber, thanks to the presence of microposts covering (Figure 5.7B). Biopsy has been completely crossed by the tracer up to interstitially distant areas from the medium distribution. Figure 5.7C shows the biopsy integrated in the microfluidic chamber after fluorescein injection. The most porous biopsy points have been showed by the presence of more intense fluorescent values.

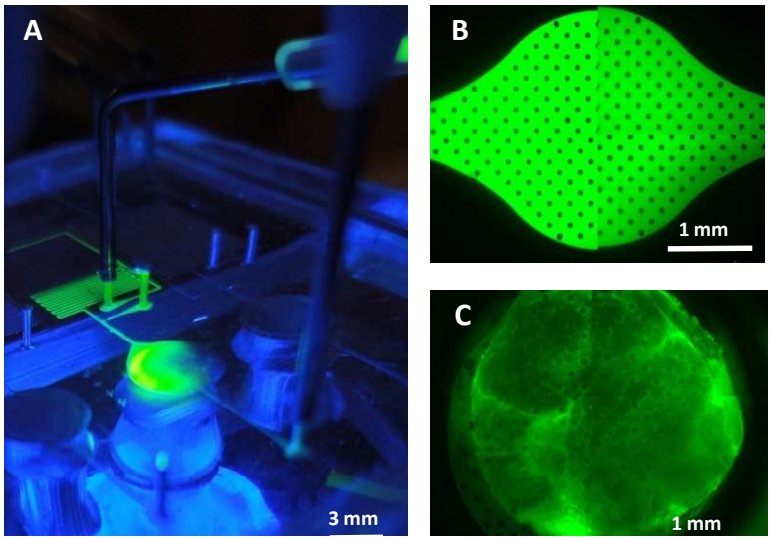

Figure 5.7. *Insulin delivery validation. (A) Insulin stimulation with automated injection system; fluoscent tracer added. (B) Image of culture chamber medium distribution after stimulus with fluorescein. (C) Image of adipose tissue within culture chamber perfused with fluorescet tracer.*

As preliminary results, I want to show data about the evaluation of insulin step effects on outlet glucose concentration in biopsies coming from diabetic and non-diabetic patients. Our strategy was to determine differences in glucose outlet concentration from stimulated and non-stimulated (controls for this experiments) biopsies, being able thus to relate the profile to diabetic or to healthy patients. We performed two set of experiments. In the first experiments, we stimulated both healthy and diabetic samples at basal glucose concentration (4 mM) with 100 nM insulin (Sigma), maintaining the same basal glucose concentration during the total length of experiment (Fig 5.8A, 5.8B). In this condition, we do not observe changing in glucose outlet concentration in healthy (Fig 5.8A) and diabetic (Fig 5.8B) patients. In the second set of experiments, we stimulated biopsies with 100 nM insulin, from basal to higher glucose level (7 mM), simulating the post-prandial phase. In healthy patients the combined effect of insulin and glucose seems to be related to an increasing of outlet glucose concentration profile with a substantial difference from stimulated and control samples (Fig 5.8C). The glucose gap during the first hour from stimulus seems to decrease for prolonged stimulation. On the other hand for diabetic patient (Fig 5.8D) there was no evidence in glucose concentration differences between the samples. The increasing measured downstream

glucose concentration seems to be not sensitive to insulin stimulus for the entire length of experiment. These data, even if they are derived only from preliminary results, seems to be promising for insulin sensitive and resistance *in vitro* experiments and they represents a proof of concept for its applicability.

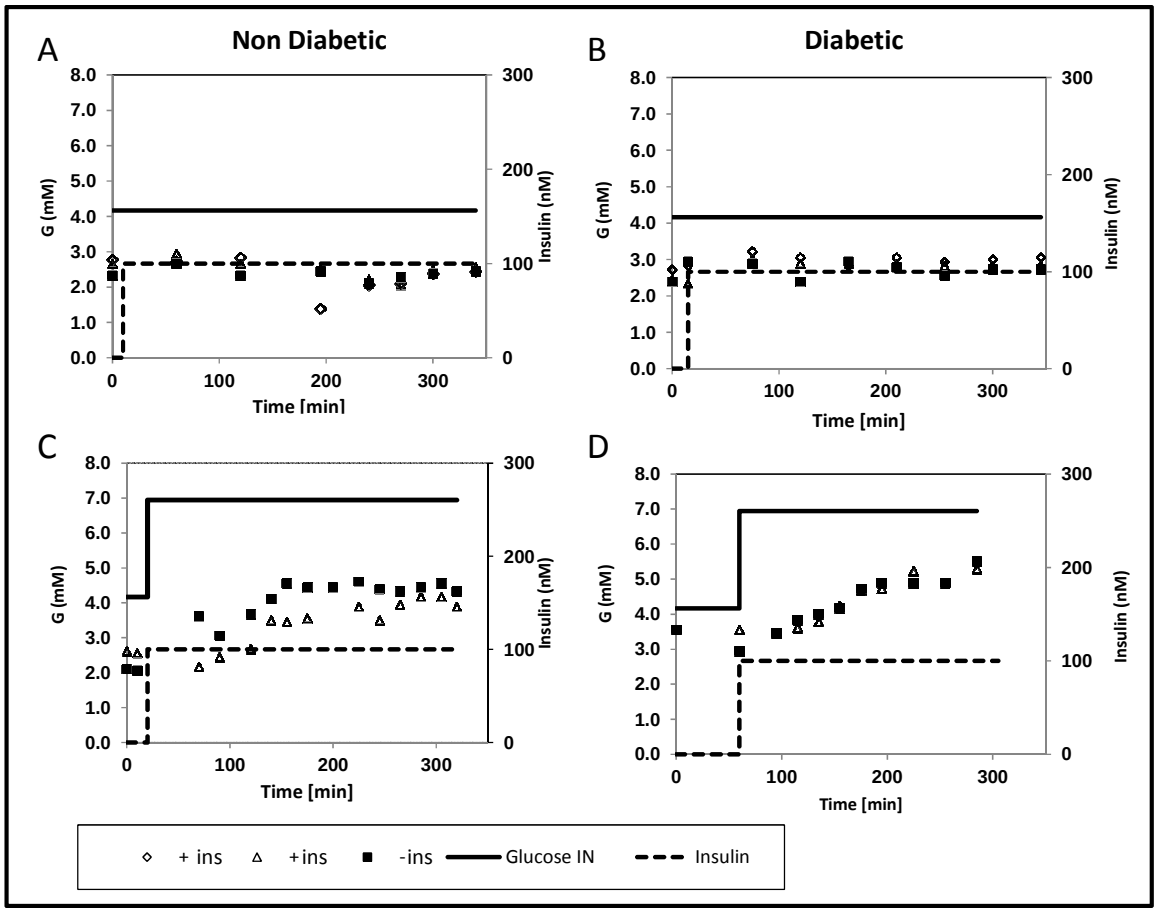

Figure 5.8. *Insulin step effects on sample from non diabetic (left) and diabetic (right) patients. (A) Effect of insulin step stimulus on glucose outlet concentration (A,B) and with the simultaneous increment of glucose inlet concentration (continue line) (C,D). Experiments were performed at 0.1 µL/min at the third day of microfluidic integration.*

5.4 Conclusions

This chapter has shown the coupling between fast FRET dynamic analysis of intracellular glucose concentration and glucose uptake measurement derived by continues medium sampling. The experimental results were obtained from myoblast cell culture of C2C12 cell line. A mathematical model assisted in the analysis of data to obtain the most relevant kinetic constants of the process. This work offers a reliable and robust method for quantitative and dynamic glucose detection at the single-cell level.

It has also reported data from adipose tissue integration. Long term viability and metabolic activity has been confirmed within microfluidic conditions. Glucose concentration has been monitored for days with the obtainment of consistent profile during times. Preliminary experiments of insulin sensitivity have been performed with our automated device. High temporal and control evolution of insulin stimulation have been achieved, with adaptable and flexible automated operations. This data are promising for further insulin responsiveness experiments from healthy and diabetic patients in order to define the insulin response dynamic with high temporal resolution.

Chapter 6

Conclusion and future perspectives

This work focused on the development of microfluidic cell culture technology for high resolution glucose uptake measurement on T2DM patient specific muscle and adipose tissue cultures.

Microfluidic cell culture integration techniques were applied for both skeletal muscle cells and *ex vivo* adipose tissue culture. Microfluidic systems obtained were able to mimic *in vivo* conditions with high control of culture microenvironment.

Cell culture chambers were specifically designed to allow long term viability and metabolic activity. For muscle cells we achieved a long term proliferation and differentiation protocol with the obtainment of differentiated miotubes. Long term culture allowed up to 12 days culture without morphological issues.

Regarding adipose tissue biopsy, the integration was achieved by using reversible microfluidic systems. Culture chambers permitted a high control of medium distribution in a reduced dead volume. We also obtained high viability and metabolic activity in up to 8 days long cultures.

Cell culture chambers have been inserted in an automated microfluidic platform, developed with a simplified microfluidic large scale integration approach. This platform was built with multilayer soft lithography techniques and it contains microvalves and micropumps for high control of medium delivery into the chambers. Medium can be flow continuously from few nanoliters up to 200 nl/min.

The microfluidic system can be easily coupled to off-chip pneumatic valves controller in order to guarantee unattended operations for days. Every chamber of the multilayer

device has an independent injection system; it guarantees drug delivery (insulin or anti-diabetic drugs) directly into the chamber with minimum dispersion.
Glucose concentration was evaluated with high temporal resolution with off-line and on-line systems. Experimental results showed strong flow rate sensitivity in extracellular glucose uptake detection with a high reproducibility. Extracellular glucose concentration was evaluated by FRET encode nanosenor. FRET detection allowed dynamic transient studies of glucose fluxes and glycolic rate within the cells and through membranes.
We coupled extracellular and intracellular detection in order to evaluate glucose uptake with a novel technique. We were able to evaluate the global kinetic constant in glucose consumption and the membrane permeability effects in muscle cells. Glucose uptake in muscle was proportional to extracellular glucose concentration.
Adipose tissues showed high flow rate sensitivity and robustness in experiments. The high variability due to the complexity of the tissues allowed to preliminary results and further investigation is still pursued.

So far we showed that the developed technology can be effectively used to investigate *in vitro* physiological and pathophysiological glucose uptake in human skeletal muscle and adipose tissues with high-temporal resolution measurements. However, there are still a number of issues that need to be carefully overcome to generate a patient specific *in vitro* model for T2DM drug screening.
As future perspective of this thesis work, it will be important to improve the robustness of cell and tissue culture integration together with the biochemical stimulations and the data acquisition systems. The envisaged technology should provide accurate and robust experimental investigations under defined glucose and insulin stimulations.
However, although the data we showed are already very promising, the experimental investigation of biological insulin resistant mechanisms in human *ex vivo* samples could be limited by the high intrinsic heterogeneity of human samples. This matter could be correlated to miscellaneous biopsy from the patients and their integration within the *in vitro* model. In the perspective to obtain a patient based assay, insulin resistant actions need to be investigated on a large number of samples from different patients. Once

these main issues are addressed, strong experiments of insulin resistant pathophysiological behaviour can be provided (Fig 1.4).

Appendix A

Microfluidic driven viral infection on cell cultures: theoretical and experimental study

Elisa CimettA.[1], Mauro Franzoso[2], Marta Trevisan[3], Elena Serena[1,2] Alessandro Zambon[1,2], Stefano Giulitti[1,2], Luisa Barzon[3], and Nicola Elvassore[1,2]

[1]Department of Chemical Engineering, University of Padova, via Marzolo 9, I-35131 Padova, Italy
[2]Venetian Institute of Molecular Medicine, Padova, Italy
[3]Department of Histology, Microbiology and Medical Biotechnologies, University of Padova, via Gabelli 63, I-35131 Padova, Italy

BIOMICROFLUIDIC
Volume 6, 024127 (2012);
doi.org/10.1063/1.4723853

A.1 Abstract

Advanced cell culture systems creating a controlled and predictable microenvironment together with computational modeling may be useful tools to optimize the efficiency of cell infections. In this paper, we will present a phenomenological study of a virus- host infection system, and the development of a multilayered microfluidic platform used to accurately tune the virus delivery from a diffusive-limited regime to a convective-dominated regime. Mathematical models predicted the convective- diffusive regimes developed within the system itself and determined the dominating mass transport phenomena. Adenoviral vectors carrying the enhanced green fluorescent protein (EGFP) transgene were used at different multiplicities of infection (MOI) to infect multiple cell types, both in standard static and in perfused conditions. Our results validate the mathematical models and demonstrate how the infection processes through perfusion via microfluidic platform led to an enhancement of adenoviral infection efficiency even at low MOIs. This was particularly evident at the longer time points, since the establishment of steady-state condition guaranteed a constant viral concentration close to cells, thus strengthening the efficiency of infection. Finally, we introduced the concept of effective MOI, a more appropriate variable for microfluidic infections that considers the number of adenoviruses in solution per cells for a certain time

A.2 Introduction

The importance of performing efficient and controlled viral infections on mammalian cell cultures has long been crucial to optimize the gene transfer procedures for basic research and gene therapy[1–4]. The common denominator is the necessity of increasing viral infection efficiency while preserving viability and biological processes of the cultured cells. The use of adenoviruses, non-integrating viruses, preserve genomic integrity and offer reduced risks for human safety. Moreover, process automatization, low volumes of reagents, and reduced costs are desirable. Standard procedures for

culture infection involve virus dilution in the media to defined concentrations, usually quantified by the multiplicities of infection (MOI), representing the number of viral particles per cell. Efficiency of transfection of some cell types may be low, thus requiring high MOIs potentially resulting in toxic side effects on the cells. In parallel, the advent and ever-increasing use of microscaled technologies and microfluidic devices for lab-on-a-chip applications has led to relevant improvements in the study of complex biological systems[5–10]. Examples of applications of microfluidic platforms have been extensively reviewed[11,12] and point at the advantages deriving from the miniaturization, integration, and automation of biochemical assays. Recent literature reflects increased interest in adopting microfluidic devices in drug discovery process[13,14], molecular detection[15], and in clinical and medical research[16]. In order to efficaciously control and exploit their potential, it is fundamental to understand the physics of mass-transport phenomena and of fluid flows at the microscale[17,18] and the fabrication processes, and properties of typically used materials[19–21] Despite the advantages and versatile applications deriving from microfluidic platforms, only few studies combining these devices and viral infections of cultured cells can be found in the literature. Examples include some applications of microfluidic bioreactors for the continuous production of retroviral vectors [22], or the dielectrophoretic capture and imaging of viral particles on microelectrodes [23]. A microscale platform was developed to detect and quantify virus growth and spread [24] and micropatterning has been used to characterize the *in vitro* propagation of viruses in cell arrays [25] Cells were infected using virus gradients [26], but the biological readout showed a low number of cells within the microchannels, and virus replication studies were performed on hepatocytes seeded within micro cell-culture chambers[27]. However, neither rational studies on the influence of perfusion nor a screening of the infection parameters were performed. Finally, most of these systems suffered some of the major limitations deriving from culturing cells within standard microfluidic channels such as lower growth rates, and the need for frequent changes of media during the preliminary phases. Here, we develop a microfluidic platform that can be easily and reversibly coupled to cell cultures, that allows performing multi-parametric experiments and exerting a precise control over the

soluble extracellular microenvironment, thus increasing the efficiency of infection. Our microfluidic device is used for the optimization of the process of cell infection through an approach that combines mathematical modeling with the experimental validation. On one hand, mathematical models evaluate the transport phenomena and the dominating regimes within a defined system, while experiments, on the other, analyze static and perfused microfluidic-driven infection processes, validating the modeled conditions and demonstrating that our microfluidic platform allows increasing the infection efficiency when compared to static conditions, even at the lowest MOIs. Infections are usually carried out in standard culture plates at defined MOIs and since the efficiency of infection is proportional to the virus adsorbed on the cellular membrane, the minimization of the total volume of viral suspension is crucial to favor the contact between viral particles and adhering cells. Viral particles are uniformly dispersed in the solvent, and their transport from the bulk of the liquid to the cell surface is purely driven by brownian-like diffusion. However, in microfluidic experimental setup, mass transport of particles is driven by both diffusion and convection phenomena. In particular, diffusion has a driving force represented by a difference in concentration (Δc), while convection results from a bulk velocity of the fluid. Consequently, convection gives an additional contribution enhancing the transport of viral particles to the cells, thus increasing the efficiency of infection. It will be crucial to define a method to compare the results of static and microfluidicperfused conditions in terms of infection efficiency. In order to have fair comparison between static and perfused conditions, a proper experimental design has been proposed to maintain the same concentration, MOI, and total volume of medium. This experimental design will allow to highlight the influence of different intrinsic properties of the hydrodynamic regimes (static and perfused) on infection efficiency. Mathematical modeling will allow to analyze the theoretical variations of the ratio of virus fluxes in static and perfused conditions and derives the optimal operative variables such as flow rates and infection times.

A.2 Materials and Methods

A.2.1 Cell culture

Mouse embryonic fibroblasts (MEFs) were purchased from Chemicon and were cultured in 79% Iscove's modified Dulbecco's medium (IMDM, Invitrogen), 20% foetal bovine serume (FBS, Invitrogen), and 1% penicillin/streptomycin (Invitrogen). Human foreskin fibroblasts (HFFs) were supplied by Dr. L. Barzon from the University of Padova and were cultured in 89% Dulbecco's modified eagles medium (DMEM, Sigma-Aldrich), 10% FBS (Invitrogen), and 1% penicillin/streptomycin (Invitrogen). Passaging of both cultures was performed with Trypsin 0.025%-EDTA (Invitrogen) and cells were either re -plated on culture flasks for further expansion or seeded on glass coverslips, both coated with 0.66% A-type pork gelatin (Sigma-Aldrich).

A.2.2. Microfluidic platform

The multilayered microfluidic platform (overall dimensions: 75 x50 mm) was designed for an easy interface with the cell system, and fabricated using lithographic techniques and molded in poly-dimethylsiloxane (PDMS)[28].The platform (Figure A.1(A)) comprised: (i) a supporting glass slide with a PDMS slab carved to accommodate the cell culture coverslip, (ii) a membrane-based vacuum system for its reversible sealing, and (iii) the microfluidic channels (width x height 0.2 x 0.1 mm) delivering fluids to the cultured cells. The circular channel creating the suction sealing the two layers, faces the PDMS slab in (i) and is thermally (and irreversibly) bonded to the upper microfluidic layer (iii). The assembled platform formed a 16x16mm culture chamber, area in which the cultured cells were exposed to the fluid streams from the microfluidic channels. The height of the chamber could be varied as needed; for all the experiments presented here we used 0.5mm high membranes. The platform was entirely optically transparent, allowing in-line observations of the cultures by easy interface with standard microscopes (Figure A.1(B)). The micro-perfusion apparatus (Figure A.1(C)) was composed of the

multilayered microfluidic platform, two syringe pumps (PHD, Harvard Apparatus, Holliston, MA), and a vacuum control system (membrane pump H35M and digital vacuum sensor, Vuototecnica, Italy). All connections between components were made using Tygon tubings (0.5mm ID, 1.5mm OD, Cole Palmer, USA).

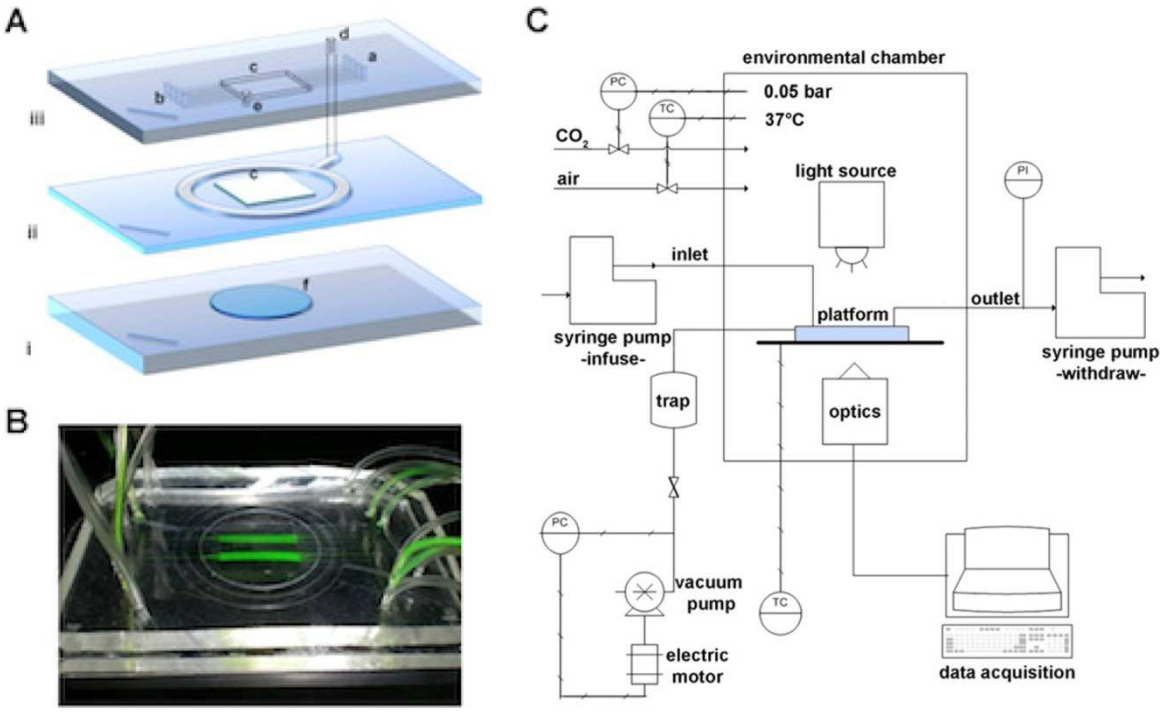

FIG. A.1. *Platform design and experimental setup. Panel (A): The platform comprised (i) a supporting glass slide with a PDMS slab carved to accommodate the cell culture coverslip (f), (ii) a membrane-based vacuum system for the reversible sealing of (i), and (iii) the microfluidic channels, 0.2 x 0.1mm (wxh), delivering fluids to the cultured cells (inlets in (a) and outlets in (b)). The assembled platform formed a 16 x 16 x 0.5mm culture chamber (c) where cells were exposed to the fluid streams. The top layer embedded connections to the vacuum system (d) and to a pressure-monitoring auxiliary service (e). Panel (B) reports an image of the assembled platform, which was entirely optically transparent, operated flowing a color tracer (fluorescein) in 2 of the 8 channels. Panel (C): The micro-perfusion apparatus was essentially composed by the multilayered microfluidic platform, two syringe pumps, and a vacuum control system. The interface with a fluorescence microscope equipped with an environmental chamber is shown.*

A brief description of the experimental procedures follows. Before assembling and coupling to the cell cultures, all components, connections, and tubings were rinsed with water and then sterilized via autoclave treatment. Tubings were then rinsed with sterile culture medium and incubated for at least 1 h prior to the platform assembly. This preconditioning of the tubings' walls reduced the potential loss of viral particles due to undesired adsorption. Sterile 3 ml syringes to be connected to the platforms outlets

were filled with 500 µl of sterile PBS, to avoid the elastic effect of air, and connected to the microtubes exiting the platform. Sterile 3 ml syringes to be connected to the platforms inlets were filled with culture medium. The open cell chamber was covered with 1 ml of culture medium and the syringe-pumps activated to stabilize the fluid flow and eliminate any residual bubble. Finally, the glass coverslip with the cultured cells was coupled to the lower layer, the entire platform assembled and the vacuum system ensuring hydraulic sealing activated. The multiple inlet and outlet channels allowed creating highly compartmentalized fluid regions within the culture chamber, thus increasing the throughput of the system potentially consenting to test several levels for a variable (i.e., virus MOIs) at a single time (Figure A.2).

A.2.3. Fluid dynamics modeling

The Navier-Stokes equations for incompressible fluids were numerically solved using the finite elements method implemented in COMSOL Multiphysics (Burlington, MA). The 2D domain of the culture chamber was geometrically modeled and a non-structured mesh was automatically generated with triangular elements. Subsequent grid refinements were required to ensure independency of the solution from the spatial discretization. No-slip boundary conditions were used for the chamber and microfluidic conduits walls, a fixed velocity for the inlet channel and finally zero pressure for the outlet. The fluid properties viscosity and density were taken from the literature[29].

To obtain concentration profiles within the chambers, the mass balance equations for a convective-diffusive regime were solved again using COMSOL Multiphysics software (Burlington, MA, USA). Fluid velocity profiles were obtained from the Navier-Stokes solutions. Defined concentrations were used as boundary conditions at the different inlets, convective flux at the outlets and insulation/symmetry elsewhere. The diffusion coefficient for the adenoviral vector (AdV) was calculated from the Stokes-Einstein equation[30]. The diffusion coefficient of a virus particle, approximated by a 90nm hydrodinamic diameter, was assumed to be 6.0×10^{-12} m^2 s^{-1}. Fundamental assumptions of our modeling approach follows. Focusing on the resistances within the media

compartment, we assumed that the virus adsorption was much faster (steadystate assumption) than the mass transport. We also assumed that all intracellular phenomena

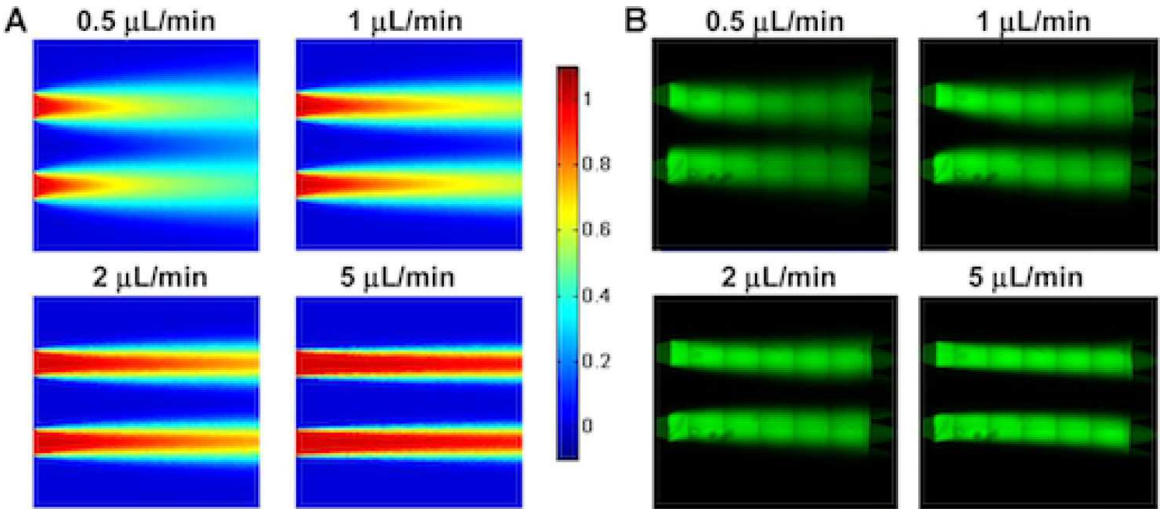

FIG. 2. *Model validation. Panel (a) reports representative results of the mathematical modeling showing concentration maps within the culture chamber. For a defined molecular species with its diffusion coefficient and fixed systems geometrical specifications, increases in the fluid flow rate change the shape of the compartment. Transport phenomena span from diffusion- to convection-dominated regimes following increases in flow rate. Panel (b) shows merged fluorescent images reconstructing the entire culture chamber, acquired during the experimental runs performed using parameters equal to the modeled ones.*

related to viral protein expression such as virus internalization, virus decay, and protein production, were not affected by the velocity profile in the media compartment. Within these assumptions, the calculated virus molar flux at cell membrane could be considered directly related to the efficiency of infection. The ratio between virus molar fluxes of dynamic and static conditions is defined as the theoretical relative efficiency, Φr. In this work, we compared Φr as a function of different parameters such as MOI, time of infection, and hydrodynamic regime. In particular, hydrodynamic regime was described through the dimensional Pe´clet number defined as Pe = v*H/D*, where v is the velocity, *H* is a characteristic length (chamber height in our case), and *D* is the diffusion coefficient. This dimensionless variable identifies flow rate conditions at defined geometrical constraints into specific diffusional or convective transport regimes. Empirical calculations were also performed (fluxes were evaluated as a function of time, diffusion coefficient, volumes) and used as a comparison to validate the mathematical modeling

(data not shown). Cell densities, MOIs, viral concentrations, and infection times were kept constant at their optimized values.

In addition, during the preliminary design and development phases, experimental validation of the modeled fluid compartmentalization in multichannel platform was performed using fluorescein dye as a tracer. Figure A.2 shows the good agreement between model prediction and experimental analysis allowing model prediction of small diffusing particles. Supplementary Figure AS1 reports additional data quantifying the fluorescence levels of the experimental images (directly correlated to concentration values)[31]. These plots can be compared to the analogous concentration curves obtained by the modeled concentration maps.

A.3 Infection protocols

A.3.1Static condition

AdVs carrying the EGFP transgene were used at different MOI to infect multiple cell lines, both in static or in perfused conditions. Briefly, AdV is based on the Ad5 genome and lacking the E1 and E3 regions was constructed by homologous recombination in *E. coli* using AdEasy vector system (Qbiogene, Carlsbad, CA). In this vector, human cytomegalovirus promoter was used to drive expression of green fluorescent protein. AdEGFP was propagated in E1- complementing HEK 293 cells, purified by cesium chloride density centrifugation, and titrated by TCID50 cpe endpoint assay according to the AdEasy production protocol. Viral vector stocks were stored at 5.0 x 10^9 pfu/ml concentration in 10% glycerol at -80 °C until use. The infection efficiency was evaluated at different time-points post-infection quantifying the EGFP expression on the live samples via image analysis. Cells were seeded on gelatin coated coverslips 24 h before infection; the volume of the viral high-titer stock solution to be used was calculated for any given cell density and experimental MOIs. The viral stock solution was thawed and aliquots prepared and diluted to the final volume with the required culture medium. Cell cultures were then incubated (37 °C, 5% CO_2, 95% humidity) with the viral solutions for defined times. Cells were rinsed with warm PBS without $CA.2^+/Mg^{2+}$ (Gibco) and

reincubated with culture medium. Post-infection incubation time varied depending on the experiment. In time-course runs, cells were re-incubated for up to 3 days. Images were acquired 48 h post infection.

A.3.2 Microfluidic perfused conditions

All of the above described procedures were followed, with the sole difference that the viral suspension was loaded in 3ml syringes and connected to the assigned inlet channels. Particular attention had to be paid at calculating the exact viral particles number which would ensure correspondence between the static and perfused infections.

A.3.3 Measurement of the infection efficiency

At the established time points, cell cultures were incubated with Hoechst 33342 (Invitrogen) nuclear dye. After this assay, images of randomly chosen positions were acquired 024127-5 Cimetta et al. Biomicrofluidics 6, 024127 (2012) (microscope Leica DMI 6000-B) on both fluorescence channels: blue for Hoechst marking all cell nuclei and green for the cytoplasmic EGFP signal expressed by the infected cells only. In order to obtain comparable set of data, the exposure, gain, and intensity values should be the same in every image. Quantification of these results was performed via image analysis on paired fluorescence pictures (blue and green channels). A custom developed script listing the command lines was implemented and run in MATLAB. Briefly, this script organized images in pairs, converted them in grayscale, enhanced contrast and finally converted them in binary format. Further processing allowed removing cell-debris, a potential source of quantification errors. The binary image of the nuclei was used to automatically count the total number of cells. After that, a pixel by pixel subtraction between the two binary images produced a new matrix creating the final image showing only the nuclei of successfully infected cells. Automated counting led to the obtainment of the number of infected cells and of the global efficiency of infection (number of infected cells over total number of cells).

A.4 Results

A.4.1Model validation

The capability of the platform to generate well-defined concentration compartments was first modeled and then validated using fluorescein as a dye tracer. The results of the mathematical modeling are shown in Figure A.2(a), where the sole culture chamber is represented for ease of visualization. The shape of the compartment can be precisely defined by simply tuning the fluid flow rate. At the lowest flow rates, transport by diffusion and convection competes determining a feather-like shaped concentration pattern. For increasing flow rates, convection becomes the dominant transport phenomena and leads to the formation of sharp compartments. Figure A.2(b) reports the results of the experimental validation, performed using the same coefficients and geometrical specifications applied for the mathematical modeling. The extremely close resemblance between the experimental concentration patterns and the modeled ones validated the model predictions and the systems performance. A quantification of this observation is available in supplementary Fig. AS1[31].

A. 4.2Modeling of the cell infection process

Figure A3 summarizes representative results of the computational modeling of the infection process. Again, Φr is the theoretical relative efficiency of microfluidic perfused versus static infection. The curves in panel A3(a) are parametric in *Pe* and reported as a function of the square root of time. The horizontal line at Φr =1 highlights the threshold at which molar fluxes (and thus infection efficiencies) of perfused and static processes are equal, thus allowing to identify the parameters characterizing the variables-space where perfused-microfluidic (Φr > 1) or standard static (Φr < 1) infection conditions are favored. For example, given the systems geometrical constraints and the duration of the infection process, increases in fluid flow rate (which directly translate into increases in *Pe* number), will favor perfused-microfluidic processes, which will result in higher

infection efficiencies. *Vice versa*, at the lowest flow rates where convection gives no significant contribution to the overall transport of viral particles from the bulk of the liquid to the cell surface, standard static infections prove to be more efficient. Panel A3(b) plots the values of Φr as a function of *Pe* for a fixed time (t=90 min) of infection. Again, it is evident how for increasing flow rates, perfused-microfluidic infections lead to higher yields with a trend plateauing for Pe higher than 200 (corresponding to a 1 µl/min flow rate and 8 µm/s linear velocity). Finally, panel A3(c) plots the times at which Φr = 1 for *Pe* ≥100, showing again how for increasing *Pe* perfused-microfluidic infections could lead to higher yields than standard static processes exposing the cells to potentially harmful viruses for shorter times.

A.4.3Cell infection

Several experiments have been performed in order to optimize the procedures and parameters characterizing the infection process, both in static and microfluidic culture. Cell line, cell density, cell passage, virus MOI, duration of the exposure to the viral solution (incubation time), and *Pe* number, were among the screened variables. From these preliminary experiments, we established optimal values and ranges: cell seeding density was kept constant at 100 cells/mm^2, MOI was varied from 10 to 100, *Pe* levels for microfluidic cultures were 10 and 100, and infection times spanned from 90min to 12 h. In reporting some of the most significant findings on HFF cells, we highlight how: (a) increases in the incubation time led to increases in the infection efficiency (Figure A4(a)) (further

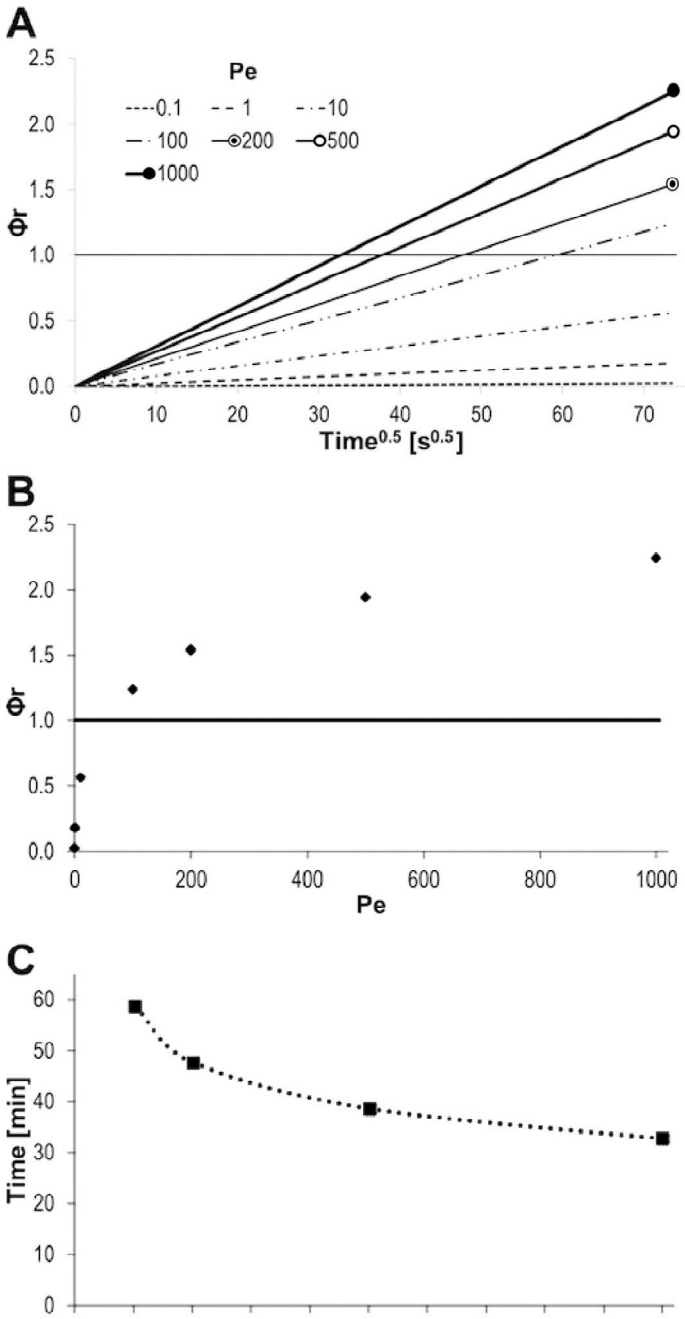

FIG. A3. *Computational modeling of the infection process. Φr is the theoretical relative efficiency of microfluidic perfused versus static infection. Panel (a) reports Φr curves parametric in Pe and as a function of the square root of time. The horizontal line at Φr = 1 (equality of perfused and static molar fluxes) separates the variables space where perfusedmicrofluidic (Φr > 1) or standard static (Φr < 1) infection conditions are favored. Panel (b) plots Φr as a function of Pe at a defined time (t=90 min) of infection. Finally, panel (c) plots the times at which Φr = 1 for Pe ≥100.*

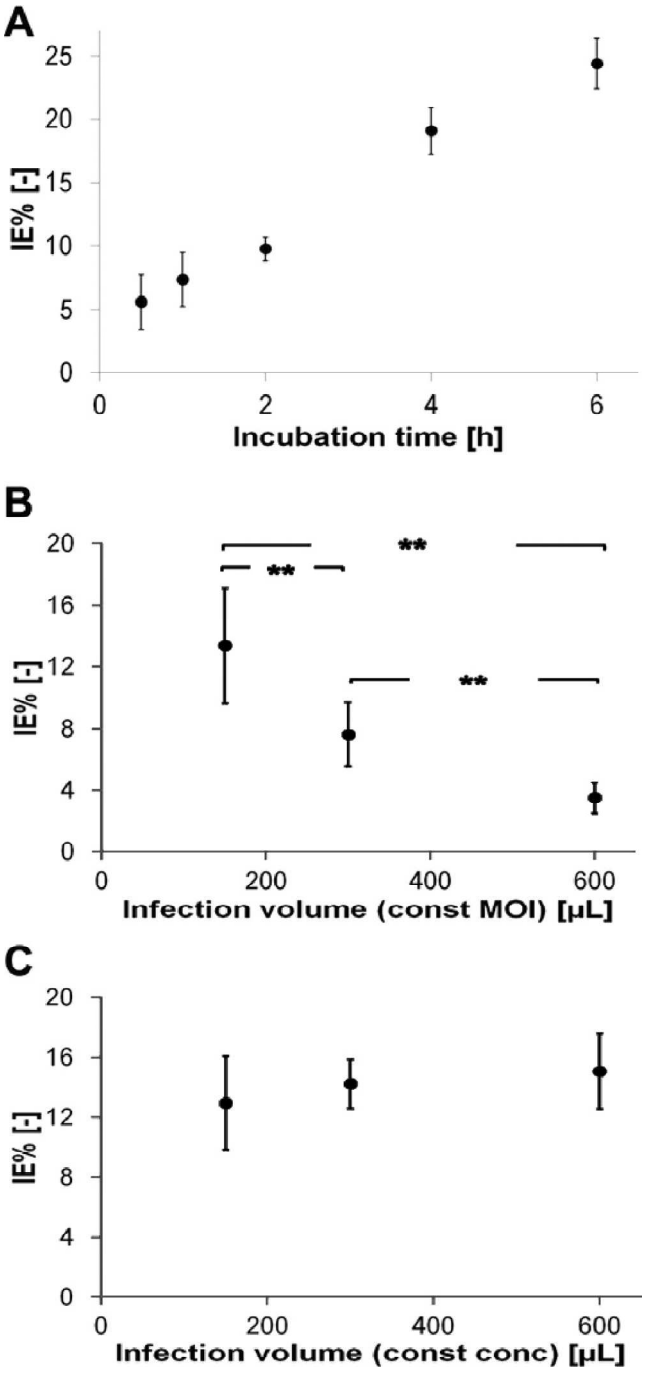

FIG. A4. *Static infections on HFF cultures. HFF were plated at a 100 cells/mm^2 density, and all infections started 24 h after seeding. MOIs were: 50 in panel (a), 100 in panel (b), and 100, 200, 400, respectively, for the data points in panel (c). In panel (a), the plotted data points demonstrate how longer incubation times of cell cultures with the viral suspension led to increases in the infection efficiency. In panel (b), increases in the viral suspension volume (at a given MOI) led to reduced infection efficiencies; in parallel, panel (c) demonstrates that no significant changes in infection efficiencies were measured for increases in the viral suspension volume at constant viral particles concentration.*

discussion will be presented in the following sections). (b) An inverse-relationship correlation was established between viral suspension volume (at a given MOI) and infection efficiency: increases in the first led to decreases in the latter (Figure A4(b)); however, no changes in infection efficiencies were measured for increases in the viral suspension volume at constant viral particles concentration (Figure A4(c)). (c) For a given infection time, observation of the cell cultures over 3 days demonstrated how the efficiency increased over the first two days and reached a plateau by day 3 (data not shown). Additional material is presented in supplementary FigureA S2[31].Fundamental relations were established between variables, to allow comparisons between the different culture and infection conditions. In particular, to ensure constant virus concentration in static and microfluidic infections, MOIs must be translated into concentrations as follows:

$$c_v = \frac{MOI * NCells_{Stat}}{Vol_{Stat}} = \frac{MOI * MCells_{\mu Fl}}{Vol_{\mu Fl}} \quad \text{(A.1)}$$

and

$$Vol_{\mu Fl} = Q * t, \quad \text{(A.2)}$$

where c_v is the virus concentration in culture medium, MOI is the number of viral particles per cell, *NCells* is the total number of cells exposed to the viruses, and *Vol* is the total volume of fluid used in the experiment. Q is the fluid flow rate and t is the duration of the infection process. Subscripts *Stat* and *Fl* refer to static and perfused-microfluidic infections, respectively. It is important to underline how the possibility of compartmentalizing fluids within the microfluidic platform would divide the culture area in 4 sections, each containing 1/4 of the total number of cells and exposing them to different MOIs; this thus need to be taken into account in evaluating virus concentrations and other variables. Rearranging the above equations, we can calculate the volume of the viral suspension to be used in standard conditions as a function of the fluid flow rate, corresponding to the chosen *Pe* value, of the microfluidic process:

$$Vol_{Stat} = \frac{NCell_{Stat}}{NCell_{\mu Fl}} * Q * t \quad \text{(A3)}$$

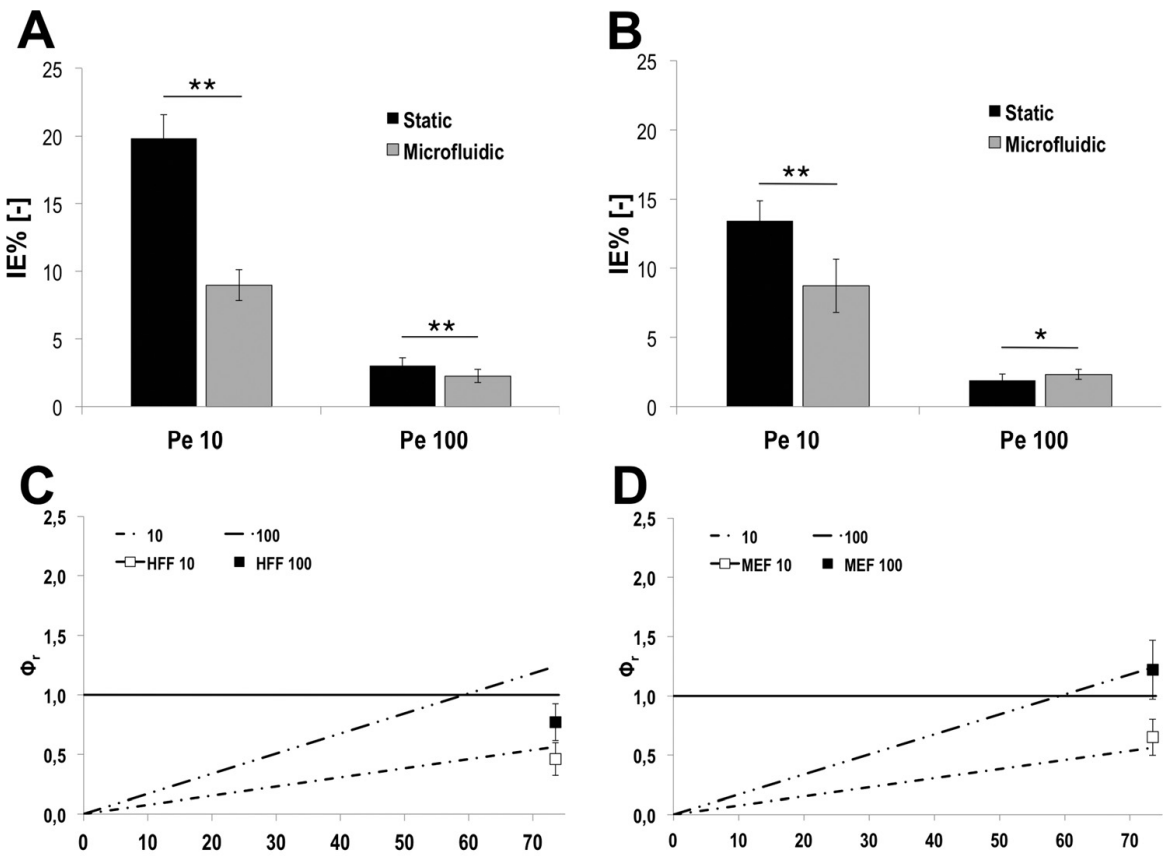

FIG. A.5. *Comparison between static and microfluidic infections at different Pe´clet numbers for two cell types. Cell density was kept constant at 100 cells/mm^2; MOI was 100, and infection time 90 min. Experiments were performed at Pe = 10 and Pe = 100. Panels (a) and (c) refer to HFF cultures, (b) and (d) to MEF. Data were obtained via image analysis of cell cultures 48 h post infection. Panels (c) and (d) graph the modeled profiles for Φr (the theoretical relative efficiency of microfluidic perfused versus static infection) and allow comparison with representative experimental results. Empty markers are for Pe=10 and filled markers for Pe=100. **p < 0:001. *p < 0:01.*

We planned the experimental runs following these variables constraints and obtained the results shown in Figure A.5. Cell seeding density was constant at 100 cells/mm^2. Experiments were performed at *Pe*=10 and *Pe*=100. Panels A.5(a) and A.5(c) refer to HFF cultures, A.5(b) and A.5(d) to MEF. Image acquisition was performed 48 h post infections on cells treated at MOI 100 for 90 min. At lower Peclet, static infections led to significantly higher infection efficiencies when compared to the corresponding microfluidic perfused ones for both cell lines, while differences were strongly reduced at the highest Pe value. This is an expected trend described by our model, as can be seen in the bottom graphs of Figure A.5 (panels A.5(c) and A.5(d)), where the relative efficiency

of microfluidic perfused versus static infection is reported as a function of the square root of time. Here, Φr resulted in significant higher values at *Pe*=100 when compared to the ones at *Pe*=10 for both cell lines. In particular, the highest Φr values were detected on MEFs, a result that led us to the use of MEFs for the following experiments. The relative infection efficiencies are in very good agreement with the theoretical ones. Higher *Pe* always led to higher infection efficiencies (measured by the theoretical relative efficiency factor) and, under the same conditions, MEFs showed higher infection efficiencies if compared to HFF. Regarding HFF, the value at higher *Pe* is overestimated by the model. It is worth to remind that the model describes the ideal case in which the delivery of viral particle is mainly limited by the transport phenomena within the liquid domain. If our hypothesis fails, an additional step normally faster than transport phenomena, such as virus adsorption or internalization, could negatively affect the overall infection efficiency. To further explore this issue we performed additional experiments, whose results are presented in Figure A.6. First of all, we analyzed the effect of increasing infection times at low MOIs. Panel A.6(a) shows infection efficiencies measured following exposure of cell cultures (MEFs) to adenoviruses at MOI 10 for times ranging from 90 min to 12 h, both in static and microfluidic perfused culture. Additional material is available in Figure S3[31]. The results highlighted how the use of microfluidics allowed obtaining higher efficiencies for longer incubation times. This is due to the fact that, while in static infections the concentration of viral particles surrounding a cell decreased with time, resulting in plateauing efficiencies, the steady state that was established perfusing the cultures ensured the maintenance of a constant concentration of viruses around cells and further increases in the infection efficiency. Finally, we introduced the new concept of “effective MOI”: as the standard MOI is the total number of viral particles per cell which varies with time as viruses are transported to cells, the effective MOI was defined as the number of viral particles surrounding a cell at a certain time. This value is considered constant in perfused conditions, according to the establishment of the

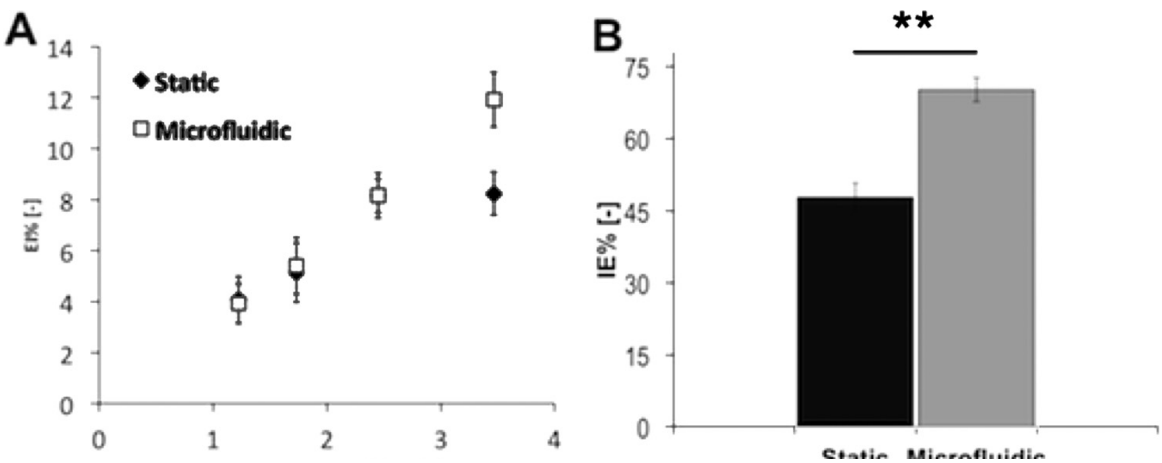

FIG. A.6. *Comparison between static and microfluidic infections for different infection times and at effective MOI. The results presented in panel (a) were obtained by exposing the cells to the viral suspension at MOI 10 for times ranging from 90 min to 12 h, both in static and microfluidic perfused culture. The use of microfluidics allowed obtaining higher efficiencies for longer incubation times. In panel (b), infections were performed at an effective MOI of 100 for 12 h and led to significantly higher efficiencies in microfluidic infections compared with those reached in static conditions. **p < 0:001.*

steady state. Now, the two MOIs are related through the fluid volumes used for the experiment (in turn determined by the chosen *Pe* number):

$$MOI_{total}=MOI_{effective}\frac{V_i}{V_{ch}} \quad \text{(A4)}$$

where V_i is the viral suspension volume used for cell infection during a single experiment and V_{ch} is the volume of the cell chamber. The total and effective MOI are equal in static conditions,where V_i corresponds to V_{ch}, and different in experiments with perfusion, where $V_i > V_{ch}$. Experiments performed using the effective MOI produced the results shown in Figure A.6(b). Exposing cells to the viral suspension at an effective MOI of 100 for 12 h led to favored efficiencies for the microfluidic perfused processes, resulting in significantly higher infection efficiencies than those reached in static conditions.

A.5 Discussion and conclusions

In this study, we present a rational approach to the issue of viral infection of cell cultures, comparing theoretical modeling and experimental evidence. An accurate analysis of the phenomenological behavior of an infection process on a cell culture,

explored the effects of transport (diffusional and convective) in static and microfluidic-perfused conditions. Rationalization of the infection steps and limiting phenomena acting on the system highlighted the pros and cons of both conditions. Static conditions, for example, represent the standard procedure and are thus routinely performed with well established techniques; however, they tend to utilize high MOIs in order to ensure high infection efficiencies, are diffusion-dependent and regulated by unpredictable and continuously varying kinetics (since virus concentration in the cells surroundings decreases uncontrollably due to virus degradation, consumption, and internalization by the cells). Perfused infections, on the contrary, can be precisely controlled and the persistence of a steady state renders the system more stable and predictable. At the steady state, the virus concentration at the cell membrane is constant and maintained at the established optimal level, thus allowing the use of lower MOIs to obtain higher infection efficiencies while reducing the risk of exposing cultures to a hostile environment. In addition, we developed a relationship between molar fluxes of viral particles and infection efficiencies, with molar fluxes determined by the systems parameters and variables (geometry, flow rates, etc.). Such variables have been translated into correlation terms that take into account the necessity of having comparable entities for static and perfused conditions. Dimensionless forms, where applicable, were favored. This approach led us to a more accurate experimental plan, where only one variable at a time was varied in parallel static and perfused infections; the obtained results were thus directly comparable. Our static controls were performed using standard multiwell plates, fitting the glass coverslips used as culture substrates. We want to point out how this choice, over that of statically operating the microfluidic platforms, allowed us to use the same total volumes reached in the perfused experiments; this is of paramount importance in sight of obtaining infection efficiency data that could be compared between the two conditions. Flow rate choices in the microfluidic experiments were translated in corresponding infection volumes in static controls ($V = Q * t$), and a variable such as MOI could then be independently changed. All together, these results show how the microfluidic technology can be used for rational

designing an infection process with high intrinsic efficiency without the risk of viral associated-cytotoxic derived by high MOI static treatment.

ACKNOWLEDGMENTS

We thank Ca.Ri.Pa.Ro., F.S.E., and Ministero della Salute for funding.

A.6 Literature cited

[1] B. Kaspar, J. Llado´, N. Sherkat, J. Rothstein, and F. Gage, Science 301, 839 (2003).

[2] J. Luo, M. Kaplitt, H. Fitzsimons, D. Zuzga, Y. Liu, M. Oshinsky, and M. During, Science 298, 425 (2002).

[3] F. C. Marini, Q. Yu, T. Wickham, I. Kovesdi, and M. Andreeff, Cancer Gene Ther. 7, 816 (2000).

[4] S. Vorburger and K. Hunt, Oncologist 7, 46 (2002).

[5] H. Andersson and A. van den Berg, Lab Chip 4, 98 (2004).

[6] E. Cimetta, C. Cannizzaro, R. James, T. Biechele, R. T. Moon, N. Elvassore, and G. Vunjak-Novakovic, Lab Chip 10,3277 (2010).

[7] E. Cimetta, E. Figallo, C. Cannizzaro, N. Elvassore, and G. Vunjak-Novakovic, Methods 47, 81 (2009).

[8] N. Jeon, S. Dertinger, D. Chiu, I. Choi, A. Stroock, and G. Whitesides, Langmuir 16, 8311 (2000).

[9] T. Keenan and A. Folch, Lab Chip 8, 34 (2007).

[10] G. M. Whitesides, Nature (London) 442, 368 (2006).

[11]D. Breslauer, P. Lee, and L. Lee, Mol. BioSyst. 2, 97 (2006).

[12] S. Haeberle and R. Zengerle, Lab Chip 7, 1094 (2007).

[13] P. S. Dittrich and A. Manz, Nat. Rev. Drug Discovery 5, 210 (2006).

14Y. Wen and S.-T. Yang, Expert Opin. Drug Discovery 3, 1237 (2008).

15B. D. Piorek, S. J. Lee, J. G. Santiago, M. Moskovits, S. Banerjee, and C. D. Meinhart, Proc. Natl. Acad. Sci. U.S.A 104, 18898 (2007).

[16] M. Toner and D. Irimia, Annu. Rev. Biomed. Eng. 7, 77 (2005).

[17] D. J. Beebe, G. A. Mensing, and G. M. Walker, Annu. Rev. Biomed. Eng. 4, 261 (2002).

[18] T. Squires and S. Quake, Rev. Mod. Phys. 77, 977 (2005).

[19] J. C. McDonald, D. C. Duffy, J. R. Anderson, D. T. Chiu, H. Wu, O. J. Schueller, and G. M. Whitesides, Electrophoresis 21, 27 (2000).

[20] S. K. Sia and G. M. Whitesides, Electrophoresis 24, 3563 (2003).

[21] G. M. Whitesides, E. Ostuni, S. Takayama, X. Jiang, and D. E. Ingber, Annu. Rev. Biomed. Eng. 3, 335 (2001).

[22] H. N. Vu, Y. Li, M. Casali, D. Irimia, Z. Megeed, and M. L. Yarmush, Lab Chip 8, 75 (2008).

[23] D. Akin, H. Li, and R. Bashir, Nano Lett. 4, 257 (2004).

[24] Y. Zhu, J. W. Warrick, K. Haubert, D. J. Beebe, and J. Yin, Biomed. Microdevices 11, 565 (2009).

[25] E. E. Endler, K. A. Duca, P. F. Nealey, G. M. Whitesides, and J. Yin, Biotechnol. Bioeng. 81, 719 (2003).

[26] G. Walker, M. Ozers, and D. Beebe, Sens. Actuators B 98, 347 (2004).

[27] T. R. Sodunke, M. J. Bouchard, and H. M. Noh, Biomed. Microdevices 10, 393 (2008).

[28] Y. Xia and G. Whitesides, Annu. Rev. Mater. Sci. 28, 153 (1998).

[29] E. Cimetta, M. Flaibani, M. Mella, E. Serena, L. Boldrin, P. De Coppi, and N. Elvassore, Int. J. Artif. Organs 30, 415 (2007).

[30] R. Bird, W. Stewart, and E. Lightfoot, Transport Phenomena (Wiley, 1960).

[31] See supplementary material at http://dx.doi.org/10.1063/1.4723853 for images of infected cells

Appendix B

Reversible alteration of calcium dynamics in cardiomyocytes during acute hypoxia transient in microfluidic platform

Sebastian Martewicz [1,2], Federica Michielin[1,2] , Elena Serena[1,2], Alessandro Zambon[1,2], Marco Mongillo [2], and Nicola Elvassore [1,]

[1]Dipartimento di Principi e Impianti di Ingegneria Chimica, University of Padova, Padova, Italy
[2]VIMM—Venetian Institute of Molecular Medicine, Via Orus 2, 35129 Padova, Italy.

INTEGRATIVE BIOLOGY
Volume 4, pages 153-64 (2012);
doi: 10.1039/c1ib00087j.

B.1 Abstract

Heart diseases is the leading cause of mortality in western countries. Apart from congenital and anatomical alterations, ischemia is the most common agent causing myocardial damage. During ischemia, a sudden decrease in oxygen concentration alters cardiomyocyte function and compromises cell survival. The calcium handling machinery, which regulates the main functional features of a cardiomyocyte, is heavily compromised during acute hypoxic events. Alterations in calcium dynamics have been linked to both short- and long-term consequences of ischemia, ranging from arrhythmias to heart failure.

In this perspective, we aimed at investigating the calcium dynamics in functional cardiomyocytes during the early phase of a hypoxic event. For this purpose, we developed a microfluidic system specifically designed for controlling fast oxygen-concentration dynamics through a gas micro-exchanger allowing in line analysis of intracellular calcium concentration by confocal microscopy. Experimental results show that exposure of Fluo-4 loaded neonatal rat cardiomyocytes to hypoxic conditions induced changes in intracellular Ca^{2+} transients. Such behavior was reversible and was detected for hypoxic levels below 5% of oxygen partial pressure. The observed changes in Ca^{2+} dynamics were mimicked using specific L-type Ca^{2+} channel antagonists, suggesting that alterations in calcium channel function occur at low oxygen levels. Reversible alteration in ion channel function, that takes place in response to changes in cellular oxygen, might represent an adaptive mechanism of cardiopreservation during ischemia.

B.2 Insight, innovation, integration

Recreating *in vitro* a low oxygen environment is fundamental for a better understanding of the cellular consequences of hypoxia and to screen novel therapeutic strategies targeting common ischemic diseases, *e.g.* coronary heart disease. Here, we present a

microfluidic platform specifically developed to expose cultured cardiomyocytes to acute hypoxic stimuli, allowing robust and high quality live confocal imaging. Thanks to this novel technology, we were able to observe rapid and reversible changes in the electrically induced cardiomyocyte calcium transients following the acute decrease of oxygen partial pressure in the cell environment. Similar changes in calcium were observed upon pharmacological inhibition of L-type Ca^{2+} channels, suggesting a possible target of hypoxia in cardiac cells.

B.3 Introduction

Cardiovascular diseases are the leading cause of mortality and morbidity in the Western countries. Heart diseases due to coronary dysfunction alone was responsible for nearly 22% of all deaths in Europe in 2008 [1]. Cardiac ischemia occurs when blood supply to part of the organ is suddenly reduced or completely interrupted for a discrete amount of time. Ischemic tissues undergo rapid changes in cellular environment such as reduced nutrient supply, accumulation of metabolic wastes, drop in oxygen concentration and increase in carbon dioxide concentration. In a highly energy demanding tissue, like themyocardium, hypoxic conditions that are generated when oxygen demand exceeds oxygen supply are reached in very short time [2].

The time scale of the changes in oxygen concentration has a great importance for cell physiology, viability and adaptation to stress conditions. In particular, the cellular response to hypoxia depends on its onset kinetics and duration: (i) rapid acute hypoxia (seconds or minutes) leads to alterations of the preexisting protein pool through post-translational modifications and protein interactions; (ii) sustained chronic hypoxia (hours or days) results in whole proteome changes through activation of different gene expression patterns [3].

In order to recreate *in vitro* ischemia pathological models, accurate gas concentration dynamics is one of the most difficult parameters to control; for instance, in hypoxia studies, gas leakage through liquid-air interface or gas permeable materials is extremely difficult to detect and may lead to low experimental reproducibility. Studies on chronic

hypoxia (lasting hours or days) can be easily performed by culturing the cells in airtight chambers in which the oxygen concentration control is exerted by tuning the gaseous partial pressure inside the chamber. In this steady state experiments, the cell response at desired time points is commonly independent from the oxygen dynamics at the initial experiment set up [4]. On the other hand, observing cellular responses to fast hypoxic transients, simulating the early phase of acute ischemic events, is essential in understanding how cell biology and physiology are affected by sudden changes in oxygen concentrations. However, investigating the immediate effects of a rapid drop in oxygen partial pressure requires tight control on the cellular environment, a condition hard to achieve with standard culture methods. As such, current technological limitations have hindered cellular experiments on hypoxia.

In this perspective, we aimed to develop a novel tool for *in vitro* investigation of the acute cellular response of cultured cardiomyocytes to fast changes in the environmental conditions, including components of the culture medium, drugs and oxygen concentration. In this work, we used such an approach to investigate the effect of acute hypoxic events on Ca^{2+} homeostasis, through in line confocal image acquisition.

Cardiomyocyte function relies upon proper ion handling during contraction cycles, involving both ion channels regulating membrane potential and intracellular calcium release. Hypoxia has been proven to modify the activity of most of the molecular components concerned in these features, resulting in unbalanced ion fluxes and generation of arrhythmias[5] . Rat ventricular cardiomyocytes under low p_{O2} conditions displayed an increase of the late Na^+ current ($I_{Na\text{-}L}$) while the fast Na^+ (I_{Na}) current appeared to be reduced [6,7]. Effects on potassium channels were also described in guinea-pig cardiomyocytes as a decrease in the slow component of the delayed rectifier K^+ channel (I_{Ks}) current, without affecting of the rapid component (I_{Kr}) [8]. Ca^{2+} handling, essential in both action potential generation and contraction triggering, seems to be influenced by hypoxia as well. In particular, the activity of the L-type Ca^{2+} channel is altered with a decrease of basal current ($I_{Ca\text{-}L}$) and unchanged current–voltage (I-V) relationship [9,10]. Sensitivity of the channel to β-adrenergic stimulation appears to be increased resulting in a pro-arrhythmic substrate during ischemic events [11]. The

precise mechanism through which hypoxia modifies the function of the L-type Ca^{2+} channel is still unclear. Both direct modifications in the C-terminal region of the channel[12,13] and indirect modulation of its function through mechanisms involving mitochondrial ROS formation [14] or protein kinases A and C [15] have been proposed

All these studies clearly show that rapid changes in oxygen concentration affect ion handling in cardiac myocytes, but so far no hypoxia-induced effects on calcium handling during excitation-contraction coupling were reported, although many components of this machinery appear to be altered under ischemia-mimetic conditions [16,17].

In this work, we aimed at analyzing calcium dynamics in Fluo-4-loaded functional rat cardiomyocytes in response to brief and sudden transients of hypoxia. In particular, we focused on the early response to hypoxia induction and re-oxygenation, by monitoring electrically stimulated Ca^{2+} changes.

For this reason, we designed and developed a device enabling confocal microscopy analysis while finely tuning the oxygen concentration in the culture medium and maintaining proximal cell environment isolated from atmospheric conditions. In addition, the device allows exposure of the cells to fast transient changes in the environment without perturbing the data acquisition process. Particular care has been taken to avoid, manipulation of the liquid phase that could generate pressure waves in the cell culture chamber and cause loss of focal plane leading to artifactual changes in fluorescence signals.

As mentioned above, conventional humidified chambers or incubators with a controlled p_{O2} in the gas phase show equilibration time of the order of hours[19], due to the great volumes involved and the low oxygen diffusion coefficient in the culture medium (2.1×10^{-5} cm^2 s^{-1}) [18]. Such characteristic time can only be slightly decreased using particular expedients like gas-permeable membrane-based dishes [20] or by forcing gas exchange through bubbling of gas mixtures in chemostats or flasks.

In this perspective, technology developed at microscale level can be an effective practical solution for obtaining a system able to accurately control oxygen partial pressure for two main reasons:

i) at microscale liquid flow regime is typically laminar, allowing to accurately

control the delivery of nutrients, soluble species and gases in the culture medium [21-23];

ii) the time scale of diffusive mass transport phenomena is related to the characteristic length of the system and scaling down the system highly accelerates the gas exchange dynamics.

For this reason, many microfluidic bioreactors were developed to provide solely moderate to long-term control of the cellular environment, including dissolved gas concentrations [24-27]. Some miniaturized devices include gas-microexchangers that generate spatial gradients of oxygen partial pressure by on-chip gas mixing and allow to study the influence of the oxygen concentration on the cell growth [28-30].

However, only few microfluidic devices for rapid generation of hypoxic conditions in cell culture were designed, due to the difficulty in obtaining fast oxygen concentration transients from a saturated level to a very low partial pressure, without perturbing the cell culture environment and the data acquisition system. For instance, Oppergard *et al.* have developed a microfabricated insert that nests into a standard multiwell plate and serves as a passive microfluidic gas network with a permeable membrane aimed to modulate oxygen delivery to adherent cell with an equilibration time on the order of few minutes [31], however no in-line analysis can be made with such device. Other groups have developed an *ad hoc* system to rapidly set the oxygen partial pressure in the cell culture and study particular cellular responses under hypoxic conditions [32,33].

The complexity of the devices previously described induces to find out a structurally simpler microfluidic platform able to perform and control fast oxygen concentration dynamics and that could be coupled with any other miniaturized bioreactor or culture chamber. Unlike other works, we are aimed to engineer a new oxygen micro-exchanger to carry out on line analysis on the cell culture, for example using confocal microscopy, during an oxygen shift in the culture medium, and acquire particular cellular responses without any perturbation of the detection system.

B.4 Experimental methods

B.4.1 Experimental set up

Our investigation on calcium transient requires a fine tuning of oxygen partial pressure inside a microfluidic cell culture chamber by a multilayer microfluidic gas-exchanger. The device has to ensure a fast and accurate oxygen concentration control inside the culture chamber in order to provide a precise and repeatable hypoxic stimulus to the cell culture. Hypoxic stimuli on a cardiomyocyte population are generated by setting only the oxygen partial pressure in the gas phase without perturbing flowing medium. Cellular calcium dynamics were analyzed directly on line by a fluorescence confocal microscope. An external system for control and data acquisition allowed to precisely set gas phase partial pressures and flow rates, while an uniform medium flow rate was maintained during all the experiments (Fig.B.1).

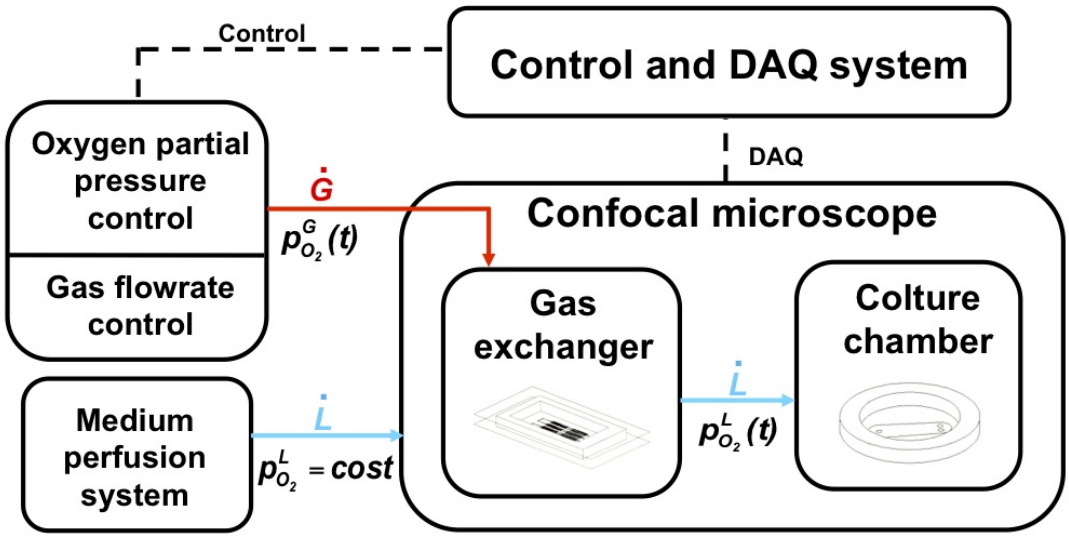

Figure B.1. *Schematic view of experimental set up. Fast and accurate control of oxygen partial pressure inside a microfluidic cell culture chamber is performed by a multilayer microfluidic gas-exchanger. Hypoxic stimuli on a cardiomyocytes population are generated by setting gas oxygen partial pressure and cells' calcium dynamics are analyzed in line by a confocal microscopy. An external system for control and data acquisition ensures fine tuning of gas phase partial pressure and flow rate, whereas a stable medium flow rate is maintained during experiments.*

B.4.2 Microfluidic gas exchanger fabrication

Fig. B.2A shows a schematic view of the multilayer microfluidic gas exchanger. The oxygen exchange process between the gas and liquid compartments takes place through a thin, non-porous, permeable membrane. A microfluidic gas exchanger consists of a three-layer structure: a fluidic layer containing cell culture medium, a gas chamber for gas flow with defined oxygen partial pressure and an oxygen permeable membrane. The fluidic layer is formed by a network of microfluidic channels in an oxygen non-permeable glass substrate to achieve complete gas sealing. The micrometric thickness of the gas permeable membrane ensures low oxygen diffusion resistance. The gas domain is a millilitre rectangular chamber that allows high gas flow rate and, consequently, almost uniform oxygen partial pressure within the gas chamber. In the fluidic layer, the flow channels network is characterized by a series of gas exchanger unit and each unit is formed by 8 parallel microchannels 100 μm wide (Fig. B.2B). This modular design allows us to add series of units, until obtaining the total length required for a given exchange efficiency. The imprinting of microchannels in the glass slide was achieved by wet-etching technique. A borosilicate glass slide 50 × 75 mm was cleaned using MICRO90 Cleaning Solution (Sigma-Aldrich, USA), placed in an oven for 1 h at 403 K, cooled at 303 K and silanized with hexamethyldisilazane, HDMS, (Sigma-Aldrich, USA) for 3 minutes at 403 K. The glass slide was spin-coated with 5 g of SPR220-7.0 positive photoresist (Rohm&Haas, Dow, USA), to obtain an homogeneous film with a thickness of 15 μm and subsequently photolithografically patterned using standard procedures [34]. The glass slide was immersed in an aqueous 40% fluoridric acid solution (HF, Sigma-Aldrich, USA) at 298 K and only exposed areas were etched. After patterning, the slide was washed with distilled water, deep into an aqueous 98% sulfuric acid solution (H_2SO_4, Sigma-Aldrich, USA) to remove etching-reaction byproducts and rinsed with distilled water. The protective photoresist layer was removed with 1-methyl-2-pyrrolidone (Sigma-Aldrich, USA) and the patterned glass slide was cleaned in piranha solution (H_2SO_4:H_2O_2, 3:1). Fig. B.2C shows an image of the etched microchannels on glass under an inverted microscope (Leica, Germany).

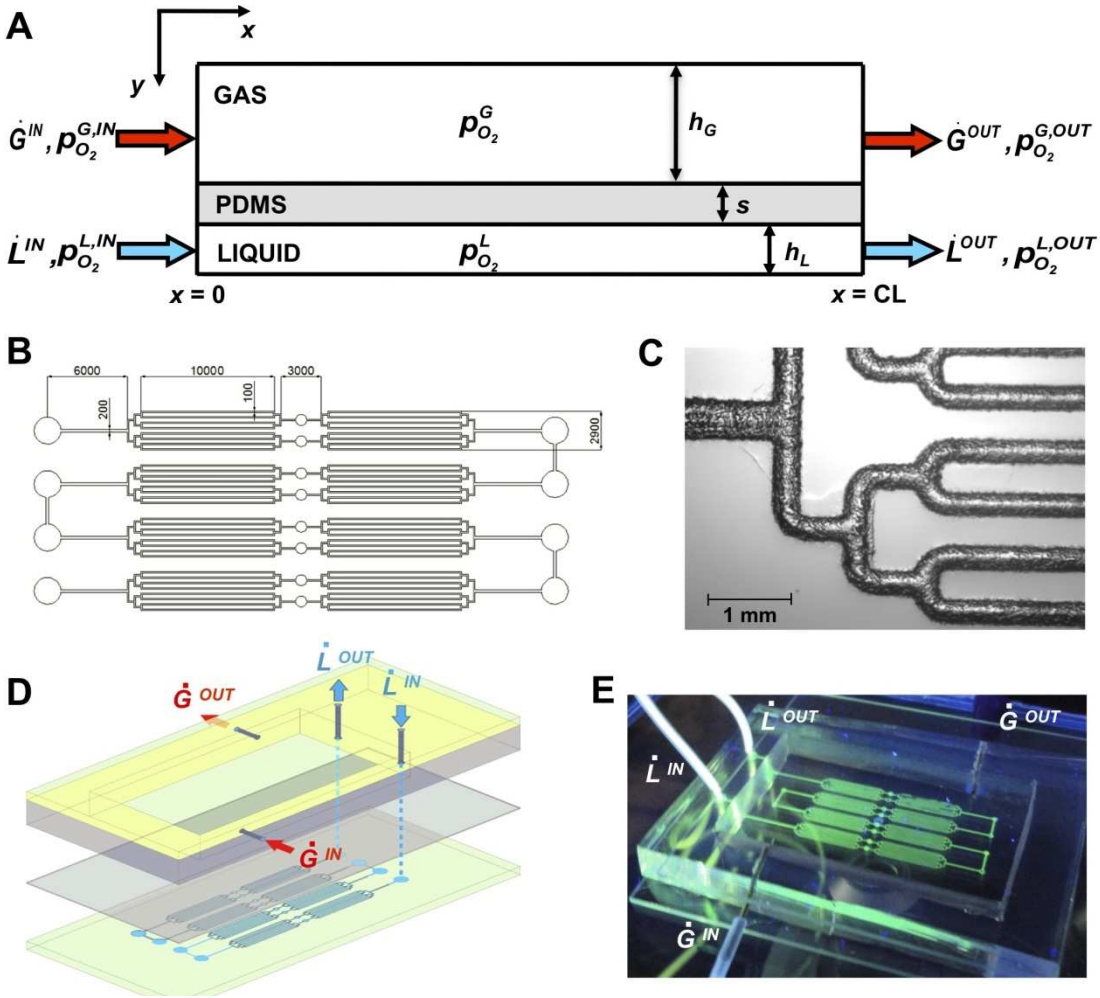

Figure B.2. *Microfluidic gas exchanger. (A) Schematic representation of the three-layered microfluidic system; inlet/outlet flow rates and oxygen partial pressure are shown for both gas, G, and liquid, L, phase. (B) Top view of the fluidic layer channel network (all dimensional values are in µm). (C) Image of glass-etched microfluidic channels network obtained by wet-etching technique and observed under inverted optical microscope. (D) Schematic view of the three different layer of the gas exchanger. Red and blue arrows show gas and liquid phase inlet and outlet inside the platform. (E) Image of the gas-exchanger with inlet/outlet connections for liquid and gas phase perfusion. The microfluidic channels are perfused with 1 mM fluorescein solution.*

Channels section shape and depth were analyzed with a profilometer (Alpha Step IQ surface profiler, KLA Tencor, USA). Rounded cross-section shape was observed, while channels depth resulted to be etching-time dependent; depths of 40, 70 and 100 µm were obtained with an immersion time of 2.5, 5 and 7.5 min, respectively in HF solution.

A thin polydimethylsiloxane, PDMS, permeable membrane with defined and homogenous thickness was obtained by spinning the unpolimerized solution on a silicon

wafer. A premixed 10:1 ratio of PDMS prepolymer and curing agent (Sylgard 184 kit, Dow Corning, USA) was spin-coated on a previously silanized 5 in Si wafer at 1400 rpm for 1 min to obtain a thickness of 40±5 μm and cured on a hotplate at 353 K for 1 h.
The gas layer consists in a 5 cm^3 PDMS chamber in which gas phase flows at defined flow rate and p_{O2}. Residence time is only of few seconds to maintain an uniform oxygen partial pressure during steady-state experiments.
PDMS layers were punched with a 22G stainless steel needle (Small Parts Inc, USA) to obtain gas and liquid inlet/outlet holes. A 50 × 75 mm glass cover slide, gas chamber, PDMS membrane and fluidic layer were assembled and sealed by plasma bonding (Plasma Cleaner, Harrick Plasma, USA). All fluidic connections to the microfluidic device were made using PTFE microtubing (Cole Parmer, USA). Fig. B.2D shows a schematic view of the assembled layers. The red arrows indicate gas inlet/outlet, whereas blue lines show the liquid track inside the platform.
Different liquid flow rates through the fluidic microchannels were obtained by a syringe pump (Harvard Pump, Harvard Apparatus, USA). A constant gas flow rate and oxygen composition were maintained in the gas chamber using air and nitrogen mass flow meters (Bronkhorst, The Netherlands), controlled through software FlowDDE32.

B.4.3 Oxygen measurement

A 100 μM solution of tris(4,7-diphenyl-1,10-phenanthroline)-ruthenium(II) dichloride, Ru(ddp), (Sigma-Aldrich, USA) in a 30% ethanol in PBS 1X (Invitrogen, USA) solution was used to measure oxygen partial pressure inside the microfluidic channels. Fluorescence of Ru(ddp) was detected by an inverted fluorescence microscope LeicaDMI6000B equipped with a mercury short-arc reflector lamp (Leica, Germany) excited at BP 450-490 nm and acquired at LP 590 (Fig. B.2E).

Oxygen partial pressure was also continuously monitored with a fiber optic oxygen sensor (OceanOptics, USA) at the microchannel outlet. Fluorescence intensity is linearly correlated to the oxygen partial pressure in the sample. Both sensors are based on fluorescence quenching that increases with the oxygen partial pressure. The degree of

quenching can be correlated to the oxygen partial pressure of the sample by the Stern-Volmer equation:

$$\frac{I_0}{I} = 1 + kp_{O_2} \quad \text{(B.1)}$$

where I_0 is the fluorescence intensity at zero partial pressure of oxygen, I is the fluorescence intensity at a particular p_{O_2} and k is the Stern-Volmer constant which depends on the chemical composition of the sensor and on the temperature. Calibration of the sensor at 298 K was achieved using five liquid standards, obtained by bubbling a gas mixture with a partial pressure of 0%, 5%, 10%, 15% and 21%. Complete oxygen removal was achieved with 8 hours of humidified argon bubbling (Rivoira, Italy). Stern-Volmer constant value was obtained by correlating experimental data.

B.4.4 Microfluidic cell culture chamber

A microfluidic cell culture chamber was made by a standard softlithography technique.[34] Briefly, the design shown in Fig. B.3A was produced by CAD program and patterned in a silicon substrate using negative photoresist SU8-2100 (Microchem, Germany). After silanization with HDMS under vacuum for 1 h, a 10 : 1 ratio of PDMS prepolymer and curing agent was casted and cured for 2 h at 343 K in an oven. Through a 27 mm punch, a PDMS mold was extracted. In order to ensure an electrical stimulation to the cell culture, a platinum wire was inserted in the PDMS mold and wired to an electrical stimulator. The glass slide hosting the cell culture was located in a standard microscopy aluminium holder (20 mm diameter hole), covered by the PDMS mold and pressure sealed by a Teflon cover (Fig. B.3B). The perfusion culture chamber was connected to the microfluidic exchanger through silica tubings in order to avoid external oxygen infiltrations. All the experiments were performed with a 100 µl min^{-1} flow rate using syringe pumps (Harvard Pump, Harvard Apparatus, USA) allowing fast exchange of medium without any apparent change in cellular calcium dynamics.

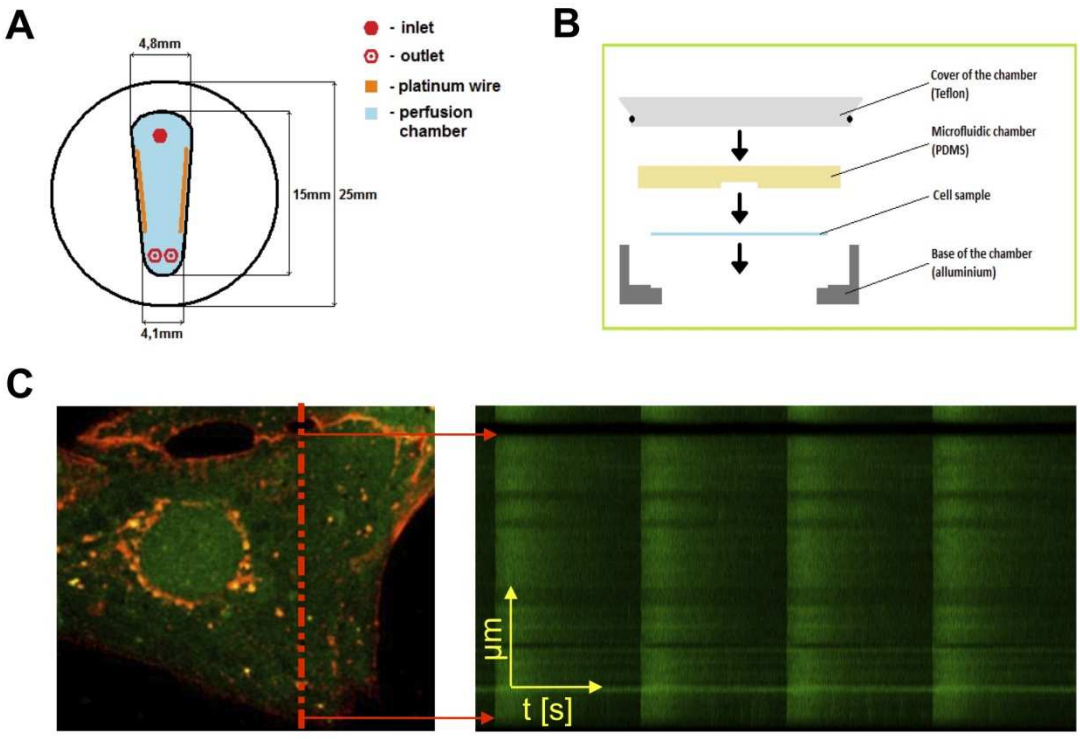

Figure 3. *Cell culture chamber and calcium dynamic acquisition. (A) Microfluidic cell culture chamber top view. The chamber is characterized by 1 inlet and 2 outlets and by 2 platinum wires placed in the lateral walls to electrically stimulate cells. (B) Assembly of the microfluidic chamber within microscope holder to perform on line detection. (C) Confocal image and calcium dynamic of a cardiomyocyte under electrical stimulation. Line scan (yellow line) is placed between nucleus and sarcolemma of the cell and calcium transient are continuously detected as a function of time.*

B.4.5 Cardiomyocyte isolation and culture

Neonatal rat cardiomyocytes were obtained from Sprague-Dawley pups 1-3 days old. The cells were plated on 20 µg/ml^{-1} laminin-coated (BD Bioscience, USA) glass coverslips in Day1 medium: 25 mM Hepes Dulbecco's Modified Eagle's Medium (Gibco, USA), 17% Medium M199 (Gibco, USA) 10% horse serum (Gibco, USA), 5% Newborn Calf Serum (Gibco, USA), 2 mM L-Glutammine (Gibco, USA), Penicillin-Streptomycin (EuroClone, Italy). After 24 hours, the Day1 medium was replaced with Day2 medium: Day1 medium with 5% horse serum and 0.5% newborn calf serum. Experiments were performed 4 days after plating. The animals were housed and operated at the Animal Colony of the Venetian Institute of Molecular Institute. All experiments with animals were approved

by Padova University's Institutional Animal Care Committee (Comitato Etico di Ateneo per la Sperimentazione Animale).

B.4.6 Calcium dynamic acquisition and analysis

Confocal Calcium measurements were performed as reported in Fig. 3C. Cardiomyocytes were loaded in serum-free D-MEM (Gibco, USA) supplemented with 3 µM fluorescent calcium dye fluo-4 AM (Invitrogen, USA) for 20 minutes at 310 K in the presence of 2 µM Pluronic F-127 (Invitrogen, USA) and 20 µM sulfinpyrazone (Sigma-Aldrich, USA), then incubated for additional 10 minutes at 310 K in Fluo-4-free D-MEM to allow complete de-esterification of the dye, and added with 0.2 µM di-8-ANEPPS (Invitrogen, USA). After loading, the coverslips were transferred to the microfluidic chamber and perfused with recording solution: NaCl 125 mM, KCl 5 mM, Na_3PO_4 1 mM, $MgSO_4$ 1 mM, Hepes 20 mM, $CaCl_2$ 2 mM, Glucose 5.5 mM, to pH 7.4 with NaOH. Line scan was acquired with a Leica TCS SP5 confocal microscope equipped with a 63x, 1,4NA oil immersion objective, with 488 nm Ar laser line as an excitation source, 700 Hz acquisition frequency . To reduce dye photo-bleaching and photo-toxic effects on the analyzed cells, the laser power was set at minimum possible. During all the experiments, the culture was constantly filed-stimulated with electrical pulses at 0.7 Hz, 20 V/cm, to overcome spontaneous beating activity allowing acquisition at the same beating rate in all cells. Nifedipine and Verapamil (Sigma-Aldrich, USA) were dissolved in DMSO (Sigma-Aldrich, USA) or deionized H_2O, respectively, at a 10 mM starting concentration and diluted to the desired concentration in recording solution immediately prior to the experiments. All data analyses were performed with ImageJ and Origin7 software.

Data are presented as means of percentage decrease normalized on the reference conditions ± standard error of mean (SEM). The effects of different oxygen concentrations on calcium transients were compared by a one way ANOVA followed by Bonferroni's mean comparison. We considered $P<0.01$ to be statistically significant.

B.4.7 Mathematical modeling

The oxygen concentration profile, and consequently the oxygen partial pressure, within the liquid phase domain of the microfluidic gas exchanger was described by simplified analytical model and by computational solution of the species mass balance. The simplified model was validated with computational analysis and used for a proper gas exchanger design.

Mass transfer was assumed to be governed by convective transport in the gas phase, diffusive resistance in the permeable membrane and convective-diffusion regime in the liquid phase. The concentration in the gas phase was assumed constant along spatial coordinates because, according to the high gas flow rate, the permanence time in the gas chamber is much smaller than the characteristic time of the membrane oxygen exchange process.

On the other hand, the oxygen concentration in the liquid phase changes from the inlet (x = 0) to the outlet (x = CL) of the microfluidic gas exchanger. For this reason, in order to describe oxygen concentration profile along y-coordinate (height of the microfluidic channel), both hydrodynamic and mass transport models should be solved simultaneously. Due to the low Reynolds numbers (1-10) an analytical solution of fully developed hydrodynamic profile between flat planes was assumed [35]. Considering that Péclet number (convection/diffusion ratio) is much greater than 1 for all experimental conditions tested in this work, we assumed that diffusive flux is relevant only in the y-direction, whereas convective flux occurs in the x-direction. Moreover, we define h_L as the equivalent channel height, which is obtained as the area of the cross-section divided by the width of the channel.

Under these assumptions and considering all mass transfer resistances localized at the interfaces, the steady-state mass balance equation in the liquid domain takes the following form:

$$\begin{cases} \frac{u}{H}\frac{\partial p_{O_2}^L(x)}{\partial x} + N_{O_2,y}(x, y = h_L) = 0 \\ p_{O_2}^L(x = 0) = p_{O_2}^{L,IN} \end{cases} \quad \text{(B.2)}$$

where $p_{O_2}^L$ is the oxygen partial pressure of the liquid phase, *u* is the axial velocity, *H* is the Henry's constant of oxygen solubility in water at experimental temperature condition, $N_{O_2,y}(x, y = h_L)$ is the total oxygen flux at liquid-membrane interface along *x*-coordinate and $p_{O_2}^{L,IN}$ is the boundary condition at channel inlet. The total oxygen flux at liquid-membrane interface, $N_{O_2,y}(x, y = h_L)$, can be expressed as the product of the overall mass transfer resistance and the total driving force:

$$N_{O_2,y}(x, y = h_L) = < K_G > (p_{O_2}^L(x) - p_{O_2}^G)a \quad \text{(B.3)}$$

$p_{O_2}^G$ is the constant oxygen partial pressure in gas phase, *a* is specific surface, which corresponds to the inverse of the equivalent channel height h_L, whereas $< K_G >$ is the averaged overall mass transfer coefficient. The analytical expression of $< K_G >$ is derived by equating oxygen fluxes for the three different domains and its general form can be expressed as follows:

$$\frac{1}{< K_G >} = \frac{1}{k_G} + \frac{s}{p} + \frac{H}{k_L}. \quad \text{(B.4)}$$

k_G and k_L are the mass transfer coefficients in the gas and liquid phase respectively, *p* the oxygen permeability in PDMS and *s* the membrane thickness.

Integration of eqn (B.2) from the inlet to the outlet of the channel leads to the following relation:

$$\frac{p_{O_2}^{L,OUT} - p_{O_2}^G}{p_{O_2}^{L,IN} - p_{O_2}^G} = \exp\left(-\frac{< K_G > HL}{h_L u}\right) \quad \text{(B.5)}$$

Equation (5) relates the oxygen partial pressure in the microchannel to the length and geometry of the channel, operative conditions and mass transfer properties. This relation is used to calculate the minimal channel length necessary to ensure a defined oxygen concentration at the outlet of the system.

The solution of eqn (B.5) requires a proper estimation of the mean overall mass transfer coefficient by eqn (B.4). Due to the high oxygen diffusivity in the gas phase compared to those in the liquid and solid phase, the first resistance term in equation (B.4) results to be negligible.

The mass transfer coefficient in the liquid phase, k_L, can be evaluated from empirical correlations for laminar flow which relate together dimensionless groups (Péclet, Reynolds and Sherwood numbers). In the developing diffusive concentration profile and for boundary layers which are extremely thin relative to the channel width, the following relation has been proposed [36]:

$$\begin{cases} \dfrac{k_L h_L}{D} = 1.233\left(\dfrac{xD}{uh_L^2}\right)^{-1/3}, \dfrac{xD}{uh_L^2} \le c_1 \\ \dfrac{k_L h_L}{D} = c_2, \dfrac{xD}{uh_L^2} > c_1 \end{cases} \tag{B.6}$$

where D is the oxygen diffusion coefficient in the liquid phase. c_1 and c_2 are constant values that can be evaluated by computationally solving oxygen mass balance equations for the system shows in Fig. B.2A.

The numerical solution of the convective-diffusion equation for the fluidic domain and the diffusive equation for the solid domain were obtained with the support of the software COMSOL Multiphysics 3.4 at different operative conditions. Boundary and initial conditions were set as follows: the top of the membrane domain is taken to be at a constant concentration in equilibrium with the adjacent gas phase, whereas oxygen concentration at the bottom surface is equilibrated with that in the fluidic domain. In the inlet section of the fluidic domain it was set a constant concentration, whereas at the outlet section it was considered only a convective flux. The remaining walls were assumed to be impermeable to oxygen. All values for the parameters used for the simulations are listed in Table B.1.

Table B.1. *Summary of physical properties.*

Property	U.M.	Value	Ref.
D, oxygen diffusion in PBS	$m^2\ s^{-1}$	2.1×10^{-9}	37
p, oxygen permeability in PDMS	$(10^{-10}\ cm^3(STP) \times cm/cm^2 \times s \times cmHg)$	800	38
O_2 solubility in PBS at 1 atm and 298 K	$mol\ m^{-3}$	1.045	39

B.5 Results and discussion

B.5.1 Microfluidic platform validation

Fig. B.4A shows the oxygen concentration distribution in the microfluidic channel obtained by computational simulation of oxygen mass balance equations. Boundary conditions were set as follows: inlet oxygen partial pressure, $p_{O_2}^{L,IN}$, was set to 21%, whereas oxygen partial pressure in the gas phase, $p_{O_2}^{G}$, is assumed to be constant at 0%. Oxygen flux through the PDMS membrane is directed from the liquid phase to the gas compartment according to the oxygen partial pressure gradient. Oxygen flux at the membrane interface decreases along the *x*-coordinate due to the progressive reduction of the gradient for 1 mm channel length as shown in Fig. B.4B.

In order to properly design the gas exchanger, the application of computational simulation to a larger portion or overall microfluidic channel could be time consuming and computational intensive. For this reason a simplified analytical theory to fairly describe mass transport inside the microfluidic device was derived. The mass balance analytical expression (eqn (B.5)) can describe oxygen profile inside the channel as a function of all operative parameters that affect mass transfer process and of the mean overall mass transfer coefficient (<K_G>) and, in particular, liquid mass transfer coefficient (k_L). In this work, we adopt the model proposed by Vollmer and coworkers [36] to our system using computational results to estimate model parameters. We found out that c_1 and c_2 constant values of eqn (B.6) are 0.10 and 2.62 respectively. Fig. 4C shows a comparison between computational simulation and modified analytical model (eqn

(B.6)) in terms of adimensional numbers.

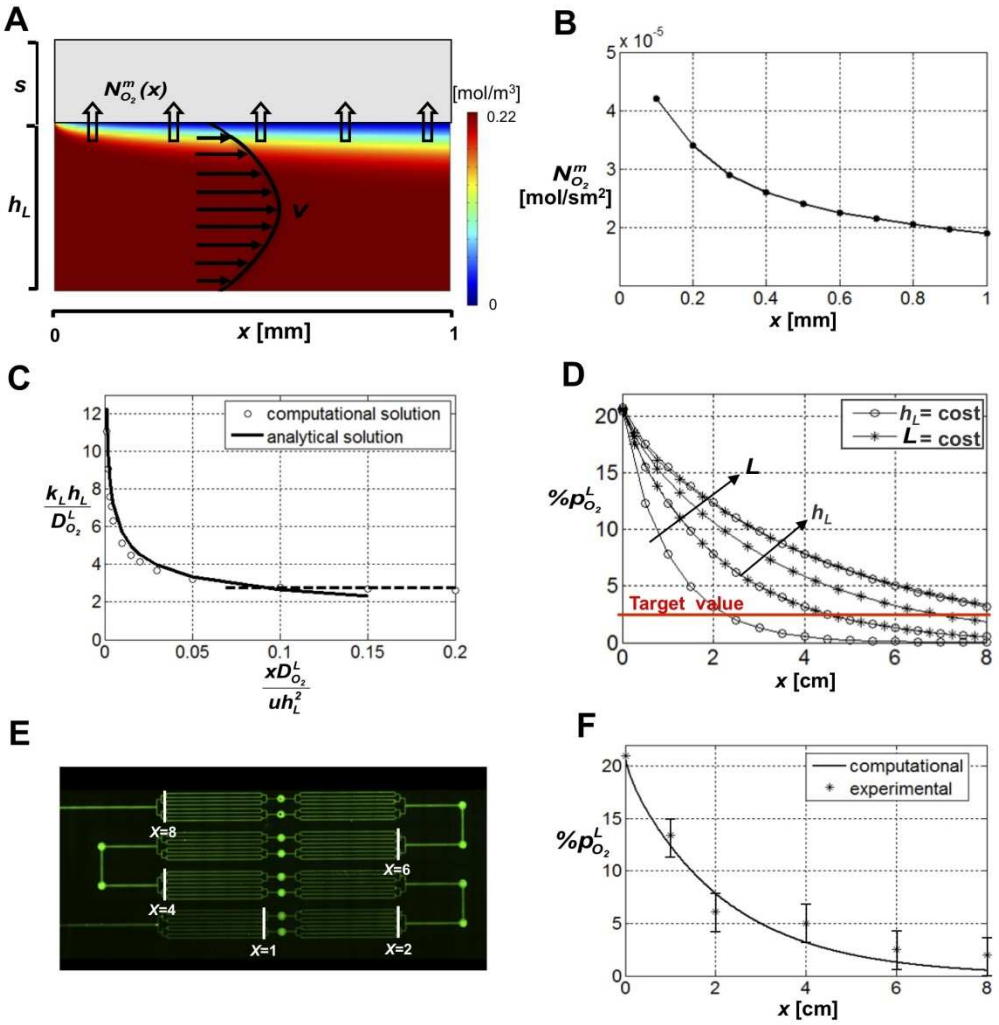

Figure B.4. *Mass transport model development and validation. (A) 2D representation of oxygen concentration obtained by computational solution of mass balance equations in the microfluidic channel longitudinal cross-section. Empty arrows show oxygen flux directed from liquid phase to the gas one, in which oxygen partial pressure is assumed to be 0%. Full arrows show y-direction velocity profile. (B) Profile of the oxygen flux normal to the PDMS membrane interface along the x-coordinate. (C) Comparison of computational and analytical solution in term of adimensional numbers according to eqn. 6. (D) Oxygen partial pressure profile obtained from analytical solution given by eqn. 5 as a function of x-coordinate, parametric in liquid flow rate, $\dot{L}$, and channel height, h_L. Red line shows design target value of 2%. (E) Fluorescence imaging of fluidic layer filled with Ru(ddp) solution, using $\dot{L}$=100 µl/min^{-1} and h_L=40 µm. White mark shows the region of interest for fluorescence quantification reported in Fig. B.4F (values of x-coordinate are in cm). (F) Comparison of $p^L_{O_2}$ experimental profile inside the fluidic layer and the analytical solution obtained by eqn.B.5.*

This analytical model allows to fairly estimate the liquid mass transfer coefficient for several experimental conditions, in particular for different liquid flow rates $(\dot{L})$ and channel heights (h_L).

On the other hand, the minimal channel length for achieving a target $p_{O_2}^L$ reduction using specific liquid flow rate and channel height can be easily estimated by eqn (B.5). Fig. B.4D shows $p_{O_2}^L$ profiles as a function of *x*-coordinate, obtained by varying both $\dot{L}$ and h_L.

In order to experimentally validate the developed theory we mapped fluorescence intensity of the oxygen sensitive dye in the overall fluidic layer of the oxygen exchanger (Fig. B.4E). Fig. B.4E shows a fluorescence intensity increase along *x*-coordinate from the inlet to the outlet according to $p_{O_2}^L$. Fig. B.4F shows a comparison of experimental $p_{O_2}^L$ measured at different *x*-coordinate values (reported in Fig. B.4E) and analytical solution obtained from eqn (B.4). Very good agreement between profiles within the experimental uncertainty has been observed. Finally, using the simplified analytical theory, we designed a gas exchanger that is able to perform a $p_{O_2}^L$ reduction of 95% with a steady state flow rate of 100 µl/min.$^{-1}$ The gas exchanger configuration consists in 8 exchanger units in series formed by 8 parallel channels with 80 mm total length, 40 µm height and 100 µm width.

B.5.1 Calcium dynamics in hypoxia

The microfluidic cell culture chamber and gas exchanger must preserve cardiomyocytes physiological characteristics while providing fast transient biochemical stimulation. The cell culture chamber was properly designed to obtain a uniform laminar flow avoiding unpaired velocity profile, back flow and stagnant dead volumes. This ideal condition was experimentally verified by observing the dynamic of a pulse of fluorescein in the cell culture chamber at different flow rates (data not shown). In addition, before each experiment, the culture was maintained in perfusion for 1 hour in normoxic solution while recording calcium dynamics. The cardiomyocytes displayed normal calcium dynamics during electrical stimulation. In order to test the time course of substance delivery to the microfluidic chamber, we injected a 50 µl bolus of 10 mM caffeine

solution in the perfusion line. The caffeine stimulated Ca^{2+} release from sarcoplasmic reticulum (SR) had a rapid onset and resulted in the change in fluorescence intensity. Such effect lasted 45 s, after which the calcium transients amplitude returned to normal indicating complete caffeine wash out (Fig. B.5A). This time is consistent with the estimated permanence time of caffeine within the microfluidic chamber, as evaluated through fluorescence dye experiments.

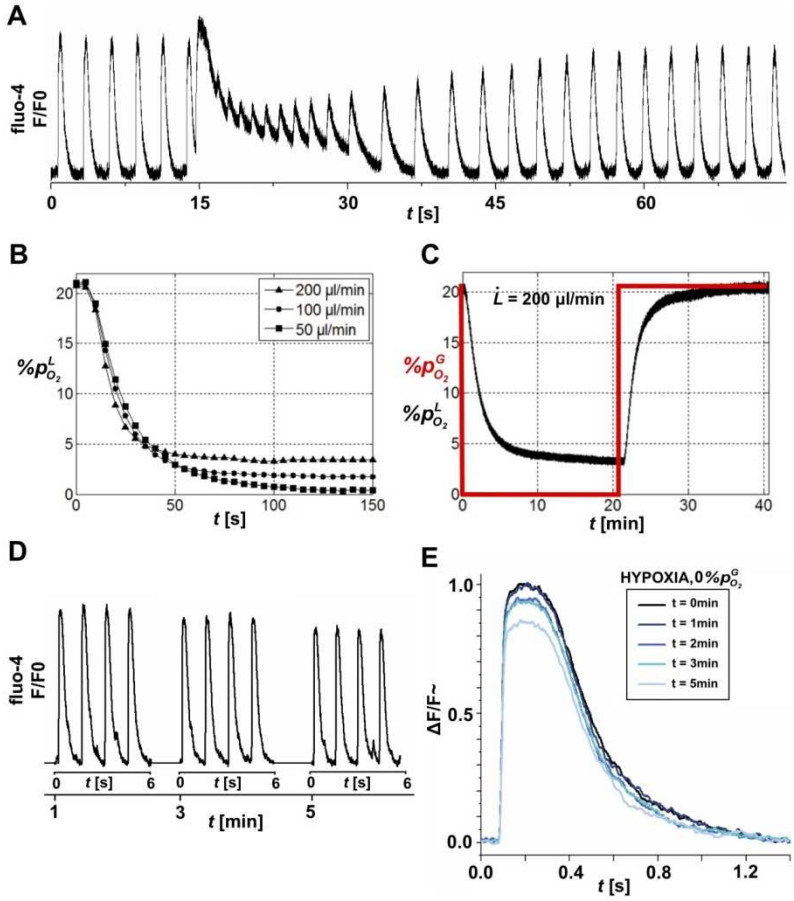

Figure 5. *Effect of hypoxia on calcium transients. (A) Calcium dynamic in a cardiomyocyte under electrical stimulation revealed through Fluo-4 in the microfluidic culture chamber during perfusion of 50 µl of 10 mM caffeine solution; cardiomyocyte displays normal Ca^{2+} transients and response to caffeine with full recovery after wash out. (B,C) Liquid phase oxygen dynamic during step impulse of the oxygen partial pressure in the gas phase monitored by Ru(ddp) with three different flowrates (B) and by optic fiber sensor with $\dot{L}$ =200 µl/min^{-1} (C) at exchanger outlet. (D) Calcium transients sequence at different time points after hypoxic stimulus to the cell culture. (E) Comparison of single normalized calcium transients at different time points after hypoxic stimulus.*

In order to analyze the early effect of hypoxic events on cardiac physiology it is fundamental to fully characterize the oxygen partial pressure dynamics after set point variations. For this reasons, oxygen partial pressure at the outlet of the gas exchanger were measured by continuously detecting intensity fluorescence of oxygen sensitive dye during a $p_{O_2}^G$ set point change from 21% to 0% at three different flow rates: 50, 100 and 200 µl/min^{-1} (Fig. B.5B). The $p_{O_2}^L$ half decay value of 10 s for all different flow rates ensures fast oxygen dynamics. Different hypoxic steady state levels ($p_{O_2}^L$ < 5%) can be achieved by varying medium flow rate (Fig. B.5B). In order to exclude gas leakage between the gas exchanger and the culture chamber, oxygen partial pressure values, $p_{O_2}^L$, were continuously monitored at cell culture chamber inlet by fiber optic probe. Fig. 5C shows $p_{O_2}^L$ steady state values (black line) reached after two $p_{O_2}^G$ set point variations (red line): 21% to 0% and 0% to 21%. Consistent measurements reported in Fig. B.5B and C confirm an efficient gas insulation.

All together, these results show that the microfluidic experimental set up (as reported in Fig. B.1) is able to accurately control oxygen partial pressure on cell culture in terms of steady state levels and rapid set point variations. It is worth to underlining that oxygen partial pressure control is achieved without any perturbations on liquid media, allowing long term confocal acquisitions on same region of interest. These technical improvements make possible to perform experimental investigations using the same cell as its own control, continuously acquiring biological data prior and during the hypoxic stimulation.

In order to rationally study the hypoxia-induced effects on calcium handling during excitation-contraction coupling it is important to investigate the duration of hypoxic stimulation that could exert a cell physiological response.

In this context, Fig. B.5D shows a sequence of calcium dynamics in response to fast $p_{O_2}^L$ drop as a function of time. A comparison of normalized calcium transient peaks at different time points (Fig. B.5E) shows a significant alteration of the fluorescence intensity peak maximum after 5 min from hypoxic stimulus. All other experiments were

performed considering this time frame as a minimal values to elicit a hypoxia-induced physiological response.

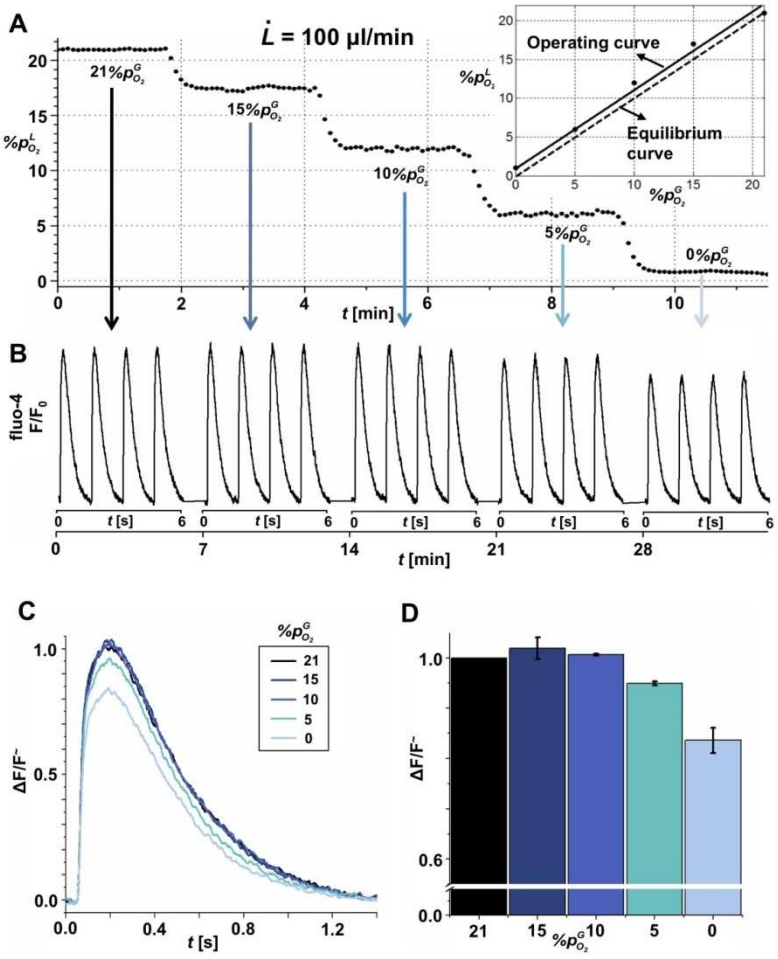

Figure 6. *Oxygen level threshold. (A) $p^L_{O_2}$ profile for five different $p^G_{O_2}$ with $\dot{L}$ =100 µl/min^{-1}. Insert shows equilibrium and operating curve obtained by calibration. (B) Calcium transients sequence at different $p^L_{O_2}$ measured 7 minutes after $p^G_{O_2}$ set-point change. Blue arrows show correspondence between $p^G_{O_2}$ set-point and calcium transient sequence (Fig. 5A). (C) Comparison of single normalized calcium transients at different oxygen partial pressure. (D) Averaged values of normalized calcium transients peak height at different oxygen partial pressure. The histogram is based on 5 replicates of same conditions.*

We then sought to determine the hypoxic level at which hypoxia-induced effects on calcium handling during excitation-contraction coupling can be recorded. A multiple step experiment was designed by setting $p^G_{O_2}$ at 5 different values from 21% to 0% with 5% interval and the resulting $p^L_{O_2}$ step profile is shown in Fig. B.6A. Corresponding values of

$p_{O_2}^L$ and $p_{O_2}^G$ were correlated to obtain operating curve shown in Fig. 6A insert. Interestingly, the operating curve differs slightly from the equilibrium curve within the accuracy used in the gas exchanger design ($p_{O_2}^L$ = 2% as target value (Fig. B.4D), corresponding to 95% reduction from normoxic conditions).

Fig. B.6B shows the corresponding sequence of calcium transients acquired for 6 s at different $p_{O_2}^L$ levels measured 7 minutes after the $p_{O_2}^G$ set-point change. Blue arrows show correspondence between $p_{O_2}^G$ set-point values and calcium transients. The baseline fluorescence maintained the same intensity for all the duration of the experiment and the effect of hypoxic stimulation emerged with a decrease of the maximum of the normalized calcium transient peak (Fig. B.6C). The analyzed cells did not display calcium cycling alterations for $p_{O_2}^G$ > 5% (n=5). At 5% a poor significant difference ($P<0.05$, n=5) decrease was observed, whereas at $p_{O_2}^G$ = 0% the alteration of calcium transient was observed with high statistical relevance ($P<0.01$, n=5) (Fig. B.6D). These data show that the observed effect reveals itself only in highly hypoxic nearly anoxic conditions, remaining latent at higher oxygen concentrations.

To test the reversibility of the hypoxia induced Ca^{2+} changes and, concurrently, exclude artifact deriving form long term confocal acquisition such as dye photo-bleaching, the cardiomyocyte culture was subjected to a fast drop of $p_{O_2}^L$ and maintained under hypoxic conditions for 10 min followed by 10 min of reperfusion with normoxic medium (Fig. B.7A).

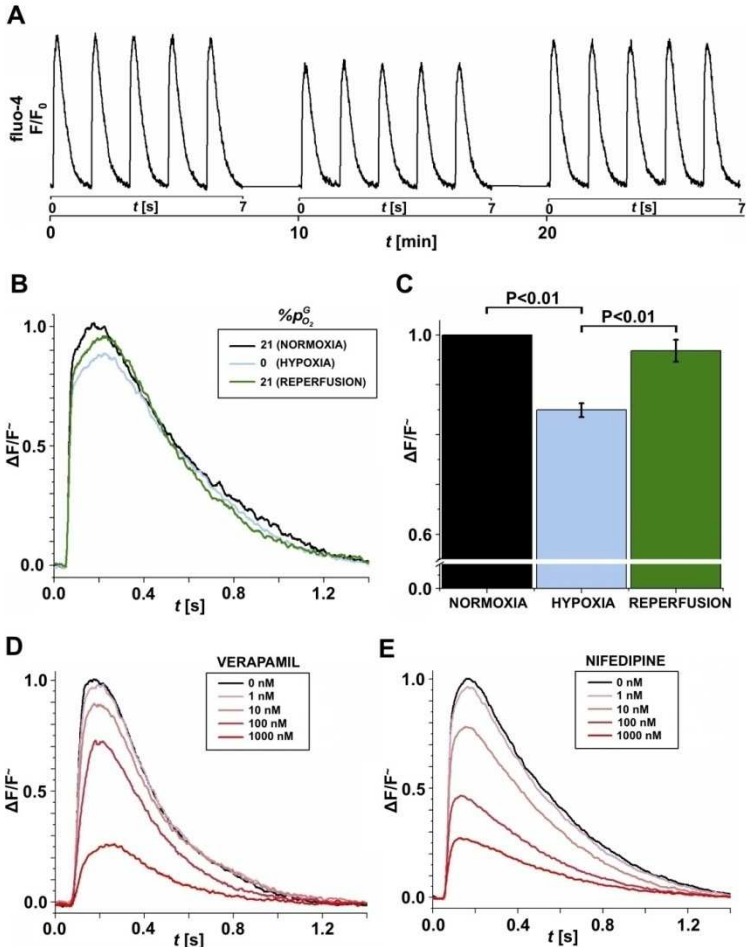

Figure B.7. *Reversible effect of hypoxia on calcium cycling. (A) Calcium transients sequence measured in normoxic, hypoxic ($p_{O_2}^G$ = 0%) and normoxic conditions. (B) Comparison of single normalized calcium transients in normoxic, hypoxic ($p_{O_2}^G$ = 0%) and normoxic condition. (C) Averaged values of normalized calcium transients peak height in normoxic, hypoxic ($p_{O_2}^G$ = 0%) and normoxic condition. The histogram is based on 5 replicates of same conditions. (D,E) Normalized calcium transients for different concentrations of L-type Ca^{2+} channel antagonist Verapamil (D) and Nifedipine (E).*

Whole-cell calcium dynamics were acquired every 10 min. In response to hypoxic stress we observed a decrease of the maximum calcium transient peak (Fig. B.7B) with no alteration of the baseline fluorescence (*n* = 8). After recovering the normoxic conditions, the cardiomyocytes displayed again the same fluorescence intensity, indicating a recovery of calcium cycling towards basal conditions. By analyzing the variation of Fluo-4 fluorescence after 10 minutes of hypoxia and subsequent 10 minutes of reperfusion by means of percentage decrease against normoxic fluorescence intensity, a statistically

relevant decrease (~15%, P<0.01) emerged (Fig. B.7C). The recovery of normal calcium transients after the return to normoxic conditions highlights the reversibility of the biological effect and excludes the responsibility of dye photo-bleaching from the observed decrease of fluorescence.

All together, these results show that there is a significant reversible alteration of calcium homeostasis in excitation-contraction coupling during fast hypoxic stimuli. This experimental evidence underlines the ability of the cell to sense oxygen level and rapidly adapt to normoxic/hypoxic/normoxic transitions by regulating either directly or through secondary pathways the molecular machinery involved in cardiac Ca^{2+} homeostasis [3]. In addition to direct channel sensing or specifically target protein modification (such as phosphorylation and cysteine reduction), hypoxia may also alter the regulation of these channels via indirect bulk mechanisms, such as changes in cell redox state by action of ROS[3]. However, all these hypoxia-induced phenomena affect membrane depolarization and concurrently alter of L-type voltage-gated calcium channels (VGCC) function, which provide the main entry pathway for extracellular Ca^{2+} into cardiomyocytes and are a major component of excitation-contraction coupling machinery. L–type VGCCs trigger the calcium-induced calcium release (CICR) process through extracellular calcium influx; calcium entry through VGCCs, which are topologically associated to calcium-release channels (ryanodine receptors) in the sarcoplasmic reticulum (SR) membrane, cause further calcium SR release within cytosol compartment. These secondary calcium dynamics can be easily measured as reported in this study. In this context, the alterations in excitation-contraction coupling under hypoxia could be related to impaired CICR for hypoxia-dependent desensitization of L-type VGCCs.

In order to explore this hypothesis, experimental investigation of calcium transients upon inhibition of the L-type Ca^{2+} channel with two antagonists was performed. Fig. B.7D and B.7E show normalized calcium transient at different concentrations of channel blocker ranging from 1 nm to 1000 nM in normoxic conditions. Similar calcium peak reductions recorded for hypoxia below 5% $p_{O_2}^{L}$ were observed with 100nM of Verapamil and 10 nM of Nifedipine Fig. B.7D and Fig. B.7E, respectively.

These findings confirm that a hypoxia-induced alteration of primary calcium entry

through L-type VGCCs could turn in a reduced calcium concentration during excitation-contraction coupling and consequently, in an alteration of the physiological activity of cardiomyocytes.

Our results suggest that a cardioprotective mechanism during early phases of acute ischemia takes place through the reduction of calcium homeostasis in excitation-contraction coupling.

A reversible adaptation of myocardium after short ischemic stress (5 min and 15 min ischemia/reperfusion) *in vivo* was first observed by Heyndrickx and co-workers[40]. They demonstrated that a fully reversible dysfunction of the ischemic heart is prolonged after hypoxic stress, named “myocardial stunning”. The molecular basis behind this physiological behavior is still unclear. Myocardial stunning results from different adaptive mechanisms such as down-regulation of myocardial metabolism, and leads to activation of long-term cardioprotective responses including activation of cell survival pathways resulting in changes in gene and protein expression [41].

In this context, we first show that a fully reversible adaptive mechanisms of cardiopreservation might take place during the early events of ischemic stress through fast alteration in ion channel function in response to changes in cellular oxygen.

B.6 Conclusions

A microfluidic gas exchanger was designed to accurately and very quickly regulate $p_{O_2}^L$ without perturbing medium flux and consequently on line acquisition. By developing an *ad hoc* mass transfer theory, supported by computational simulations, we were able to predict $p_{O_2}^L$ inside the cell culture chamber as a function of operative parameters (liquid flow rate). Experimental validation of $p_{O_2}^L$ profile inside the gas-exchanger microchannels confirmed that both constructive method and analytical model were valid.

With the support of the developed technological system we observed a significant calcium handling alteration in a neonatal rat cardiomyocyte population after an exposure to 5 min of hypoxic conditions. Thanks to accuracy in tuning oxygen level in our

system we found a threshold value of 5% $p_{O_2}^L$, above which no significant calcium transients peak decreases were observed.

The recovery of normal calcium transients after the return to normoxic conditions highlights the reversibility of the biological effect and excludes the responsibility of sample damaging phenomena like dye photo-bleaching from the observed decrease of fluorescence.

We also explored the hypothesis that calcium-handling alteration in hypoxia could be affected by the desensitization of voltage gated calcium channels. In order to support our hypothesis we compared calcium transients peak obtained during a hypoxic stimulus and those obtained under effect of L-type calcium antagonist, Verapamil and Nifedipine.

Rational understanding of how the cardiomyocyte adapts to acute ischemic stress and sustains its survival represents an important challenge because it might help in finding novel strategies to enhance cardiomyocytes survival in patients.

Acknoledgments

This work was supported by: Progetti di Eccellenza CaRiPaRo Grant, ES to Fondo Sociale Europeo (grant code 2105/1/10/1268/2008). The research leading to these results has received funding from the European Community's Seventh Framework Program FP7/2007-2013 under *grant agreement* n° HEALTH-F2-2009-241526, EUTrigTreat." (to MM)

B.7 Literature cited

[1] S. Allender, C. Foster, L. Hutchinson and C. Arambepola, J. Urban Health., 2008, 85, 938–951.

[2]R.J. Diaz and G.J. Wilson, Cardiovascular Res., 2006, 70, 286-296.

[3]L.A. Shimoda and J. Polak, Am. J. Physiol. Cell Physiol., 300, C951-C967.

[4]A.L. Russ, K.M. Haberstroh and A.E. Rundell, Exp.Mol.Pathol., 2007, 83, 143-159.

[5]D.A. Saint, Brit. J. Pharmacol., 2009, 153, 1133-1142.

[6]Y.K. Ju, D.A. Saint and P.W. Gage, The Journal of Physiology, 1996, 497, 337-347.

[7]W.P. Wang, J.H. Ma, P.H. Zhang and A.T. Luo, Pflug. Arch. Eur. J. Phy., 2007, 454, 461-475.

[8]L.C. Hool, J. Physiol-London, 2004, 554, 743-754.

[9]I.M. Fearon, A.C.V. Palmer, A.J. Balmforth, S.G. Ball, G. Mikala, A. Schwartz and C. Peers, J. Physiol-London, 1997, 500, 551-556.

[10] L.C. Hool, Circ. Res., 2000, 87, 1164-1171.

[11] N. Gaur, Y. Rudy and L. Hool, Circ. Res., 2009, 105, 1196-1203.

[12] I.M. Fearon, G. Varadi, S. Koch, I. Isaacsohn, S.G. Ball and C. Peers, Circ. Res., 2000, 87, 537-539.

[13] S. Movafagh and M. Morad, Ann. NY Acad. Sci., 2010, 1188, 153-15

[14] L.C. Hool, C.A. Di Maria, H.M. Viola and P.G. Arthur, Cardiovasc. Res., 2005, 67, 624-635.

[15] T.J. Kamp and J.W. Hell, Circ. Res., 2000, 87, 1095-1102.

[16] P. Kaplan, E. Babusikova, J. Lehotsky and D. Dobrota, Mol. Cell Biochem., 2003, 248, 41-47.

[17] L. Guerra, E. Cerbai, S. Gessi, P.A. Borea and A. Mugelli, Brit. J. Pharmacol., 1996, 118, 1278-1284.

[18] J.W. Allen and S.N. Bhatia, Biotechnol. Bioeng., 2002, 82, 253-262.

[19] C.B. Allen, B.K. Schneider and C.W. White, AM. J. Physiol-Lung C., 2001, 281, L1021-L1027

[20] D.E. Powers, J.R. Millman, S. Bonner-Weir, M.J. Rappel and C.K. Colton, Biotechnol. Progr., 2010, 26, 805-818.

[21] L. Kim, Y. Toh, J. Voldman and H. Yu, Lab. Chip, 2007, 7, 681-694.

[22] D.J. Beebe, G.A. Mensing and G.M. Walker, Annu. Rev. Biomed. Eng., 2002, 4, 261-286.

[23] D.N. Breslauer, P.J. Lee and L.P. Lee, Mol.Biosyst., 2006, 2, 97-112.

[24] Z.Y. Zhang, P. Boccazzi, H.G. Choi, G. Perozziello, A.J. Sinskey and K.F. Jensen, Lab. Chip, 2006, 6, 906-913.

[25] A. Groisman, C. Lobo, H.J. Cho, J.K. Campbell, Y.S. Dufour, A.M. Stevens and A.

Levchenko, Nat. Methods, 2005, 2, 685-689.

[26] E. Leclerc, Y. Sakay and T. Fujii, Biotechnol. Progr., 2004, 20, 750-755.

[27] R. Gomez-Sjoberg, A.A. Leyrat, D.M. Pirone, C.S. Chen and S.R. Quake, Anal. Chem., 2007, 79, 8557-8563.

[28] M. Polinkovsky, E. Gutierrez, A. Levchenko and A. Groisman, Lab. Chip, 2009, 9, 1073-1084.

[29] M. Adler, M. Polinkovsky, E. Gutierrez and A. Groisman, Lab. Chip, 2009, 10, 388-391.

[30] R.H.W. Lam, M.C. Kim and T. Thorsen, Anal. Chem., 2009, 81, 5918-5924

[31] S.C. Oppegard, K.H. Nam, J.R. Carr, S.C. Skaalure and T. Eddington, Plos. One, 2009, 4, e6891.

[32] P. Abbyad, P.L. Tharaux, J.L. Martin, C.N. Baroud and A. Alexandrou, Lab. Chip, 2010, 10, 2505-2512.

[33] J.E. Baumgardner and C.M. Otto, Resp. Physiol. Neurobi., 2003, 136, 131-139.

[34] E. Figallo, C. Cannizzaro, S. Gerecht, J.A. Burdick, R. Langer, N. Elvassore and G. Vunjak-Novakovic, Lab. Chip, 2007, 7, 710-719.

[35] R.B. Bird, W.E. Stewart and E.N. Lightfoot, 2001, John Wiley & Sons, 2nd Edition.

[36] A.P. Vollmer, R.F. Probstein, R. Gilbert and T. Thorsen, Lab. Chip, 2005, 5, 1059-1066.

[37] H. Shiku, T. Saito, C.C. Wu, T. Yasukawa, M. Yokoo, H. Abe, T. Matsue, and H. Yamada, Chem. Lett., 2006, 35, 234-235.

[38] T.C. Merkel, V.I. Bondar, K. Nagai, B.D. Freeman and I. Pinnau, J. Polym. Sci. Pol. Phys., 1999, 38, 415-434.

[39] S.A.M. van Stroe-Biezen, A.P.M. Janssen and L.J.J. Janssen, Anal. Chim. Acta, 1993, 280 ,217-222.

[40] G.R. Heyndrickx, R.W. Millard, R.J. McRitchie, P.R. Maroko and S.F. Vatner, J. Clin. Invest., 1975, **56**, 978-985.

[41]C. Depre and S.F. Vatner, Heart Failure Reviews, 2007, **12**, 307-317.

Appendix C

Flow biosensing and sampling in indirect electrochemical detection

Francesco Lamberti[1,2], Camilla Luni[1,2], Alessandro Zambon[1,2], Pier Andrea Serra[3], Monica Giomo[1], and Nicola Elvassore[1,2]

[1]Department of Industrial Engineering, University of Padova, Via Marzolo 9, 35131 Padova, Italy
[2]VIMM—Venetian Institute of Molecular Medicine, Via Orus 2, 35129 Padova, Italy.
[3]Department of Neuroscience, Medical School, University of Sassari, V.le S. Pietro 43/b, 07100 Sassari, Italy

BIOMICROFLUIDIC
Volume 6, 024114 (2012);
doi: 10.1063/1.4705368

C.1 Abstract

Miniaturization in biological analyses has several advantages, such as sample volume reduction and fast response time. The integration of miniaturized biosensors within lab-on-a-chip setups under flow conditions is highly desirable, not only because it simplifies process handling but also because measurements become more robust and operator-independent. In this work, we study the integration of flow amperometric biosensors within a microfluidic platform when analyte concentration is indirectly measured. As a case study, we used a platinum miniaturized glucose biosensor, where glucose is enzymatically converted to H_2O_2 that is oxidized at the electrode. The experimental results produced are strongly coupled to a theoretical analysis of fluid dynamic conditions affecting the electrochemical response of the sensor. We verified that the choice of the inlet flow rate is a critical parameter in flow biosensors, because it affects both glucose and H_2O_2 transport, to and from the electrode. We identify optimal flow rate conditions for accurate sensing at high time resolution. A dimensionless theoretical analysis allows the extension of the results to other sensing systems according to fluid dynamic similarity principles. Furthermore, we developed a microfluidic design that connects a sampling unit to the biosensor, in order to decouple the sampling flow rate from that of the actual measurement.

C.2 Introduction

Miniaturization in biological analyses has several advantages, the most relevant being sample volume reduction, low cost, and relatively fast response time [1]. Furthermore, down-scaling the average dimension of the biosensing device permits to enhance measurement sensitivity exploiting different physical scaling laws [2]. Integrating the analysis step in lab-on-a-chip applications for inflow process monitoring is highly desirable, not only because it simplifies the handling of the process but also because measurements become more robust and operator-independent. Online measurements

can be advantageously coupled with both in vitro experiments and ex vivo. Glucose sensors have been implanted in living tissues, but their use is still limited because of the deterioration of sensor performance and inflammatory response [3]. Therefore, non-invasive glucose monitoring seems the most viable alternative in this field and recent commercial products have been produced for performing both extraction and sensing functions,[4] or for coupling with microdialysis[5,6]. Also chemiluminescence metabolite sensors have been integrated into microfluidic platforms [7], as well as systems based on optical absorbance measurement[8]. In this frame, electrochemical biosensors represent an interesting approach offering the possibility to combine the analytical capability of electrochemical techniques with the specificity of biological recognition processes. The selectivity of these devices can be designed immobilizing a specific biologically active compound such as a cell receptor, an antibody or an enzyme, at the surface of an electrode where it converts the effects of the biological process into a quantitative electric response [9,10]. For online monitoring miniaturized amperometric biosensors are increasingly used [11,12]. Evaluating their performance when used under flow-through conditions requires an analysis of the effect of working conditions such as flow rate, minimum sample volume, sensitivity, limit of detection, and time resolution of the measurement. In fact, in non-flow conditions, once the biosensing device has been set up, the measurement output is completely defined by the intrinsic physical properties of the species involved, such as enzyme kinetics and diffusion coefficients. On the contrary, in flow-through biosensors, fluid dynamic conditions, depending on the inlet flow rate, affect the measurement output. Different regimes can occur due to the relative characteristic times of the physical phenomena overlapping. A comprehensive study on this topic was pursued by Squires et al. for flow-through biosensors that measure the analyte directly [13,14]. However, several biologically interesting compounds, such as glucose, lactate, acetylcholine, and glutamate, are measured by amperometric biosensors with higher accuracy indirectly [15]. In this case, the analyte is converted by specific enzymes into electrochemically detectable components that act as mediators for the measurement [16]. Throughout this work, indirect detection refers to the condition where the actual compound producing the electric signal during the

measurement of the analyte is the mediator. The influence of the flow in indirect measurements has been addressed both in sensor and biosensor electrodes [17–21]. Interestingly, few papers report that increasing the flow rate in indirect enzymatic biosensors the amperometric current decreases[18,21,22]. However, a clear phenomenological explanation have not been properly addressed yet. In this perspective, a rational understanding and the availability of tools that allow to select and realize optimal flow conditions for accurate sensing at high time resolution is of paramount importance for a flexible and cost effective approach in improving the performance of these devices. In this work, we investigate how the electrochemical measurement of an analyte involving the detection of a mediator is affected by flow conditions in a miniaturized biosensor. As for the experimental results, we focus on a glucose biosensor where glucose is amperometrically detected after its enzymatic conversion to H2O2 by glucose oxidase (GOx), according to the following reactions:

$$glucose + O_2 \xrightarrow{GOx} gluconic\ acid + H_2O_2 \quad \text{(C1)}$$

$$H_2O_2 \xrightarrow{electrode} O_2 + 2H^+ + 2e^- \quad \text{(C2)}$$

In this system, the current variation is affected by glucose and peroxide mass transport within the microfluidic channel. The experimental setup serves as a case study within a more general investigation of the behavior of indirect analyte detection. A model-based theoretical analysis allows a generalization of the results and represents a tool for design and optimization of flowthrough biosensing devices. Moreover, biosensor performance can be improved by decoupling sampling and analysis systems whenever a different flow rate is required for optimal sampling and analysis process. Although there are few papers discussing indirect flow biosensing using a decoupled experimental configuration [23–26], we propose an improved design of a flow sampling and biosensing unit easy to incorporate in lab-on-a-chip applications.

C.3 Method

C.3.1 Device description

The biosensor used in this work was produced modifying a previously described procedure [27] and is shown in Fig. 1. As highlighted in the schematic view in Fig. C1(a), the fluid sample enters in the system and passes the reference (R), counter (C), and working (W) electrodes.

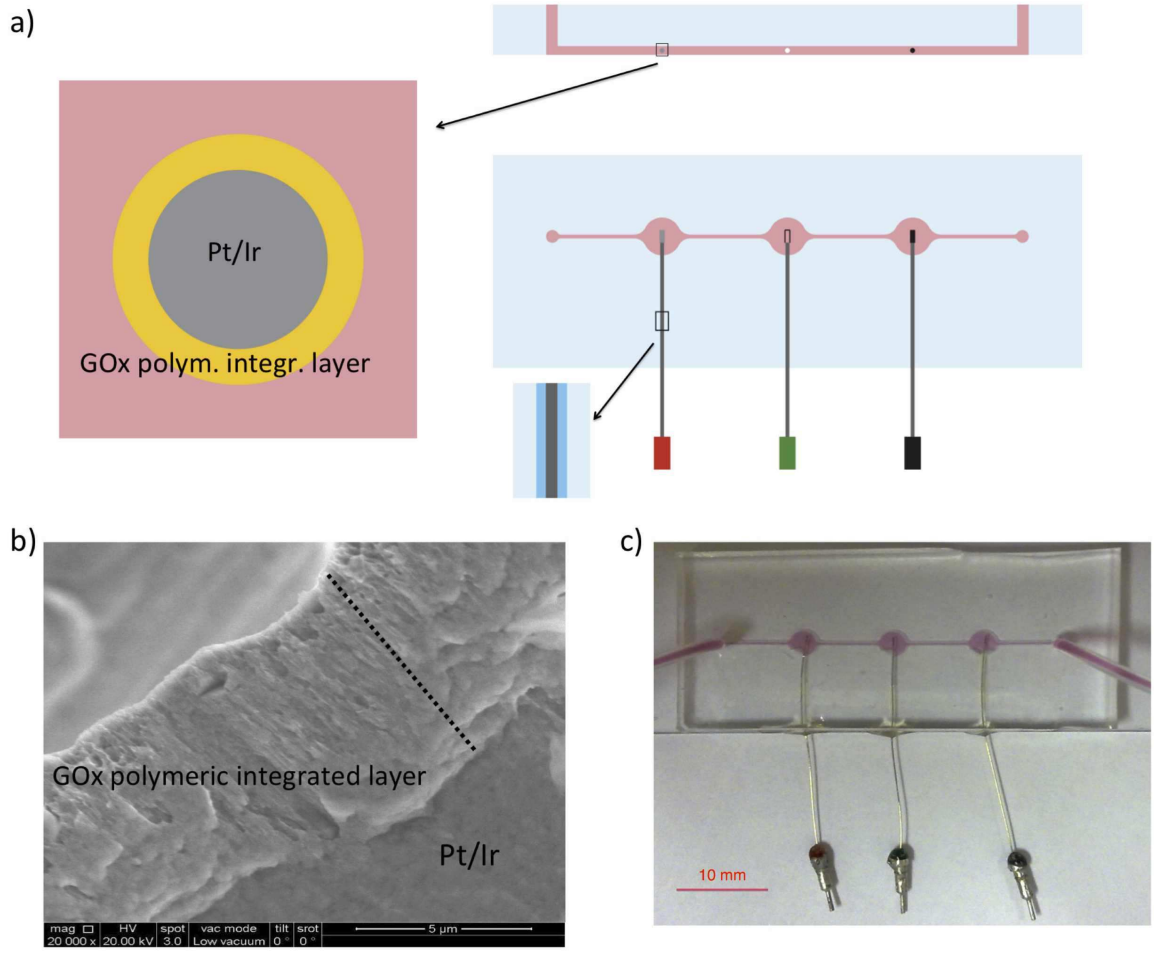

Figure C1: *Microfluidic biosensor. (a) Lateral and top views of the main channel. Working (red), reference (green), and counter (black) electrodes. Enlargements of the transversal and longitudinal sections of the working electrode tip and of the insulated part, not on scale. (b) Scanning electron micrograph of the transversal section of the electrode tip: a GOx polyurethane integrated layer, whose thickness is indicated by the dotted line, coats a Pt/Ir wire. (c) Picture of the microfluidic system schematically described in (a) with pink medium flowing*

The distance between reference and working electrodes is sufficiently small not to affect the measurement, as we tested interchanging electrode positions. The enlargement of the channel section at the electrodes guarantees complete wetting of the sensing tip in case of bubble formation at the walls. The 1-mm long electrode tip, made of Pt/Ir 90/10% and with a diameter of 125 lm, is coated with a porous polymeric layer (polyethylenimine and polyurethane) absorbed with the enzyme glucose oxidase (GOx) from Aspergillus Niger. This GOx-integrated layer was estimated by scanning electron microscopy to be approximately 8 lm thick (Fig. C1(b)). The stability of GOx in this structure was extensively studied by our group [28,29] and others [30]. Glucose is enzymatically converted into H_2O_2 in the porous layer, and the electrochemical oxidation of H_2O_2 at the electrode produces the amperometric current measured. The polymeric layer did not show observable damage due to the production of oxygen and H_2O_2 for the whole duration of the experiments. The biosensor was calibrated under static conditions (Fig. CS1 of the supplementary material[31]) and then used for flow-through measurements.

C.3.2 Microfabrication

C.3.2.1 microfluidic sensing

A single-layer channel (300 lm), containing the biosensors lateral inlets (400 lm), was made using soft lithographic techniques [32,33] (Fig. C1(a)). The silicon substrate was coated with SU8- 2100 (MicroChem Corp., MA,USA) to obtain a thickness of 250 lm. Then, soft bake, exposure, and post-exposure bake followed the coating. The development was achieved in methoxymetacrilate (Sigma-Aldrich, Italy) and further rising with Isopropanol. Polydimethylsiloxane (PDMS, Dow Corning, USA) was used for molding in the ratio 10:1 (base:cure agent) and baked at 353K for 2 hours. The cured PDMS chip was bounded to a borosilicate glass (Vetrotecnica Italy) by plasma treatment (70 W, 30 s). After the wires insertion, the lateral inlets were sealed using UV glue (DYMAX Corp., USA) that was polymerized in situ using a UV lamp for 5 s (DYMAX 3067, USA). A syringe pump (PHD 22/2000 HPSI, Harvard Apparatus, USA) connected to the

chip via 0.02 in. inner diameter Tygon tubing, allowed to change the flow rate. Syringes of 3 – and 5-ml volume (Becton Dickinson, USA) were used to obtain the desired fluid flow.

C.3.2.2 Microfluidic sampling and sensing

To create the loop system, containing flow and control channels [34,35], two molds were prepared. 36 lm of SPR 220-7 (Dow Corning) were spun on a vapor-treated silicon wafer HDMS (Sigma Aldrich). After bake at 363K for 90min and rehydration for 3 h, each mold was exposed at 200 mJ/cm2 (k¼365 nm, OAI 150, USA). 400 lm-wide flow layer channels were obtained by development in agitated MF319 (Dow Corning) and further rinsing with D-water. A hard baking up to 463K with 10 K/h ramp was done to reflow the polymer and obtain round channels. For the control layer, SU8-2100 (Microchem Corporation) was used to make square channels of 100 lm height and 300 lm width. PDMS (10:1 base:cure agent) was spun on the flow mold at 1000 rpm for 90 s to obtain a thin membrane of 80 lm in total. The control mold was covered instead with a thick layer of PDMS and both layers were then baked at 353K for 30min. A further very thin layer of cure agent was painted on the flow mold, and the control chip was then aligned on it. A further baking for 2 h produces irreversible bonding between the two layers. The final chip was bonded via plasma treatment to a borosilicate glass. The valves were activated pressurizing the control channels.

C.3.3 Potentiostatic measurement

Potentiostatic amperometric measurements were performed using a potentiostat/galvanostat (AUTOLAB, PGSTAT 128N EcoChemie, The Netherlands) controlled by NOVA 1.6 Software. The biosensor was used as the working electrode, a Pt wire as the counter electrode and Ag/ AgCl as the pseudo-reference (Fig. C1(a)). The working electrode was biased 0.7V versus the pseudo-reference electrode. Static measurements were performed for calibration in usual electrochemical commercial cells, outside the microfluidic chip. Static calibration was used as a performance check

on the sensor before integration in the microfluidic channel. Solutions used were PBS 1X (Vetrotecnica, Italy), 1mM Dulbecco's Modified Eagle Medium High Glucose (DMEM High Glucose, 4.5 mg/l D-Glucose, Invitrogen, Italy), 5mM Dulbecco's Modified Eagle Medium Glucose free (DMEM Glucose Free, Invitrogen, Italy), and H_2O2 solutions prepared by diluting 80% H_2O_2 (Sigma-Aldrich, Italy) with milliQ water (Millipore, Italy). All solution used were sterile.

C.3.4 Mathematica model

C.3.4.1 Numerical mathematical model

A mathematical model of the steady-state flow biosensing device was developed. The system geometry includes: a microfluidic channel, a cylindrical electrode inserted across the channel, and a porous layer coating the electrode and containing GOx. The 2-dimensional model represents a longitudinal section of the device described. Modeling was carried out breaking the system down into two sub-domains: the microfluidic channel and the porous layer coating the electrode. As for the microfluidic channel, both convective and diffusive transport are described. While in the porous layer coating the electrode, glucose conversion by a homogeneously distributed enzyme is modeled together with diffusion. The velocity field in the microfluidic channel was obtained solving the continuity equation and the equation of motion for an incompressible Newtonian fluid. The concentration fields of H_2O_2 and glucose were obtained in the microfluidic channel and in the porous layer, solving the respective equations of continuity. The effective diffusivities in the porous layer were obtained multiplying their bulk values, $D_{glucose}$; bulk and $D_{H_2O_2,bulk}$ by a factor, ε, accounting for both the porosity and tortuosity of the material. The rate of glucose conversion, catalyzed by GOx in the porous layer, was assumed linear with kinetic parameter k_{GOx}, a good approximation in the glucose concentration range simulated. The electric current, I, produced at the electrode, is given by:

$$I = 2F \int_{S_{el}} F_{H_2O_2,el} dS_{el} \qquad \text{(C3)}$$

where the factor 2 represents the number of electrons involved in the charge transfer at the electrode surface according to Eq. (C2), F is Faraday's constant, $F_{H_2O_2,el}$ is H_2O_2 molar flux at the electrode, and S_{el} is the geometrical electrode surface. In the simulations where a flow containing only H_2O_2 enters the system, the actual current value was obtained multiplying I by a corrective factor, λ. This correction accounts for the observed reduction of current in these conditions, probably due to a net production of O_2 polarizing the electrode. The model was numerically solved by COMSOL MULTIPHYSICS (COMSOL, Inc, Stockholm, Sweden) using the parameter values summarized in Table I. In particular, model parameters ε, k_{GOx}, and λ were determinedby fitting the experimental data. Details on the numerical model are reported in the supplementary material [31].

C.3.4.1 Analytical mathematical model

The model equations for glucose and H2O2 in the porous layer coating the electrode were also solved analytically under steady-state conditions for a simplified geometry, i.e., a flat electrode with the same surface area of the electrode considered in the numerical model. Details of analytical model development are reported in the supplementary material [31]. The fluxes of glucose and H_2O_2 across the surface of the porous layer, $F_{glucose,b/l}$ and $F_{H_2O_2,b/l}$ are related to the Reynolds number, Re, at the entrance of the convective system by

$$F_{glucose,b/l} = \frac{D_{glucose,bulk}(c_{glucose,in} - c_{glucose,b/l})}{H} \alpha Re^{\beta} \quad \text{(C4)}$$

and

$$F_{H_2O_2,b/l} = \frac{D_{H_2O_2,bulk}(c_{H_2O_2,in} - c_{H_2O_2 b/l})}{H} \alpha Re^{\beta} \quad \text{(C5)}$$

where $c_{glucose,in}$ and $c_{H_2O_2,in}$ are glucose and H_2O_2 concentrations at the entrance of the convective system, $c_{glucose,b/l}$ and $c_{H_2O_2 b/l}$at the surface of the porous layer, H is the convective system characteristic length (the channel height in the numerical model), a and b are constants, whose values are determined according to fluid dynamic similarity principles, as explained in the supplementary material [31].

C.3 Results and discussion

C.3.1 Effect of fluid flow

Extending the use of an electrochemical biosensor with indirect detection to flow working conditions, requires the definition of an optimal flow rate. We analyzed the mass transport mechanisms occurring, both experimentally and theoretically. In order to evaluate how fluid dynamic affects the biosensor behavior, a set of experiments was carried out feeding a solution containing H_2O_2. In this way, it is possible to highlight the effect of the flow rate on the direct electrochemical measurement of the solute, without the overlapping kinetics of the intermediate production. Results highlight that at low flow rates the overall process is limited by mass transport through the stagnant layer in the liquid domain surrounding the porous coating. The current increases at increasing flow rates because this diffusive stagnant layer gets thinner (Fig. C2(a)). Then, current tends to a plateau at very high flow rates, when the external mass transport becomes faster and the overall mass transport is only limited by diffusion of species in the porous coating. However, the current variation detected is only approximately 10%, even for large differences in the flow rate, from 10 µl/min to 400 µl /min (Fig. C2(a), inset). This behavior is barely affected by concentration, as verified with a change of one order of magnitude, from 10 to 100mM (Fig. C2(a), inset).

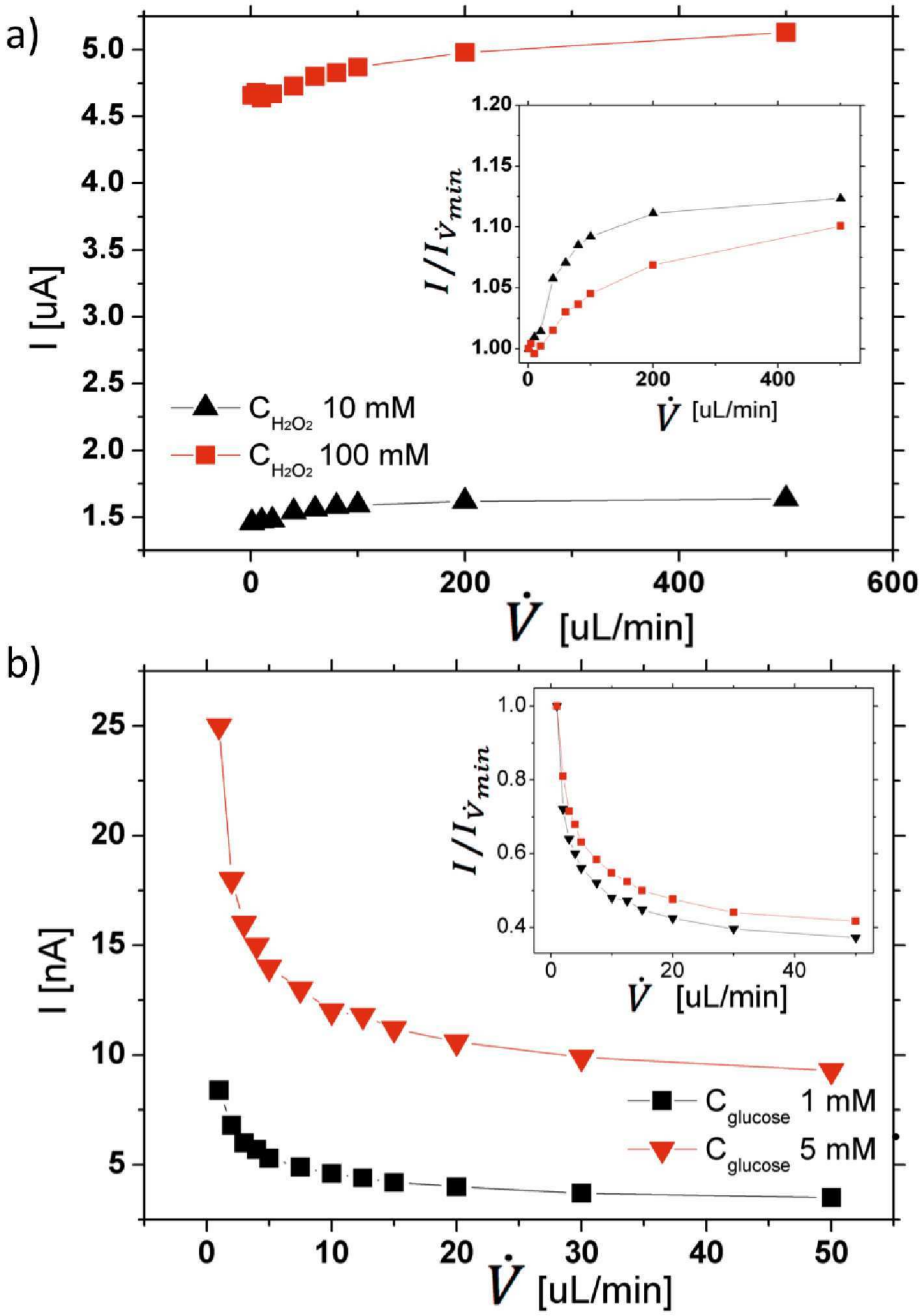

FIG. C2. *Effect of flow rate on (a) hydrogen peroxide and (b) glucose in-flow detection at different concentrations. The current collected at the electrode is plotted as a function of the flow rate. Inset graphs show the current normalized by its value at the minimum flow rate used in the experiments (1 µl/min* $I_{\dot{V}min}$

.Then, we studied the effect of the flow rate for biologically relevant working conditions of the biosensor, i.e., with a glucose solution in the concentration range 1–5mM, entering the system with flow rates of 1–50 µl/min. In this case, the current detected decreases at increasing flow rates (Fig. C2(b)), for both glucose concentrations used (1

and 5mM) confirming literature data.39 In particular, it decreases of about 60% in the flow rate range tested, while the concentration negligibly affects this behavior (Fig. C2(b), inset). These observations show how using an electrochemical biosensor with enzyme-mediated detection under flow conditions requires a careful understanding of the phenomena that come into play, posing the flow rate as a key variable to analyze. These experimental observations for glucose amperometric detection are fully consistent with those reported in literature [18,21,22], whereas H_2O_2 analyses allow the dissection of the contribution of flow rate influence on substrateand mediator detection.

C.3.2 Efficiency and time of response of biosensor

For practical purposes, the effective efficiency, η_{eff}, for an indirect electrochemical biosensor, can be defined by the following expression:

$$\eta_{eff}=\frac{I_{glucose}}{I_{H_2O_2}} \tag{C6}$$

where $I_{glucose}$ and $I_{H_2O_2}$ stand for the current produced when a glucose or a stoichiometric H_2O_2 solution enters the system, respectively. $I_{H_2O_2}$ represents the maximum amount of H2O2 detectable at the electrode if all glucose flowing through the system were converted. Fig. C3(a) shows how the efficiency, calculated according to Eq. (C6), decreases as a function of the flow rate. Furthermore, flow rate also affects the biosensor time of response, which is the time needed to detect a stable current for constant inlet conditions (Fig. CS3 of the supplementary material [31]). The time of response is an important variable for biosensor use because it determines the maximum temporal resolution, i.e., the smallest increment of time between two successive measurements. Fig. C3(b) shows that the time of response is a decreasing function of the flow rate. Thus, in order to have a high-performance online, biosensor an optimal flow rate is required as a trade-off between high efficiency and high time resolution.

C.3.3 Numerical simulation

Experimental data suggest a flow rate-dependent leak of H_2O_2, not oxidizing at the electrode and decreasing the measurement efficiency. We further investigated the physical phenomena occurring within the biosensor by means of a mathematical model. The geometry of the system simulated closely reproduces the experimental setup and is described in Fig. C4(a). Convective flow occurs in bulk medium along the x-direction, while a cylindrical electrode tip is placed across the flow along the z-direction. Glucose is converted into H_2O_2 in the porous layer coating the electrode. Both species move within this layer exclusively by diffusion according to a concentration gradient. Part of the H_2O_2 produced reaches the electrode where it is immediately oxidized, while part of it leaves the porous layer at the external surface and is washed out by the convective flow. Figs. C4(b) and C4(c) illustrate H_2O_2 concentration profiles obtained by the model at two flow rates, 1 and 50 µl/min, respectively. At low flow rates, a concentration gradient develops throughout the channel section (Fig. C4(b)), while at high flow rates, H_2O_2 is rapidly washed-out and its bulk concentration is about null at short distance outside the porous layer (Fig. C4(c)). The results from the numerical model simulations confirm the experimental data presented in Fig. C3(a), and, specifically, show a decreasing efficiency at higher flow rates (Fig. C4(f)). We further investigate this aspect in Fig. C4(g), after calculating two non-dimensional quantities: $Ratio_{glucose}$ and $Ratio_{H_2O_2}$. $Ratio_{glucose}$is defined as the ratio of the total glucose consumed per unit time to the glucose molar flow rate entering the system, according to the following expression:

$$Ratio_{glucose} = \frac{N_{glucose,rx}}{N_{glucose,in}} \quad \text{(C7)}$$

and $Ratio_{H_2O_2}$ are given by the ratio of the H_2O_2 molar flow rate leaving the porous layer towards the bulk to the total H2O2 produced per unit time in the layer, that is

$$Ratio_{H_2O_2} = \frac{N_{H_2O_2,out}}{N_{H_2O_2,rx}} \quad \text{(C8)}$$

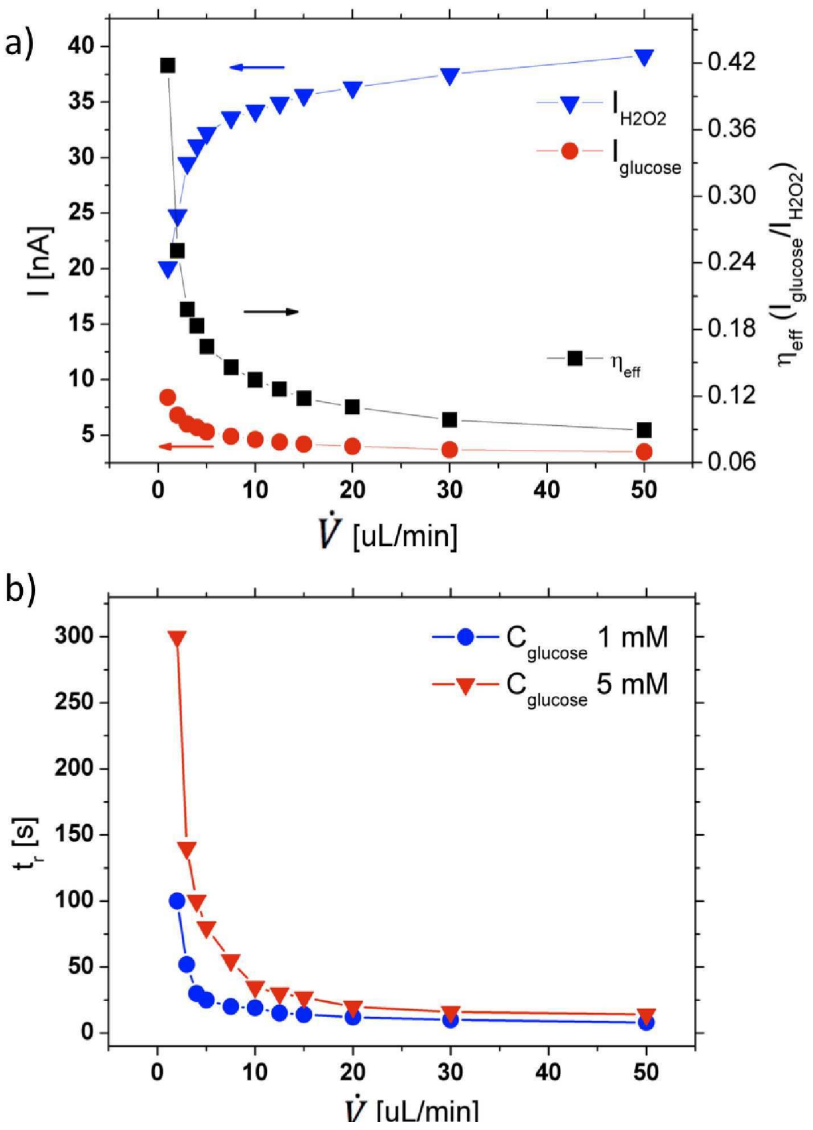

FIG. C3. Effect of flow rate on measurement efficiency and response time of the biosensor. (a) The currents $I_{glucose}$ and $I_{H_2O_2}$ detected when measuring samples with concentrations of 1mM glucose and 1mM H_2O_2, respectively, are plotted as a function of the flow rate. They are used to calculate the efficiency, η_{eff} , defined as the ratio of $I_{glucose}$ to $I_{H_2O_2}$, also shown. (b) Biosensor response time (Fig. CS3 of supplementary material [31]) as a function of flow rate for two different inlet concentrations.

The flow rates in Eqs. (C7) and (C8) are defined in Fig. C4(a). $Ratio_{glucose}$ decreases at increasing volumetric flow rates, because a larger amount of glucose flows through the system without having time to diffuse in the porous layer (Fig. C4(g)). On the contrary, $Ratio_{H_2O_2}$ increases at higher flow rates (Fig. C4(g)), that is, a larger amount of H_2O_2 is washed-out from the porous layer without oxidizing at the electrode, what explains the decrease of measurement efficiency. The numerical model is also able to give H_2O_2 and

glucose concentration profiles in the channel along the r-coordinate highlighted in Fig. C4(b). H_2O_2 concentration shows a peak inside the porous layer coating the electrode (Fig. C4(d)), whose position depends on the relative importance of the two molar flow rates, $N_{H_2O_2,b/l}$ and $N_{H_2O_2,el}$, defined in Fig. C4(a). On the contrary, glucose concentration along the same direction shows a monotonic profile, as all glucose entering the layer is converted to H_2O_2 (Fig. C4(e)). The GOx-catalyzed reaction occurs throughout the whole thickness of the porous layer in our system, as demonstrated by the only slight decrease of glucose concentration in the layer (Fig. C4(e)). This is confirmed by the high rate of glucose diffusion in the layer compared to the reaction rate, about ten times larger. Taken together both experimental and computational observations show that glucose efficiency reduction at higher flow rates is related to the ratio between H_2O_2 wash-out and discharge at the electrode. In order to extend this result to a wider class of biosensors, we derived a simple analytical model as a function of dimensionless variables taking into account all the transport phenomena involved.

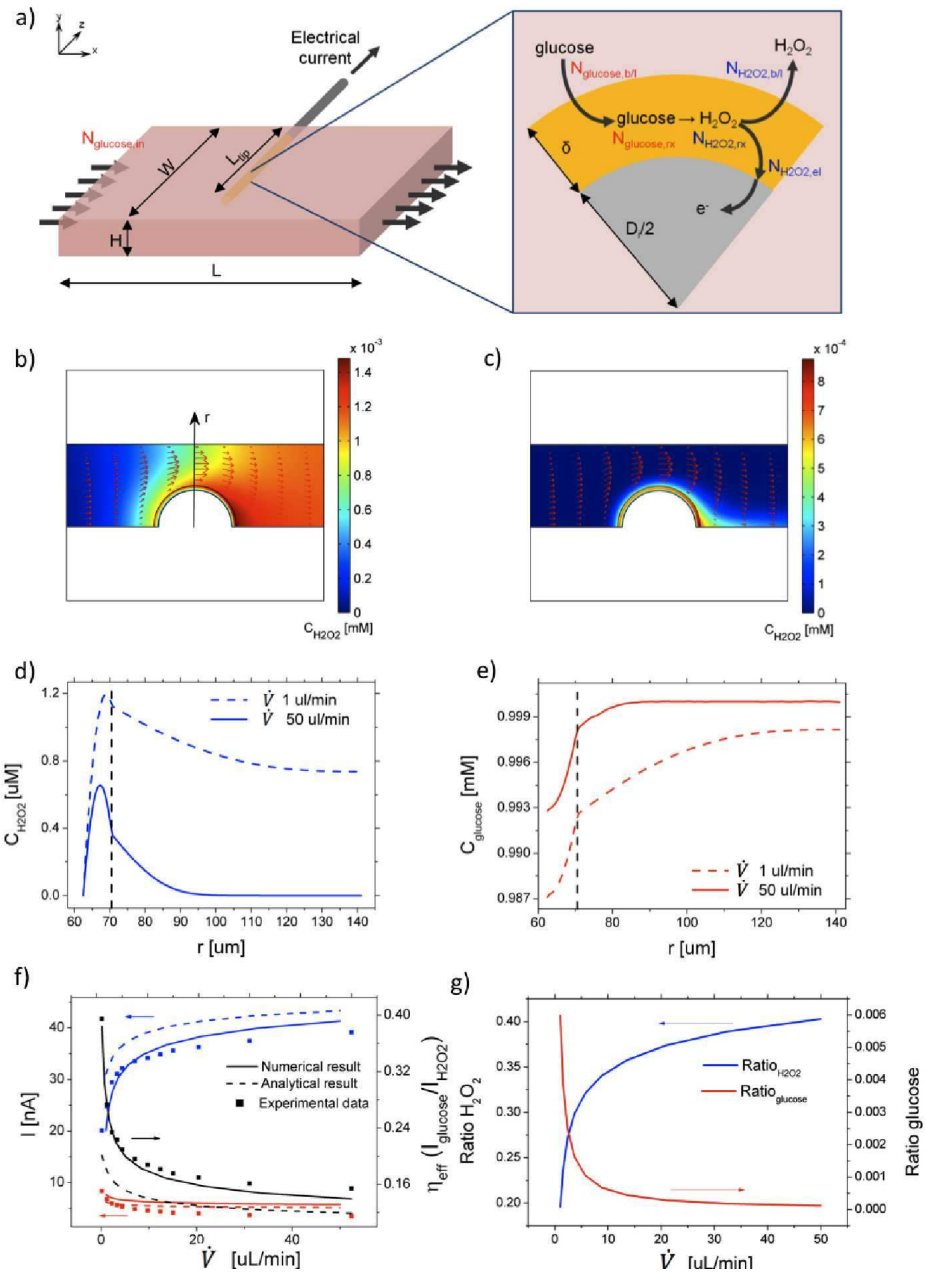

FIG. C4. *Results obtained from the simulations of the numerical model. (a) Schematic representation of the model geometry. System size, coordinate system, and molar flow rates of glucose and H_2O_2 are also indicated. (b) and (c) Concentration profile of H_2O_2 in the channel and in the porous layer coating the electrode surface when a 1-mM solution of glucose is fed to the system at two flow rates: 1 µl /min (b) and 50 µl/min (c). Red arrows represent the velocity field. (d) and (e) Concentration profiles of H_2O_2 and glucose along the r-axis indicated in (b), obtained under the same conditions of (b) and (c). The black dashed line indicates the edge of the porous layer coating the electrode. (f) Comparison of the electric current discharged at the electrode as a function of the flow rate obtained experimentally and by the numerical and analytical models. Red lines refer to an inlet of 1-mM glucose solution, blue lines to a 1-mM H2O2 solution. Efficiency, η_{eff}, given by the ratio of the two currents, is displayed in black. The comparison is qualitative because geometries are not identical in the three cases, as discussed in the main text. (g) $Ratio_{H_2O_2}$ and $Ratio_{glucose}$, defined in Eqs. (C7) and (C8), are shown as a function of the flow rate*

C.3.4 Analytical results

We analytically solved the mathematical model in the porous layer for the simplified geometry previously described, to obtain a rational insight into the experimental data. The resulting efficiency, g, given by the ratio of the current produced feeding a glucose solution to that produced feeding a stoichiometric H_2O_2 solution, is analytically expressed as

$$\eta = \frac{D_{glucose,bulk}}{D_{H_2O_2,bulk}} \left[1 - \frac{1}{cosh\Phi + \frac{R_g \Phi}{\alpha Re^{\beta}} sinh\Phi} \right], \quad \text{(C9)}$$

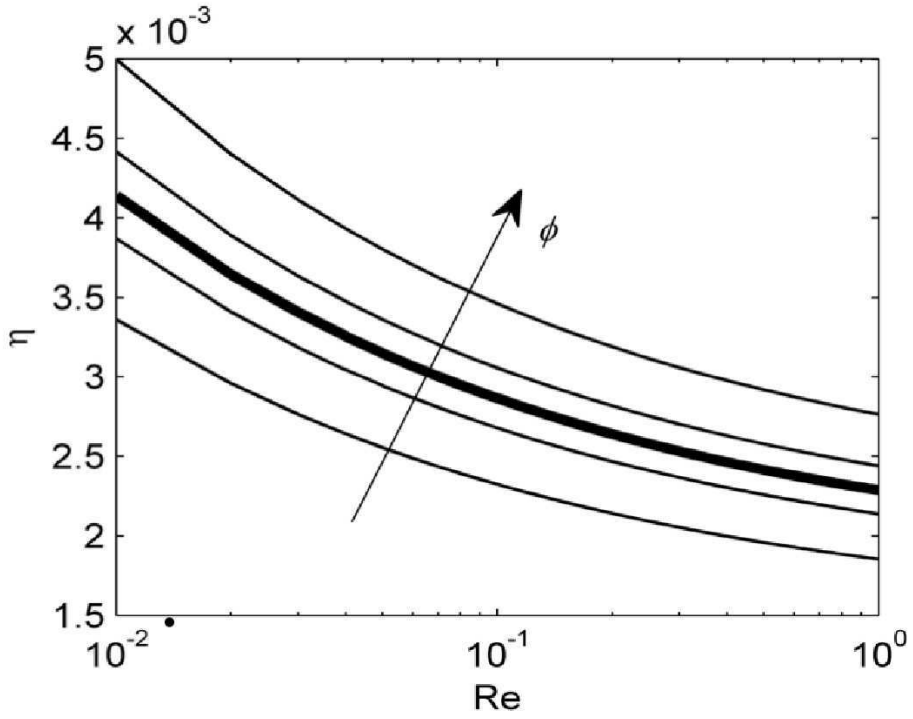

FIG. C5. *Dimensionless results of biosensor efficiency, η. Efficiency is plotted as a function of Reynolds number, according to Eq. (9), within the range used in the experiments. Curves are parametric in Thiele's modulus, in the range ±10% of the experimental Thiele's modulus, shown by the thicker line.*

where $R_g = \varepsilon\, H/\delta$ is a dimensionless geometric ratio, $\Phi = \delta\sqrt{k_{GOx}/(\varepsilon\, D_{glucose,bulk})}$ is a Thiele's modulus. All other variables are defined in Fig. C4(a) and Sec. II. η is a theoretical efficiency and neglects the reduction of current occurring when feeding an H_2O_2 solution. Thus, it is related to η_{eff} by the following expression: $\eta = \eta_{eff}\lambda$. Expression (C9) shows that, once defined geometry and physical properties of the

system, the efficiency only depends on Reynolds number, Re, which is proportional to the volumetric flow rate. For Re →0, the efficiency η tends to its maximum, equal to the ratio of the bulk diffusivities, $D_{glucose,bulk}/D_{H_2O_2,bulk}$, always less than one because of the relative size of the two species. Keeping constant the diffusivity and the geometric ratios, we studied the dependence of the efficiency from Re and Thiele's modulus (Fig. C5). g is a decreasing function of Re, and this further confirms the experimental trend. A comparison between experimental, numerical, and analytical results is presented in Fig. C4(f). The slight discrepancies are due to the increasingly simplified geometry between the three systems. However, the shape of the profiles is confirmed in all cases. Thiele's modulus quantifies the ratio of the reaction rate to the diffusion rate in the porous layer. When glucose conversion to H_2O_2 is fast in comparison with the mass transfer rate in the layer (high Φ), efficiency increases, because glucose concentration gradient through the layer is larger in these conditions, and consequently the diffusive flow of glucose into the layer is greater. It is worth to highlight that Eq. (C9) can be easily extended to different enzymatic biosensors by changing the intrinsic properties of the substances involved. Although it is an approximated solution of a more complex system, it can be used to properly analyse the effect of fluid dynamics on substrate detection assisting the identification of optimal operative conditions.

C.3.5 Decoupling system

The previous analysis highlighted the importance to control the volumetric flow rate during biosensor use. For this reason, we developed a new design for performing biosensing measurements that decouples the flow rate used for the measurement from the sampling flow rate. The new system includes a loop filled offline with the sample at an independent flow rate respect to that in the main channel (Fig. C6(a)). The loop is connected to the main inlet through a valve system and can be connected/disconnected (on/off) when requested (Fig. CS4 of the supplementary material [31]). The advantage of this design is to fill the loop at high flow rates, when it is switched off during sampling,

and to have the sample entering near the working electrode at a low independent flow rate when it is switched on.

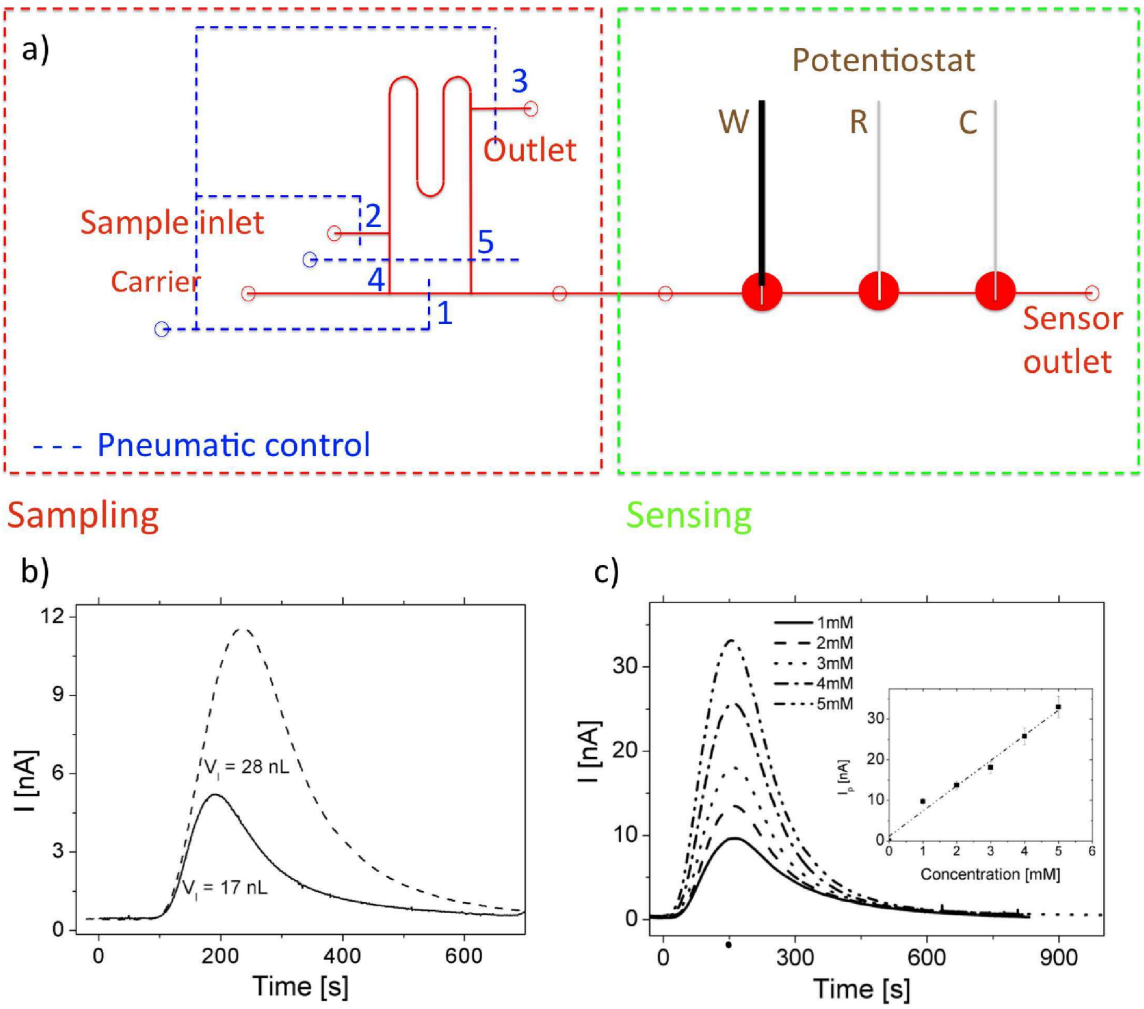

FIG. C6. *Sampling and sensing units integration. (a) Schematic view of the entire system. Loop loading: open 1, 2, 3; close 4, 5. Sample analysis: open 1, 2, 3; close 4, 5. (b) Amperometric measurement for two loop volumes, V_l. Sample glucose concentration is 2mM and flow rate is 10 µl/min. (c) Amperometric measurement for a 28-nl loop at different glucose concentrations in the range 1-5 mM. Flow rate is 10 µl/min. The inset shows the dependence of the peak current, I_p, from glucose concentration. Squares represent experimental data (error bars indicate standard deviations), and the dashed line the linear fitting regression.*

As an example, in this work, a sensing flow rate of 10 µl/min was used to obtain a response time of less than 1min (Fig. C3). Instead of having a plateau in the current detected, a peak shape response is obtained because of the finite volume of the loop (Figs. C6(b) and C6(c)). Larger loops produce higher peaks of current, as shown in Fig.

C6(b) for two different loop volumes (17 and 28 nl). Depending on the sample amount available and the temporal resolution required, the loop volume should be chosen to increase biosensor sensitivity, which is 6.22 nA/mM for the 28-nl loop. The peak maximum of the current curve is taken as the measurement value of glucose concentration. We verified that this measure is proportional to glucose concentration in the sample for a fixed loop volume and thus represents a reliable measurement (Fig. C6(c)). The response time at these conditions is about 100 s (Fig. C6(c)). The biosensor works under highly controlled conditions, measurements are very repeatable, and the linearity of the response is independent from the loop volume (Fig. CS5 of the supplementary material [31]). The detection limit is 0.18mM for the 28-nl loop, which is very low compared to other electrochemical biosensors in the literature [40]. Instead, electrochemical sensors for H_2O_2 detection, have a lower limit, in the range 2–15 μM [41,42].

C.4 Conclusion

We have studied the effect of convective flow in the indirect amperometric detection of an analyte. The experimental results were obtained for the case study of a glucose miniaturized biosensor. The proposed model-based theoretical analysis gives generality to these results. The outcome shows that the fluid flow rate plays a significant role in the performance of the biosensor. In particular, for high-time resolution and high-efficiency measurements, the choice of flow rate requires optimization. The good quantitative agreement between experimental data and numerical predictions shows that the mathematical model can be advantageously used to define the more suitable operating conditions for online indirect detection. All together these results show that with flow conditions the mediator wash-out can be a critical point in all electrochemical indirect measurements. We also developed a lab-on-a-chip application for integrated sampling and biosensing that decouples the two flow rates allowing their independent control. This offers a reliable and robust method of detection that can be easily incorporated in biological experiments for online in-flow measurements.

Acknoledgments

This research was supported by University of Padova and by the Italian Ministry of Research.

C.5 Literature cited

[1] K. Liu, R. Wu, Y. Chuang, H. Khoo, S. Huang, and F. Tseng, "Microfluidic systems for biosensing," Sensors 10, 6623–6661 (2010).

[2] E. Verpoorte, "Microfluidic chips for clinical and forensic analysis," Electrophoresis 23, 677–712 (2002).

[3] M. Frost and M. Meyerhoff, "In vivo chemical sensors: Tackling biocompatibility," Anal. Chem. 78, 7370–7377 (2006).

[4] M. Tierney, H. Kim, M. Burns, J. Tamada, and R. Potts, "Electroanalysis of glucose in transcutaneously extracted samples," Electroanalysis 12, 666–671 (2000).

[5] R. Rhemrev-Boom, R. Tiessen, A. Jonker, K. Venema, P. Vadgama, and J. Korf, "A lightweight measuring device for the continuous in vivo monitoring of glucose by means of ultraslow microdialysis in combination with a miniaturised flowthrough biosensor," Clin. Chim. Acta 316, 1–10 (2002).

[6]A. Maran, C. Crepaldi, A. Avogaro, S. Catuogno, A. Burlina, A. Poscia, and A. Tiengo, "Continuous glucose monitoring in conditions other than diabetes," iabetes/Metab.Res. Rev. 20, S50–S55 (2004).

[7]Y. Lv, Z. Zhang, and F. Chen, "Chemiluminescence microfluidic system sensor on a chip for determination of glucose in human serum with immobilized reagents," Talanta 59, 571–576 (2003).

[8]V. Srinivasan, V. Pamula, M. Pollack, and R. Fair, "A digital microfluidic biosensor for multianalyte detection," in IEEE The Sixteenth Annual International Conference on Micro Electro Mechanical Systems, 2003. MEMS-03 Kyoto (IEEE, 2003), pp. 327–330.

[9]G. Harwood and C. Pouton, "Amperometric enzyme biosensors for the analysis of drugs and metabolites," Adv. Drug Delivery Rev. 18, 163–191 (1996).

[10] S. Borgmann, A. Schulte, S. Neugebauer, and W. Schuhmann, "Amperometric biosensors," Adv. Electrochem. Sci. Eng. 1–83 (2012).

[11] J. Wang, “Amperometric biosensors for clinical and therapeutic drug monitoring: A review,” J. Pharm. Biomed. Anal. 19, 47–53 (1999).

[12] E. Zilkha, T. Obrenovitch, A. Koshy, H. Kusakabe, and H. Bennetto, “Extracellular glutamate: On-line monitoring using microdialysis coupled to enzyme-amperometric analysis,” J. Neurosci. Methods 60, 1–9 (1995).

[13] T. Squires and S. Quake, “Microfluidics: Fluid physics at the nanoliter scale,” Rev. Mod. 77, 977 (2005).

[14] T. Squires, R. Messinger, and S. Manalis, “Making it stick: Convection, reaction and diffusion in surface-based biosensors,” Nature Biotechnol. 26, 417–426 (2008).

[15] F. Lamberti, M. Giomo, and N. Elvassore, Carbon Nanotubes: Growth and Applications, Electrochemical Biosensing with Carbon Nanotubes, edited by M. Naraghi (Intech, 2011).

[16] P. Pantano and W. Kuhr, “Enzyme-modified microelectrodes for in vivo neurochemical measurements,” Electroanalysis 7, 405–416 (1995).

[17] W. Breen, J. Cassidy, and M. Lyons, “Theoretical study of permselective layers on amperometric electrodes in flowing streams,” Anal. Chem. 63, 2263–2268 (1991).

[18] F. Palmisano, D. Centonze, and P. Zambonin, “An in situ electrosynthesized amperometric biosensor based on lactate oxidase immobilized in a poly-o-phenylenediamine film: Determination of lactate in serum by flow injection analysis,” Biosens. Bioelectron. 9, 471–479 (1994).

[19] J. Cooper and R. Compton, “Channel electrodesa review,” Electroanalysis 10, 141–155 (1998).

[20]N. P. Rodrigues, Y. Sakai, and T. Fujii, “Cell-based microfluidic biochip for the electrochemical real-time monitoring of glucose and oxygen,” Sens. Actuators B 132, 608–613 (2008).

[21] O. Frey, S. Talaei, P. van der Wal, M. Koudelka-Hep, and N. de Rooij, “Continuous-flow multi-analyte biosensor cartridge with controllable linear response range,” Lab Chip 10, 2226–2234 (2010).

[22]M. Hashimoto, S. Upadhyay, and H. Suzuki, "Dependence of the response of an amperometric biosensor formed in a micro flow channel on structural and conditional parameters," Biosens. Bioelectron. 21, 2224–2231 (2006).

[23]R. Appelqvist, G. Markovarga, L. Gorton, A. Torstensson, and G. Johansson, "Enzymatic determination of glucose in a flow system by catalytic-oxidation of the nicotinamide coenzime at a modified electrode," Anal. Chim. Acta 169, 237–247 (1985).

[24] Q. J. Chi and S. J. Dong, "Flow-injection analysis of glucose at an amperometric glucose sensor-based on electrochemical codeposition of pallaium and glucose-oxidase on a glassy-carbon electrode," Anal. Chim. Acta 278, 17–23 (1993).

[25]F. Mizutani and S. Yabuki, "Flow injection analysis for glucose using an amperometric enzyme electrode based on lipidmodified glucose oxidase as the detector," Biosens. Bioelectron. 9, 411–414 (1994).

[26] C. Huang, Y. Chen, C. Wang, T. Chou, and G. Lee, "Integrated microfluidic systems for automatic glucose sensing and insulin injection," Sens. Actuators B 122, 461–468 (2007).

[27] P. A. Serra, G. Rocchitta, G. Bazzu, A. Manca, G. M. Puggioni, J. P. Lowry, and R. D. O'Neill, "Design and construction of a low cost single-supply embedded telemetry system for amperometric biosensor applications," Sens. Actuators B 122, 118–126 (2007).

[28] G. Calia, G. Rocchitta, R. Migheli, G. Puggioni, Y. Spissu, G. Bazzu, V. Mazzarello, J. Lowry, R. ONeill, M. Desole et al., "Biotelemetric monitoring of brain neurochemistry in conscious rats using microsensors and biosensors," Sensors 9, 2511–2523 (2009).

[29] P. Serra, G. Puggioni, G. Bazzu, G. Calia, R. Migheli, and G. Rocchitta, Design and Construction of a Distributed Sensor NET for Biotelemetric Monitoring of Brain Energetic Metabolism Using Microsensors and Biosensors (InTech, 2010).

[30] O. Schuvailo, O. Soldatkin, A. Lefebvre, R. Cespuglio, and A. Soldatkin, "Highly selective microbiosensors for in vivo measurement of glucose, lactate and glutamate," Anal. Chim. Acta 573, 110–116 (2006).

[31] See the supplementary material at http://dx.doi.org/10.1063/1.4705368 for supporting text and figures.

[32] Y. N. Xia and G. M. Whitesides, “Soft lithography,” Angew. Chem., Int. Ed. 37, 551–575 (1998).

[33] J. McDonald and G. Whitesides, “Poly (dimethylsiloxane) as a material for fabricating microfluidic devices,” Acc. Chem. Res. 35, 491–499 (2002).

[34] M. Unger, H. Chou, T. Thorsen, A. Scherer, and S. Quake, “Monolithic microfabricated valves and pumps by multilayer soft lithography,” Science 288, 113–116 (2000).

[35] H. Chou, M. Unger, and S. Quake, “A microfabricated rotary pump,” Biomed. Microdevices 3, 323–330 (2001).

[36] Handbook of Chemistry and Physics, edited by R. C. Weast, 53rd ed. (The Chemical Rubber Publishing, 1972).

[37] E. L. Cussler, Diffusion Mass Transfer in Fluid Systems (Cambridge University Press, 1984).

[38] S. Van Stroe-Biezen, F. Everaerts, L. Janssen, and R. Tacken, “Diffusion coefficients of oxygen, hydrogen peroxide and glucose in a hydrogel,” Anal. Chim. Acta 273, 553–560 (1993).

[39] P. Nien, P. Chen, C. Hsu, and K. Ho, “On-chip glucose biosensor based on enzyme entrapment with pre-reaction to lower interference in a flow injection system,” Sens. Actuators B 157, 64–71 (2011).

[40]M. Rahman, P. Kumar, D. Park, and Y. Shim, “Electrochemical sensors based on organic conjugated polymers,” Sensors 8, 118–141 (2008).

[41] P. Miller, S. Gittard, T. Edwards, D. Lopez, X. Xiao, D. Wheeler, N. Monteiro-Riviere, S. Brozik, R. Polsky, and R. Narayan, “Integrated carbon fiber electrodes within hollow polymer microneedles for transdermal electrochemical sensing,” Biomicrofluidics 5, 013415 (2011).

[42] J. Yan, V. Pedrosa, J. Enomoto, A. Simonian, and A. Revzin, “Electrochemical biosensors for on-chip detection of oxidative stress from immune cells,” Biomicrofluidics 5, 032008 (2011).

C.6 Supplentary information

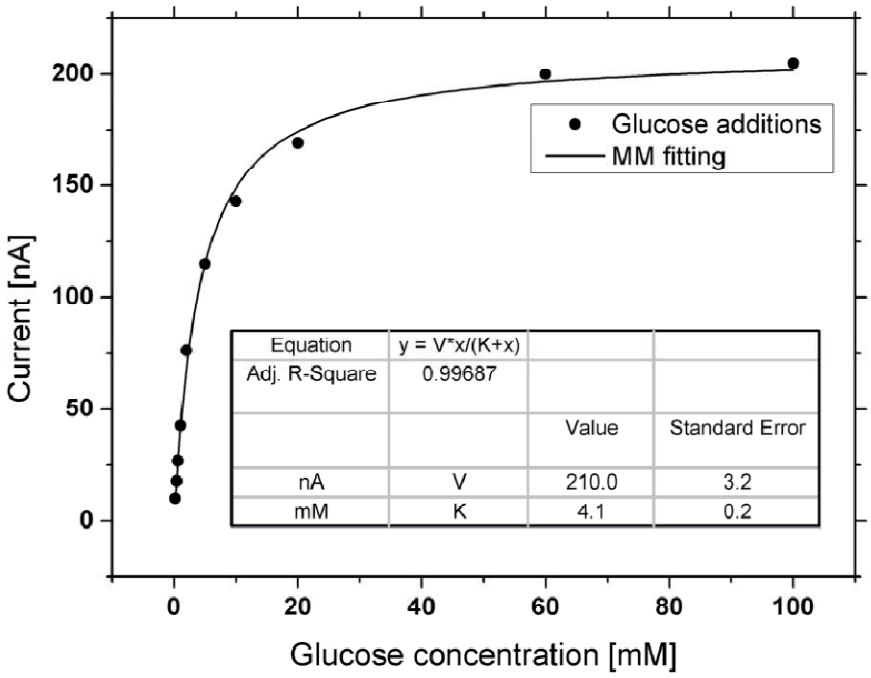

Figure CS1. *Biosensor static calibration. Current is plotted as a function of glucose concentration in the sample. Experimental data were fitted by Michaelis-Menten kinetics, whose V and K parameter values are given in the inset table.*

C.6.1 Dynamic similarity between numerical and analytical models

Many fluid dynamic conditions were simulated by the numerical model fixing different Reynolds numbers, Re, at the inlet of the system, in the range 10^{-1}-10^{1}. The corresponding average mass transport coefficient, $k_{c,glucose}$, between bulk and the porous layer coating the electrode was then calculated by the following expression:

$$k_{c,glucose} = \frac{\bar{F}_{glucose,b/l}}{c_{glucose,in} - c_{glucose,b/l}} \quad \text{(CS1)}$$

Where $\bar{F}_{glucose,b/l}$ is the average flux of glucose entering the porous layer at steady-state, and the denominator represents glucose concentration change between bulk and interface. Knowing $k_{c,glucose}$for the system, Sherwood number, Sh, was calculated according to its definition:

$$Sh = \frac{k_{c,glucose} H}{D_{glucose,bulk}} \qquad \text{(CS2)}$$

From fluid dynamic similarity principles (considering that Schmidt number is a constant for the system under consideration), Sh is related to Re by:

$$Sh = \square Re^{\beta} \qquad \text{(CS3)}$$

where α and β are constant parameters determined by the linear regression shown in Figure CS2. The results of the analytical model can be related to those of the numerical model assuming fluid dynamic similarity, once the derived values of α and β are substituted in the formulas (C3) and (C4) of the main text.

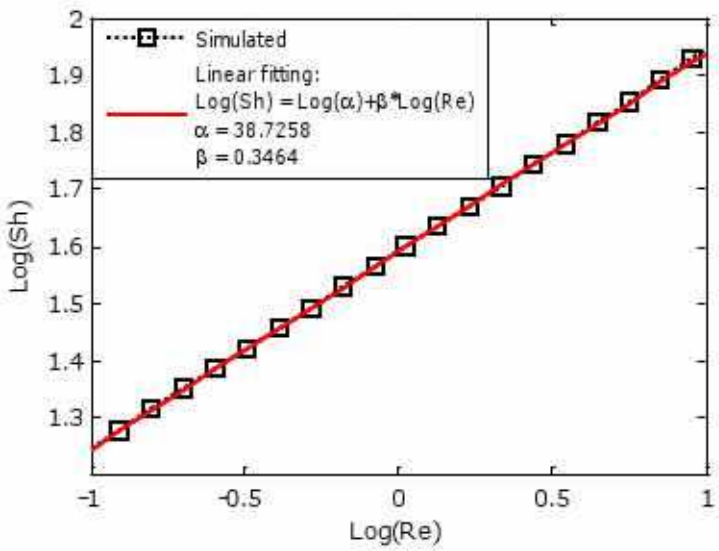

Figure CS2. *Relationship between Sh and Re obtained by the numerical model. A linear regression was performed to obtain and parameters, specific for the fluid dynamic conditions described by the numerical model.* □□

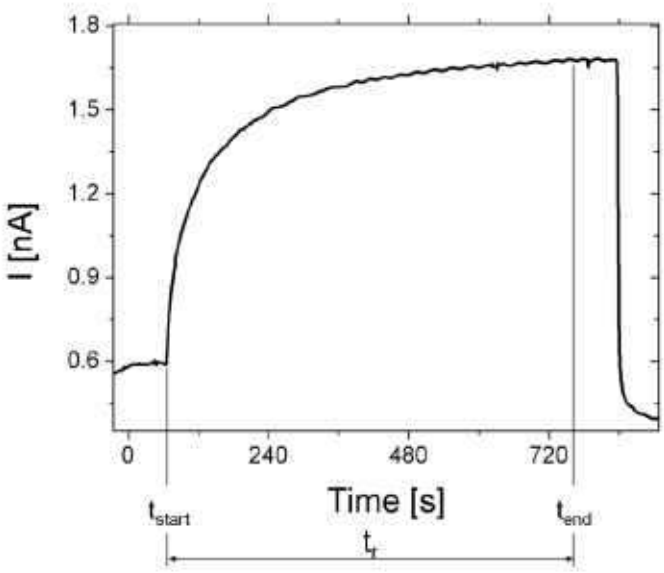

Figure CS3. *Example of current temporal profile measured with the biosensor. Glucose concentration is 3 mM and flow rate 0.025 uL/min. Biosensor response time, tr, is defined as shown, where tend represents the time point when current reaches a plateau (less than 1 % variation), and tstart the time point when the current starts to increase, i.e. the sample has reached the working electrode.*

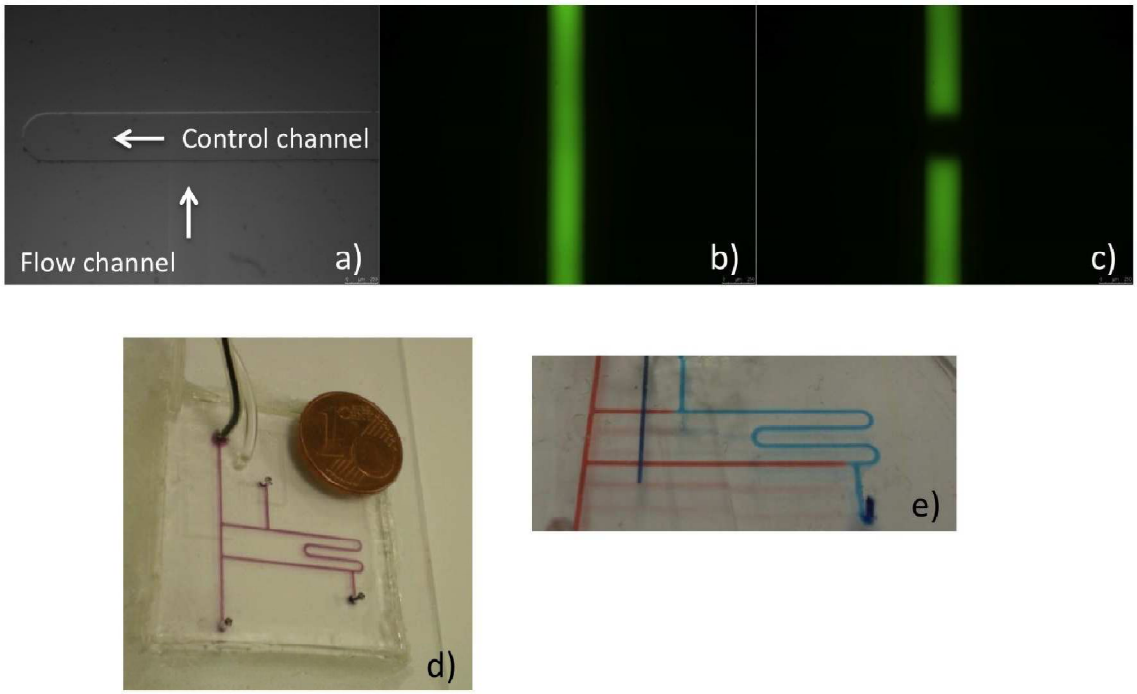

Figure CS4. *Loop configuration. (a-c) Functioning of the pneumatic control of the valves: the flow channel can be closed by pressurizing the control channel. d) Size of the loop system. e) Snapshot immediately after filling the loop: sample fluid is shown in light blue, carrier fluid in red, the pressurized control channel separating the carrier fluid from the loop in dark blue.*

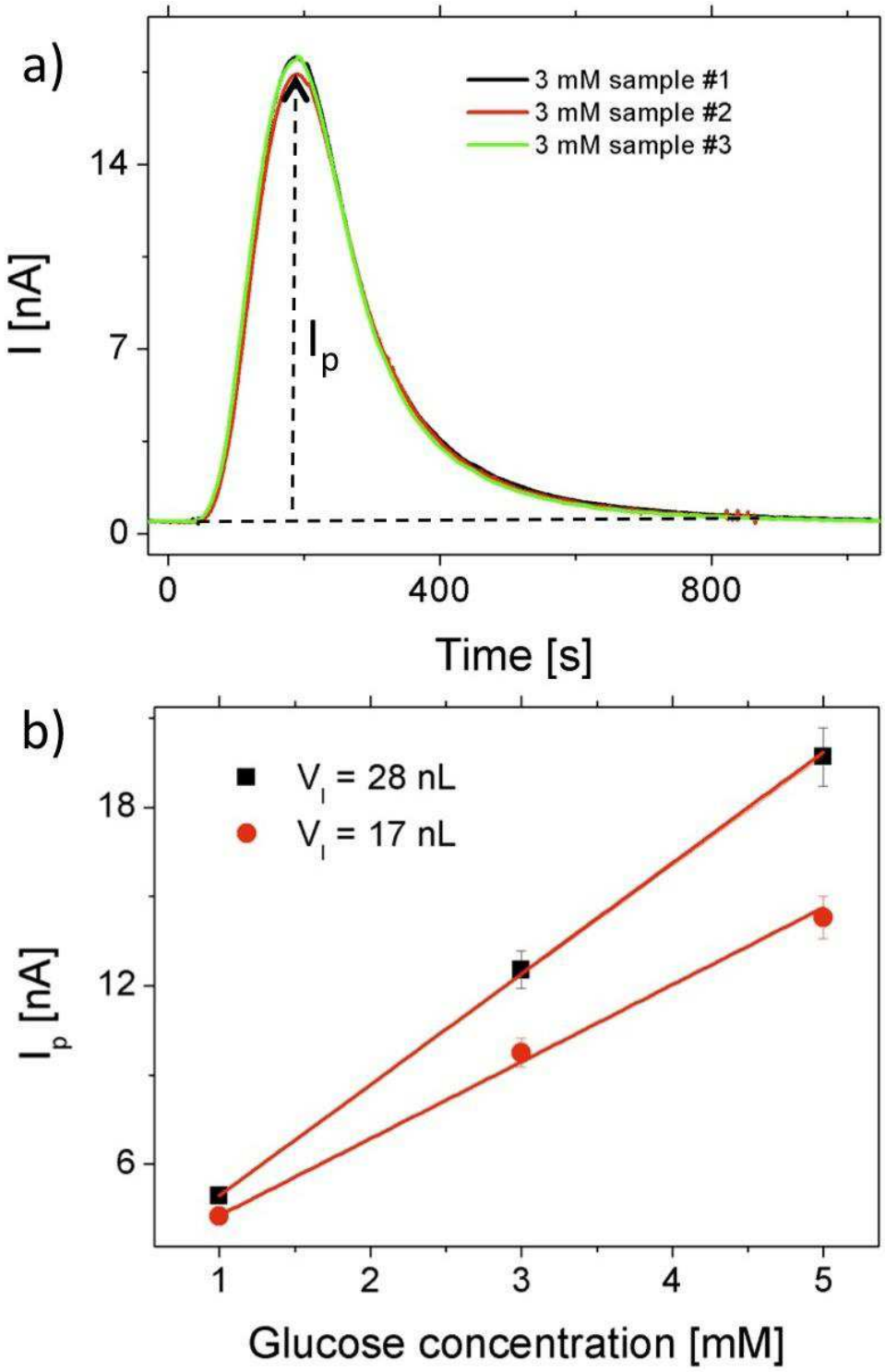

Figure CS5. *Consistency of the biosensor performance. a) Temporal profile of the current measured when the sample collected in the loop is analyzed at a flow rate of 10 uL/min Three repetitions were performed to check the reproducibility of the measurement. The maximum current deviation between the three repeated measurements is less than 5%. b) Peak current (as indicated in a)) is plotted as a function of glucose concentration in the sample to check the linearity of the response for the two loop volumes specified in the legend.*

C.6.2 Extended methods

C.6.2.1 Numerical Model.

A steady-state model was developed to theoretically investigate the physical phenomena involved in the glucose sensor performance. The system geometry includes: a micro-fluidic channel along the x-axis of length L, whose rectangular section has dimensions H and W, in y and z directions respectively; a cylindrical electrode of diameter D_i inserted across the channel in z direction, whose active length is L_{tip} (the non-active length represents the insulation-coated part of the electrode); a porous layer of thickness δ coating the electrode and containing the glucoxidase.

The 2-dimensional model developed reproduces the xy section of the system described. It includes two sub-domains: the fluid inside the micro-fluidic channel, and the fluid in the porous layer coating the electrode. Because of the symmetrical geometry of the system, half of the channel was simulated.

The velocity field in the micro-fluidic channel was obtained solving the continuity equation for an incompressible fluid:

$$\nabla \cdot v = 0, \qquad \text{(CS4)}$$

and the equation of motion for an incompressible Newtonian fluid:

$$-\nabla p + \mu \nabla v + \rho g = 0, \qquad \text{(CS5)}$$

where v is the velocity vector, p is the pressure, μ the dynamic viscosity, ρ the mass density, and g the gravitational acceleration. A parabolic velocity profile was defined at the inlet of the channel, and non-slippery boundary conditions were set on the channel walls and at the porous layer surface.

The concentration fields of H_2O_2 and glucose were obtained in the micro-fluidic channel and in the porous layer solving the respective equations of continuity:

$$\nabla(-D_j \nabla c_j + c_j v) = R , \qquad \text{(CS6)}$$

where j represents either H_2O_2 or glucose, D_j is the diffusivity of the species j , $_j c$ its concentration, and R_j the chemical reaction rate of production of H_2O_2 or of consumption of glucose. The diffusivities in the porous layer are obtained multiplying their bulk values by a factor,ε , accounting for the effective porosity of the layer. The reaction rate between glucose and glucoxidase, occurring only in the porous layer, was assumed linear with

kinetic parameter k_{GOx}, a good approximation in the glucose concentration range simulated (below 1 mM) according to Figure S1. The boundary conditions were set to zeros-flux across the walls of the channel for both H_2O_2 and glucose, and at the electrode surface only for glucose, and zero concentration for H_2O_2 at the electrode surface, where the release of electrons is much faster than the rate of H_2O_2 production. The electric current, I, produced at the electrode was calculated as follows:

$$I = \cdot 2F \cdot \int_{S_{el}} F_{H2O2}\, dS_{el}, \qquad \text{(CS7)}$$

where F is Faraday's constant, F_{H2O2} is H_2O_2 flux at the electrode, and S_{el} is the electrode surface. The factor 2 in (CS7) accounts for stoichiometry, as 1 mole of H_2O_2 produces 2 moles of electrons, according to expression (1). In the simulations where a flow rate containing only H_2O_2 is fed to the system, the effective current value was obtained multiplying I by an efficiency factor, λ, determined by comparison with the experimental data.

Two non-dimensional quantities, $Ratio_{H2O2}$ and $Ratio_{glucose}$, were calculated for analysis purposes: $Ratio_{H2O2}$ represents the ratio between the H_2O_2 molar flow rate leaving the porous layer without being discharged and the total H_2O_2 produced per unit time in the layer; $Ratio_{glucose}$ is defined as the ratio between the total glucose consumed per unit time and the glucose flow rate entering the system.

The model was implemented in COMSOL MULTIPHYSICS V3.4 (COMSOL, Inc, Stockholm, Sweden). The Eq. (CS4), (CS5), and (CS6) were solved to determine the velocity and the concentration fields within the system, using the parameter values summarized in Table CI. A relative tolerance of 10^{-6} was used for the solution. Coarsening and refining the mesh space grid ensured that the results were independent of the spatial discretization. Furthermore, the match of molar flow balances of H_2O_2 and glucose were checked in each simulation to guarantee discrepancies of less than 1%.

C.6.2.2 Analytical Model.

The analytical model was derived applying the equations of continuity for glucose and hydrogen peroxide within the GOx-integrated layer. The following assumptions were taken:

- steady-state;

- constant diffusivities for glucose and H_2O_2;
- incompressibility of the fluid;
- no convection (only diffusion takes place within the porous layer);
- flat electrode, covered with the porous layer having thickness δ in the y direction, and having length and width much larger than thickness.

The resulting equation system is:

$$\begin{cases} -D_{glucose,layer}\dfrac{d^2c_{glucose}}{dy^2} = -k_{GOx}c_{glucose} \\ -D_{H_2O_2,layer}\dfrac{d^2c_{H_2O_2}}{dy^2} = -k_{GOx}c_{glucose} \end{cases} \quad \text{(CS8)}$$

where $D_{glucose,layer} = \varepsilon D_{glucose,bulk}$, as explained in the main text, and an equivalent expression holds for $D_{H_2O_2,layer}$. The boundary conditions at the electrode ($y = 0$) were null glucose flux and null H_2O_2 concentration (assuming the electron discharge occurs much faster than H_2O_2 production). At the interface between the porous layer and liquid bulk ($y = \delta$) we fixed the concentrations:

$$\begin{cases} c_{glucose} = c_{glucose,b/l} \\ c_{H_2O_2} = c_{H_2O_2,b/l} \end{cases} \quad \text{(CS9)}$$

where $c_{glucose,b/l}$ and $c_{H_2O_2,b/l}$ are fixed but unknown concentrations (it would not have made any difference fixing the fluxes). With these boundary conditions, equation system (CS8) was analytically solved to get the amperometric current, I , per unit electrode surface, S , from:

$$\frac{I}{S} = -D_{H_2O_2,layer}\left.\frac{dc_{H2O2}}{dy}\right|_{y=0} 2F \quad \text{(CS10)}$$

When a sample containing only H_2O_2 enters the system, the solution is:

$$\frac{I_{H2O2}}{S} = -\frac{2c_{H2O2,b/l}\ D_{H2O2,layer}\ F}{\delta} \quad \text{(CS11)}$$

whereas feeding a glucose solution gives the following expression:

$$\frac{I_{glucose}}{S} = -\frac{2(c_{glucose,b/l}\ D_{glucose,layer}(-1+\exp(\Phi))^2 + c_{H2O2,b/l}\ D_{H2O2,layer}\ (1+\exp(2\Phi)))F}{\delta(1+\exp(2\Phi)} \quad \text{(CS12)}$$

The bulk-layer interface concentrations $c_{glucose,b/l}$ and $c_{H2O2,b/l}$ were determined by dynamic similarity using equations (CS1-3), and substituted in (CS11-12).

Appendix D

Method for dynamically measuring intracellular glucose kinetics with single-cell resolution

Alessandro Zambon[1,2], Alice Zoso[1,2], Camilla Luni[1,2], Wolf B. Frommer[3], Nicola Elvassore[1,2]

[1]Department of Industrial Engineering, University of Padova, Via Marzolo 9, 35131 Padova, Italy
[2]VIMM—Venetian Institute of Molecular Medicine, Via Orus 2, 35129 Padova, Italy.
[3] Carnegie Institute of Science, Department of Plant Biology.Carnegie Institution,260 Panama Street Stanford, CA 94305

To be submitted to Integrative Biology

D.1 Abstract

Glucose is the main energy source for cells in an organism and its blood concentration is tightly regulated in healthy individuals. However, impaired blood glucose control has been found in diseases such as metabolic syndrome and diabetes, with serious consequences for patients. Detecting the components involved in the different steps of intracellular glucose processing is very relevant to identify which mechanisms are disrupted under disease conditions. In this work, we have developed a methodology for measuring glucose uptake and phosphorylation rates in culture with single-cell resolution and fast dynamics. We coupled the detection of intracellular glucose concentration at single-cell level via a FRET nanosensor, with glucose uptake derived from direct enzymatic measure of cell metabolic perturbation of glucose concentration in culture medium. In order to perform these experiments, an ad hoc microfluidic platform that allowed precise temporal stimulation of cells through cyclic pulses of glucose concentration, online microscopy, and sampling with minimal disruption of culture conditions was developed. Furthermore, because of the high surface-to-volume ratio of microfluidic setup, we could detect glucose uptake from measurements of bulk medium concentration with high sensitivity and high temporal resolution. The kinetic constants of cell glucose handling were obtained by analyzing the experimental data through a simple mathematical model and, parameters for glucose membrane flux and phosphorylation rates were provided.

D.2 Introduction

Glucose is the main energy source for cells in an organism and its blood concentration is tightly regulated in healthy individuals (3.9-6.1 mmol/L) [1, 2]. However, impaired blood glucose control has been found in diseases such as metabolic syndrome and diabetes, with serious consequences for patients[3, 4]. *In vivo*, the study of glucose regulation is complicated by the limited accessibility to measurements (usually peripheral blood

samples are taken) and by the interconnected action of multiple organs (pancreas, liver, skeletal muscle, adipose tissue...), despite mathematical models help dissecting the different contributions [5]. On the other hand, *in vitro* studies can take advantage of biological measurements with even single-cell resolution.

Detecting the components involved in the different steps of intracellular glucose processing is very relevant to identify which mechanisms are disrupted under disease conditions. However, measuring the rate of each single step is not an easy task also *in vitro.* Glucose uptake represents the quantity of glucose that enters cells from the extracellular space. Once within cells, glucose is phosphorylated by the enzyme hexokinase. Phosphorylated glucose then proceeds through glycolysis. In patients showing insulin resistance, a pre-diabetic state, cells in adipose tissue and skeletal muscle show impaired glucose uptake dynamics [6]. However, the defect could be related both to the mechanism of glucose uptake itself or to other downstream reactions that limit the overall rate of the process.

Conventionally, the single step of glucose uptake is measured *in vitro* using non-metabolizable glucose analogs. The most commonly used are radioactive hexoses, such as 2-[^{14}C]-deoxyglucose (2DG). They were designed similar to glucose, to cross cell membrane (in both directions) by facilitated diffusion through membrane proteins, called glucose transporters (GLUTs). However, unlike glucose, they are not processed intracellularly through glycolysis. Thus, it is possible to estimate the uptake rate of these glucose analogs by measuring their intracellular concentration, proportional to cell radioactivity [7]. Since the use of radiolabeled analogs requires specialized training and equipment, fluorescent glucose analogs [8] and F-2-deoxy-2-fluoro-glucose (FDG) [9] were developed: these compounds are detectable by using fluorescence microscopy and positron emission tomography (PET), respectively. Moreover, enzymatic assays that take advantage of non-radiolabeled 2DG are now established. These assays indirectly measure 2DG uptake quantifying by fluorescence microscopy specific intracellular metabolites involved in its oxidation. However, this last approach requires a

considerable number of cells and may have background interference due to other biochemical molecules [10].

All the methods described above show some criticalities: glucose analogs are not handled by enzymes in the same way as glucose, and can be toxic even at low doses [11]; glucose analogs can have slightly different kinetics compared to glucose because of a different interaction with the membrane GLUTs; isotopic techniques offer low spatio-temporal resolution which precludes detecting rapid dynamics. Furthermore, the inconvenience and cost associated to radioactive waste disposal and cleanup leads to practical routine issues.

Recently, a new method has been developed for real-time glucose detection at single-cell resolution [12]. It is based on the interaction of intracellular glucose with a nanosensor that, upon glucose binding, undergoes a conformational change detectable thanks to the phenomenon of Förster resonance energy transfer (FRET). Thus, monitoring of FRET can be correlated to intracellular glucose concentration in real-time. This high temporal resolution opens the prospect of measuring not only intracellular glucose concentration but also glucose flux through cell membrane and through phosphorylation, by monitoring cell response to dynamic extracellular perturbations, such as a step or sequential pulses of glucose concentration. To fully exploit the potential of glucose FRET nanosensors, the extracellular environment should be accurately controlled at the micrometer scale, with high space and time resolution. Microfluidic technology is well suited for this [13].

In this work, we have developed a methodology for measuring glucose uptake and phosphorylation rates in culture with single-cell resolution and fast dynamics. We coupled the detection of intracellular glucose concentration via FRET nanosensors at single-cell level, with the enzymatic measurement of glucose concentration in culture medium off-line. We then analyzed these experimental data through a simplified mathematical model to obtain the kinetic constants of each step of the process.

Cell cultures were performed within a microfluidic platform that allowed online microscopy. Furthermore, we exploited the potential of this technology to precisely stimulate cell culture with different glucose concentrations and temporal patterns of stimulation. Because of the high surface-to-volume ratio, we could detect glucose uptake from measurements of medium concentration with high sensitivity.

D.3 Material and method

D.3.1 Single-layer microfluidic chip fabrication

The microfluidic chip was fabricated according to standard photolithographic techniques [14]. Briefly, the silicon substrate was spin-coated with the negative photoresist SU8-2100 (MicroChem, USA) to obtain a 100 µm thickness of resist layer. After soft baking, UV exposure, post-exposure baking, and development in SU-8 Developer (MicroChem), the mold was hard baked up to 433 K and then cooled to room temperature. Polydimethylsiloxane (PDMS) (Sylgard, Dow Corning, USA) was used for replica molding in the ratio 10:1 (base:cure agent). The mold was treated with chlorotrimethylsilane (Sigma-Aldrich, Italy) vapor for 15 min before casting. The input/output holes on the PDMS chip were made using a 20G needle punch (Small Parts, USA). The PDMS chip was bonded by plasma treatment (Harrick Plasma, USA) onto a 25x60x0.1 mm borosilicate glass cover slip (Menzel Glaser, Germany). Medium reservoirs were built at the inlet and outlet of the chip by adding an additional layer of PDMS. Specifically, holes were made with a 3 mm diameter Biopsy Punch (Integra LifeSciences, USA) in two 25x10x3 mm PDMS slices, and then bonded by plasma treatment on top of the main chip in correspondence to the input/output holes.

D.3.2 two layer microfluidic chip fabrication

For the multi-inlet chip, two molds were required to obtain a two-layer PDMS chip [15]. The former had 25 µm round channels (round mold), obtained from SPR 220-7 (Dow

Corning) after reflow during the hard bake time. The latter had 25 µm square channels (square mold) obtained from SU-8 2025 (MicroChem). PDMS was spun on the square mold to obtain a 50 µm thickness layer, and on the round mold to make a thick layer (4-5 mm). The thicker PDMS chip was bonded and aligned under a microscope onto the thin one, at the end of the curing phase. The final two-layer chip was bound on a 25x75x1 mm microscope borosilicate glass slide (Menzel Glaser).

D.3.3 Cell line

C2C12 (ATCC, Italy), an immortalized murine myoblast cell line, were maintained on tissue culture dishes in low-glucose Dulbecco's Modified Eagle Medium (DMEM) (Sigma-Aldrich), supplemented with 10% fetal bovine serum (FBS) (Life Technologies, Italy), and 1% penicillin-streptomycin (pen-strep) solution (Life Technologies). Before confluence, cells were trypsinized with Trypsin-EDTA 0.05% (Life Technologies) for culture either in new dishes or in the microfluidic chip. Cells were maintained in a humidified incubator at 37°C with 5% CO_2.

D.3.4 Cell culture within microfludic platform

Prior to cell seeding, microfluidic channels and cell culture chambers within the chip were filled with 4°C cold Matrigel® (Becton-Dickinson, USA) 5% in DMEM, incubated at room temperature for at least 1 hour, and washed with DMEM. A cells suspension was then introduced in the microfluidic chambers in order to obtain a seeding density of 200 cell/mm^2. After 1 hour incubation at 37°C and 5% CO_2, culture medium was added drop by drop into the reservoirs to prevent evaporation and the whole culture system was placed in an incubator. Medium changes were performed every 24 h, by adding fresh medium in the inlet reservoir and aspirating from the outlet using a vacuum pipette.

D.3.5 Glucose uptake measurement

DMEM, supplemented with 10% FBS and 1% pen-strep, having 3- to 10-mM glucose concentrations, was conditioned overnight in an incubator. Using sterile plastic syringe (Becton-Dickinson), conditioned medium was used to wash four 0.02" ID Tygon® tubes (Cole-Palmer, USA). Each tube was then connected at one end to a 100 µL volume Hamilton syringe (Hamilton, USA) pre-loaded with conditioned medium, and at the other end to a 21G stainless-steel needle (Small Parts) inserted in the microfluidic chip inlet. Particular attention was paid in avoiding bubble formation in the connections for their detrimental effect on cells when transported to the culture chambers during perfusion. Hamilton syringes were set up on a syringe pump (Harvard Apparatus, USA) and perfusion started at flow rates in the range 0.0125-0.5 µL/min. At the outlets of the microfluidic chambers needles were inserted to facilitate medium collection at different time points. Medium samples (minimum 0.3 µL) were analyzed off-line with FreeStyle Lite® glucometer and strips (Abbott Diabetes Care, Italy) to measure glucose concentration.

D.3.6 Cell transfection within microfluidic chip

Plasmid pcDNA3.1-FLIPglu-600µΔ13V was previously developed in our lab [12] and was amplified using a conventional silica membrane column-based maxiprep method, GenElute HP Plasmid MaxiPrep Kit (Sigma-Aldrich) [16]. For cell transfection, two solutions were prepared: (1) 0.2 µg DNA in 25 µL Opti-MEM (Life technologies), and (2) 1.5 µL Lipofectamine in 25 µL Opti-MEM. They both were incubated for 5 min at room temperature, mixed together, and incubated for 20 min at room temperature. The final transfection solution was then prepared adding 100 µL of Opti-MEM to the previous mixed solution. Part of this transfection solution was used to suspend the cells to be seeded at a concentration of 5000 cell/µL and injected into the microfluidic chip. Cells adhered to the surface in about 30 min. The remaining solution was injected in the chip without cells, to change the solution within the chip every hour until the end of transfection (5 h). Then, culture medium was injected into the chip.

D.3.7 Imaging acquisition for FRET and analysis

Imaging was performed 24-48 h after transfection at the inverted microscope IX81 (Olympus, Italy) with a 40X/1.30 oil immersion objective (Olympus). The microscope was equipped with a CCD camera (SIS F-View), an illumination system MT20 (Olympus), and a beam-splitter optical device (Multispec Microimager; Optical Insights). Dual emission intensity ratio were simultaneously recorded using cellR 2.0 software (Olympus) after both excitation at 430/25 and 500/20 for the two emission filters (470/30 CFP an 535/30 for YFP). Images were acquired within the linear detection range of the camera at intervals of 20 s for up to 1 hour. Exposure time was usually set at 200 ms. All experiments were carried out at room temperature (22–25°C). Cells were imaged in DPBS +Ca +Mg 1X (Life Technology) glucose free or with glucose added (Sigma-Aldrich). Perfusion was performed at 5 µL/min using a microfluidic multi-inlet system placed upstream of the culture chamber and connected by 5 cm long peek tube (IDEX, USA), allowing up to 9 glucose concentrations for experiment. Cyclic pulses of different glucose concentrations were alternated with glucose-free medium infusion every 4 min. Duration, frequency and concentration of the pulses were controlled via Lab-view software (National Instruments, Italy). Images were analyzed as previously reported [12], with spectral bleed-through (SBT) and baseline correction using polynomial fit. The analysis produced the normalized baseline-corrected FRET index, F^c/D, an indirect measure of intracellular glucose. Peak areas were calculated by integration of specific intervals.

D.3.8 Simplified analytical model

We developed a simplified analytical model to obtain the kinetic parameters of glucose uptake and phosphorylation from measurements of glucose uptake and of cytosolic glucose concentration via FRET nanosensor.

A single-cell mass balance was performed to analyze FRET data. The equation is given by:

$$\frac{dG_{cyt}}{dt} = \frac{N_m}{V_{cell}} - R_{gly} \tag{D.1}$$

where the left-hand side term accounts for the accumulation of glucose inside the cell with time, t, and the two terms on the right represent glucose inflow through the cell membrane, N_m, per unit cell volume, V_{cell}, and glucose consumption rate through glycolysis, R_{gly}, respectively.

Glucose inflow through plasma membrane was expressed as:

$$N_m = k_m A_{cell} \left(G_{bulk} - G_{cyt} \right) \tag{D.2}$$

where k_m is the overall mass transfer coefficient, A_{cell} is cell surface, G_{bulk} and G_{cyt} represent glucose concentration in medium bulk and in the cytosol, respectively. G_{bulk} is assumed equal to glucose inlet concentration, G_{IN}. The difference of glucose concentrations represent the overall driving force of two sequential processes: glucose transport from medium bulk to cell membrane and glucose passage through the membrane. An average intracellular glucose concentration, G_{cyt}, was used, neglecting the spatial inhomogeneity within the cell.

Intracellular glucose consumption due to glycolysis was assumed to occur irreversibly and according to a linear kinetic expression:

$$R_{gly} = k_g G_{cyt} \tag{D.3}$$

where k_g is a kinetic parameter.

We integrated Eq. (D.1) after substituting the terms in Eq. (D.2) and (D.3) with, as initial condition, a null intracellular glucose concentration. We obtained the following analytical solution:

$$G_{cyt} = G_{bulk} \frac{k_m^{'}}{k_m^{'} + k_g} \left[1 - \exp\left(-\left(k_m^{'} + k_g \right) t \right) \right] \tag{D.4}$$

where $k_m^{'} = k_m A_{cell} / V_{cell}$.

As already mentioned, the normalized FRET index, F^c/D, is correlated to glucose intracellular concentration, G_{cyt}, according to the following expression:

$$G_{cyt} = \alpha\left(1 - F^c/D\right) \tag{D.5}$$

where α is a parameter used to convert concentration to fluorescence units. Substituting (D.4) in (D.5), we obtained the equation:

$$\frac{F^c}{D} = 1 - \frac{G_{bulk}}{\alpha}\frac{k_m^{'}}{k_m^{'} + k_g}\left[1 - \exp\left(-\left(k_m^{'} + k_g\right)t\right)\right] \tag{D.6}$$

that was used to obtain the value $\left(k_m^{'} + k_g\right)$ by fitting FRET experimental data at different glucose concentrations.

A macroscopic mass balance was also performed considering the whole culture chamber as the system of interest. Fixing glucose concentration at the inlet, G_{IN}, medium flow rate, $\dot{V}$, and the number of cells in the culture chamber, N_{cell}, glucose concentration at the outlet, G_{OUT}, was measured experimentally, once the system reached steady-state, after sampling. From these data, the average glucose uptake per cell, $N_m^{\exp}$, was calculated by the following expression:

$$N_m^{\exp} = \frac{G_{IN} - G_{OUT}}{N_{cell}} \cdot \dot{V} \tag{D.7}$$

Eq. (D.2) was used to fit the experimental data derived in (D.7) and to obtain the value of each parameter, $k_m^{'}$ and k_g.

D.3 Results

D.3.1 Experimental set up and operations

We developed an experimental system composed of a microfluidic chip for cell culture, a liquid handling apparatus, a detection system, and an external system for control and data acquisition (Figure D.1A). The microfluidic culture system is composed of 3 culture chambers where experiments are performed independently in parallel (Figure D.1B and C). Medium perfusion was performed by two different means: by external pumping and by pressure-driven perfusion (Figure D.1A). The second method was chosen for experiments where fast dynamic changes of glucose inlet concentration were required.

We performed two sets of experiments using C2C12 cells. First, we performed experiments at different glucose concentrations at the inlet and different flow rates, measuring glucose concentration at the outlet at multiple time points by sampling and off-line sensing via enzymatic assay. These experiments were used to detect glucose uptake of the whole cell population. In a second set of experiments, we used a multilayer microfluidic platform that included an integrated microvalve system to connect medium reservoirs with different glucose concentrations to the culture chamber with high temporal accuracy (Figure D.1B and C). This setup was used during FRET experiments under a fluorescence microscope to detect single-cell intracellular glucose concentration.

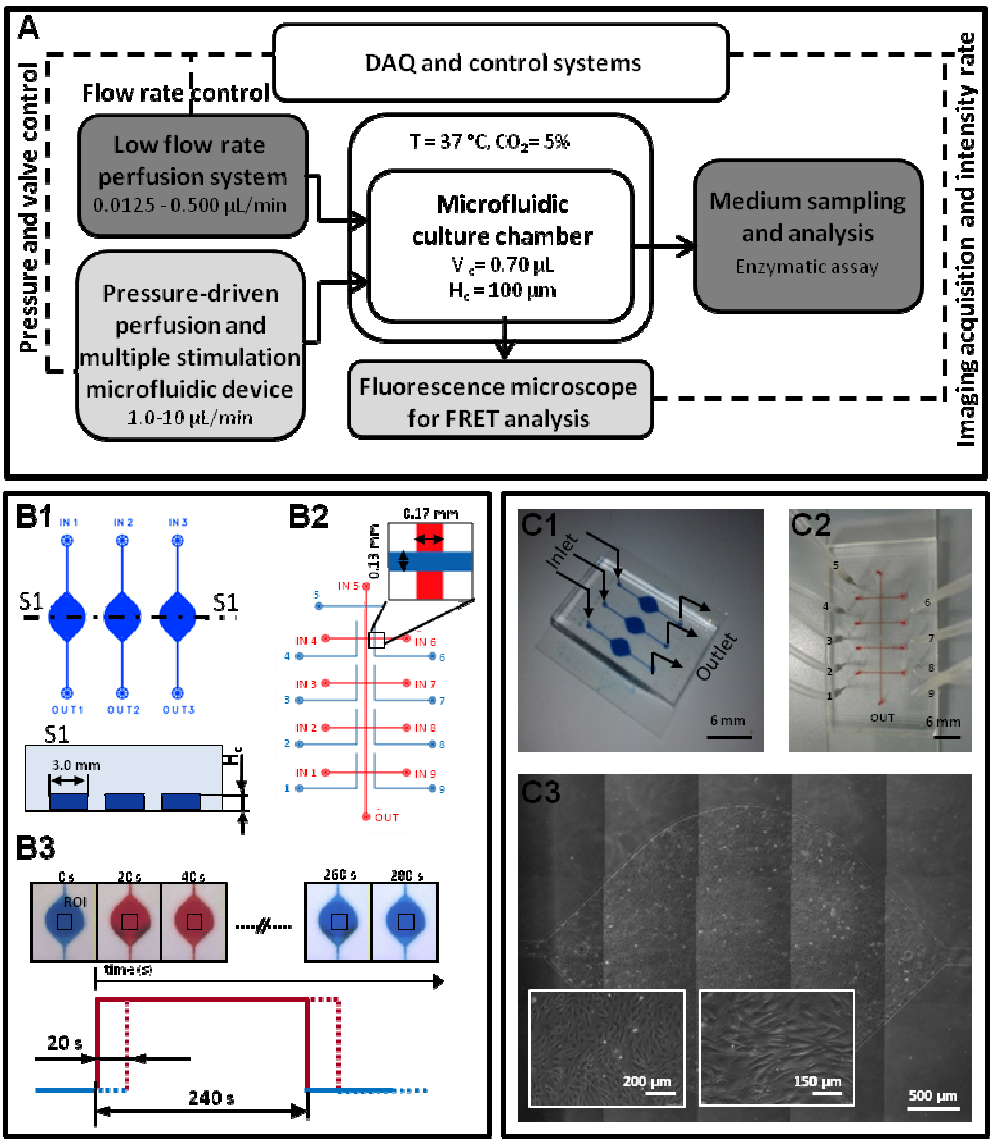

Figure D.1 *Experimental setup. (A) Schematic view of experimental setup. Dark gray boxes describe off-line medium glucose measurements, light gray boxes experiments with FRET nanosensor. (B1) Schematic representation of the 3 culture chambers in the microfluidic chip (top view and section). (B2) Schematic representation of the microfluidic device used to change inlet medium glucose concentration. Round flow channels in red and square control channels in blue. (B3) Sequence of chamber images during the fast stimulation simulated by red and blue dyes. (C1) Image of PDMS culture chamber chip. (C2) Image of multiple stimulation microfluidic platform; flow channels were filled with a red dye; tubes are connected to pressure-driven control channels. (C3) Microscopic image of the whole culture chamber with confluent C2C12, 2 days after seeding. Insets represent different magnifications.*

D.3.2 Calibration of glucose uptake measurements

Glucose uptake was calculated by equation (D.7) from experiments where off-line glucose concentration, G_{OUT} , was measured at the outlet of culture chamber. Measurements were taken using a glucometer after sampling a medium volume of 0.6 µL, a bit larger than the minimum required by the instrument. The time needed to obtain the sampling volume is inversely dependent on medium perfusion rate (Figure D.2, inset), and this poses an upper bound to the temporal resolution achievable.

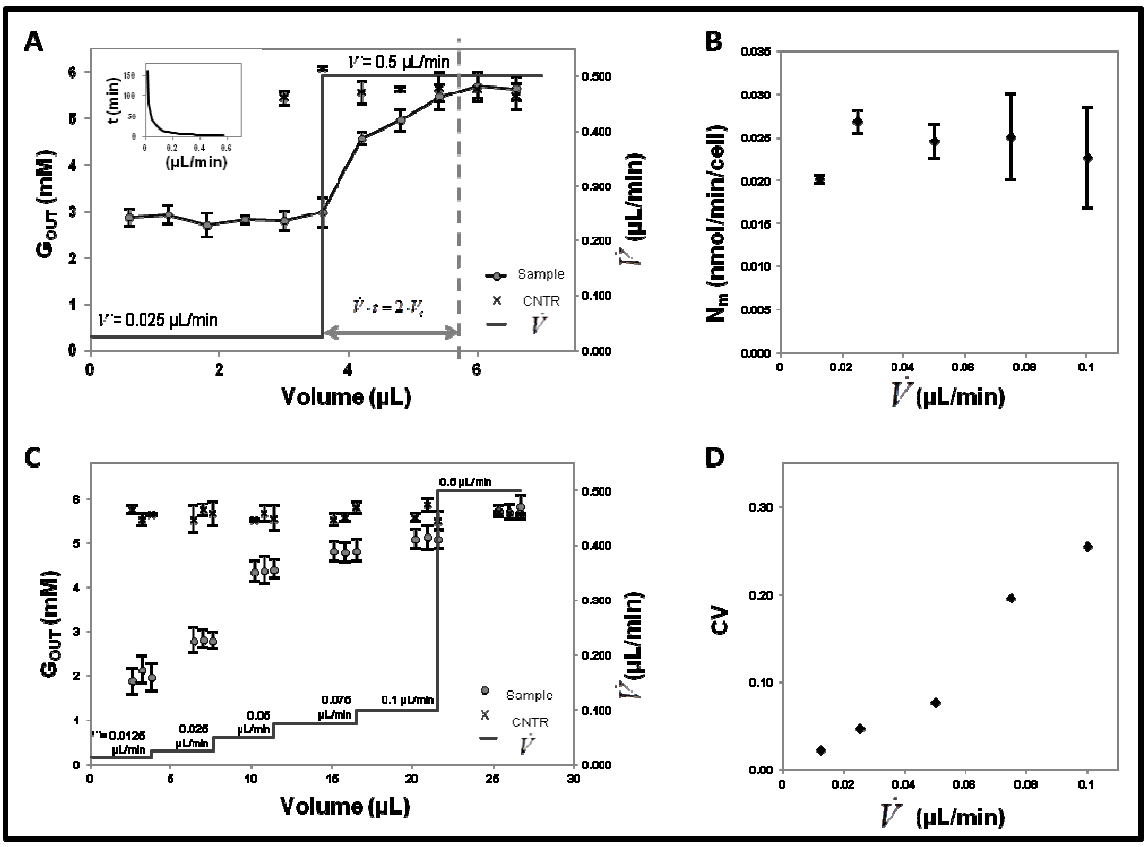

Figure D.2. *Effect of flow rate on glucose uptake measurements. (A) Transient of G_{OUT} concentration after a change in flow rate. G_{OUT} is shown as a function of the eluted volume. Sampling was performed continuously (each 0.6 µL-volume collected was analyzed). Results from 3 repeated experiments. Inset shows duration of sampling as a function of volumetric flow rate for a sampling volume of 0.6 µL. (B) Steady-state glucose uptake calculated by (D.7) from G_{OUT} measurements in (C) at different flow rates. (C) Steady-state G_{OUT} measurements at different flow rates. For each condition, 3 samples were taken at steady-state from each of the 3 culture chambers and analyzed. (D) Coefficient of variation of N_m as a function of flow rate. (A-D) G_{IN} was fixed and equal to 5.5 mM. Error bars represent standard deviations.*

We studied the effect of different operative variables on measurement sensitivity (Figure D.2). In particular, for a fixed inlet glucose concentration (5.5 mM), we analyzed the measurement sensitivity at different flow rates and the duration of the transient before a new steady-state is established after changing flow rate. These experiments were performed at maximum time resolution, i.e. medium was continuously collected and analyzed every 0.6 µL eluted. Thus, at low flow rate (0.025 µL/min) measurements were taken every 24 min, while at high flow rate (0.5 µL/min) every 1.2 min (Figure D.2A).

On the other hand, the higher temporal resolution at high flow rate comes at the expenses of reduced measurement sensitivity. Specifically, the steady-state outlet concentration at 0.5 µL/min is not significantly different respect to the concentration of the control experiment (perfusion through a chamber without cells), despite the small variance of the data between samples, and the signal-to-noise ratio is too small for accurate detection.

The residence time, t_r, of medium in the culture chamber is calculated by the following equation:

$$t_r = \frac{V_c}{\dot{V}} \tag{D.8}$$

where V_c represents the cell chamber volume. As during this time cells uptake glucose, the longer is t_r, the lower is G_{OUT}. In our experimental system, the culture chamber had a volume of 0.7 µL/min. Thus, residence time was reduced from 24 min to 1.2 min increasing the flow rate as in Figure D.2A.

We also calculated the duration of transient after a change in flow rate. A new steady-state is established after infusing into the culture chamber an amount of medium that is approximately the double of its volume (Figure D.2A).

To define the optimal trade-off between high temporal resolution and sensitivity of measurement, we performed an experiment where step changes of flow rate were

applied to 3 culture chambers in parallel (Figure D.2C). The experimental values obtained for G_{OUT} were then used to calculate steady-state glucose uptake, $N_m^{\exp}$, from equation (D.7). As expected, glucose uptake does not depend on the flow rate, when this is high enough to avoid extracellular mass transfer limitations, as in the case of 0.0125 µL/min (Figure D.2B). However, variability is higher at large flow rates due to measurement inaccuracy (Figure D.2D). Taken together, these considerations supported the choice of using a flow rate of 0.05 µL/min in next experiments, allowing a 10 min temporal resolution.

D.3.3 Dynamic measurements of intracellular glucose concentration via FRET nanosensor

We tested FRET nanosensor performance in our system (Figure D.3). We used C2C12, a cell line of murine myoblasts. Two cells transfected with the sensor were analyzed under a fluorescence microscope, collecting the signal at the wavelength of cyan (CFP) and yellow (YFP) fluorescent proteins at high temporal resolution. When glucose concentration in a cell increases, CFP fluorescence intensity decreases and YFP fluorescence increases, because of the conformational change of the nanosensor (Figure D.3A). F^c/D represents a normalized value of the emission ratio of CFP/YFP. After analyzing a sequence of images like those in Figure 4A, we obtained F^c/D as a function of time during a cyclic pulse stimulation of cells with 1.5 mM glucose concentration. The normalized FRET index decreases when a high glucose concentration enters the system and returns to its baseline value when glucose is removed (Figure D.3B). The results are consistent and reproducible for the two cells measured.

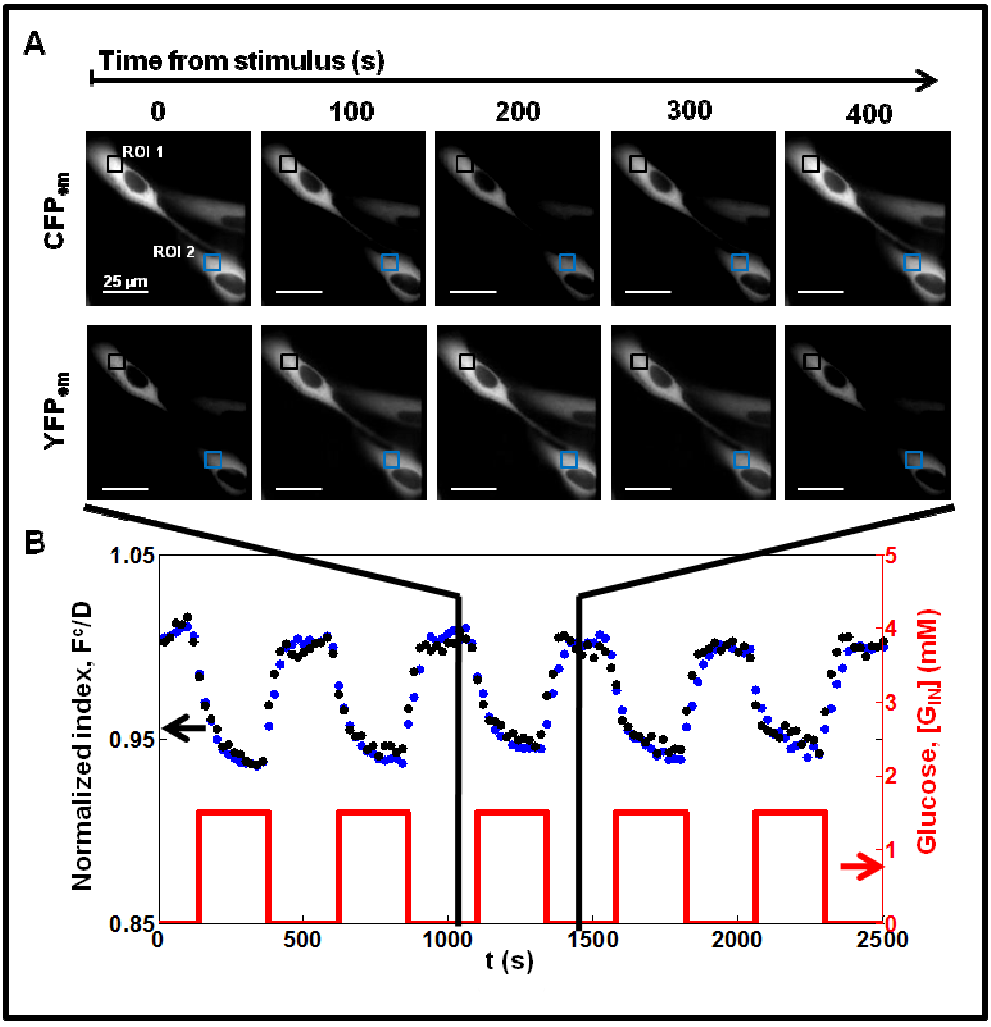

Figure D.3. *Dynamic measurements of intracellular glucose concentration via FRET nanosensor. (A) Sequence of images, obtained by fluorescence microscopy, of cyan (CFP) and yellow (YFP) fluorescent proteins during pulse perfusion at 1.5 mM glucose concentration. (B) Normalized FRET index, F^C/D, during an experiment of cyclic pulses of 1.5-mM glucose concentration. Blue and black dots refer to the two regions of interest (ROIs) shown in (A).*

We repeated the experiment described above, applying glucose pulses of increasing concentration (Figure D.4). The signal from 3 cells was collected and analyzed. Consistent results were obtained, FRET index had larger amplitude of oscillation for pulses of higher glucose concentration (Figure D.4A). Measurement noise was relevant at low glucose concentration, but the sensor response showed good signal-to-noise ratio for concentrations higher than 1 mM (Figure D.4A). We calculated the integral of F^c/D during each pulse of stimulation as a measurement of the total glucose up taken during

that time span. Results show that the sensor has a linear response up to about 4 mM (Figure D.4B).

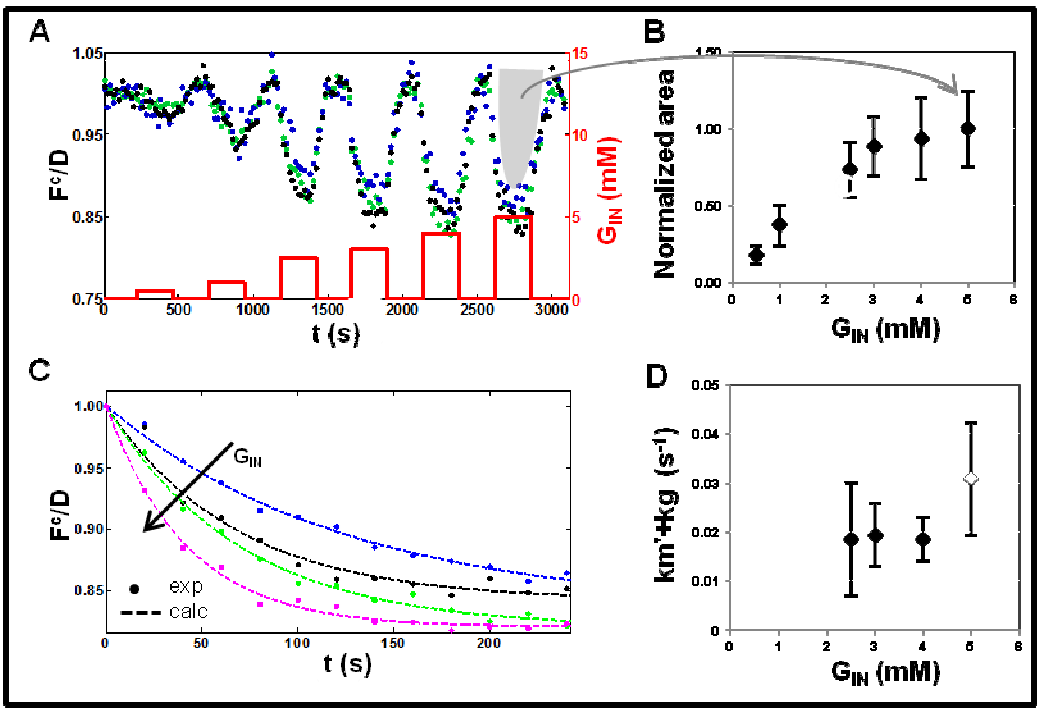

Figure D.4. Effect of glucose concentration on FRET nanosensor response. (A) Normalized FRET index, F^c/D, as a function of time during repeated pulses of increasing glucose concentration (0.5, 1, 2.5, 3, 4, and 5 mM). Black, blue and green dotes refer to the signal from 3 different cells. Flow rate was 4 µL/min. (B) Integral of Fc/D during each glucose pulse, normalized by its value at 5 mM glucose concentration. (C) Transients of FRET sensor response at different glucose concentrations (2.5, 3, 4, and 5 mM) were overlapped and fitted by Eq. (D.6). (D) Results of the fitting performed in (C), $k_m^{'} + k_g$ are represented as a function of glucose concentration.

We studied the transient of the normalized FRET index during the pulses at different glucose concentrations. Curves from Figure D.4A were overlapped in Figure D.4C. Qualitatively, the data show a faster response during cellular uptake at higher glucose concentrations (Figure D.4C). We performed a fitting of these data by Eq. (D.6) to quantify this trend. We obtained the value of $\left(k_m^{'} + k_g\right)$ at different glucose concentrations (Figure D.4D). This sum represents the inverse of the time constant of the overall process (uptake and phosphorylation). The data showed that the simplified model we developed is able to capture the main dynamics involved, as it shows a constant value for $\left(k_m^{'} + k_g\right)$ at different glucose concentrations. A little discrepancy is

visible for 5 mM glucose concentration, which is attributable to the loss of sensor linearity at this concentration (Figure D.4B).

D.3.5 Estimation of kinetic parameters

We coupled the kinetic information obtained during FRET experiments with measurements of glucose uptake at different glucose concentration. We measured glucose uptake at a flow rate of 0.05 µL/min at 3, 5, and 10 mM glucose concentrations. Glucose uptake by the whole cell population was linear within this range (Figure D.5A). We fitted these results by Eq. (D.2) to discriminate between the values of $k_m^{'}$ and k_g, as we obtained only their sum from FRET experiments. We obtained a constant value for the two parameters throughout glucose concentrations as a demonstration of the goodness of fit (Figure D.5B).

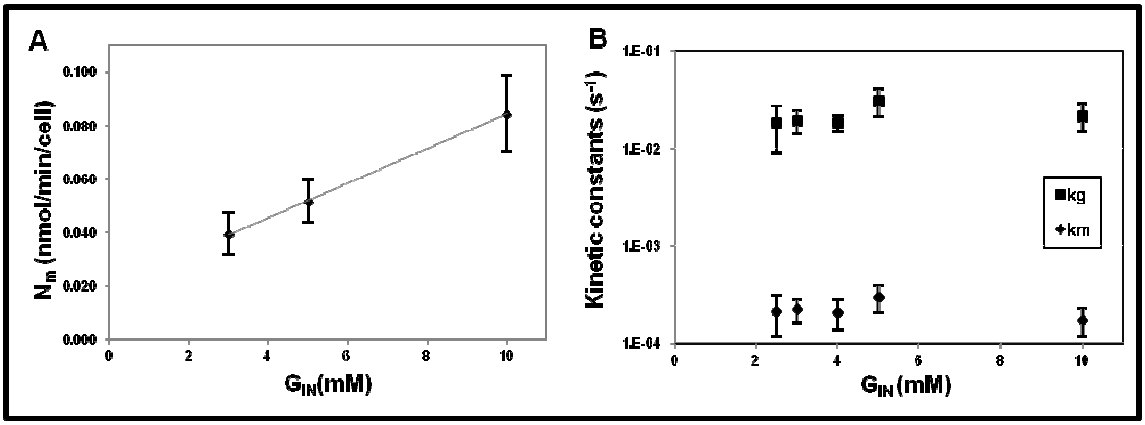

Figure D.5. *Glucose uptake and parameter evaluation. (A) Glucose uptake calculated from off-line measurements of* G_{OUT} *at different glucose inlet concentrations. Flow rate was 0.05 µL/min. (B) Results of parameter estimation at different glucose concentrations*

In coupling the information from the two measurement methodologies, we neglected the differences in the external mass transfer, due the different flow rate used in the two sets of experiments. However, both the fitting results (Figure D.5D and D.6A) and a theoretical estimation of the overall mass transfer coefficients in the two systems by non-dimensional analysis (data not shown) support this assumption. Thus, for perfusion

as low as 0.05 µL/min in our culture system, glucose concentration at cell membrane can be approximated with bulk (or inlet) glucose concentration.

D.4 Conclusions

We have developed a methodology for deriving glucose uptake and phosphorylation kinetics in a single cell with high temporal resolution within a microfluidic system. The experimental results were obtained from cell cultures of C2C12. The operative conditions for obtaining the experimental measurements were optimized to improve time resolution and sensitivity. A mathematical model assisted in the analysis of data to obtain the most relevant kinetic constants of the process. This work offers a reliable and robust method for quantitative and dynamic glucose detection at the single-cell level.

D.5 Literature cited

[1] Frier, B. M. Diabetologia 52, 31–34 (2009).

[2] Laakso, M. Diabetes 48, 937–942 (1999).

[3] Cryer, P. E., Davis, S. N. & Shamoon, H. Diabetes Care 26, 1902–1912 (2003).

[4] Rolo, A. P. & Palmeira, C. M. Toxicology and Applied Pharmacology 212, 167–178 (2006).

[5] Ferrannini, E. & Cobelli, C. Diabetes Metab Rev 3, 335–363 (1987).

[6] Odegaard, J. I. & Chawla, A. Science 339, 172–177 (2013).

[7] Sokoloff et al., J. Neurochem. 28, 897–916. (1977)

[8] Yamada et al., J. Biol. Chem., 275, 22278–22283 (2000)

[9] Maschauer et al., J. Nucl. Med. 45, 455–460. (2004)

[10] Yamamoto et al., Anal. Biochem. 404, 238–240, (2010)

[11] Kurtoglu et al., Antioxidants & Redox Signaling; 9(9):1383-1390 (2009)

[12] Hou et al., Nat Protoc.; 6(11):1818-33 (2011)

[13] Tsung-Hsi Hsieh, Microfluidics and Nanofluidics (2009), Volume 6, Issue 3, pp 391-401,

[14] McDonald J. & Whitesides G., Acc. Chem. Res. 35, 491–499 (2002).

[15] Melin J. & Quake SR. Annu Rev Biophys Biomol Struct.;36:213-31. (2007)

[16] Birnboim, H. C.; Doly, J. Nucleic Acids Res., 7, 1513-1522 (1979)

Appendix E

Multilayer Soft Lithography: mold and chip fabrication

Protocols, method and some details reported in this appendix have been adapted from previous works in literature [1-5] and from Stanford Foundry [6]

E.1 Mold fabrication materials

E.1.1 Reagents and substrates

100 mm silicon wafer, orientation any, material type CZ silicon, dopant any, thickness min 400-600 um, resistivity 0-100 ohm cm, FrontSideFinished polished, BackSide Etched; (MCR Microsystems, Germany).
Photoresist: SPR 220-7 (Dow Corning), SU8 2005 (Microchem), SU8 2010 (Microchem), SU8 2025 (Microchem), SU8 50 (Microchem)
Developer: MF319 developer (Dow Corning), SU8 developer (Microchem)
Solvent: Ethanol (Sigma), Isopropanol (Sigma), Methanol (Sigma), Acetone (Sigma)
1,1,1,3,3,3 hexamethyl-disilazane (HDMS), reagent grade 97% (Sigma)

E.1.2 Equipments and other

Spin coater (Laurell WS-400b-6npp/lLITEHOR)
programmable hot plate (Torreypines scientific)

Rocking shaker (Reliable scientific inc)

Karl suss alignment

Karl suss UV intencity meter- model 1000

Olympus TCH microscope ergolux (Olympus)

White nitril gloves and clothes for clean room facilities (cover shoes, hairnet, bunny suit/frock, booties)

Flat bottom and straight sides glass tank 125x75 (VWR)

Wafer tweezers

120 mm Petri dishes

E.1.3 Mold procedure

Molds are produced with photoresist-based photolithographic techniques. 4" silicon wafer are in general cleaned rinsing consecutively with Acetone, Methanol (Sigma Aldrich) and distilled water. To prevent humidity silicon wafer is placed on a hot plate at 383 K for at least 10 minutes. These operations are needed again after every hard baking, before the subsequently coating. The flow mold is made by first treating a silicon wafer with hexamethyldisilazane (Sigma Aldrich) vapor for 10 min at room temperature. Then one layer of SPR-220-7 positive photoresist (Rohm and Haas, Dow corning) is spin-coated (Laurell Technology Corporation) onto the wafer, to obtain a thickness of 15 to 20 µm. The coated is baked on a hot plate at 65°C for 5 min followed by 45 min at 90°C. The photoresist is then rehydrate at room temperature overnight in the dark. The day after the SPR photoresist is exposed to 2.3 J/cm2 of collimated UV light (365 nm center wavelength, on a Suss MA6 contact aligner, SÜSS MicroTec AG, Munich, Germany) through a high resolution transparency mask containing the design of the flow channels. The mask is printed at 20,000dpi (Fineline Imaging Inc., Colorado Springs, Colorado) from an AutoCAD (AutoDesk Inc., San Rafael, California) design file. After exposure, the photoresist is developed in Microposit MF-319 developer (Rohm and Haas) for 10 to 30 min. The development is stopped immersing the photoresist in distilled water. Finally, the photoresist is re-flowed and hardbaked on a hot plate ramped from 65ºC to 190ºC at

10ºC/hour for a total time of 15 hours. Round channels are obtained from re-flowing and hard baking. Round channels correspond to all the channel sections where valves are needed. The round channels have a peak height of 20 to 30 µm after hard baking. Subsequently, a 45 to 55 µm thick layer of SU8-50 negative photoresist (Microchem Corp., Newton, Massachusetts) is spin-coated on the wafer and baked on a hot plate at 65°C for 5 min followed by 15min at 95°C and again 65°C for 2 minutes. The SU8 is exposed to 200 mJ/cm2 of collimated UV light using a new mask aligned on the previous geometry. Baking at 65°C for 2 min then 95°C for 5 min and again 65°C for 2 min. Development in SU-8 developer (Microchem) for 2 min and rinsing with Iso-Propan-Alcohol (IPA). An Hardbaking on a hot plate ramped from 65°C to 160°C at 120°C/hour for 2 hours is needed to fully crosslink the SU8. This layer forms all the flow channels and chambers on the mold. At the end a 15 to 25 µm thick layer of SU8-2010 (Microchem) is spin-coated, baked on a hot plate at 65 °C for 2 min, then 95°C for 5 min and again 65°C for 2 min. It is exposed to UV at 180 mJ/cm2 with another mask aligned on the previous, baked on a hot plate at 65 °C for 2 min, then 95°C for 5 min and again 65°C for 2 min and developed in SU-8 developer for 1 min and rinse with IPA. This last layer of SU-8 forms the microposts arrays on top of the chambers. The wafer is finally hard-baked as the previous SU-8 layer.

For the control mold 3 layers of SU-8 negative photoresist are needed. First, SU8-2005 is coated on a 4" silicon wafer, to a thickness of approximately 5 µm, and baked at 65°C for 2min, 95 °C for 5 min and again 65°C for 2min. The SU8 is exposed to 180 mJ/cm2 of UV light (without a mask) and baked again as previously. This blanket SU8 layer provides a surface with uniform wetting properties to the PDMS, which ensures a uniform PDMS spin-coating thickness when making the chip. On the blanket layer a 20 to 25 µm thick layer of SU8-2025 is spin-coated, baked on a hot plate at 65°C for 2min, 95 °C for 5 min and again 65°C for 2min, exposed to UV at 160 mJ/cm2 using the control channel mask. Subsequently it is baked on a hot plate as before the exposure, and developed for 3 min and rinse. The wafer is finally hardbaked with the same ramp used for SU-8 in the flow mold. The last layer form the chamber-via layer: 45-55 µm of SU-8 2025 is spun and baked at 65°C for 5min, 95 °C for 7 min, exposed to UV at 160 mJ/cm2 aligning another

mask on the previous marks. Subsequently it is baked again at 65°C for 1 min and 95 °C for 6 min, and developed for 2 min Hardbaking fully crosslink the photoresist. Another mold is made for generate the biopsy hole chamber using SU-8 2025 to obtain 20 to 25 µm thick. The method is the same described previously for the second layer in the control mold.

E.2 Chip fabrication materials

E.2.1 Reagents and substrates

Chloromethylsilane (C 72854-500ml Sigma Aldrich)

Sylgard 184 Dow corning kit (base and cure agent)

Glass slide: Brain Research laboratories n 1 thickness 48x60

VWR micro slides 25x75 (cat n 48300-025)

VWR micro slides 50x75 cat 48300-050

E.2.2 Equipments and others

PDMS Mixer (Thinky AR-250)

spic coater (Laurell WS-400b-6npp/lLITEHOR)

Vacuum system (vacuum pump and crystallization tank)

Stereomicroscope Nicon SMZ1500

Convective Oven (VWR model NO 1350 FM)

Punch machine (Schmidt technology press and camera)

Plasma Machine

Cutter

White tape

Wafer tweezers

Al foil

TX 1109 Non waven wipers Technicloth II

TX 1010 Vectro Alpha 10, Vectro Sealed-border wipers

Petri dishes 150x15 mm (VWR 25384-326 and 25384-302 100x15mm)

E.2.3 Chip procedure

A chip consist of three (for adipose application) or two (skeletal muscle application) layers of PDMS. The first has the channels where liquid flow occurs (flow layer; the second has dead-ended channels that control the valves (control layer); the third has holes to insert the biopsy and the cup. For skeletal muscle cell application, the chip is bonded via plasma treatment to a glass slide instead to the third PDMS layer.

At the beginning every mold is treated with Chlorotrimethylsilane (Sigma Aldrich) vapor for 10 min at room temperature. The flow layer is made by pouring uncured PDMS (Sylgard, Dow Corning; 5:1 elastomer:crosslinker ratio) onto the flow mold to a thickness of 3 to 5 mm. The control layer is made by spin-coating (2200 rpm/75sec) uncured PDMS (20:1 elastomer:crosslinker ratio) onto the control mold and letting it sit on a level surface for 1.5 hour, to form a uniform 40 to 50 µm thick layer. After curing the PDMS on the molds by baking at 60ºC for 35 minutes (flow layer) and 45 min (control layer), the thick flow layer is peeled off its mold and aligned over the control layer (still on the mold). Irreversible bonding of the two layers is achieved by baking them at 60ºC for 15 minutes and then at 80°C for 90 min. After bonding, the layers are peeled off the control mold and bonded to the biopsy layer made by 7-9 mm thick PDMS 10:1 elastomer:crosslinker ratio, cured at 60°C for 4 hours. Bounded is achieved by plasma treatment (Harrick) for 33 sec at 70W.After the bounding the final chip is baked at 80°C overnight to promote the plasma bonding and fully crosslink the PDMS. The holes are made previously using a 4mm diameter biopsy punch. Both for the flow and the control, input/output ports for the channels are created by punching the PDMS layers using a 20 gauge round hole cutter (Technical Innovations Inc., Brazoria, Texas). These ports permit the connection of 1/16” Tygon tubing to the chip using 23-gauge stainless steel tubes (New England Small Tube Corp., Litchfield, New Hampshire), which fit tightly into both the ports on the chip and the inside of the Tygon tubing, for both the flow and control

layers. Before using, the chip is tested: valves control lines are pressurized slowly from 0 to 2 bar to check their functionality. After that, sterilization is achieved by 121°C steam in autoclave.

E.3 Mask and mold design

During this Ph.D. work, two multilayer design have been drawn. The former is the first generation multi layer chip mold for adipose tissue and muscle cells, the latter is an evolution of the previous for the additional integration of direct sampling and biosensing in the chip. The design is very similar for the two generations chip. In this section the CAD design will be reported for both. As example, the second generation design will be presented to explain the design phases, therefore, the former is only shown (Figure E1).

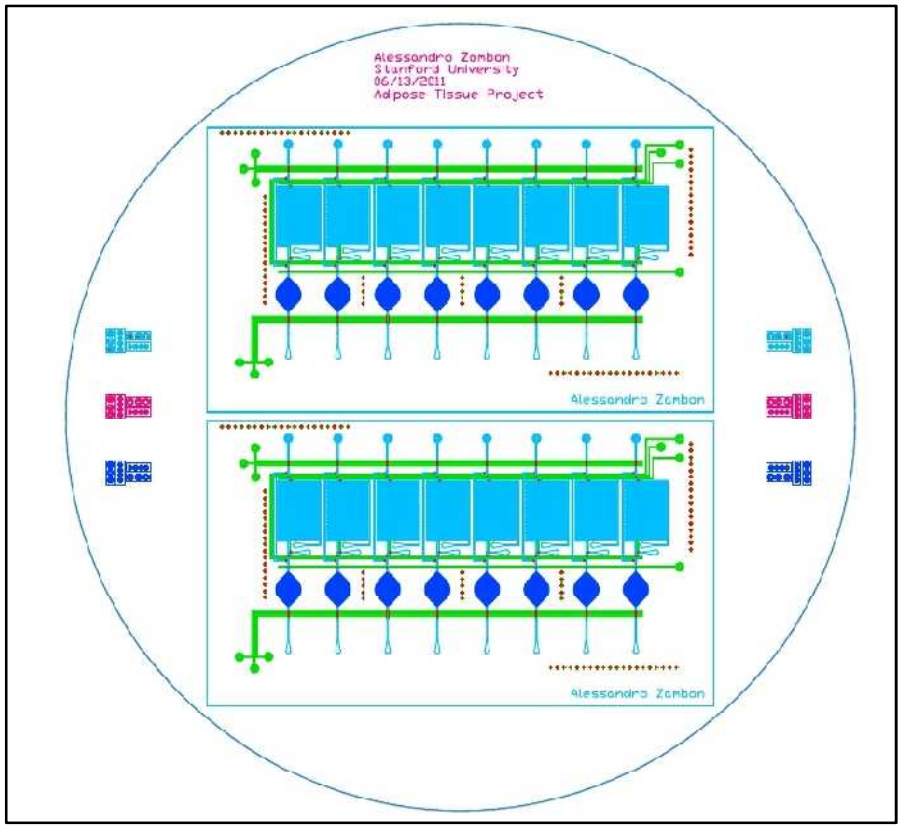

Figure E1*: First generation multilayer mask for adipose and muscle cells. Each color corresponds to a different layer.*

Following are reported some rules for mask design with AutoCAD® 2D for multi layer devices and the second generation chip is used as example (for single layer the design it's easier but the phases are pretty much the same). For more information visit http://www.stanford.edu/group/foundry [7].

E.3.1 Procedure for multilayer mask design

1 AutoCAD setting

AutoCAD has to be set to the correct units: Length Type: Decimal, Length Precision: 0.0000, Scale: Microns

2 Layers

Each mold has o bet be drawn in a separate AutoCAD layer. Each layer has to be overlapped each other.

3 Space and distribution

Fit on it as many devices as possible onto a single mold but ensure that there is enough space between chips for chip alignment and bond. Leave a ring area of approximately 0.5 cm free around the mold perimeter to avoid any critical due to photoresist imperfection around the perimeter of the wafer.

4 Borders

Add chip borders to indicate where the PDMS should be cut around the perimeter for the devices.

5 Text labels

Add text labels to identify the layer, with design date, name and department

6 Mask alignment and line of the features

Add mask alignment marks for multi height mold and chip. All features should be composed of closed polylines.

7 Scale up

Before painting, pattern corresponding to a thick layer of PDMS that is peeled off the mold for subsequent alignment and bonding onto a patterned thin layer will be scaled up by 1.5% to compensate for the shrinkage of the PDMS after peeling

8 Paint

Paint use black and white using Adobe Illustrator. Black is used for dark area and white for transparency area.

9 Print

Print the Masks on transparent foil at high resolution depending on minimum geometry features. For minimum channels features of 50 µm 8000 dpi are enough.

Figure E2*: Second generation multilayer mask for adipose and muscle cells. Each color corresponds to a layer and consequently a mold: control channel (green), control chamber (purple), Flow round channel (red), Flow square channel (blue), Pillar (yellow).*

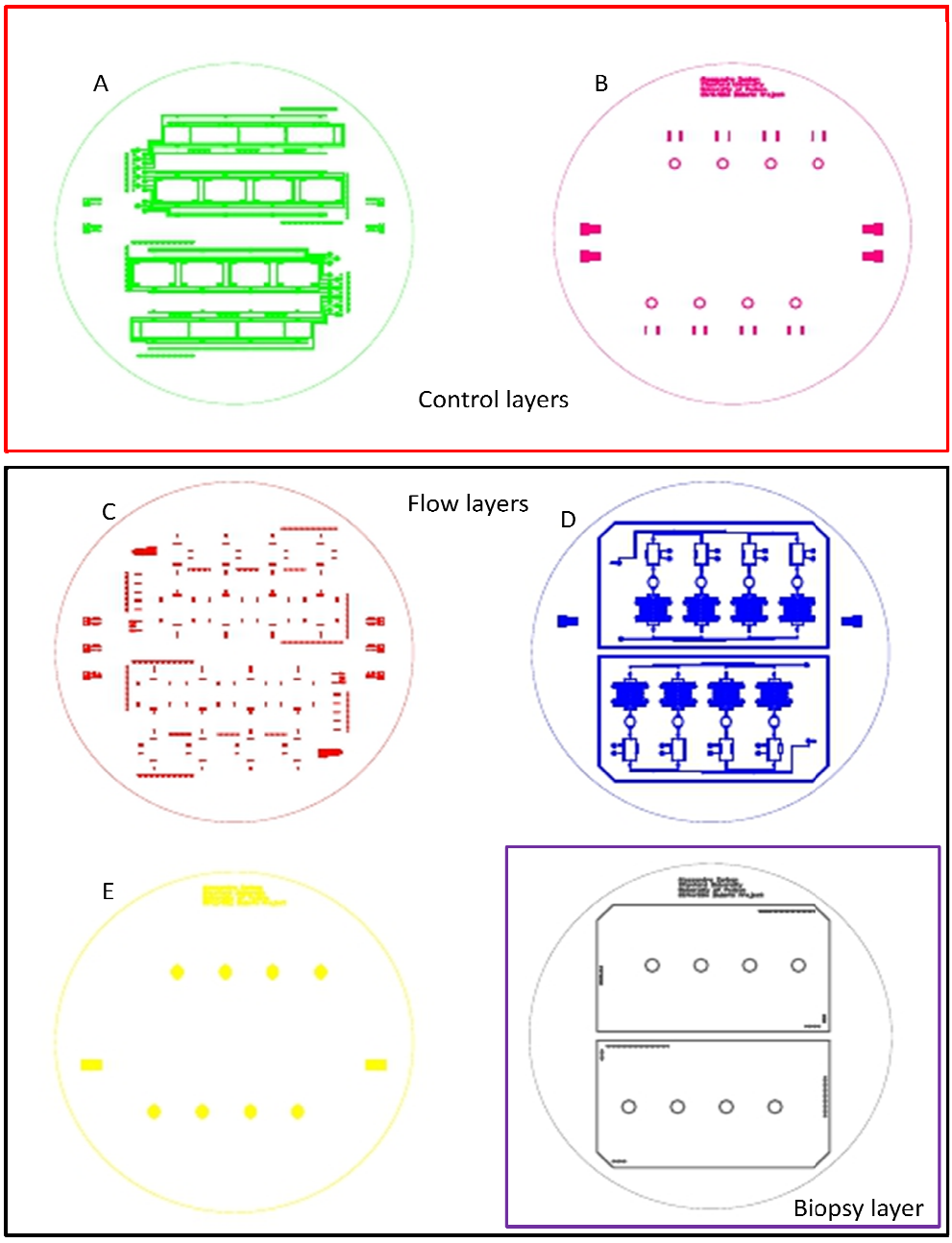

Figure E3*: Before painting the multilayer design (Figure E2) has to be shifted in single layer. At this point the pattern corresponding to the thick layer has to be scaled to avoid shrink (Flow mold in this specific case). Control layers: square channel (A), Chamber (B); Flow layers: round channel (C), Square channel (D), Pillar (E).*

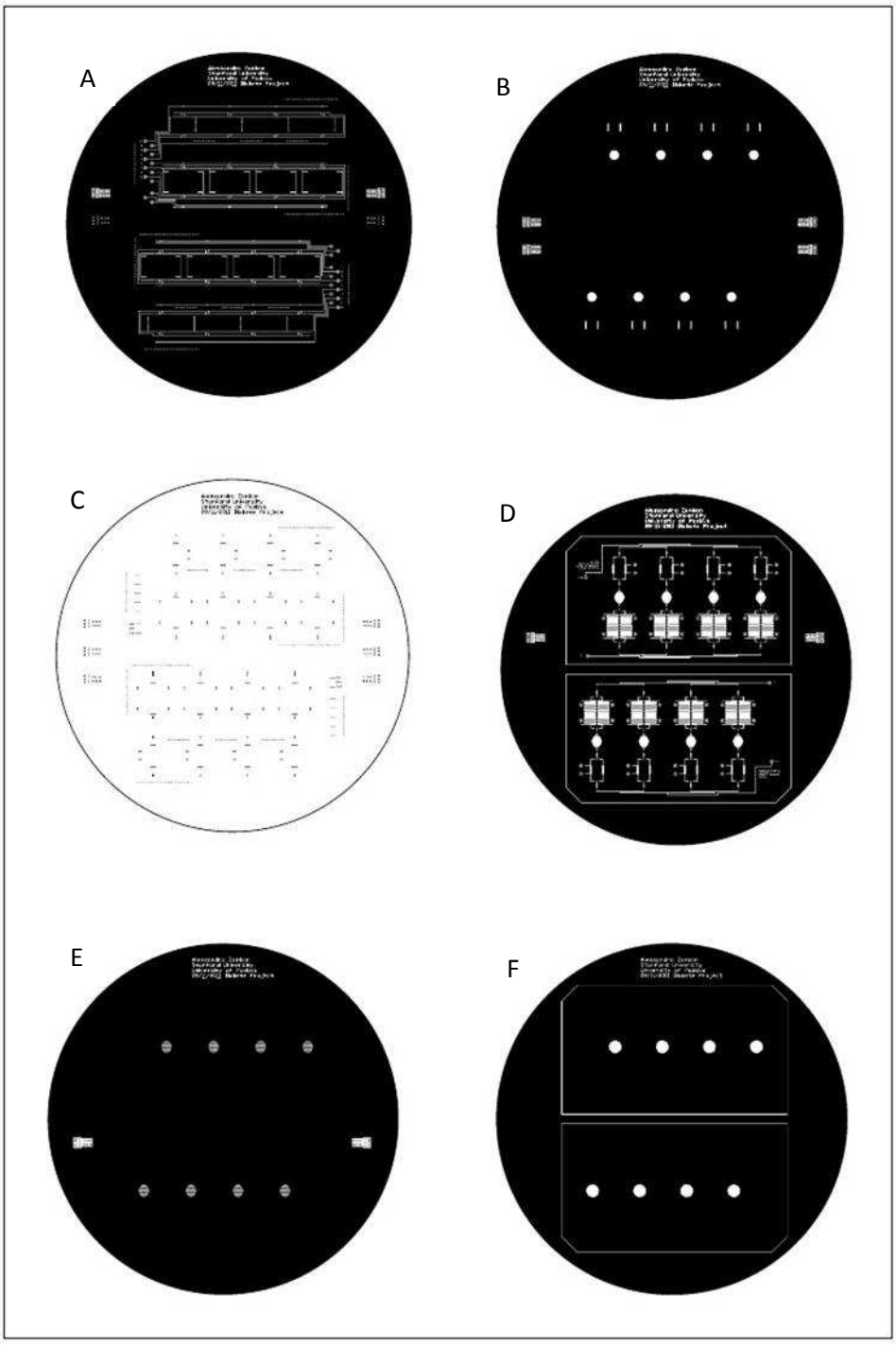

Figure E4*: Single layer mask (Fig.E3) after being painted. The masks are then printed at high resolution.*

E.3.2 Chip design

Chip design is a critical step, because most of the constrain, either of future applications, are decided at this time. Before to start the drawn, very important decisions have been to be chosen, for example valves type, channels and chambers height, channels distribution, number of inputs and outputs, volumes, dimensions ext.

Table E1*: Chip characteristics for the first generation (8 chambers chip) and for the second generation (4 chambers chip)*

Characteristics	First generation	Second generation	unit
Chip material*[1]	PDMS-Sylgard	PDMS-Sylgard	-
Bounding*[1]	Thermal/Plasma	Thermal/Plasma	-
Valve type*[2]	Push up	Push up	-
Valve area	130x170	200x200	µm
Minimum closing pressure	0.6	0.3	bar
Control channel width*[3]	100	200	µm
Flow channel width	170	200	µm
Chamber diameter*[4]	3000	3000	µm
Total chambers number	8	4	-
Micropost diameter	50	50	µm
Chip dimension	62x35	64x36	mm
Round channel height*[5]	30	30	µm
Square channel height*[5]	50	50	µm
Control channel height	25	25	µm
Chamber height*[6]	100	100	µm
Micropost height	15	15	µm
Reservoirs volume*[7]	1	1	µL
Flow Input	8	1/4*[8]	-
Flow output	8	1/4*[8]	-
Control input*[9]	8	13	-
Total valves number	64	68	-
Total pumps number	8	4	-
Total injections number	8	8	-
Total biosensor chambers number*[10]	0	4	

* Table E1 note

1 Sylgard is the most used for mammalian/human cells application in order to its better biocompatibility. Thermal bounding protocol has been modified from the original recipe (with RVT) and adapted for Sylgard 184. Plasma bounding is used to bind the biopsy layer in the application with adipose tissue or to glass slides with muscle cells.

2 Push up valves guarantee higher flow channel and less operative pressure
3 Control channels have a smaller width when they overlap other flow channel than don't have to be closed. The width decrease about 40-50 um.
4 Round chamber for adipose slices insertion. Big diameter guarantee high ratio surface/volume, in order to measure glucose uptake in outlet medium with reasonable flow rate (reasonable flow rate means enough medium sample with a detectable glucose value in short time)
5 Flow channels have round shape only in valve area, therefore they have square shape. Higher square shape avoids sealing when control channels overlap flow channels; moreover they permit the creation of bigger number of valves with a small number of control lines.
6 Total chamber height as results of square flow channel (50) and the space from thin PDMS membrane (50 um) left before further bound to glass slide or biopsy layer (see point 10 in chip procedure A.6)
7 Reservoirs are created with a long channel serpentine before culture chamber. Total volume is enough to change more that the total chamber volume (0,7 µL).
8 In the second generation chip during chip making additional input and output can be created in order to have single input-output for each chamber. When biosensors are used, only one input and output are needed.
9 Control inputs correspond to the number of electron valves needed for the automation.
10 In the second generation chip a biosensor chamber has been added for each chamber. This chamber will collect and analyze glucose and other metabolites on line. This chambers has not to be used yet.

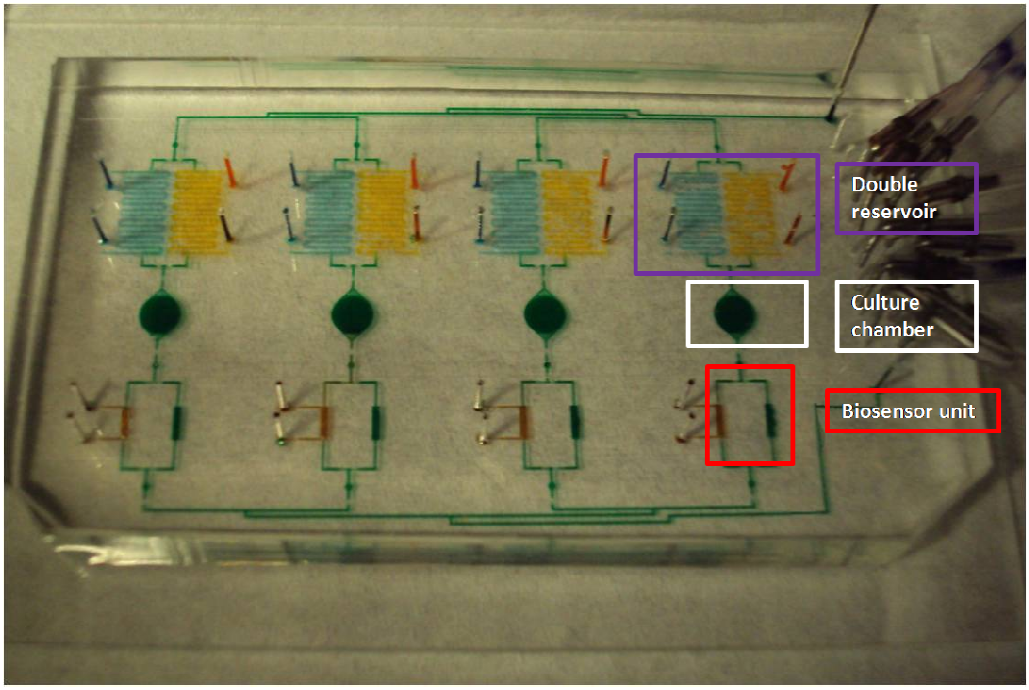

Figure E5*: Picture of second generation chip. With dye are indicated medium channels and chambers (green), double reservoir (blue and yellow) and the biosensor chamber unit (brown). For the first generation chip picture is reported in Chapter 3.*

When a new chip has to be designed, its purposes have to be evaluated with attentions in order to design the best chip for the specific applications. More often a preexistent chip has to be adapted for a study that was not designed for and the researcher will have to evaluate the set of operations that the chip can offer. Table E1 reports characteristics and parameter with some important values of the two chips designed.

E.4 Automation

Automation is achieved by valve control with custom software. Figure E6 shows our lab-made system. All the valves in the chip are driven by miniature pneumatic solenoid valves (24V, CKD Corporation) which are in turn controlled by electronic unit for the generation of digital signal (NI USB-6501, National Instruments) connected to the USB port of a computer. The electronic unit is plugged to a 24V transformer. There is also a system composed of rechargeable battery to guarantee charge during relocation, for example from the incubator to the microscope in another room (up to 15 minutes declared).

Each solenoid valve can switch more valves in the chip between atmospheric pressure (on-chip valve open) and 250 kPa (on-chip valve closed). Custom software developed using Labview® (National Instruments) operates the chip. This software permits fully automated and unattended operation of the system during an experiment.

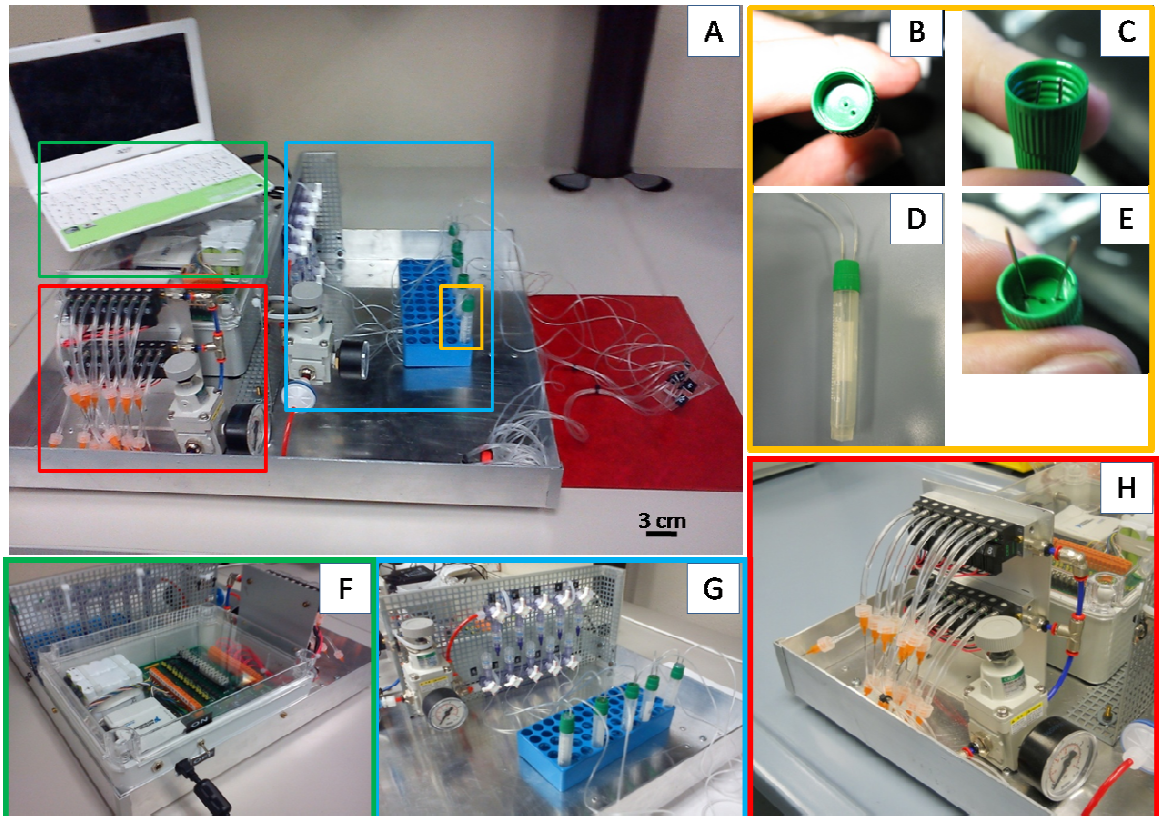

Figure E6*: Automation system: (A) It is mounted on a aluminum plate to easily relocation in different rooms. It is composed of 3 major parts: generator signal (green square), electron valves (red square) and pressurized vials (blue square). (B),(C),(D),(E) Images shows the vial for medium storage and some particulars for its fabrication. (F) Electronic unit for the generation of digital signal, battery and current amplificatory. (G) Pressurized vial system is composed of pressure regulator (CDK, Japan) and 360° polycarbonate luer connector (Cole Parmer). (H) electron valves are connected with 10 cm PVC tube (D4, Panar Automazioni Italy) filled with distilled water. PVC tubes are connected to a male luer (Male Luer Lock X 1/8" Hose Barb, Cole Parmer) and a 23 dispensing needle (Nordson EFD), connected also to 40 cm of Tygon tube (ID 0,02 inch). Tygon tubes end with a steel needle (21G), in order to be plugged to the control input holes.*

Cell culture medium is places inside vials and they are pressurized at 70 kPa using a given gas mixture (typically air or nitrogen). Vials (*Cryovial* -Greiner Bio-one) have 2 holes on the cup in which 2 needles (ID 21G, OD 0.8mm, Chemil) are inserted and sealed with epoxy glue (LOCTITE M-31CL HYSOL, medical device epoxy adhesive). There two needles are the vial inlet for the pressure air and outlet for the medium. The medium outlet has a long tygon tube (ID 0.02 inch OD 0.06 inch, Cole Parmer) that connects the needle to the bottom of the vial; when the vial is pressurized the liquid purges the tube and comes out and purge channels. Driving flows with this positive pressure allows fast

fluid exchange and channel rinsing (the peristaltic pump would be too slow for flushing and rinsing), while at the same time avoiding bubbles. Bubbles only enter the chip when the input tubes are first filled, but they quickly disappear by gas diffusion into the PDMS. Additionally, positive pressure improves the opening speed of the on-chip valves. Precise injection of fresh medium into the chambers for cell feeding is accomplished by using the on-chip peristaltic pump.

E.5 Peristaltic pump

A microfluidic peristaltic pump can be generated by 3 microvalves in series when they are actuated with a specific pump sequence 101, 100, 110, 010, 011, 001 (1 refer valve close, 0 valve open) respectively (Figure E7).

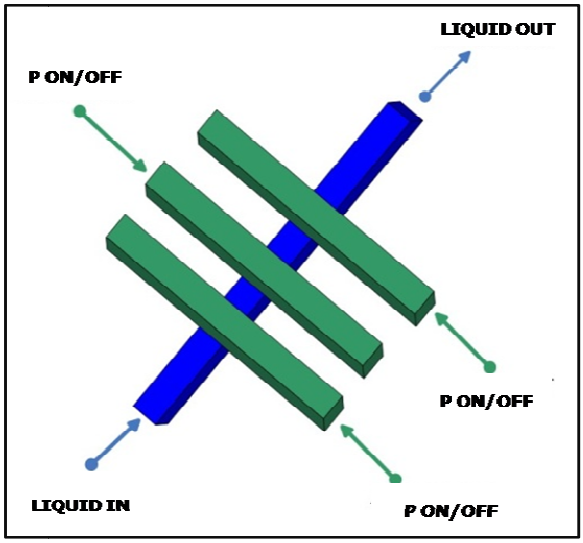

Figure E7*: Schematic image of a peristaltic pump (left) with blue flow channel and green control channels. On the right the actuation pump sequence.*

E.5.1 Pump calibration

Pump calibration has been achieved in order to determine the pumping rates. Pumping rates were determined by measuring the distance traveled by a column of water in thin (ID 0.51 mm, OD 1.52 mm) tubing (Figure E8).

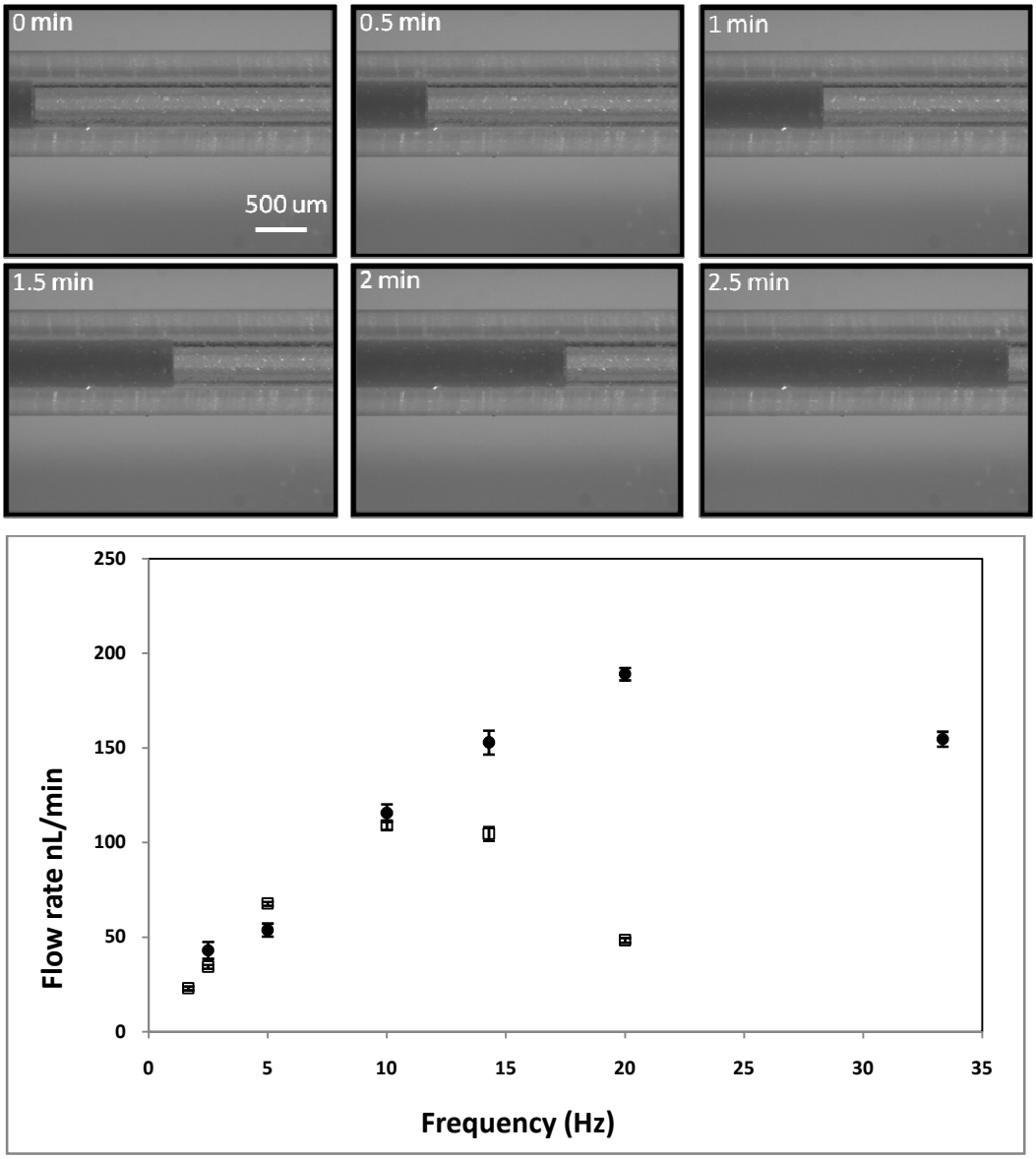

Figure E8*: Time laps images every 30 seconds at 10 Hz in the tube and experimental flow rate values for the first generation chip (black) 130x170x25 µm, and the second generation chip (empty) 200x200x25 µm. Data from 5 experiments for each frequency repeated in 4 different chips.*

E6 References

[1] Younan Xia and George M. Whitesides, Soft lithography,Annual Review of Materials Science Vol. 28: 153-184, DOI: 10.1146/annurev.matsci.28.1.153

[2] Melin and Quake, Microfluidic large-scale integration: the evolution of Design rules for Biological Automation.

[3] Sollier et al., Rapid prototyping polymers for microfluidic devices and high pressure injections, Lab Chip, 2011, 11, 3752

[4] Thorsen et al, Microfluidic Large Scale Integration, Science 2002, vol 298, 380-384

[5] Marc A. Unger, *et al.* Monolithic Microfabricated Valves and Pumps by Multilayer Soft Lithography, *Science* 288, 113 (2000); DOI: 10.1126/science.288.5463.113

[6] Seok Woo Lee and Seung S. Lee, Shrinkage ratio of PDMS and its alignment method for the wafer level process, Microsyst Technol (2008) 14:205–208, DOI 10.1007/s00542-007-0417-y

[7] Sjöberg et al., Analytical Chemistry 79, no. 22 (2007): 8557-8563 (and supporting info)

[8] Stanford Microfludic Foundry, http://www.stanford.edu/group/foundry/

Appendix F

Biological protocols

F.1 Skeletal muscle cells protocol

F.1.1 C2C12 proliferation and differentiation

C2C12 is an immortalized cell line of murine myoblasts. Protocol for cells expansion was described by Zatti *et al.* [1] and adapted for the culture in the microfluidic chip.

Briefly, C2C12 were expanded in tissue culture 10 mm dishes with proliferation medium: Dulbecco Modified Eagle Medium (DMEM, Sigma-Aldrich), 10% Fetal Bovine Serum (FBS, Life Technologies), 1% Penicillin-Streptomycin mix (Life Technologies). Before reaching the confluence, cells were trypsinized with Trypsin-EDTA 0.05% (Life Technologies) and replated either in new dishes or into the microfluidic chip.

Before cell seeding, microfluidic chip was sterilized by autoclave processing. After its sterilization, it is moved into a 35 mm Petri dish under sterile hood and injected with cold Matrigel® (Becton-Dickinson), 5% in DMEM; the chip was kept at room temperature for at least 1 hour. The Matrigel® coating was then removed by washing microfluidic chamber with proliferation medium. A cells suspension was then prepared in order to obtain a cell seeding density of 200 cell/mm^2 and injected in the chip. The bottom of the dish was covered with 1 ml of PBS 1X, in order to maintain proper humidity. The cells were kept in incubator at 37°C, 5% CO_2 for 3 to 5 hours, until they adhered to the bottom glass of the chip. After their adhesion, the chamber is washed with fresh medium. Medium is replaced every 6 hours using a flow rate of 0.1 µL/min by the action

of integrated micropump (or external syringe pump) for 20 minutes. Cells are maintained in incubator.

For manual feeding operation turnover, medium is changed every 12 hours by the help of lateral reservoir well placed on the top of inlet/outlet channels. Medium was changed by adding new medium in the lateral wells and rapidly perfusing it inside the chambers with the help of a vacuum pipette.

Differentiation of C2C12 into myotubes in the chip was achieved spontaneously, after 4 to 5 days from seeding. To help differentiation, medium at this point was replaced every 24 h with same procedure reported for proliferation. Myotubes are clearly visible after 8 days from seeding.

F.1.2 Human Myoblast extraction, proliferation and differentiation

Human primary myoblasts were isolated from skeletal muscle biopsies derived from patient undergoing surgery. Human myoblasts isolation was performed in collaboration with Dr. Karim Bouzakri (University of Genève) following methods reported in [2].

Skeletal muscle biopsy was maintained, right after explant, in physiological solution at +4°C for 2 hours to permit blood coagulation. The biopsy was then processed under sterile hood with scalpels, where the single muscle fibers are isolated from connective, adipose and blood vessel tissues. The isolated fibers was then maintained in a solution 0.05% Trypsin-EDTA at 37°C for 3 hours in order to extract single cell myoblasts precursors. Surnatant trypsin was then moved in a new tube adding an equal amount of Fetal Calf Serum (FCS, Life Technologies) in order to stop its action and avoid cells disruption. The solution of FCS and trypsin is centrifuged at 200 g for 5 min. The pellet was resuspended in 10 ml of Skeletal Muscle Cell Basal Medium (PromoCell) and pre-plated in a Petri dish in order to facilitate fibroblasts adhesion; after 2 h, at the medium was collected and plated in a tissue-culture flask. Primary human myoblasts was visible after 7 days of culture. When myoblasts start to grow, before they reach confluence, they can be passed in culture after trypsinization with Trypsin-EDTA 0.05%.

Cell seeding into the microfluidic chip followed the same procedure described for C2C12 in F.1.1. Differentiation of human myoblasts into the microfluidic chip were achieved by switching the Basal medium with Differentiating Medium composed by DMEM, 2% Horse Serum (HS, Life Technologies) once cells reached confluence. Well differentiated human myotubes were obtained after 8 days in differentiating medium.

F.1.3 Immunofluorescence

Myoblasts and myotubes cultured in the microfluidic chip were analyzed with immunofluorescence analyses. Briefly, cells were fixed with paraformaldehyde (PFA, Sigma-Aldrich), 2% in PBS 1X (Life-Technologies) for 30 min. After washes with PBS, cells were treated with Tryton (Sigma-Aldrich) 0.25% in PBS for 8 min and saturated with HS 2% in PBS. Followed incubation with proper primary and secondary antibodies diluted in BSA (Sigma-Aldrich), 3% in PBS. More specifically, mouse monoclonal primary antibody against Myosin Heavy Chain II (MHC, Sigma-Aldrich) or mouse monoclonal primary antibody against Actinin (Sigma-Aldrich) was applied for 1 h at 37 °C, while the Alexa488 fluorescence-conjugated anti-Mouse IgG secondary antibody (Invitrogen) was applied for 45 min at 37 °C. Nuclei were finally counterstained with DAPI.

F.2 *Ex vivo* adipose tissue

F.2.1 Biopsy preparation

Biopsies of omental adipose tissue are kindly provided from prof. Avogaro from Policlinic Hospital, right after surgery. Protocol for their *in vitro* culture, was adapted from [3]. Before processing, they are maintained in 5 ml of DMEM 5 mM glucose (Sigma-Aldrich), for no more than 3 hours at room temperature. Under sterile hood, biopsy is put in a 100 mm Petri dish, with 5 ml of complete medium (DMEM 5 mM glucose, 10% FBS (Invitrogen), 1% penicillin-streptomycin (Invitrogen)) previously conditioned in incubator (37°C, 5% CO_2, 95% relative humidity) and cut in 4 mm diameter, 1 mm high slides with

sterile punch and scalpel. Each slice is then placed in a 48well plate with 300 µl of complete medium for at least 12 hours before performing dynamic culture, in order to permit sample adaptation.

F.2.2 Biopsy integration within the platform and culture

DMEM 4 mM glucose is previously conditioned in incubator (37°C, 5% CO_2, 95% relative humidity) into a Petri dish, for at least 2 hour. Then medium is loaded in 4 sterile plastic syringes, 3 ml volume (Becton-Dickinson). After the medium loading, inlet Tygon® tubes are then connected to the syringe; medium is then flown inside the tubes. Syringes are set up on the syringe pump (Harvard Apparatus). Helped by sterile tweezers, inlet ends are connected to the microfluidic chip, and the syringe pump is started at 10 µl/min flow rate. Tubes are connected to an empty microfluidic chip. It is conditioned at 1 µl/min for at least 4 hours in order to wash out PDMS residual and avoid cytotoxicity. Flow perfusion is decreased or stopped during biopsy insertion. Chambers are filled with at least 3 biopsy slides for experiments, one slide for one chamber. Sealing is ensured covered with biocompatible sterile PMMA and PDMS cup. One microfluidic chamber is kept empty as control for glucose concentration measurements. Microfluidic platform system is finally put in the incubator for the culture. Pumps are set at a flow rate of 25 nl/min.

F.2.3 Hematoxylin & Eosin stain

At the end of the cultures, adipose tissue biopsies can be frozen for further histological analyses. Adipose tissue slides are removed from the microfluidic chip, embedded in liquid OCT® and rapidly passed in liquid nitrogen and stocked at -80°C. Each sample was then cryosectioned into 20 um thick slices. Cryosections were cut onto poly-L-lysine coated glass microscope slides (SuperFrost® Menzel-Glazer) and slides store at -80°C.
Hematoxylin and Eosin (H&E) is an hystochemical analysis that permit to visualize cytoplasm in orange/red and nuclei in violet/blue. Briefly, slides with adipose tissue cryosections were kept at room temperature for 10 min approximately. Then slides were

passed in Hematoxylin (Sigma-Aldrich) for 2 min, followed by a rinse with running tap water for 15 min. Slides were passed in Eosin (Sigma-Aldrich) for 2 min and dehydrated with three consecutive passages in increasing concentration of ethanol: EtOH 80% for 1 min, EtOH 96% for 3 min, absolute EtOH for 5 min. At the end slides were mounted with mounting medium HI-MO (Lab-Optica).

F.2.4 MTT

MTT test permits to evaluate adipose tissue viability. 1 ml of MTT (Sigma-Aldrich), 0.5 mg/mL in PBS, is added to samples and incubated for 3 h at 37°C. Solution is then removed, and 1 ml of 10% DMSO (Sigma-Aldrich) in isopropanol (Sigma-Aldrich) is added. DMSO/isopropanol solution is incubated at 37°C and maintained until complete dissolution of the salt formed by the MTT. Surnantant is finally removed and absorbance read at 580 nm.

F.3 References

[1] Zatti S. et al. 2012. Langmuir. 28(5):2718-26.

[2] Bouzakri K. et al. 2003. Diabetes. 52(6):1319-25.

[3] Smith U. 1974. J Clin Invest. 53(1):91-8.